Improving the selectivity of nickel-based catalysts for vapour-phase furfural hydrogenation

KATHRYN LOUISE MACINTOSH

Improving the selectivity of nickel-based catalysts for vapour-phase furfural hydrogenation

Department of Chemistry, Durham University

2018 – 2022

Thesis submitted for the degree of Doctor of Philosophy

By

Kathryn Louise MacIntosh

Declaration

This thesis is based on work carried out by the author in the Department of Chemistry at Durham University, during the period October 2018 – January 2022. All of the work detailed in this thesis is original, unless specifically acknowledged in the text or references. None of this work has been submitted for another degree in this or any other university.

Copyright

Abstract

Furfural is a key bio-based platform chemical, and its hydrogenation allows access to a variety of important chemical intermediates, particularly furfuryl alcohol, which is widely used to make resins. Here, nickel and tin-nickel catalysts have been thoroughly investigated for vapour-phase furfural hydrogenation as a replacement for the highly carcinogenic and environmentally damaging current commercial catalyst, copper chromite. The addition of tin to incipient wetness impregnation (IWI) nickel-based catalysts (metal particle size: 9 ± 4 nm) resulted in a markedly improved selectivity to furfuryl alcohol of up to 86 %; however mass activity was decreased by an order of magnitude. A commercially available copper chromite catalyst was used for comparison and exhibited similar mass activity and stability to the tin-doped IWI catalysts but with a slightly higher furfuryl alcohol selectivity of around 90 %. To understand the selectivity change that occurred upon the introduction of tin, more well-defined and uniform SnNi-based catalysts were prepared by synthesising colloidal SnNi bimetallic nanoparticles. Smaller nanoparticles (~4 nm) could be successfully synthesised using only an amine capping agent, however larger nanoparticles (12 – 15 nm) required a phosphine capping agent. The use of a phosphine capping agent led to phosphorus incorporation into the surface of the nanoparticles (as shown by near ambient pressure X-ray photoelectron spectroscopy (NAP-XPS)), even when the bulk structure exhibited no evidence of phosphorus incorporation. Silica supported small phosphorus-free SnNi nanoparticles (Ni:Sn molar ratio of ~3) had a superior furfuryl alcohol selectivity (96 %) when compared to the IWI catalysts, however significant sintering occurred in the *in situ* reduction step prior to reaction (*i.e.* the active catalyst was sintered). The silica supported nanoparticles prepared with a phosphine capping agent exhibited minimal to no sintering. The presence of phosphorus in nickel nanoparticles led to an increased furfuryl alcohol selectivity (~67 %) when compared to IWI nickel and amine-capped nickel nanoparticle catalysts (~50 %). The furfuryl alcohol selectivity of the phosphine capped nanoparticles could be further improved by the introduction of small amounts of tin, reaching around 92 % for nanoparticles with a Ni:Sn molar ratio of ~18. NAP-XPS was used to investigate the structure and composition of the nanoparticles, revealing the top surface of both the small phosphorus-free and larger phosphorus-containing nanoparticles consisted of a tin-nickel phase with a Ni:Sn molar ratio of ~3, followed by a tin rich layer and then a nickel-based core. This provides a potential explanation for the similar furfuryl alcohol selectivities achieved by the nanoparticle catalysts, despite the very different bulk Ni:Sn molar ratios. Overall, the introduction of tin to nickel catalysts was found to drastically improve the furfuryl alcohol selectivity during vapour-phase furfural hydrogenation, affording a potential less toxic alternative to chromium-based catalysts for a future bio-refinery process.

Acknowledgements

Firstly, I would like to thank my supervisor, Dr. Simon Beaumont, for all the advice, guidance and support throughout my PhD (and putting up with all my silly questions!).

I would also like to thank Dr. Phil Dyer for his advice and support, Prof. John Evans for carrying out the Rietveld refinements and helping to interpret my pXRD data and Dr. Nicole Hondow for the STEM-EDX analysis.

A lot of the characterisation included in this thesis would not have been possible without the guidance and support of the excellent analytical staff members in the Chemistry and Physics departments at Durham University and so I would like to thank them for all their help. Additionally, I would like to thank Prof. Georg Held and the other beamline scientists at B07, Diamond Light Source, for their guidance and advice with the NAP-XPS experiments.

I would also like to acknowledge the EPSRC for providing the funding for this project (EP/R513039/1).

I have very much enjoyed my time at Durham, and a large part of that has been due to my group and the many other friendly and helpful people in the department that I have met throughout my PhD. I am very grateful for all of their help and support - and for the (occasional…) distraction from my work, which was definitely necessary at times!

Finally, I would like to thank all my friends and family who put up with all my complaining, listened to many of my presentations (thanks Beth!) and nodded along as I told them about my latest interesting experiments/results!

This thesis is dedicated to my pancreas, who made a great (but probably unnecessary) sacrifice in order for me to complete my PhD.

Table of contents

List of Abbreviations

2-MF – 2-methylfuran

acac (*e.g.* $Ni(acac)_2$, $Pt(acac)_2$) - acetylacetonate

AES – Auger electron spectroscopy

BET - Brunauer, Emmett and Teller

BF – bright field

BTB – borane *tert*-butylamine complex

CCD – charge coupled device

CNT – classical nucleation theory

CP – cross polarisation

CPME - cyclopentyl methyl ether

DBE – dibenzyl ether

DCM - dichloromethane

DPE – diphenyl ether

DRIFTS – diffuse reflectance infrared Fourier transform spectroscopy

EDX – energy dispersive X-ray (analysis)

EI – electron ionisation

$\mathbf{E_{ph}}$ – photon energy

fcc – face centred cubic

FFT – fast Fourier transform

FID – flame ionisation detector

FOL – furfuryl alcohol

FUR – furfural

FWHM – full width at half maximum

GC-FID – gas chromatography – flame ionisation detector

IWI – incipient wetness impregnation

KE – kinetic energy

LDH – layered double hydroxide

m/z – mass-to-charge ratio

MAS – magic angle spinning

MOF – metal-organic framework

NAP-XPS – near ambient pressure – X-ray photoelectron spectroscopy

OAm – oleylamine

PEG – polyethylene glycol

PMT – photomulplier tube

PTFE - polytetrafluoroethylene

PVP – polyvinylpyrrolidone

pXRD – powder X-ray diffraction

SEM – scanning electron microscopy

SMSI – strong metal support interactions

SS NMR – solid state nuclear magnetic resonance (spectroscopy)

SSIMS – static secondary ion mass spectrometry

STEM – scanning transmission electron microscopy

TCD – thermal conductivity detector

TDS – thermal desorption spectroscopy

TEM – transmission electron microscopy

TGA – thermogravimetric analysis

THFA – tetrahydrofurfuryl alcohol

TOP – tri-n-octylphosphine

GC-MS – gas chromatography – mass spectrometry

HAADF – high angle annular dark field

HPPD - high power proton decoupling

HRTEM – high resolution transmission electron microscopy

ICP-MS – inductively coupled plasma – mass spectrometry

ICP-OES – inductively coupled plasma – optical emission spectroscopy

ICSD - inorganic crystal structure database

TOS – time on stream

TPO – temperature programmed oxidation

TPR – temperature programmed reduction

UHV – ultra high vacuum

UV – ultraviolet

XPS – X-ray photoelectron spectroscopy

XRF – X-ray fluorescence

Chapter 1: Introduction

The demand on fossil fuels for energy and various consumer products is increasingly unsustainable, with a major focus now placed on the use of renewable and environmentally friendly resources. One such resource is biomass, due to the more renewable and sustainable nature of the feedstock. However, biomass can be a challenging material to successfully process due to the complexity of the chemical structures, increased functionalisation and higher oxygen levels compared with more traditional petrochemical feedstocks.[1, 2]

In order to efficiently and selectively produce useful chemicals and fuels from complex biomass materials, the development and understanding of selective, active and stable catalysts is crucial. A catalyst is defined as a material that lowers the activation energy of a reaction, thereby increasing the reaction rate of one or more possible product pathways, whilst not being consumed in the process.[3] The selectivity of a catalyst is highly dependent on whether the catalyst lowers the activation energy of a single pathway significantly more than others, or whether it lowers the activation energy of several pathways by a similar amount; the latter would lead to several products and poor selectivity. There are three main categories of catalysts; enzymatic which involves the use of a biological catalyst; homogeneous where the catalyst is in the same phase as the reagents (*e.g.* both in the liquid phase) and heterogeneous where the catalyst is in a different phase to the reagents (*e.g.* solid catalyst with liquid or gaseous reagents).[3] Heterogeneous catalysts are most widely used in industry, mainly due to the significantly simplified separation of the products and catalyst compared to homogeneous systems, which often require separation by expensive and wasteful distillations or extractions.[4, 5]

Whilst the use of biomass for the production of chemicals and fuels clearly has benefits compared to petrochemical feedstocks, the widespread use of food crops for biomass is a concern, as is the case for so-called 'first generation' bio-fuel systems. In order to sustain current fuel and chemical requirements, a huge demand would be placed on food crops, leading to a substantial increase in the price of staple foods, whilst at the same time reducing biodiversity. Additionally, there are concerns regarding the environmental impact and economic efficiency of these processes.[1, 6] The use of lignocellulosic biomass, such as corncobs, bagasse and oat husks amongst many others, is one way of reducing the impact on food prices since these materials are inedible and generally regarded as waste. These systems, which use lignocellulosic biomass rather than food crops, are referred to as 'second generation'. The economic efficiency can be improved by producing value added chemicals from biomass, as opposed to fuels, since the generally higher market prices of the products make this a more economically feasible option.[1]

Furfural is frequently discussed in the literature as a bio-derived chemical of interest since it has a variety of uses (Figure 1 and Table 1).[1, 2, 7, 8] The global production of furfural is estimated to be around 270000 tonnes per year.[7] It can be used directly as a processing agent in lubricant oil manufacture or in the flavourings and perfume industry, however most of the current feedstock (~60%)[9] is hydrogenated to furfuryl alcohol (FOL) for use as an adhesive, resin or corrosion resistant coating.[10, 11]

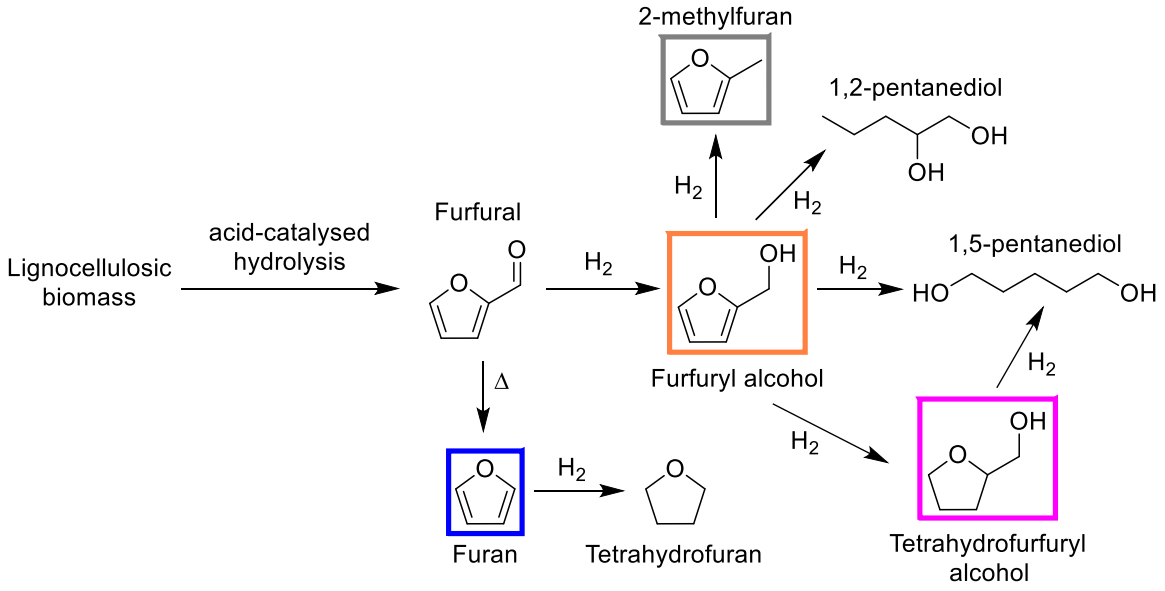

Figure 1: Scheme showing products formed during the hydrogenation of furfural

Table 1: The potential uses of products from furfural hydrogenation

Product	Potential uses
Furfuryl alcohol	Resins for use in the foundry industry, viscosity reducers for epoxy resins, polyesters, polyurethane foams, fragrances[7, 8]
Tetrahydrofurfuryl alcohol	Solvent, printing inks, cleaner for electronics, biocides and pesticides for the agriculture industry[7, 9, 12, 13]
2-methylfuran	(Mainly) production of anti-malarial drugs, other heterocycles (N- or S-containing)[7, 9]
Furan	Solvent, production of nitro- and sulphur-substituted furans used as biocides/fungicides and flavourings respectively[7]

The production of furfural was first developed by Quaker Oats, who described an economically viable production method in a patent filed in 1922.[14] Whilst the intricacies of the current production methods are generally not revealed in detail, it is most commonly prepared by variants of the general process outlined in Figure 2.[7]

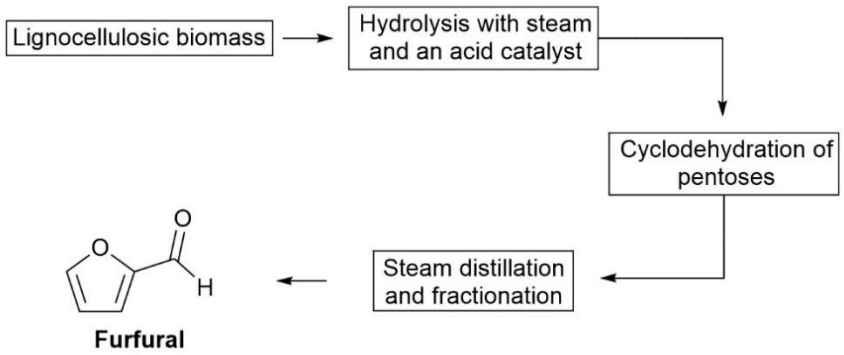

Figure 2: Schematic overview of the common method for producing furfural[7]

In order to then hydrogenate furfural into the important commercial product FOL, copper chromite catalysts are generally employed.[15] However, these catalysts contain highly carcinogenic and mutagenic Cr(VI). This is strictly regulated in many parts of the world, including the EU where under the REACH regulations, chromium trioxide is listed as a 'substance of very high concern' and included in the candidate list of chemicals that require authorisation before use.[16] The significant health concerns, along with the likely costs and time required to address these concerns, make this catalyst less attractive for industry. Consequently, the development of a novel catalyst to replace the current copper chromite-based system is greatly needed.

This review will discuss the current relevant catalysts described in the literature for furfural hydrogenation and the possible approaches for improving the performance of replacement catalysts. Key methods for producing more uniform, model versions of promising catalysts that can be used to aid their study will also be examined.

1.1 Copper chromite catalysts

In a patent filed in 1931, Röhm and Haas described the use of a copper chromite catalyst including an alkali or alkaline earth oxide promoter for the hydrogenation of furfural.[17] They reported that this catalyst had improved properties including higher yields, shorter reaction times and increased stability compared to any other previous catalysts, including nickel-based catalysts. There are additionally reports in the literature around the same time describing copper chromite catalysts with alkaline earth promoters for similar hydrogenations.[18] However, without advanced analytical techniques, the understanding of how this catalyst operated was limited.

Whilst copper chromite-based catalyst formulations have been widely used to carry out furfural hydrogenation for many years, they have also been extensively used for several other significant hydrogenation reactions such as the water-gas shift reaction and the synthesis of methanol from syn-gas. Since these are industrially important, there is a significant body of literature on copper chromite catalysts for these reactions. Therefore, whilst it is important to note that different reactions may rely on different active sites, even when using similar catalysts, reports that discuss catalyst properties such as the structure or the nature of any active sites present, are still likely to be worth consideration.

Monnier *et al.*[19] investigated a copper chromite catalyst for the production of methanol from H_2 and CO. Based on an XRD study, they reported that the reduced catalysts contained $CuCrO_2$ (rhombohedral structure; space group R -3 m H; ICSD code: 26676[20] ‡) and that the maximum specific methanol activity correlated well with the concentration of $CuCrO_2$. Consequently, they suggested that the catalytic activity was linked to the concentration of $CuCrO_2$. Additionally, an XPS study was used to investigate the oxidation states of copper on the surface of the catalyst and found that the catalytic activity increased with increasing surface concentrations of Cu^+. The highest surface concentrations of Cu^+ also correlated well with the samples that had the highest $CuCrO_2$ concentrations as determined by XRD. This suggests that the active site is Cu^+, which exists as the stable crystalline phase, $CuCrO_2$. Without the presence of the chromium oxide, the reducing conditions of the reaction (*i.e.* H_2) would likely lead to the formation of Cu^0 metal, which provides a plausible explanation for the requirement of chromium in the catalyst.

There is some debate regarding the active site or sites present on copper chromite-based catalysts for hydrogenation reactions such as furfural hydrogenation or the hydrogenation of α,β-unsaturated carbonyl compounds in general.[21] Some refer to the work of Monnier *et al.*[19], as discussed above, that suggests Cu^+ sites are the sole active sites on copper chromite catalysts. Others, such as Rao *et al.*[21] who investigated furfural and crotonaldehyde hydrogenation, agree that a strong correlation between the number of Cu^+ species and catalytic activity suggests that Cu^+ sites are involved in the reactions. However, they propose that since H_2 dissociation should occur more readily on Cu^0 than Cu^+ sites, both active sites are required for successful hydrogenation.

Ultimately, whilst there is debate over the nature of the active sites in copper chromite catalysts, most reports appear to agree that the presence of Cu^+ sites is necessary. This means chromium is playing a crucial role in the stability of the active sites in copper chromite catalysts and so achieving an effective copper-based catalyst without chromium may be challenging.

‡the authors did not report the full diffraction pattern, the source of the data used to confirm identification or the structure/space group of the phase reported, however the position of the most intense reflection ($CuCrO_2$(200)) is consistent with the data in this ICSD entry from Dannhauser *et al.*[20] and therefore the information regarding structure/space group included above is based on the data from this paper

1.2 Nickel catalysts

Nickel catalysts are generally regarded as low cost and are typically highly active for simple hydrogenation reactions such as CO methanation and the hydrogenation of vegetable oils.[22] However, this high activity can often come at the cost of selectivity and stability, with nickel catalysts known to suffer significant deactivation due to coking.[23] Despite these possible drawbacks, the generally high activity of nickel catalysts means that they have been investigated for furfural hydrogenation.

Whilst nickel catalysts have been reported for the liquid-phase reaction,[13, 24-27] this thesis focuses on the vapour-phase reaction; as such, these examples are more relevant and will be discussed in further detail. A summary of the catalytic performance of nickel-based catalysts reported in the literature for vapour-phase furfural hydrogenation can be found in

Table 2, along with some examples of copper chromite as a reference. Nakagawa *et al.*[28] investigated the use of Ni/SiO_2 catalysts for vapour-phase furfural hydrogenation. The authors found that FOL was the favoured product at low furfural conversions, but the selectivity for tetrahydrofurfuryl alcohol (THFA) rapidly increased at high conversions of furfural. This suggested that there was a competitive adsorption of furfural and FOL, and that furfural was more strongly adsorbed onto the nickel catalyst than FOL. Hence, at low conversions, FOL is the dominant product, but this switches to THFA at conversions close to 100 %. It should also be noted that the catalysts reported appear to be very selective, producing either FOL or THFA in varying amounts dependent on conversion. However, the reaction temperature is an important consideration here. The authors carried out the reaction at 130 °C, which is around 30 °C lower than the boiling point of furfural (~162 °C), meaning that the furfural is likely condensing on the catalyst bed. It is unclear what effect this may have on the catalysis, but lower reaction temperatures would, in general, be expected to lead to increased selectivity and so this may be a contributing factor to the high selectivity observed for these catalysts. The catalysts were in general found to be relatively active, however the operating conditions did have an impact on both catalyst activity and selectivity. Under the conditions used to achieve a high FOL selectivity of 95 % (W/F (defined as mass of catalyst/flow rate): 0.053 g_{cat} h mol_{total}^{-1}, temperature: 130 °C, gas composition: furfural:H_2:N_2 1:18:90), the activity was found to be 91 $mmol_{prod}$ g_{cat}^{-1} h^{-1}.

Vargas-Hernández *et al.*[29] investigated SBA-15 supported nickel catalysts for vapour-phase furfural hydrogenation and decarbonylation. The highest FOL selectivity was achieved by the 20 wt. % nickel catalyst at 170 °C, however this was still only 53 %, with a range of other products also forming including furan. The catalyst was found to have a relatively low activity of 5.5 $mmol_{prod}$ g_{cat}^{-1} h^{-1}. The

selectivity changed when the reaction temperature was increased to 230 °C, with the 5 wt. % nickel catalyst having a furan selectivity of 98 % at 5 h time on stream (TOS). Therefore, for nickel catalysts, increasing reaction temperature appears to significantly favour the decarbonylation pathway to furan, over hydrogenation to FOL. It is important to note however that the reagent feed used in this paper consisted of 5 v/v% furfural in cyclopentyl methyl ether (CPME), rather than pure furfural, and it is unclear whether this would have any impact on the catalysis.

Nickel-based hydrotalcite catalysts (Ni-Mg-Al) have also been considered for vapour-phase furfural hydrogenation.[30] The authors were able to achieve a high furfuryl alcohol selectivity of 89 %, however the activity of the catalyst was moderate at around 32 $mmol_{prod}\ g_{cat}^{-1}\ h^{-1}$. The authors hypothesise that the combination of Ni^0 metal sites and strongly basic sites led to the high FOL selectivity. The adsorption *via* the C=O group onto basic sites would produce an activated nucleophilic oxygen species, which would promote the addition of dissociated hydrogen from the nickel metal surface.

Jones *et al.*[31] investigated nickel-based mixed metal oxide catalysts for vapour-phase furfural hydrogenation. The authors evaluated both Ni-Mg-Al and Ni-Co-Al catalysts and found that they consistently had a FOL selectivity of ~80 %. Whilst all catalysts had very similar selectivities, the activities did vary, with the optimal catalyst composition (1.1Ni-0.8Co-Al) found to give an activity of 440 $mmol_{prod}\ g_{cat}^{-1}\ h^{-1}$. In comparison to the similar hydrotalcite-based catalysts discussed above[30], the mixed metal oxide catalysts are an order of magnitude more active, however they are also less selective.

A nickel catalyst that was supported on a rice-husk derived carbon-silica support was reported by Kang *et al.*[32] for vapour-phase furfural hydrogenation. With their optimised catalyst (15 wt. % Ni), they reported a high furfuryl alcohol selectivity of 96 %, however the activity was low at 11 $mmol_{prod}\ g_{cat}^{-1}\ h^{-1}$. There was also a roughly 15 % decrease in conversion over the course of 10 h TOS, indicating that the catalyst does suffer some deactivation, which the authors hypothesise is due to coking.

Overall, nickel catalysts can exhibit relatively high activities, however those that were found to have a high furfuryl alcohol selectivity, generally had lower activities. This implies that there is likely an inverse relationship between activity and selectivity, and therefore, a careful balance is likely required to achieve an optimal catalytic performance. Additionally, this also suggest that it is possible to achieve a high furfuryl alcohol selectivity with modified nickel-based catalysts.

Table 2: Comparison of literature nickel and copper chromite catalysts run in vapour phase or pseudo-vapour phase (trickle bed) continuous reactors; mass activities were calculated at low conversions where possible, however some examples only included data for close to 100 % conversion; [a]mass activity after 0.5 h TOS; [b]mass activity after 1 h TOS, [c]estimated value since this is a commercial sample and the exact composition is unknown; [d]mass activity at 4 h TOS.

Catalyst	**Ni or Cu loading / wt. %**	**Temperature / °C**	**Mass activity after 5 h TOS / $mmol_{fur}\ g_{(cat)}^{-1}\ h^{-1}$**	**Furfuryl alcohol selectivity / %**	**Furfural:H_2 ratio**
Ni/SiO_2[28]	10	130	91[a]	95	1:18
Ni/SBA-15[29]	20	170	5.5	53	1:12
1.1Ni-0.8Co-Al mixed metal oxide[33]	57	155	440[b]	79	1:25
Mg:Al:Ni (MAN-2)[34]	48	180	32	89	1:3
Ni/carbon-silica (15Ni/RHCS)[35]	15	180	11	96	1:7
Copper chromite (Cu 1800P)[36]	40[c]	200	42[d]	96	1:25
Copper chromite (Cu 1800P)[37]	40[c]	180	9	99	1:2.5
Copper chromite[38]	40	200	18	94	1:25

1.3 The role of the support

Metal catalysts are commonly supported since this can often lead to highly dispersed small metal particles and increased stability to sintering due to the interactions between the support and the metal.[39-41] These supports are sometimes thought of as inert, since the catalysis is occurring *via* the active sites on the metallic particles. However, the supports used can often play a role in the catalysis, such as through the introduction of acidic/basic sites or effects such as strong metal support interactions (SMSI), both of which are discussed further below.

1.3.1 Acidity of the support

Certain supports contain acid sites, which, dependent on strength and nature (*i.e.* Lewis versus Brønsted), can have an impact on catalysis. Silica is often considered inert due to the relatively weak nature of the Brønsted acidic silanol groups on its surface.[42-44] However, when using a silica support for furfural hydrogenation, this weak acidity should still be considered, since the polymerisation of both furfural and furfuryl alcohol is catalysed by acid sites.[45-49] The formation of furfural or furfuryl alcohol oligomers or polymers may contribute to coking and therefore the deactivation of the catalyst.

Another common support is alumina and it is known to predominantly have Lewis acidic sites, which are present due to coordinatively unsaturated aluminium ions, although small numbers of Brønsted acid sites are also often present on alumina.[50-52] Titania is also known to contain weakly acidic Lewis acid sites, however typically Brønsted acid sites are not present.[53, 54] Similarly, ceria also contains weakly acidic Lewis acid sites.[55] Most reports discussing furfuryl alcohol polymerisation use Brønsted acid catalysts,[45-48] however the use of a Lewis acidic catalyst and a catalyst that had a combination of Lewis and Brønsted acidic sites has been reported.[56] The presence of any acidic catalyst was found to increase the efficiency of the furfuryl alcohol polymerisation compared to the thermally induced reaction. However, the presence of Brønsted acid sites promoted polymerisation more than when only Lewis acid sites were present, allowing the polymerisation occur at lower reaction temperatures (T_{max} of 122 - 124 °C versus 162 °C) and leading to an increase in the total heat released during the reaction.[56] A combination of Lewis and Brønsted acid sites was found to be optimal for furfuryl alcohol polymerisation. Therefore, a support that only contains weak Lewis acid sites, such as titania or ceria, as opposed to a support with Brønsted acid sites (*e.g.* silica) or a support with a combination of both types of acid site (*e.g.* alumina), may help to limit furfuryl alcohol oligomerisation and therefore catalyst deactivation.

1.3.2 Strong metal support interactions

For many years, catalyst supports were generally regarded as inert. However, based on work carried out by Tauster *et al.,*[57-59] it was discovered that certain supports, such as titania, could form 'strong metal support interactions' (SMSI). This interaction between the metal particles and the support occurred after activation at elevated temperatures in H_2 gas. The initial experiments that revealed the strange behaviour explained by SMSI involved H_2 and CO chemisorption experiments on group 8-10 metals supported on titania that had either been reduced in H_2 at 200 °C or 500 °C.[57] In the case of the samples reduced at 500 °C, the amount of H_2 or CO adsorbed was greatly lowered compared to the amount adsorbed by the samples reduced at the lower temperature and in most cases was actually close to zero. This behaviour could potentially be explained by the metal particles sintering during reduction at the higher temperature and the authors report that the formation of particles of between 10 - 25 nm could potentially explain the results. However, a combination of pXRD and TEM revealed this was not the case, with the TEM study giving an average particle size of around 3 nm in the samples reduced at 500 °C. Another potential explanation for the results involves encapsulation of the metal particles due to the collapse of the pores in the support. Again however, evidence suggests this is not the case, since, for example, the BET surface area of the materials remained almost constant after reduction at both temperatures. Poisoning of the catalyst from impurities in the titania could also potentially lead to the observed results, however the authors report the levels of impurities present would have very little impact on the amount of H_2 or CO adsorbed and cannot explain the dramatic effect observed. Therefore, the authors conclude that the most likely explanation is SMSI, in which at elevated temperatures, the noble metal atoms form bonds with the titania support and these electronic interactions result in the changes in the properties of the materials observed.

Later reports suggested that another possible explanation for SMSI effects was the migration of the titania support onto the surface of the metal particles, which could account for the large decrease in the ability of the metal particle to adsorb H_2 and CO.[60] The authors used a model Rh/TiO_2 system for their experiments, consisting of an oxidised Ti(0001) single crystal onto which rhodium was vapour deposited. Using a combination of surface science techniques including static secondary ion mass spectrometry (SSIMS), thermal desorption spectroscopy (TDS) and Auger electron spectroscopy (AES), the authors were able to observe the presence of reduced TiO_x (where $x<2$) on the surface of rhodium overlayers after heating the sample to 502 °C. This potentially suggests that in some cases the reason for the lowered chemisorption ability of the metal particles could be that the active sites are being blocked by the migration of reduced titania deposits.

In more recent years, the term 'SMSI' has been more generally used to describe any effects on the catalytic behaviour of group 8-10 metals supported on a reducible oxide after an elevated temperature reduction step, rather than just reasoning to explain a loss of chemisorption capacity.[61] When considering general effects on catalysis, electronic and geometrical reasoning did not explain all the changes in catalytic behaviour. Therefore, a third effect, proposing changes to active sites at the boundary of the metal and the support, was explored to explain some observed differences in activity and selectivity. For example, Efstathiou *et al.*[62] investigated the kinetics and mechanism of the water gas shift (WGS) reaction (CO/H_2O to CO_2/H_2) using a Pt/TiO_2 catalyst and proposed that the boundary of the platinum particles and the titania support played an important role. The authors suggested that the CO adsorbs on the platinum particles before diffusing towards the boundary with the titania. At this metal-support boundary, the CO molecule reacts with labile oxygen from the titania and produces CO_2 (see Figure 3). The strong interaction between the metal particles and the support is essential to produce suitable sites at the boundary in order to allow the adsorbed CO to 'spillover' onto the titania and react with an oxygen atom.

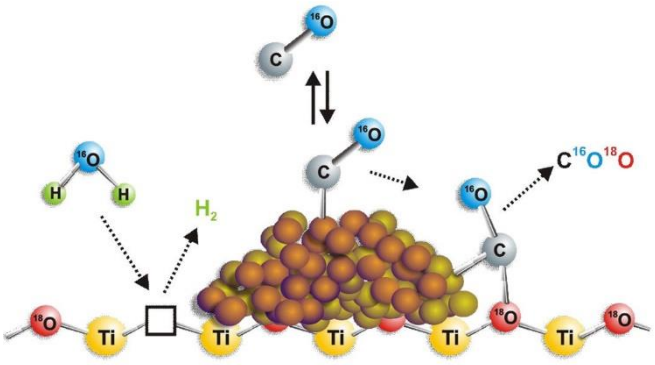

Figure 3: Illustration of the importance SMSI effects involving the metal-support boundary in WGS reaction with a Pt/TiO_2 catalyst,[62] reprinted with permission from Efstathiou *et al.*[62]. Copyright 2009. Elsevier.

Overall, if using supports that are prone to SMSI, such as titania, it is important to take into account these effects when interpreting catalytic data. Additionally, since high temperature treatments promote SMSI effects, the catalyst pre-treatment conditions should be carefully considered.

1.4 Bimetallic catalysts

As discussed above, nickel catalysts typically require modification in order to achieve a high furfuryl alcohol selectivity. One such way to modify the catalyst is the introduction of a second metal to produce a bimetallic catalyst. Therefore, it is instructive to first consider some key points regarding bimetallic catalysts in general, before then discussing bimetallic nickel catalysts for furfural hydrogenation.

1.4.1 Surface structure

When discussing doping the surface of metal nanoparticles, it is first important to understand the typical structures and sites present on the surface of metal nanoparticles. The formation of a surface must be energetically unfavourable otherwise, thermodynamically, atoms would tend to move from the bulk to the surface of a particle.[63] Therefore, surfaces must require more energy than the bulk and this can generally be explained by the fact that the atoms at the surface have less neighbouring atoms than those in the bulk. In order to minimise the energy requirements of the surface, changes in the surface structure can occur, such as the surface layers contracting in the direction perpendicular to the surface or more significant surface reconstruction in the top layers. Solid surfaces of particles also almost always contain steps or kinks, which are thought to arise from slight orientational differences in the atomic planes. The flat surfaces in between these steps and kinks are referred to as terraces. Notably for catalysis, there are differences between planar surface sites (such as those in the terraces), edge sites and corner sites, since edge sites are less coordinated than planar sites and corner sites are even less coordinated than edge sites. This means that different sites on the surface of the particle have different energies, with edge and corner sites being of higher energy than the planar sites. Therefore, in structure sensitive reactions, this generally translates to edge and corner sites being more reactive than those on the flat surface.[63] Additionally, the adsorption geometry of reagents on these sites may be different, which can lead to altered selectivity depending on the numbers of each site present.

The size of metal particles is highly important to achieve high catalytic activities, primarily because smaller particles give higher metal surface areas. The size of the particles also effects the relative ratio of corner and edge sites to planar sites. Figure 4 shows how the fraction of edge/corner (low coordination) and planar (higher coordination) surface sites, with respect to the total number of atoms, vary with particle size for a nickel face centred cubic (fcc) cubooctahedron (structure depicted in Figure 5).[64-66] The equations used for these calculations are shown in Appendix 1. As the size of a particle increases, the fraction of planar sites initially increases before slowly decreasing as the fraction of total surface sites decreases. The fraction of corner/edge surface sites is initially high but decreases rapidly as particle size increases. Therefore, smaller particles have a higher ratio of corner/edge surface sites, relative to the fraction of planar surface sites, than larger particles. Additionally, the largest change in the fraction of edge/corner sites occurs over a particle size range of around 1 – 7 nm, indicating that this is a more important consideration for small nanoparticles in this size range. Overall, the particle size can impact not only the number of active sites available (through increased surface area), but also the relative ratio of different sites available.

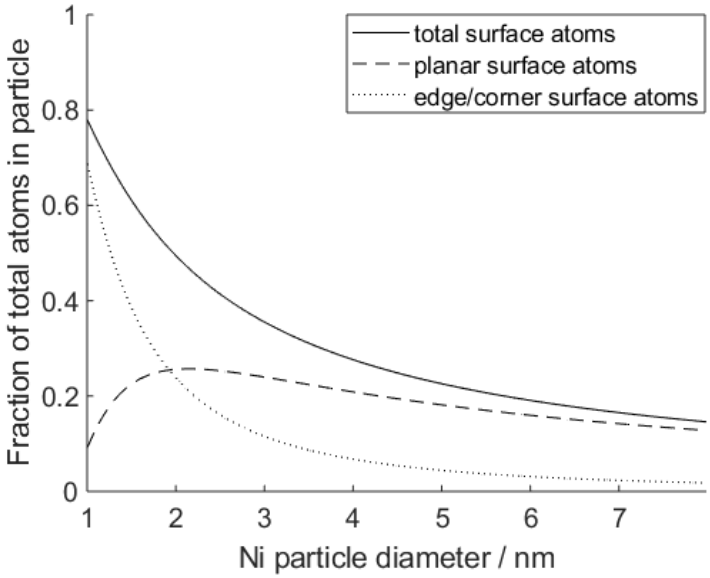

Figure 4: The variance of the surface statistics for nickel fcc cuboctahedron particles with particle size, based on the work of Hardeveld and Hartog[64], Blackmond *et al.*[65] and Király *et al.*[66]

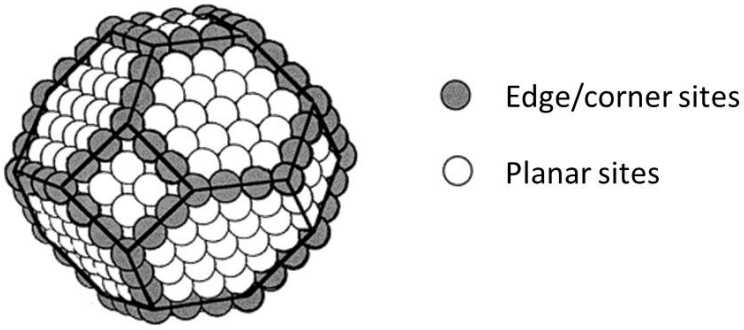

Figure 5: Diagram of a cubooctahedron particle, highlighting the edge/corner sites and the planar sites, reprinted with permission from Blackmond *et al*.[65] Copyright 1999. American Chemical Society.

1.4.2 Ensemble vs. electronic effects

The introduction of a new species to a catalyst can result in a variety of effects dependent on the dopant and the original catalyst. The typical effects are often explained by whether the dopant affects the geometric structure of the catalyst surface (ensemble effect) or the electronics of the metal (electronic effect). One example of this is a comparison of the surface deposition of copper or zinc on a Pd(111) surface.[67] The addition of copper to the surface only led to a change in the CO adsorption geometry and a decrease in the methanol dehydrogenation capability at fairly high coverages of copper, suggesting that the copper is effectively blocking surface sites *i.e.* the ensemble effect. However, the addition of relatively small amounts of zinc resulted in large changes in the CO adsorption and methanol dehydrogenation behaviour, suggesting that zinc modifies the

electronics of the palladium catalyst and that the electronic effect is dominant in this case. Preliminary DFT calculations were only partly consistent with the temperature programmed desorption (TPD) data, however they do suggest that zinc would have more of an effect on the electron density differences of palladium than copper. Additionally, in comparison to copper, zinc has more electrons in its valence shell and has a larger difference in electronegativity with respect to palladium. Therefore, this likely explains why ensemble effects are dominant with the addition of copper, whereas electronic effects are dominant with the addition of zinc. However, it should be noted that, in most cases, the introduction other metals to a catalyst leads to both ensemble effects and electronic effects and the outcome is often decided by which effect is more dominant. Therefore, this can sometimes make it challenging to differentiate between the two effects and determine which effect is leading to any observed changes in the catalyst activity, selectivity or deactivation.

1.4.3 Sn-Ni catalysts

One possible way of improving the selectivity and/or stability of nickel catalysts is the introduction of a second metal. Whilst steam reforming is a very different process to furfural hydrogenation, it is a widely used and well-established industrial process that often employs nickel-based catalysts. This means there is a large body of research on the process and so it is instructive to consider the ways in which nickel-based catalysts have been modified to improve selectivity and stability in this process and whether these could be relevant to furfural hydrogenation studied in this work.

The introduction of tin to nickel-based catalysts has been shown to have a positive impact on the amount of coke formed during steam reforming.[68] A tin-doped catalyst, containing 1 % tin with respect to the amount of nickel and supported on yttria-stabilised zirconia (YSZ), was used for the steam reforming of isooctane. The post-reaction samples had no measurable carbon content by XPS, XRD and STEM, whereas the nickel-only catalyst was coated in a thick layer of carbon that was detected by all 3 techniques (see Figure 6). This suggests the addition of a small amount of tin can almost completely suppress coke formation. XPS of the tin-doped catalysts revealed that the surface of the tin-doped catalysts was enriched with higher amounts of tin. For instance, in the sample that contained 1 wt. % tin w.r.t. nickel, the surface contained around 25 wt. % tin w.r.t to nickel. The catalyst was prepared by sequential impregnation, and so some surface enrichment would be expected. DFT calculations support these results and so offer a possible explanation for the behaviour observed. A nickel-tin surface alloy has a lower formation energy than that of a bulk nickel-tin phase or separate nickel and tin phases, hence the surface enrichment of tin. Additionally, it was determined that it is thermodynamically favourable for tin to displace nickel in the step-edge

sites. As discussed above, these step-edge sites are frequently associated with carbon formation, and so replacing these sites with tin could help with the suppression of coke formation.

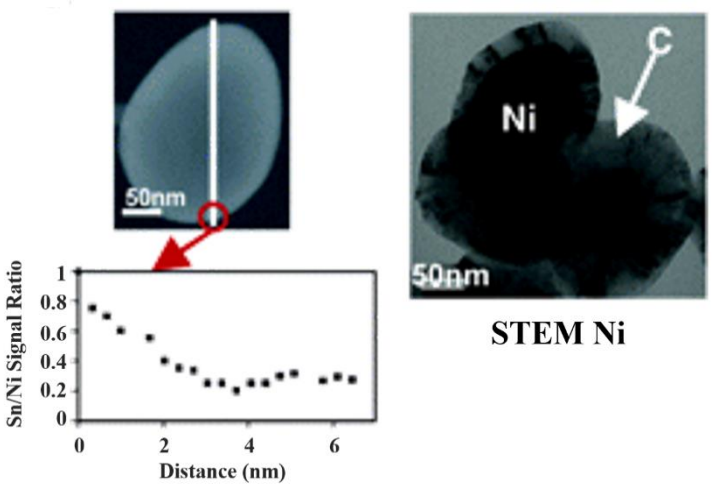

Figure 6: STEM/EDX of catalysts after steam reforming of isooctane (left) Sn-Ni/YSZ; (right) Ni/YSZ, reprinted with permission from Linic *et al.*[68] Copyright 2006. American Chemical Society.

Nickel-tin alloys have also been studied for furfural hydrogenation in both the vapour and liquid phase, with the results summarised in Table 3.[69-73] A series of nickel-tin alloys with different nickel to tin ratios were prepared *via* the layered double hydroxide (LDH) synthesis route.[69] Subsequent annealing in H_2 resulted in the formation of nanoparticles of nickel-tin intermetallic compounds separated by alumina. The Ni-Sn/Al_2O_3 particles were fairly large ranging from around 20 nm to 140 nm and most materials had a wide distribution of sizes (*e.g.* 40 – 120 nm for one $Ni_{1.5}Sn/Al_2O_3$ material). Vapour-phase furfural hydrogenation was carried out at an atypically high temperature (280 °C), possibly due to the fact that the catalyst particles were large, meaning lower surface area to volume ratios and therefore lower activities. The different nickel-tin phases formed in this LDH-based study, based on the ratio of nickel and tin added, displayed very different activities and selectivities. The catalysts with a Ni_3Sn phase exhibited higher activities (~4 $mmol_{fur}\ g_{cat}^{-1}\ h^{-1}$) but poor selectivity to FOL (~30 %). The catalysts with a Ni_3Sn_4 phase had a high selectivity towards FOL of above 70 %, however the catalytic activity was very low (~0.2 $mmol_{fur}\ g_{cat}^{-1}\ h^{-1}$). The catalysts with a Ni_2Sn_3 phase had activities of around 3.5 $mmol_{fur}\ g_{cat}^{-1}\ h^{-1}$ and a selectivity to FOL of around 60 %. It should also be noted the catalysts were tested for only 3 hours, and later stability tests revealed that the catalyst with the Ni_3Sn phase rapidly deactivated after 3 hours on stream, whereas the catalyst with the Ni_3Sn_2 phase showed an initial drop in activity for the first 7 hours on stream before maintaining a stable activity for the remaining 3 hours of the test. The authors attempted to explain the differing selectivities by using TEM to determine the exposed surface plane(s) present in the

different materials and then carrying out DFT calculations to determine the most likely adsorption energies and geometries for furfural on the identified plane(s). This revealed that the adsorption energy and the geometry of the adsorbed furfural showed a good correlation with the conversions and selectivity observed. The geometry of the adsorbed furfural particularly could be related to the major products observed, with the results summarised in Figure 7. The authors conclude that the catalyst with the Ni_3Sn_2 phase performed the best, achieving a moderate conversion and selectivity.

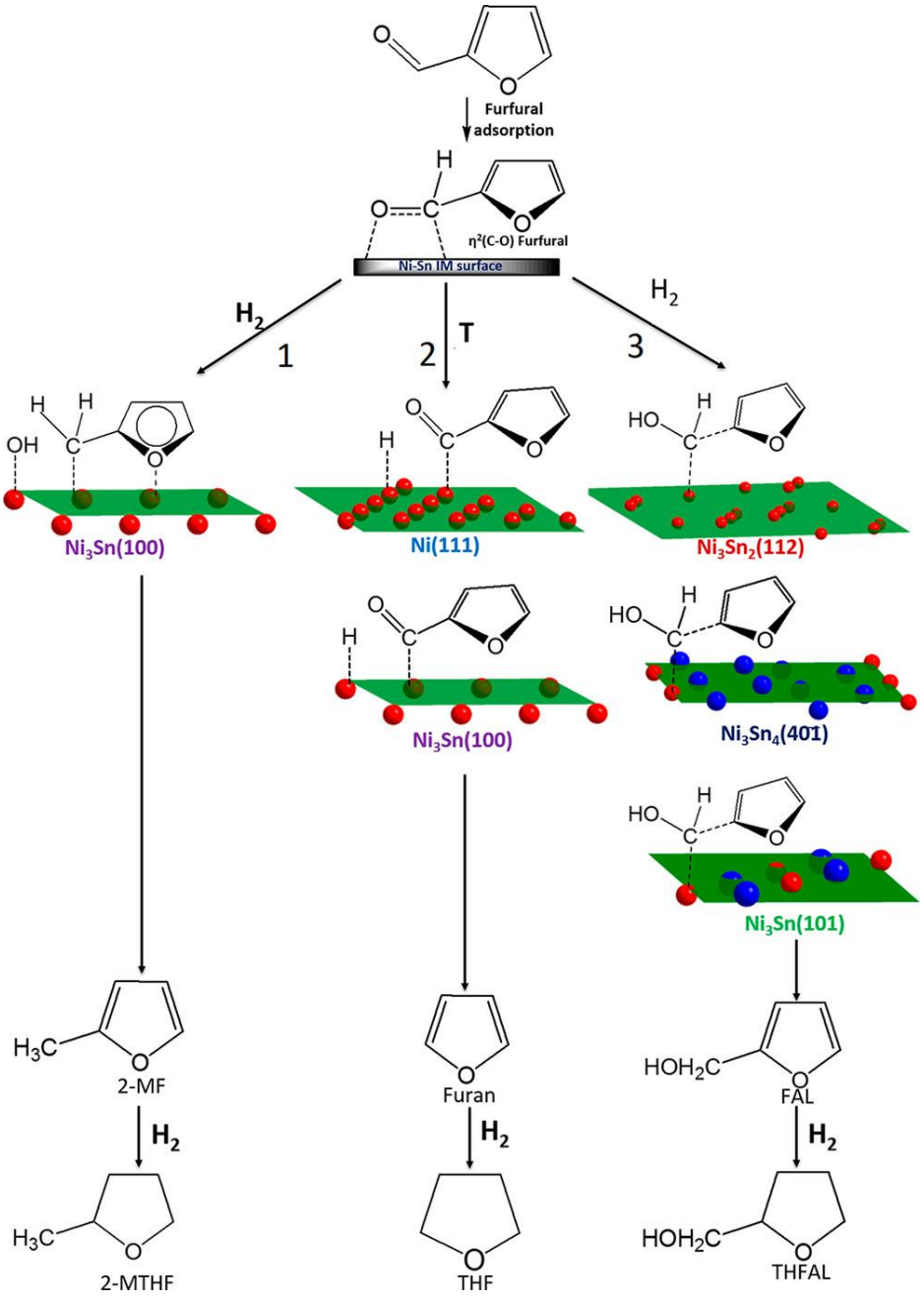

Figure 7: Potential mechanism for the differing selectivities of the various Ni-Sn phases (where red atoms = Ni and blue atoms = Sn) based on the crystal planes on the surface of the particles as determined by high-resolution TEM (HR-TEM), reprinted with permission from Peter *et al.*[69] Copyright 2018. American Chemical Society.

Rodiansono *et al.* investigated nickel-tin alloys for liquid-phase furfural hydrogenation.[70-72] Initially, both bulk nickel-tin materials and supported materials were tested for a variety of ketone/aldehyde hydrogenation reactions including furfural hydrogenation.[70] The material with the best performance was a Ni_3Sn_2/TiO_2 catalyst that had an activity of 17 $mmol_{fur}\ g_{cat}^{-1}\ h^{-1}$ and selectivity to FOL of 100 %, however other Ni_3Sn_2 catalysts with different supports showed a poorer activity and selectivity. A raney-nickel/Al(OH) catalyst exhibited the same activity, however the catalyst favoured the formation of THFA and had a selectivity of 100 % for this product. This suggests that by alloying nickel with tin, assuming the correct support is chosen, the activity of the catalyst can be maintained whilst drastically improving the FOL selectivity of the catalyst.

A later report investigated a Ni-Sn alloy supported on Al(OH) that was synthesised by modifying a Raney-nickel catalyst with a tin salt (Ni/Sn ratio of 3).[71] The non-doped Raney-nickel parent material exhibited exclusive selectivity towards THFA, however the tin-doped material had a selectivity of 94 % to FOL. Both catalysts had the same activity (22 $mmol_{fur}\ g_{cat}^{-1}\ h^{-1}$), suggesting that the incorporation of tin into the catalyst did not have a significant effect on activity. However, it should be noted that the results were reported for 100 % conversion, which, for batch reactions, means that the activity value reported is the lower bound and differences in activity could be missed if the reaction is not frequently monitored until completion. The authors also investigated the stability of the nickel-tin alloy catalyst and found that only a small drop in activity was observed over the course of 6 runs (22 $mmol_{fur}\ g_{cat}^{-1}\ h^{-1}$ to 20 $mmol_{fur}\ g_{cat}^{-1}\ h^{-1}$). The decrease in activity can likely be explained by the fact that some metal leaching was observed; by the end of run six, 0.96 % of the nickel, 4.8 % of the tin and 2.0 % of the aluminium had leached into the solution. Whilst there was only a small drop in activity, the leaching of metals into either solvent or products could lead to problems with disposal of the solvent or the future application for the product.

A further paper investigated the impact of a variety of supports for a Ni_3Sn_2 catalyst for liquid-phase furfural hydrogenation.[72] The majority of the Ni_3Sn_2 catalysts showed 99 % or higher selectivity to FOL, suggesting that the choice of support does not seem to have a significant impact on the selectivity of the catalysts. The notable exception to this was the Ni_3Sn_2/MgO catalyst, which had no selectivity towards FOL or THFA, as well as a low conversion (<10 %), indicating this catalyst is not very suitable for furfural hydrogenation. The best performing catalyst was found to be a titania supported catalyst, which achieved an activity of 17 $mmol_{fur}\ g_{cat}^{-1}\ h^{-1}$. The stability of a zirconia supported catalyst, which showed similar results to those of the titania supported catalyst in terms of both activity and selectivity to FOL, was examined. A 50% loss of activity was observed dropping from 16 $mmol_{fur}\ g_{cat}^{-1}\ h^{-1}$ to 8.8 $mmol_{fur}\ g_{cat}^{-1}\ h^{-1}$ by the fifth run, however heating the catalyst to 400 °C for 1 hour in H_2 before a sixth reaction resulted in the full recovery of the initial activity. This

suggests that the loss of activity was likely due to adsorbed species blocking the active sites rather leaching (as seen previously by the author with a related catalyst[71]) since a high temperature treatment would not recover lost metal.

Nickel catalysts that were supported on silica and surface doped with tin were investigated for liquid-phase furfural hydrogenation.[73] A $NiSn_{0.2}/SiO_2$ catalyst showed an improved activity of 5.2 $mmol_{fur}\ g_{cat}^{-1}\ h^{-1}$ compared to the parent Ni/SiO_2 catalyst that had an activity of 3.7 $mmol_{fur}\ g_{cat}^{-1}\ h^{-1}$, however the selectivity of both catalysts for FOL were very similar (around 77 %). The introduction of more tin, to form a $NiSn_{0.8}$ catalyst, resulted in an activity of 3.7 $mmol_{fur}\ g_{cat}^{-1}\ h^{-1}$, which is very similar to the mono-metallic nickel catalyst, however there was a significant improvement in the FOL selectivity (97 %).

Whilst there are limited reports on the impact of introducing tin to nickel-based catalysts for vapour-phase furfural hydrogenation, the reports of Sn-Ni catalysts for the liquid-phase reaction generally suggest that the introduction of tin significantly improves FOL selectivity. However, in some cases, the introduction of tin did lead to a decrease in the activity of the catalyst. The drastic improvement in FOL selectivity seen for the liquid-phase reactions means that this may also be applicable to the vapour-phase reaction. Ultimately then, the introduction of tin to nickel-based catalysts shows significant promise for improving the FOL selectivity during vapour-phase furfural hydrogenation.

Table 3: Comparison of literature tin-nickel catalysts run in either vapour phase continuous reactors or liquid phase batch reactors; mass activities were calculated at low conversions where possible, however some examples only included data for close to 100 % conversion

Catalyst	**Liquid- or vapour-phase reaction?**	**Temperature / °C**	**Pressure / MPa**	**Conversion / %**	**Mass activity / $mmol_{fur}\ g_{(cat)}^{-1}\ h^{-1}$**	**Furfuryl alcohol selectivity / %**
$Ni_{3.08}Sn_{2.14}$-$(Al_2O_3)_{0.59}$[69]	Vapour	280	atmospheric	67.8	3.5	61
Ni_3Sn_2/TiO_2[70]	Liquid	110	3.0	>99	17	>99
Ni-Sn/AlOH (Ni/Sn ratio 3)[71]	Liquid	180	3.0	98	22	94
Ni_3Sn_2/TiO_2[72]	Liquid	110	3.0	>99	17	100
$NiSn_{0.8}/SiO_2$[73]	Liquid	100	1.0	31	3.7	97

1.5 Colloidal nanoparticle synthesis

One way of preparing more well-defined, uniform catalysts is to synthesise colloidal nanoparticles. These nanoparticles can act as model catalysts, since the increased uniformity means that the interpretation of data from characterisation techniques is simplified and complex structure-reactivity relationships are more easily elucidated. Colloidal nanoparticles typically require a capping agent to stabilise the surface, which helps to prevent sintering and produce a narrow particle size distribution. The theories that describe the mechanisms for colloidal nanoparticle synthesis are discussed in significant detail the methodology section (Chapter 2). Here, the different synthetic approaches for the formation of colloidal nickel nanoparticles will be discussed, including the benefits and possible drawbacks of relevant capping agents.

1.5.1 Polymer capped nanoparticles

Polymeric capping agents such as polyvinylpyrrolidone (PVP) and polyethylene glycol (PEG) have been used to synthesise colloidal nanoparticles of a wide variety of metals such as Pt[74, 75], Ru[76], Ag[77, 78], Au[79, 80] and Pd[81, 82]. Although to a lesser extent, there are also syntheses that report the use of PVP or PEG for colloidal nickel nanoparticles.[83-85] For instance, Metin *et al.*[84] was able to produce nickel nanoparticles with an average particle size of 3.6 ± 1.6 nm using PVP as the capping agent. Whilst the authors did find that the PVP:Ni ratio had to be optimised (too much PVP led to low activity, whereas too little led to agglomeration of the nanoparticles), they were able to produce catalytically active nanoparticles for the hydrolysis of sodium borohydride. However, whilst acceptable catalytic activity was observed here, the presence of the bulky polymers on the surface often significantly restricts access to the active sites, leading to low catalytic activity. Therefore, there are many reports that discuss the attempted removal of PVP from nanoparticles.[75, 86-90]

The removal of PVP from metal nanoparticles has been attempted using a variety of methods including decomposition of the capping agent *via* high temperature treatments (typically in oxidising environments or cycling oxidising/reducing environments), extensive washing of the nanoparticles with a suitable solvent or treatment of the catalyst with UV light/ozone.[91, 92] However, there are often issues with these capping agent removal methods; for instance, high temperature treatments can lead to sintering and changes to the shape of the nanoparticles.[93] Additionally, thermal treatments may not completely remove the capping agent, which can lead to coke formation that prevents access to active sites.[92] Washing the nanoparticles is more suited to weakly bound capping agents, however, even in these cases, it typically results in incomplete removal.[94] Supported nanoparticles are often stable to UV/ozone treatments, however there is evidence that this method does not lead to complete removal of organic species, with Somorjai *et al.*[95] finding

residual pyrrolidone monomers present after the UV/ozone treatment of PVP-capped Pt nanoparticles. Ultimately, the use of polymeric capping agents frequently leads to lower catalytic activity due to the lack of access to active sites and the removal of these capping agents can often be very challenging.

1.5.2 Reverse micelle synthesis method

Another approach to the synthesis of well-defined and uniform nanoparticles is the reverse micelle synthesis method, in which small droplets of water are homogeneously dispersed in a hydrocarbon with the aid of a surfactant.[96, 97] The size and shape of the micelles can be controlled by the ratio of water to hydrocarbon, which is important for obtaining nanoparticles with the desired size.[97] The reverse micelle synthesis method has been used to prepare a variety of metallic nanoparticles with small particle sizes such as Pt (~5 nm),[98] Pd (~4 nm),[99] Ag (~5 nm)[100] and, most relevant here, Ni (~4 nm[101] and ~6 nm[102]).

There are certain benefits of this synthetic method, such as the ability to produce uniform, monodisperse nanoparticles and the possibility to vary the nanoparticle size by controlling the size of the micelles. However, the major disadvantage of this method is the extremely small quantities of nanoparticles that can be synthesised, especially when compared to the large amounts of solvent required.[96] Therefore, this method is unlikely to be able to produce suitable quantities of material for catalytic testing and characterisation and so is not an appropriate method for preparing the model catalysts required for this thesis.

1.5.3 Amine capped nanoparticles

Another common method for the synthesis of colloidal nanoparticles involves the use of long chain amines, such as oleylamine or octadecylamine, as capping agents.[103] The syntheses of oleylamine capped nanoparticles of various catalytically relevant metals have been reported, such as Pt,[104] Pd,[105, 106], Rh,[107] Ir[108] and Ni.[109, 110] The methods for nickel nanoparticle synthesis using oleylamine as the capping agent will be discussed in further detail below.

Chen *et al.*[109] reported the synthesis of large nickel nanoparticles (20 – 60 nm) prepared with oleylamine as the capping agent. The smallest and therefore most catalytically relevant (higher surface area to volume ratio) nanoparticles were synthesised through direct thermolysis of the $Ni(acac)_2$ precursor at 215 °C. The nanoparticles had an average particle size of 22 nm and had a fairly broad particle size distribution of 28 %. Increasing the reaction temperature to 240 °C produced nanoparticles with a slightly narrower particle size distribution (20 %), but also led to a significant increase in average particle size (35 nm). The authors also explored other synthetic

methodologies for obtaining narrower particle size distributions, such as seeded growth and hot injection, however these methods led to substantially larger nanoparticles (>45 nm) that will have very low surface area to volume ratios and so are not as useful or relevant for catalytic applications. Overall, this synthetic approach generally leads to larger nanoparticles with relatively broad particle size distributions.

Metin *et al.*[110] also reported a synthesis of nickel nanoparticles prepared with oleylamine as the capping agent, however they included a strong reducing agent (borane tributylamine (BTrB)) and used a mix of oleylamine and oleic acid. The nanoparticles obtained using this method had an average particle size of 3.2 nm, with a narrow distribution of ~7 %. The use of the strong reducing agent meant that the Ni(II) pre-cursor could be reduced at the low temperature of 90 °C and therefore the reaction could be carried out at significantly lower temperatures than those reported by Chen *et al.*[109] Additionally, the authors found that decreasing the BTrB:Ni ratio led to increased particle size and broader particle size distributions, suggesting the reducing agent is contributing to the uniformity of the nucleation and growth of the nanoparticles.

The inclusion of oleic acid was also found to be crucial, since if omitted, polydisperse nanoparticles were produced. At this stage, the role of oleic acid in producing monodisperse nanoparticles is unclear, however there is a report that explores the role of oleic acid for a similar precursor, $Pt(acac)_2$, in presence of oleylamine.[111] The authors hypothesise that oleic acid may catalyse the aminolysis reaction between oleylamine and the $acac^-$ ligand. Although not definitive, the authors suggest that when only oleylamine is used, oleylamine replaces the $acac^-$ ligand leading to the formation of $[Pt(oleylamine)_4]^{2+}+2(acac^-)$. However, when oleic acid is included, the aminolysis reaction occurs, which results in the formation of $[Pt(oleylamine)_4]^{2+}+2(R\text{-}COO^-)$ (where the counter ion is deprotonated oleic acid) and the oleylamine-acac amino-ketone as a side product. The authors then suggest that these complexes follow different nanoparticle formation mechanisms. Under the assumption that oleic acid may be playing a similar role with $Ni(acac)_2$/oleylamine, this offers a possible explanation for differences observed when oleic acid is included/excluded from the reaction.

Metin *et al.*[110] also reports that these nickel nanoparticles have a very high activity for the hydrolysis of an ammonia-borane complex, without any attempts to remove capping agent, suggesting that the presence of the oleylamine capping agent is having a limited impact on catalysis. In summary, this method produces small, monodisperse nanoparticles (~3 nm), which is ideal for catalysis since the small size means a high surface area to volume ratio and the narrow particle size distribution means good uniformity. Additionally, the presence of the oleylamine capping agent appears to have

a limited impact on catalytic activity. Therefore, this method has been used for the production of some of the model nanoparticle catalysts required in this thesis (Chapter 4).

1.5.4 Synthesis of larger nickel nanoparticles

As discussed above, there is a widely used synthesis for the production of small (3 - 4 nm) monodisperse colloidal nickel nanoparticles that only requires the use of C, H, N and O atom containing capping agents – *i.e.* oleic acid and an amine capping agent (oleylamine)[110]. However, preparing larger nickel nanoparticles with a similar approach is challenging, often obtaining broad particle size distributions.[112-114] Therefore, in order to obtain larger nickel nanoparticles with narrow particle size distributions, phosphine capping agents (typically tri-n-octylphosphine) are almost invariably used.[113-115]

The synthetic conditions employed when using a phosphine capping agent are important, since it is possible to get phosphorus incorporation leading to the formation of amorphous nickel phosphides or a variety of crystalline nickel phosphide phases.[116-119] Two key factors in determining the structure and morphology of the nanoparticles are the P:Ni molar ratio and the reaction temperature.[117] At P:Ni molar ratios of $\leq$1 and a temperature of 240 ^{o}C, it was reported to be possible to form metallic nickel nanoparticles. However when the P:Ni molar ratio was increased to >9, phosphorus incorporation was observed; at a reaction temperature of 240 ^{o}C, amorphous Ni_xP_y nanoparticles were formed and upon increasing the reaction temperature to 300 ^{o}C, crystalline Ni_2P nanoparticles were produced. Sanchez *et al.*[114] found that P:Ni ratios of as low as 4 were enough to lead to a broad pXRD signal, however in this case, the authors suggest it corresponds to 'amorphous' nickel (note: amorphous here meaning poorly crystalline, as some order must be present to give rise to a broad XRD feature). A similar broad signal at a similar angle was previously assigned as 'amorphous' nickel phosphide,[117] and so it appears it is difficult to distinguish between 'amorphous' nickel and 'amorphous' nickel phosphide using pXRD alone. The authors do also state that the decomposition temperature of tri-n-octylphosphine (TOP) is in the range of 280 – 350 ^{o}C and given their reaction was carried out at 220 ^{o}C, phosphorus incorporation was unlikely. However, Tracy *et al.*[117] observed the formation of what they assigned as amorphous nickel phosphide at the only moderately higher temperature of 240 ^{o}C, which is also considerably below the decomposition temperature range of TOP. Therefore, further and more detailed analysis is required to clarify whether it is possible for phosphorus to be incorporated from the use of TOP as a capping agent at lower temperatures.

Robinson *et al.*[118] carried out a detailed study of the structure of amorphous and crystalline nickel phosphide nanoparticles that were prepared using TOP as the phosphorus source. Two sets of

nanoparticles were produced using the same P:Ni molar ratio of 5.6, but with other reaction conditions altered such as temperature (230 °C vs. 350 °C). The pXRD pattern for the reaction carried out at 230 °C had a broad reflection centred around 44.5 °, consistent with an 'amorphous' nickel structure. However, the reaction carried out at 350 °C had a pattern consistent with crystalline Ni_2P. TEM confirmed that whilst the nanoparticles from the reaction carried out at the lower temperature had an non-crystalline structure, the higher temperature nanoparticles were crystalline with d-spacings that matched well with Ni_2P and had a hollow structure due to the Kirkendall effect (where the Kirkendall effect is as described by Kirkendall[120] and Smigelskas and Kirkendall[121]).[‡‡] X-ray absorption spectroscopy (XAS) was then used to investigate the structure of the amorphous and crystalline nanoparticles further. Extended X-ray absorption fine structure (EXAFS) analysis of the XAS data showed that whilst it was possible to get a good fit for the crystalline nanoparticles based on Ni_2P as expected, it was not possible to fit the data from the amorphous nanoparticles using the Ni fcc structure alone. The best fit for the amorphous particles was achieved using a mix of the Ni fcc structure and Ni_2P, with around 10 atomic % coming from Ni in Ni fcc, 57 atomic % coming from Ni in Ni_2P and the remaining percentage as P. Therefore, the majority of Ni in the amorphous particles was actually found to be present as Ni_2P, with only small amounts adopting the Ni fcc structure, which is contrary to the pXRD assignment of 'amorphous' Ni fcc. EXAFS analysis and elemental analysis determined that both sets of nanoparticles were atomically around two thirds nickel and one third phosphorus, which is consistent with the stoichiometry of Ni_2P. This means that at temperatures as low as 230 °C and with a moderate P:Ni ratio of 5.6, significant phosphorus incorporation can occur. Additionally, despite the majority of the Ni being present as Ni_2P, the pXRD pattern resembles amorphous Ni fcc, and so without doing more detailed analysis such as XAS, the phosphorus incorporation may not be detected. Based on these results, it is likely that when nickel nanoparticles are prepared using TOP as a capping agent under similar conditions, especially if the nanoparticles appear to be amorphous, a significant amount of phosphorus is being incorporated into the structure.

Arrigo *et al.*[122] also carried out a detailed study of the structure of nickel nanoparticles synthesised using TOP as the capping agent. Whilst in previous papers, it has been reported the molar ratio of P:Ni is an important factor in determining phosphorus incorporation,[117] the authors here report that the ratio of oleylamine (OAm) to TOP also plays a crucial role.[122] When 2.5 eq. of OAm and 1.5 eq. of TOP with respect to the nickel pre-cursor were used, the authors found that the nanoparticles produced were amorphous and had some phosphorus incorporation. There was fairly strong evidence for phosphorus incorporation as a variety of techniques all indicated this was the case;

[‡‡]When the diffusion coefficients of two components (A and B) of a mixture are different, then the diffusion of one component (*e.g.* A into B) will be faster than the diffusion of the other (*e.g.* B into A), resulting in the formation of voids.

Raman showed the presence of Ni-P bonds, HAADF-STEM images showed voids in the centre of some nanoparticles due to the Kirkendall effect, STEM-EDX mapping showed the co-location of Ni and P in the nanoparticles and XPS showed the presence of a $Ni^{\delta+}$ species that is associated with nickel phosphides. However, when the amount of oleylamine was increased (5 eq. or 10 eq.; TOP kept constant at 1.5 eq.) crystalline nickel nanoparticles were produced and the authors found no evidence of phosphorus incorporation using Raman, HAADF-STEM and pXRD. However, the XP spectrum for the sample prepared with 5 eq. of OAm did have a small amount of the $Ni^{\delta+}$ species associated with nickel phosphide present. When the OAm amount was increased to 10 eq., the $Ni^{\delta+}$ species could no longer be identified. The authors also investigated some silica supported nanoparticles prepared using a similar method and found that their results were consistent with the unsupported nanoparticles. EXAFS analysis of XAS data showed that low OAm:TOP ratios resulted in amorphous nanoparticles with some phosphorus incorporation and samples with higher ratios produced crystalline nickel nanoparticles with some oxidation but minimal phosphorus incorporation. Overall, this suggests that as the molar ratio of OAm:TOP is increased, the amount of phosphorus incorporation decreases significantly and becomes negligible at high ratios.

As discussed above, the synthetic conditions required to obtain crystalline nickel nanoparticles when using TOP as the capping agent have to be chosen very carefully. Nonetheless, there are many syntheses in the literature that report the production of such nanoparticles.[113-115, 122-129] However, even when the synthetic conditions are carefully chosen and crystalline nickel nanoparticles are obtained, Robinson *et al.*[130] found that phosphorus incorporation is still likely to be occurring. Initial pXRD and HRTEM data indicated the formation of crystalline nickel fcc nanoparticles, however, the authors found evidence of phosphorus incorporation from various other analytical techniques. XAS experiments revealed that whilst the nanoparticles had a crystalline nickel fcc structure, there was a significant reduction in the spectral intensity amplitude for the nanoparticle sample compared to a nickel foil reference. This reduction in amplitude was too large to be explained by nanoscale effects alone, and so, based on previous reports, where phosphorus incorporation into bulk nickel led to reductions in the amplitude,[131] the authors proposed that it was likely due to a combination of nanoscale effects and phosphorus incorporation.[130] Further evidence for phosphorus incorporation came from EXAFS analysis of the XAS data; the authors found that they could not achieve a good fit using the Ni fcc structure alone or a mix of Ni and NiO fcc structures. The fit was improved when a mix of Ni fcc and Ni_2P was used, however it was still fairly poor. The authors only achieved a good fit when they used a mix of Ni fcc and an artificially created Ni_3P fcc structure (*i.e.* the authors substituted one out of the four Ni atoms in the unit cell for a P atom in the standard Ni fcc structure). This model was then used to estimate that there was a P content of around 5.3 %,

which is a significant amount, especially considering that there was very little evidence of this from HRTEM and pXRD. Elemental analysis was also consistent with P incorporation, since the P content was too high compared to the C content for the P to only be present as TOP. The authors then investigated the effect of increasing reaction time and temperature and found that both correlated with increasing P content. As the P content of the nanoparticles increased, the authors also noticed some small differences in the pXRD pattern; increasing P content correlated with a lower 2θ angle and larger d-spacing for the Ni(111) reflection, with a shift of around 0.5 ^{o} and 0.02 Å for the 2θ angle and d-spacing respectively for samples with a P content of around 10 %. Therefore, whilst the pXRD pattern was still consistent with a Ni fcc structure, there were some subtle changes that became more noticeable with increasing P incorporation. Overall, the data and analysis presented in this report provides good evidence for P incorporation despite standard analytical techniques (HRTEM and pXRD) suggesting the formation of Ni fcc nanoparticles. Therefore, it is likely that a significant number of the syntheses that use TOP as a capping agent for nickel nanoparticles result in some degree of P incorporation.

Most syntheses discussed thus far have used reaction temperatures of $\geq$210 ^{o}C in order to form colloidal nickel nanoparticles. Despite these temperatures being significantly below the standard decomposition temperature of TOP (reported as 280 – 350 ^{o}C[114]), there have been several reports of phosphorus incorporation.[117, 118, 122, 130] However, the standard decomposition temperature does not take into account the presence of nickel, which may play a role in TOP decomposition. Carenco *et al.*[132] studied the deposition and decomposition of TOP on a Ni foil using NAP-XPS. TOP was first deposited at room temperature and then subsequently heated to 100 ^{o}C in 100 mTorr of H_2 (to mimic the reducing conditions typically used during nanoparticle syntheses). The room temperature and 100 ^{o}C spectra were very similar, with both showing partially oxidised nickel metal and phosphorus peaks with binding energies that corresponded to phosphorus interacting with the metal surface (a doublet of peaks with binding energies of 132.1 and 133 eV). However, when the sample was heated to 150 ^{o}C (still under 100 mTorr H_2), a significant change in the P 2p spectrum was observed. A new peak with a binding energy of 129.3 eV appeared, which is consistent with nickel phosphide formation. Therefore, in the presence of a Ni(0) surface, TOP can decompose at temperatures as low as 150 ^{o}C, indicating that Ni(0) surfaces acts as a catalyst in TOP decomposition. In typical nickel nanoparticle syntheses using TOP, the Ni(II) pre-cursor isn't reduced to Ni(0) metal until temperatures significantly above 150 ^{o}C (typically >200 ^{o}C), however, once Ni(0) metal surfaces are present, the reaction temperature is sufficient for them to catalyse the decomposition of TOP. Therefore, this explains why phosphorus incorporation is so common in nickel nanoparticle syntheses that include TOP, despite moderate reaction temperatures.

Computational studies corroborate the low temperatures required for the decomposition of TOP in the presence of nickel metal surfaces.[133] DFT was used to model the interactions of TOP with Ni(111) and Ni(100) surfaces and found that these surfaces can break the P-C bond in TOP ligands, which leads to the substitution of a surface nickel atom with a phosphorus atom. The energy required for this process is low and in agreement with previously reported temperatures (150 ^{o}C).[132] The authors also modelled TOP decomposition on NiO surfaces and found that they were inert when fully oxidised. Heating nickel oxide is known to lead to oxygen vacancies and the authors found that in order for Ni_xO_y to be active for phosphine decomposition, there would need to be areas that were so oxygen depleted that they behaved as nickel metal. This would require a temperature of around 250 ^{o}C, and so nickel oxide based materials would likely need significantly higher reaction temperatures before phosphorus incorporation became an issue.

Overall, the use of TOP as capping agent in the synthesis of nickel nanoparticles is likely to lead to the incorporation of phosphorus, even if the synthetic conditions are carefully chosen to limit this. Additionally, careful and detailed analysis of data from sophisticated analytical techniques is often required to reveal the phosphorus incorporation, and so it is easily missed using standard techniques. Therefore, it is important to consider the possibility of phosphorus incorporation and any effects this may have in the desired application for the nanoparticles (*e.g.* catalysis, magnetic properties).

1.6 Nickel phosphide catalysts

Since the syntheses required for larger colloidal nickel nanoparticles are likely to result in the incorporation of phosphorus, it is instructive to consider the literature surrounding nickel phosphide catalysts for hydrogenation reactions. Nickel phosphide catalysts have been explored for a range of hydroprocessing reactions such as hydrodesulfurisation[134], hydrodeoxygenation[135-138] and hydrodenitrogenation[139] as well as for the hydrogenation of a variety of compounds including cinnamaldehyde[140], nitrobenzene[141-143] and acetophenone[144, 145]. The excellent activity, and often selectivity, of these catalysts is typically attributed to the presence of a slightly electron deficient Ni species, $Ni^{\delta+}$ ($0 < \delta < 2$), which forms due to a small charge transfer from Ni to P. [146-148]

The electron deficient $Ni^{\delta+}$ species can act as a Lewis acid, however nickel phosphide catalysts also often contain Brønsted acid sites due to the formation of P-OH species.[146-148] The importance of acid sites in catalysts for furfural hydrogenation/hydrodeoxygenation was illustrated by Zhu *et al.*[149] with a series of copper-based catalysts. Selectivity towards the hydrodeoxygenation product, 2-methylfuran, was correlated with the presence of weak acid sites, whereas catalysts with less acid sites were found to favour the hydrogenation product, furfuryl alcohol. Therefore, it might be

expected that, compared to metallic nickel, nickel phosphide based catalysts may favour hydrodeoxygenation. A summary of the catalysts discussed below can be found in Table 4.

Wu *et al.*[146], who investigated unsupported nickel phosphide (Ni_2P) nanoparticles for the liquid-phase hydrodeoxygenation of furfural, found that 2-methylfuran was the dominant product in all catalysts tested. The authors found that the selectivity was dependent on the Lewis and Brønsted acidity of the catalyst, with both types of acid sites required to achieve high selectivity to 2-methylfuran. However, it should be noted that the authors used NH_3-TPD to distinguish between Lewis and Brønsted acidic sites; in most cases, this technique should only be used to provide information on the number and strength, not type, of acid sites present.[150] The authors also report that the strength of the acid sites played an important role in selectivity, since stronger acid sites led to a slower dissociation of 2-methylfuran from the catalyst, allowing for further transformations to take place. The optimised catalyst, which had an appropriate mix of Lewis and Brønsted acid sites of a suitable strength, achieved a selectivity of 91.2 % to 2-methylfuran at complete conversion (1.5 MPa H_2, 260 ^oC).

Maireles-Torres *et al.*[151] explored silica supported nickel phosphide catalysts for the vapour-phase hydrodeoxygenation of furfural. Regardless of P:Ni ratio, all catalysts formed a Ni_2P crystalline phase, however the P:Ni ratio did significantly affect the selectivity of the catalysts. Catalysts with P:Ni molar ratios of 1 or 2 favoured the production of 2-methylfuran, however when the P:Ni ratio was increased to 3, decarbonylation to furan was found to be the dominant pathway. This is a somewhat unexpected result, since furan is also the dominant product for the metallic nickel reference catalyst at the chosen reaction temperature. The authors hypothesise that at lower P:Ni ratios, the decrease in the number of Ni atoms on the surface of nickel phosphide nanoparticles compared to nickel metal, disfavours the interaction of the carbonyl group in furfural with the surface, which leads to the decreased furan formation. However, with increasing P:Ni ratio, the number of Brønsted acidic P-OH species increases, and so the authors propose that these species could be involved in decarbonylation and therefore lead to the increased furan selectivity seen at higher P:Ni ratios. This hypothesis is contrary to that proposed by Wu *et al.*[146] for the liquid-phase reaction, as they suggest that the Brønsted acidic sites are required to carry out the hydrogenolysis of furfuryl alcohol to 2-methylfuran. However, this remains as speculation until further investigations are carried out to clarify the roles of the different acid sites in this complex catalyst. Maireles-Torres *et al.*[151] found that the optimised catalyst (P:Ni ratio of 2) achieved a selectivity of 82.4 % to 2-methylfuran at 5 h TOS and a conversion of 88 %. Whilst this is a significant improvement in 2-methylfuran selectivity compared to the metallic nickel reference catalyst, this is lower than that achieved by Wu *et al.*[146] (91.2 %) for the liquid-phase reaction. The main reason

for this lower selectivity appears to be the formation of furan through decarbonylation, which remains as a significant side-product in the vapour-phase reaction.

Wu *et al.*[152] later went on to explore Ni_3P and carbon covered Ni_3P (Ni_3P@C) catalysts for liquid-phase furfural hydrogenation. In comparison to the previously studied Ni_2P catalysts[146], Ni_3P catalysts favoured the production of furfuryl alcohol. Whilst a Ni_2P reference catalyst had a 68.5 % selectivity to furfuryl alcohol, with the major side-product being 2-methylfuran, Ni_3P had a selectivity of 98.2 % to furfuryl alcohol (1.4 MPa H_2, 160 ^oC). The high selectivity of Ni_3P was comparable to the selectivity achieved by the nickel reference catalyst and it was also found to be around twice as active. The authors propose that since the Ni-Ni bond length in Ni_3P is similar to that of metallic nickel, Ni_3P will, in some regards, behave like metallic nickel, which explains the high selectivity to furfuryl alcohol. The increase in activity can be explained by the introduction of phosphorus leading to more p-electrons at energies higher than the fermi level, which leads to an increase in hydrogen dissociation capability. The authors also found that the Ni_3P@C catalyst had a significantly higher activity, whilst maintaining a high selectivity, however this appears to predominantly be a simple particle size effect since supporting the particles led to significantly smaller estimated crystallite sizes. Whilst the Ni_3P@C catalyst achieved high selectivity to furfuryl alcohol at moderate temperatures ($\leq$160 ^oC), increasing the temperature switched the selectivity to the hydrodeoxygenation product, 2-methylfuran, achieving a 93.9 % selectivity at 260 ^oC. Therefore, at the same temperature, the Ni_3P@C catalyst actually achieved a slightly higher selectivity to 2-methylfuran than the Ni_2P catalyst (91.2 %) previously studied by Wu *et al.*[146]

Hu *et al.*[153] investigated a series of nickel phosphide catalysts, supported on γ-Al_2O_3, for the liquid-phase conversion of furfural to cyclopentanone. The authors produced catalysts with a variety of phases including Ni_3P, Ni_2P and $Ni_{12}P_5$ and found that at lower temperatures (150 ^oC, 3 MPa H_2), Ni_3P was able to achieve a reasonable selectivity to cyclopentanone (87.4 %). However, catalysts that contained predominantly Ni_2P and $Ni_{12}P_5$ required higher temperatures (190 ^oC, 3 MPa H_2) to produce significant quantities of cyclopentanone and also produced cyclopentanol as a notable side-product. This is in contrast to the other nickel phosphide catalysts discussed previously[146, 151, 152], as they predominantly favoured 2-methylfuran or furfuryl alcohol. The difference in selectivity could be related to the choice of support, especially as it had strong interactions with phosphorus, which resulted in the formation of an $AlPO_4$ phase. However, further investigation is required to determine with certainty the reasons for the differing selectivity compared to other similar catalysts.

Golubeva *et al.*[154] found that the choice of solvent played a significant role in the selectivity of nickel phosphide catalysts for liquid-phase furfural hydroprocessing. When the reaction was carried out in toluene, with a catalyst that contained both Ni_2P and $Ni_{12}P_5$ crystalline phases, the major product was found to be 2-methylfuran, with furan as the main side-product. This remained true at a variety of temperatures, however the selectivity to 2-methylfuran increased as reaction temperature increased, achieving a 77 % selectivity at 350 ^oC (5 MPa H_2). This is in contrast to the reaction carried out in ethanol, with a catalyst that contained only Ni_2P, where a much broader range of products were formed. Depending on reaction conditions, 2-methylfuran, ethyl levulinate and furfuryl alcohol were often produced in significant quantities as well as many other minor products. Notably, with ethanol as the solvent, decarbonylation to furan was completely inhibited, whereas it was a significant competing reaction when toluene was used as the solvent. Decarbonylation has been found to be a significant competing pathway for nickel phosphide catalysts in the vapour-phase reaction[151], however, it was not seen in the other liquid-phase reactions, which is likely explained by the fact that polar solvents, such as propanol, were used in these cases.[146, 152] Therefore, solvent choice appears to play an important role in the selectivity achieved by nickel phosphide catalysts in the liquid-phase reaction, and so it should be taken into account when comparing the performance of different catalysts.

Li *et al.*[155] investigated a carbon covered nickel phosphide (Ni-P@C) catalyst derived from a metal-organic framework (MOF) for liquid-phase furfural hydrogenation. The authors found that heating the Ni-P-MOF to 600 ^oC under nitrogen led to the production of a Ni_2P crystalline phase. The Ni-P@C catalyst achieved a selectivity of 86.9 % to furfuryl alcohol at 140 ^oC (2 MPa H_2). This is consistent with Wu *et al.*[146] who found similar selectivity for their Ni_2P based catalyst at comparable temperatures. However, at increased temperatures (260 ^oC), the Ni-P@C catalyst favoured the production of 2-methyltetrahydrofuran, with a selectivity of 57.3 %. 2-methylfuran had a selectivity of less than 20 % and significant quantities of tetrahydrofurfuryl alcohol were also produced. This is notably different from other Ni_2P catalysts at higher temperatures since they favour 2-methylfuran.[146, 151]

Whilst the majority of nickel phosphide catalysts used for hydroprocessing reactions are crystalline, amorphous nickel phosphide has also been shown to be an active and selective catalyst for hydrogenation reactions.[156, 157] Liu *et al.*[156] investigated an unsupported amorphous nickel phosphide nanoparticle catalyst for cinnamaldehyde hydrogenation, however they also found their catalyst was active and selective for a variety of other substrates including furfural. In the case of furfural, it was found that the catalyst had a high selectivity of 95.6 % to furfuryl alcohol (80 ^oC, 1 MPa H_2). Whilst a previously discussed crystalline Ni_3P@C catalyst achieved a similar selectivity

to furfuryl alcohol,[152] this amorphous catalyst is an order of magnitude more active (mass activity of 150 vs. 14.6 $mmol_{fur}\ g_{(cat)}^{-1}\ h^{-1}$). Additionally, the amorphous catalyst was able to achieve this excellent activity with a reaction temperature of 80 °C, compared to 160 °C for the Ni_3P@C catalyst. Therefore, amorphous nickel phosphides appear to have the potential to out-perform the crystalline analogues in furfural hydrogenation.

Overall, at higher temperatures (generally ≥260 °C), nickel phosphide catalysts often favour the hydrodeoxygenation product, 2-methylfuran, which is likely related to the presence of both Lewis and Brønsted acidic sites that promote the hydrogenolysis of furfuryl alcohol to 2-methylfuran. However, at lower temperatures (generally ≤160 °C), nickel phosphide catalysts typically start to favour the hydrogenation product, furfuryl alcohol. For catalysts with lower phosphorus contents (*i.e.* Ni_3P vs. Ni_2P), it was possible to achieve a high furfuryl alcohol selectivity (<96 %). Additionally, an amorphous nickel phosphide catalyst showed promise for furfural hydrogenation; the catalyst was found to have a 95.6 % selectivity to furfuryl alcohol and an activity that was an order of magnitude higher than crystalline equivalents. Whilst most of these conclusions are based on results from liquid-phase reactions, the general principles are still likely to be applicable to the vapour-phase reaction. Therefore, these conclusions may help with the interpretation of the catalytic data for vapour-phase furfural hydrogenation with the phosphine-capped nanoparticles discussed in later this thesis (Chapter 6).

Table 4: Summary of nickel phosphide based catalysts for furfural hydrogenation run in either vapour-phase continuous reactors or liquid-phase batch reactors; mass activities were calculated at low conversions where possible, however some examples only included data for close to 100 % conversion.

Catalyst	Vapour- or liquid-phase reaction?	Solvent	Temperature / °C	Pressure of H_2 / MPa	Conversion / %	Mass activity / $mmol_{fur}\ g_{(cat)}^{-1}\ h^{-1}$	Major product	Selectivity to major product / %
Ni_2P[146]	Liquid	2-propanol	260	1.5	100	20.1	2-methylfuran	91.2
Ni_2P/SiO_2[151]	Vapour	N/A	190	Atmospheric	88	13.7	2-methylfuran	82.4
Ni_3P[152]	Liquid	2-propanol	160	1.4	22	3.32	Furfuryl alcohol	98.2
Ni_3P@C[152]	Liquid	2-propanol	160	1.4	97	14.6	Furfuryl alcohol	96.3
			260	1.4	~100	15.1	2-methylfuran	93.9
Ni-P/γ-Al_2O_3[153]	Liquid	Water	150	3	98.2	5.16	Cyclopentanone	87.4
$Ni_2P/Ni_{12}P_5$[154]	Liquid	Toluene	350	5	100	-	2-methylfuran	77
Ni_2P[154]	Liquid	Ethanol	350	5	100	-	Ethyl levulinate	40
Ni_2P@C [155]	Liquid	Ethanol	140	2	55.9	28.0	Furfuryl alcohol	86.9
			260	2	100	50.0	2-methyltetrahydrofuran	57.3
Amorphous Ni-P[23]	Liquid	Water	80	1.0	99.2	150	Furfuryl alcohol	95.6

1.8 Summary

Furfural is a key bio-based platform chemical, and its hydrogenation allows access to a variety of important chemical intermediates, particularly furfuryl alcohol, which is widely used to make resins. The current industrial catalyst, copper chromite, contains the highly carcinogenic and environmentally toxic Cr(IV) and so an alternative catalyst would be ideal. Nickel-based catalysts were generally found to have good activity for furfural hydrogenation, however often had lower selectivity. Careful selection of a suitable support (such as those with strongly basic sites) could lead to some improvements in FOL selectivity, however generally, this led to lower activity. The introduction of tin to nickel-based catalysts significantly improved FOL selectivity in liquid-phase reactions, however there were limited reports on the vapour-phase reaction. Such drastic improvements in FOL selectivity following the introduction of tin to nickel-based catalysts for the liquid-phase reaction, means that this approach may also be applicable in the vapour-phase. Colloidal nickel nanoparticles can act as model catalysts due to their high uniformity. Small, mono-disperse (~3 nm) nickel nanoparticles can be synthesised using oleylamine as a capping agent, however larger nickel nanoparticles (~12 – 15 nm) require the use of a phosphine capping agent, which can lead to phosphorus incorporation.

1.9 Aims and objectives

Based on the key results from the literature review, this thesis aims to:

(i) Benchmark the performance of nickel-based catalysts for vapour-phase furfural hydrogenation

(ii) Synthesise mono-disperse and uniform colloidal nickel and tin-nickel nanoparticles to act as model catalysts

(iii) Determine the impact of tin on vapour-phase furfural hydrogenation and understand its role through advanced characterisation

(iv) Determine the impact of phosphorus on nickel and tin-nickel colloidal nanoparticle catalysts for vapour-phase furfural hydrogenation and understand its role through advanced characterisation

1.10 References

1. J. J. Bozell and G. R. Petersen, *Green Chemistry*, 2010, **12**, 539-554.
2. Y. Luo, Z. Li, X. Li, X. Liu, J. Fan, J. H. Clark and C. Hu, *Catalysis Today*, 2019, **319**, 14-24.
3. P. W. Atkins, J. d. Paula and J. Keeler, *Atkins' Physical Chemistry*, Oxford University Press, Oxford, 2018.
4. P. T. Anastas, M. M. Kirchhoff and T. C. Williamson, *Applied Catalysis A: General*, 2001, **221**, 3-13.
5. P. W. Atkins and J. De Paula, *Elements of physical chemistry*, Oxford University Press, Oxford, 2009.
6. D. M. Alonso, J. Q. Bond and J. A. Dumesic, *Green Chemistry*, 2010, **12**, 1493-1513.
7. C. S. M. J. Biddy, C. Kinchin, *Chemicals from Biomass: A Market Assessment of Bioproducts with Near-Term Potential*, Report NREL/TP-5100-65509, 2016.
8. R. Mariscal, P. Maireles-Torres, M. Ojeda, I. Sádaba and M. López Granados, *Energy & Environmental Science*, 2016, **9**, 1144-1189.
9. K. Yan, G. Wu, T. Lafleur and C. Jarvis, *Renewable and Sustainable Energy Reviews*, 2014, **38**, 663-676.
10. A. Mandalika, L. Qin, T. K. Sato and T. Runge, *Green Chemistry*, 2014, **16**, 2480-2489.
11. M. Besson, P. Gallezot and C. Pinel, *Chem. Rev. (Washington, DC, U. S.)*, 2014, **114**, 1827-1870.
12. L. Balcaen, M. J. Baxter, J. A. Caruso, J. M. Cook, H. M. Crews, E. H. Evans, A. Fisher, M. Foulkes, H. R. Hansen, G. M. Hieftje, S. J. Hill, J.-M. Mermet, D. L. Miles, C. O'Connor, G. O'Connor, S. A. Pergantis, P. Robb, B. B. M. Sadi, J. R. Shann, B. L. Sharp, K. L. Sutton, P. Taylor, F. Vanhaecke and A. P. Vonderheide, *Inductively Coupled Plasma Spectroscopy and its Applications*, Blackwell Publishing, Oxford, 2 edn., 2007.
13. S. Sang, Y. Wang, W. Zhu and G. Xiao, *Research on Chemical Intermediates*, 2017, **43**, 1179-1195.
14. *United States Pat.,* 1735084, 1929.
15. K. Egeblad, J. Rass-Hansen, C. C. Marsden, E. Taarning and C. Hviid Christensen, in *Catalysis*, eds. J. J. Spivey and K. M. Dooley, The Royal Society of Chemistry, Cambridge, UK, 2009, vol. 21, pp. 13-50.
16. Candidate List of substances of very high concern for Authorisation - ECHA, https://echa.europa.eu/candidate-list-table).
17. *Great Britain Pat.,* 410148, 1934.
18. R. Connor, K. Folkers and H. Adkins, *Journal of the American Chemical Society*, 1932, **54**, 1138-1145.
19. J. R. Monnier, M. J. Hanrahan and G. Apai, *Journal of Catalysis*, 1985, **92**, 119-126.
20. W. Dannhauser and P. A. Vaughan, *Journal of the American Chemical Society*, 1955, **77**, 896-897.
21. R. Rao, A. Dandekar, R. T. K. Baker and M. A. Vannice, *Journal of Catalysis*, 1997, **171**, 406-419.
22. I. Chorkendorff and J. W. Niemantsverdriet, *Concepts of modern catalysis and kinetics*, Wiley-VCH, Weinheim, 2nd edn., 2007.
23. R. A. van Santen and H. W. Niemantsverdriet, *Chemical kinetics and catalysis*, Springer US, New York, 1995.
24. W. Gong, C. Chen, H. Zhang, Y. Zhang, Y. Zhang, G. Wang and H. Zhao, *Molecular Catalysis*, 2017, **429**, 51-59.
25. Á. O'Driscoll, J. J. Leahy and T. Curtin, *Catalysis Today*, 2017, **279**, 194-201.
26. Y. Su, C. Chen, X. Zhu, Y. Zhang, W. Gong, H. Zhang, H. Zhao and G. Wang, *Dalton Transactions*, 2017, **46**, 6358-6365.

27. Y. Xu, S. Qiu, J. Long, C. Wang, J. Chang, J. Tan, Q. Liu, L. Ma, T. Wang and Q. Zhang, *RSC Advances*, 2015, **5**, 91190-91195.
28. Y. Nakagawa, H. Nakazawa, H. Watanabe and K. Tomishige, *ChemCatChem*, 2012, **4**, 1791-1797.
29. D. Vargas-Hernández, Rubio-Caballero, J. , Moreno-Tost, R. , Mérida-Robles, J. , Santamaría-González, J. , Jiménez-López, A. , Pérez-Cruz, M. , Hernández-Huesca, R. and Maireles-Torres, P., *Modern Research in Catalysis*, 2016, **5**, 85-94.
30. M. Manikandan, A. K. Venugopal, K. Prabu, R. K. Jha and R. Thirumalaiswamy, *Journal of Molecular Catalysis A: Chemical*, 2016, **417**, 153-162.
31. T. P. Sulmonetti, S. H. Pang, M. T. Claure, S. Lee, D. A. Cullen, P. K. Agrawal and C. W. Jones, *Applied Catalysis A: General*, 2016, **517**, 187-195.
32. V. R. Madduluri, K. K. Mandari, V. Velpula, M. Varkolu, S. R. R. Kamaraju and M. Kang, *Fuel*, 2020, **261**, 116339.
33. T. P. Sulmonetti, S. H. Pang, M. T. Claure, S. Lee, D. A. Cullen, P. K. Agrawal and C. W. Jones, *Appl. Catal., A*, 2016, **517**, 187-195.
34. M. Manikandan, A. K. Venugopal, K. Prabu, R. K. Jha and R. Thirumalaiswamy, *J. Mol. Catal. A: Chem.*, 2016, **417**, 153-162.
35. V. R. Madduluri, K. K. Mandari, V. Velpula, M. Varkolu, S. R. R. Kamaraju and M. Kang, *Fuel*, 2020, **261**.
36. D. Liu, D. Zemlyanov, T. Wu, R. J. Lobo-Lapidus, J. A. Dumesic, J. T. Miller and C. L. Marshall, *Journal of Catalysis*, 2013, **299**, 336-345.
37. B. M. Nagaraja, V. Siva Kumar, V. Shasikala, A. H. Padmasri, B. Sreedhar, B. David Raju and K. S. Rama Rao, *Catalysis Communications*, 2003, **4**, 287-293.
38. H. Zhang, C. Canlas, A. Jeremy Kropf, J. W. Elam, J. A. Dumesic and C. L. Marshall, *Journal of Catalysis*, 2015, **326**, 172-181.
39. T. Bell Alexis, *Science*, 2003, **299**, 1688-1691.
40. S. E. Wanke and P. C. Flynn, *Catalysis Reviews*, 1975, **12**, 93-135.
41. S. Hu and W.-X. Li, *Science China Technological Sciences*, 2019, **62**, 762-772.
42. D. Wang, N. Liu, J. Zhang, X. Zhao, W. Zhang and M. Zhang, *Journal of Molecular Catalysis A: Chemical*, 2014, **393**, 47-55.
43. A. A. Tsyganenko, E. N. Storozheva, O. V. Manoilova, T. Lesage, M. Daturi and J. C. Lavalley, *Catalysis Letters*, 2000, **70**, 159-163.
44. P. G. Rouxhet and R. E. Sempels, *Journal of the Chemical Society, Faraday Transactions 1: Physical Chemistry in Condensed Phases*, 1974, **70**, 2021-2032.
45. A. O. Iroegbu and S. P. Hlangothi, *Chemistry Africa*, 2018, **1**, 187-197.
46. T. Kim, R. S. Assary, C. L. Marshall, D. J. Gosztola, L. A. Curtiss and P. C. Stair, *ChemCatChem*, 2011, **3**, 1451-1458.
47. L. He, D. Li, D. Dong, J. Yao, Y. Huang and H. Wang, *Journal of Applied Polymer Science*, 2012, **124**, 3383-3391.
48. T. Kim, R. S. Assary, H. Kim, C. L. Marshall, D. J. Gosztola, L. A. Curtiss and P. C. Stair, *Catalysis Today*, 2013, **205**, 60-66.
49. K. J. Zeitsch, *The chemistry and technology of furfural and its many by-products*, Elselvier Science, Amersterdam, The Netherlands, 1 edn., 2000.
50. M. R. Gafurov, I. N. Mukhambetov, B. V. Yavkin, G. V. Mamin, A. A. Lamberov and S. B. Orlinskii, *The Journal of Physical Chemistry C*, 2015, **119**, 27410-27415.
51. A. V. Fionov, *Surface Science*, 2002, **507-510**, 74-81.
52. S. Kiatphuengporn, A. Junkaew, C. Luadthong, S. Thongratkaew, C. Yimsukanan, S. Songtawee, T. Butburee, P. Khemthong, S. Namuangruk, M. Kunaseth and K. Faungnawakij, *Green Chemistry*, 2020, **22**, 8572-8583.
53. K. Nakajima, R. Noma, M. Kitano and M. Hara, *The Journal of Physical Chemistry C*, 2013, **117**, 16028-16033.

54. K. Bhattacharyya, A. Danon, B. K.Vijayan, K. A. Gray, P. C. Stair and E. Weitz, *The Journal of Physical Chemistry C*, 2013, **117**, 12661-12678.
55. N. C. Nelson, Z. Wang, P. Naik, J. S. Manzano, M. Pruski and I. I. Slowing, *J. Mater. Chem. A*, 2017, **5**, 4455-4466.
56. R. Zavaglia, N. Guigo, N. Sbirrazzuoli, A. Mija and L. Vincent, *The Journal of Physical Chemistry B*, 2012, **116**, 8259-8268.
57. S. J. Tauster, S. C. Fung and R. L. Garten, *Journal of the American Chemical Society*, 1978, **100**, 170-175.
58. S. J. Tauster, S. C. Fung, R. T. K. Baker and J. A. Horsley, *Science*, 1981, **211**, 1121.
59. S. J. Tauster, *Accounts of Chemical Research*, 1987, **20**, 389-394.
60. D. N. Belton, Y. M. Sun and J. M. White, *Journal of the American Chemical Society*, 1984, **106**, 3059-3060.
61. C.-J. Pan, M.-C. Tsai, W.-N. Su, J. Rick, N. G. Akalework, A. K. Agegnehu, S.-Y. Cheng and B.-J. Hwang, *Journal of the Taiwan Institute of Chemical Engineers*, 2017, **74**, 154-186.
62. C. M. Kalamaras, P. Panagiotopoulou, D. I. Kondarides and A. M. Efstathiou, *Journal of Catalysis*, 2009, **264**, 117-129.
63. G. A. Somorjai and Y. Li, *Introduction to surface chemistry and catalysis*, Wiley, Hoboken, N.J., 2010.
64. R. Van Hardeveld and F. Hartog, *Surface Science*, 1969, **15**, 189-230.
65. J. Le Bars, U. Specht, J. S. Bradley and D. G. Blackmond, *Langmuir*, 1999, **15**, 7621-7625.
66. B. Veisz, Z. Király, L. Tóth and B. Pécz, *Chemistry of Materials*, 2002, **14**, 2882-2888.
67. E. Jeroro, M. P. Hyman and J. M. Vohs, *Physical Chemistry Chemical Physics*, 2009, **11**, 10457-10465.
68. E. Nikolla, A. Holewinski, J. Schwank and S. Linic, *Journal of the American Chemical Society*, 2006, **128**, 11354-11355.
69. V. S. Marakatti, N. Arora, S. Rai, S. C. Sarma and S. C. Peter, *ACS Sustainable Chemistry & Engineering*, 2018, **6**, 7325-7338.
70. Rodiansono, S. Khairi, T. Hara, N. Ichikuni and S. Shimazu, *Catalysis Science & Technology*, 2012, **2**, 2139-2145.
71. Rodiansono, M. D. Astuti, U. T. Santoso and S. Shimazu, *Procedia Chemistry*, 2015, **16**, 531-539.
72. R. Rodiansono, M. D. Astuti, S. Khairi and S. Shimazu, *Bulletin of Chemical Reaction Engineering & Catalysis*, 2016, **11**, 1-9.
73. V. Vetere, A. B. Merlo, J. F. Ruggera and M. L. Casella, *Journal of the Brazilian Chemical Society*, 2010, **21**, 914-920.
74. W.-x. Tu, X.-b. Zuo and H.-f. Liu, *Chinese Journal of Polymer Science*, 2008, **26**, 23-29.
75. M. Luo, Y. Hong, W. Yao, C. Huang, Q. Xu and Q. Wu, *J. Mater. Chem. A*, 2015, **3**, 2770-2775.
76. S. Peng, J. Liu, Q. Li, J. Zhang and Q. Niu, *Integrated Ferroelectrics*, 2016, **170**, 83-91.
77. Y. Wang, D. Wan, S. Xie, X. Xia, C. Z. Huang and Y. Xia, *ACS Nano*, 2013, **7**, 4586-4594.
78. B. He, J. J. Tan, K. Y. Liew and H. Liu, *Journal of Molecular Catalysis A: Chemical*, 2004, **221**, 121-126.
79. F. Kim, S. Connor, H. Song, T. Kuykendall and P. Yang, *Angewandte Chemie International Edition*, 2004, **43**, 3673-3677.
80. M.-C. Daniel and D. Astruc, *Chemical Reviews*, 2004, **104**, 293-346.
81. Q. Shen, Q. Min, J. Shi, L. Jiang, J.-R. Zhang, W. Hou and J.-J. Zhu, *The Journal of Physical Chemistry C*, 2009, **113**, 1267-1273.
82. Y. Wang, S. Xie, J. Liu, J. Park, C. Z. Huang and Y. Xia, *Nano Letters*, 2013, **13**, 2276-2281.
83. E. G. C. Neiva, M. F. Bergamini, M. M. Oliveira, L. H. Marcolino and A. J. G. Zarbin, *Sensors and Actuators B: Chemical*, 2014, **196**, 574-581.
84. Ö. Metin and S. Özkar, *Journal of Molecular Catalysis A: Chemical*, 2008, **295**, 39-46.

85. A. Wang, H. Yin, H. Lu, J. Xue, M. Ren and T. Jiang, *Catalysis Communications*, 2009, **10**, 2060-2064.
86. R.-Y. Zhong, J.-W. Yang, Z. Hu and B.-Q. Xu, *ACS Applied Nano Materials*, 2019, **2**, 5720-5729.
87. L. Yang, G. Cheng, Y. Guo, D. Li, L. Xia and H. Liu, *Nanoscale*, 2018, **10**, 11992-11996.
88. R.-Y. Zhong, K.-Q. Sun, Y.-C. Hong and B.-Q. Xu, *ACS Catalysis*, 2014, **4**, 3982-3993.
89. A. J. F. van Hoof, D. A. J. Michel-Ligthart, H. Friedrich and E. J. M. Hensen, *ChemCatChem*, 2017, **9**, 1018-1024.
90. B. Donoeva and P. E. de Jongh, *ChemCatChem*, 2018, **10**, 989-997.
91. Z. Niu and Y. Li, *Chemistry of Materials*, 2014, **26**, 72-83.
92. Y. Borodko, H. S. Lee, S. H. Joo, Y. Zhang and G. Somorjai, *The Journal of Physical Chemistry C*, 2010, **114**, 1117-1126.
93. M. Crespo-Quesada, J.-M. Andanson, A. Yarulin, B. Lim, Y. Xia and L. Kiwi-Minsker, *Langmuir*, 2011, **27**, 7909-7916.
94. J. A. Lopez-Sanchez, N. Dimitratos, C. Hammond, G. L. Brett, L. Kesavan, S. White, P. Miedziak, R. Tiruvalam, R. L. Jenkins, A. F. Carley, D. Knight, C. J. Kiely and G. J. Hutchings, *Nature Chemistry*, 2011, **3**, 551-556.
95. C. Aliaga, J. Y. Park, Y. Yamada, H. S. Lee, C.-K. Tsung, P. Yang and G. A. Somorjai, *The Journal of Physical Chemistry C*, 2009, **113**, 6150-6155.
96. T.-D. Nguyen, *Nanoscale*, 2013, **5**, 9455-9482.
97. I. Capek, *Advances in Colloid and Interface Science*, 2004, **110**, 49-74.
98. H. H. Ingelsten, R. Bagwe, A. Palmqvist, M. Skoglundh, C. Svanberg, K. Holmberg and D. O. Shah, *Journal of Colloid and Interface Science*, 2001, **241**, 104-111.
99. M. Iida, S. Ohkawa, H. Er, N. Asaoka and H. Yoshikawa, *Chemistry Letters*, 2002, **31**, 1050-1051.
100. M. P. Pileni, *Pure and Applied Chemistry*, 2000, **72**, 53-65.
101. D.-H. Chen and S.-H. Wu, *Chemistry of Materials*, 2000, **12**, 1354-1360.
102. A. Kumar, A. Saxena, A. De, R. Shankar and S. Mozumdar, *Advances in Natural Sciences: Nanoscience and Nanotechnology*, 2013, **4**, 025009.
103. S. Mourdikoudis and L. M. Liz-Marzán, *Chemistry of Materials*, 2013, **25**, 1465-1476.
104. C. Wang, H. Daimon, T. Onodera, T. Koda and S. Sun, *Angewandte Chemie International Edition*, 2008, **47**, 3588-3591.
105. V. Mazumder and S. Sun, *Journal of the American Chemical Society*, 2009, **131**, 4588-4589.
106. Ö. Metin, S. Duman, M. Dinç and S. Özkar, *The Journal of Physical Chemistry C*, 2011, **115**, 10736-10743.
107. K. H. Park, K. Jang, H. J. Kim and S. U. Son, *Angewandte Chemie International Edition*, 2007, **46**, 1152-1155.
108. C. A. Stowell and B. A. Korgel, *Nano Letters*, 2005, **5**, 1203-1207.
109. H. T. Zhang, G. Wu, X. H. Chen and X. G. Qiu, *Materials Research Bulletin*, 2006, **41**, 495-501.
110. Ö. Metin, V. Mazumder, S. Özkar and S. Sun, *Journal of the American Chemical Society*, 2010, **132**, 1468-1469.
111. X. Yin, M. Shi, J. Wu, Y.-T. Pan, D. L. Gray, J. A. Bertke and H. Yang, *Nano Letters*, 2017, **17**, 6146-6150.
112. W. L. Vrijburg, J. W. A. van Helden, A. J. F. van Hoof, H. Friedrich, E. Groeneveld, E. A. Pidko and E. J. M. Hensen, *Catalysis Science & Technology*, 2019, **9**, 2578-2591.
113. Y. Chen, D.-L. Peng, D. Lin and X. Luo, *Nanotechnology*, 2007, **18**, 505703.
114. S. Carenco, C. Boissière, L. Nicole, C. Sanchez, P. Le Floch and N. Mézailles, *Chemistry of Materials*, 2010, **22**, 1340-1349.
115. M. Heilmann, H. Kulla, C. Prinz, R. Bienert, U. Reinholz, A. Guilherme Buzanich and F. Emmerling, *Nanomaterials*, 2020, **10**, 713.

116. X. Lu, M. A. Baker, D. H. Anjum, W. Papawassiliou, A. J. Pell, M. Fardis, G. Papavassiliou, S. J. Hinder, S. A. A. Gaber, D. A. A. Gaber, Y. Al Wahedi and K. Polychronopoulou, *ACS Applied Nano Materials*, 2021, DOI: 10.1021/acsanm.1c00044.
117. J. Wang, A. C. Johnston-Peck and J. B. Tracy, *Chemistry of Materials*, 2009, **21**, 4462-4467.
118. L. M. Moreau, D.-H. Ha, H. Zhang, R. Hovden, D. A. Muller and R. D. Robinson, *Chemistry of Materials*, 2013, **25**, 2394-2403.
119. E. Muthuswamy, G. H. L. Savithra and S. L. Brock, *ACS Nano*, 2011, **5**, 2402-2411.
120. E. O. Kirkendall, *Trans. AIME*, 1942, **147**, 104-110.
121. E. Kirkendall and A. Smigelskas, *Trans. AIME*, 1947, **171**, 130-142.
122. R. Arrigo, S. Gallarati, M. E. Schuster, J. M. Seymour, D. Gianolio, I. da Silva, J. Callison, H. Feng, J. E. Proctor, P. Ferrer, F. Venturini, D. Grinter and G. Held, *ChemCatChem*, 2020, **12**, 1491-1503.
123. J. Park, E. Kang, S. U. Son, H. M. Park, M. K. Lee, J. Kim, K. W. Kim, H.-J. Noh, J.-H. Park, C. J. Bae, J.-G. Park and T. Hyeon, *Advanced Materials*, 2005, **17**, 429-434.
124. V. Sharma, Tarachand, C. Chotia, G. S. Okram, K. J. M. and Y. S., *AIP Conference Proceedings*, 2017, **1832**, 050085.
125. K. Guo, H. Li and Z. Yu, *ACS Applied Materials & Interfaces*, 2018, **10**, 517-525.
126. M. Li, Y. Chen, N. Ji, D. Zeng and D.-L. Peng, *Materials Chemistry and Physics*, 2014, **147**, 604-610.
127. Y. Pan, R. Jia, J. Zhao, J. Liang, Y. Liu and C. Liu, *Applied Surface Science*, 2014, **316**, 276-285.
128. T. Ishizaki, K. Yatsugi and K. Akedo, *Nanomaterials*, 2016, **6**, 172.
129. K. P. Donegan, J. F. Godsell, D. J. Otway, M. A. Morris, S. Roy and J. D. Holmes, *Journal of Nanoparticle Research*, 2012, **14**, 670.
130. L. M. Moreau, D.-H. Ha, C. R. Bealing, H. Zhang, R. G. Hennig and R. D. Robinson, *Nano Letters*, 2012, **12**, 4530-4539.
131. J. Song, Z. Wei, Z. Pan, Z. Xie and S. Wei, *AIP Conference Proceedings*, 2007, **882**, 453-456.
132. S. Carenco, Z. Liu and M. Salmeron, *ChemCatChem*, 2017, **9**, 2318-2323.
133. R. García-Muelas, Q. Li and N. López, *The Journal of Physical Chemistry B*, 2018, **122**, 672-678.
134. Z. H. Yang, L. C. Li, Y. F. Wang, J. L. Liu, X. Feng and X. H. Lu, *Chin. J. Catal.*, 2012, **33**, 508-517.
135. S. K. Wu, P. C. Lai and Y. C. Lin, *Catalysis Letters*, 2014, **144**, 878-889.
136. P. J. Hsu and Y. C. Lin, *Journal of the Taiwan Institute of Chemical Engineers*, 2017, **79**, 80-87.
137. P. M. de Souza, C. V. M. Inocencio, V. I. Perez, R. C. Rabelo-Neto, V. O. O. Goncalves, G. Jacobs, F. Richard, V. T. da Silva and F. B. Noronha, *CATALYSIS TODAY*, 2020, **356**, 366-375.
138. P. Zhang, Y. Sun, M. H. Lu, J. Zhu, M. S. Li, Y. H. Shan, J. Y. Shen and C. S. Song, *Energy & Fuels*, 2019, **33**, 7696-7704.
139. M. H. Lu, A. J. Wang, X. Li, X. P. Duan, Y. Teng, Y. Wang, C. S. Song and Y. K. Hu, *Energy & Fuels*, 2007, **21**, 554-560.
140. P. Liu, Y. L. Zhu, L. Zhou, W. H. Zhang and Y. X. Li, *Catalysis Letters*, 2020, **150**, 2695-2702.
141. P. Liu, W. T. Chang, X. Y. Liang, J. Wang and Y. X. Li, *Catalysis Communications*, 2016, **76**, 42-45.
142. Y. Wang, X. Y. Chen, B. Yue and H. Y. He, *Topics in Catalysis*, 2012, **55**, 1022-1031.
143. P. Liu, Z. X. Zhang, S. W. Jun, Y. L. Zhu and Y. X. Li, *React. Kinet. Mech. Catal.*, 2019, **126**, 453-461.
144. D. C. Costa, A. L. Soldati, G. Pecchi, J. F. Bengoa, S. G. Marchetti and V. Vetere, *Nanotechnology*, 2018, **29**, 11.
145. J. N. Wang, Y. L. Wang, G. L. Chen and Z. J. He, *Catalysts*, 2018, **8**, 12.
146. Y. Wang, X. Feng, S. Yang, L. Xiao and W. Wu, *Journal of Nanoparticle Research*, 2020, **22**, 67.

147. K. Li, R. Wang and J. Chen, *Energy & Fuels*, 2011, **25**, 854-863.
148. Y.-K. Lee and S. T. Oyama, *Journal of Catalysis*, 2006, **239**, 376-389.
149. F. Dong, Y. Zhu, H. Zheng, Y. Zhu, X. Li and Y. Li, *Journal of Molecular Catalysis A: Chemical*, 2015, **398**, 140-148.
150. F. Hemmann, C. Jaeger and E. Kemnitz, *RSC Advances*, 2014, **4**, 56900-56909.
151. C. P. Jiménez-Gómez, J. A. Cecilia, R. Moreno-Tost and P. Maireles-Torres, *ChemCatChem*, 2017, **9**, 2881-2889.
152. Y. Tian, Y. Wang, H. Zhang, L. Xiao and W. Wu, *Catalysis Letters*, 2021, DOI: 10.1007/s10562-021-03680-y.
153. G. Gao, Y. Shao, Y. Gao, T. Wei, G. Gao, S. Zhang, Y. Wang, Q. Chen and X. Hu, *Catalysis Science & Technology*, 2021, **11**, 575-593.
154. M. A. Golubeva and A. L. Maximov, *Applied Catalysis A: General*, 2020, **608**, 117890.
155. F. Li, S. Jiang, T. Zhu, Y. Wang, T. Huang and C. Li, *ChemistrySelect*, 2020, **5**, 2271-2278.
156. P. Liu, Y.-L. Zhu, L. Zhou, W.-H. Zhang and Y.-X. Li, *Catalysis Letters*, 2020, **150**, 2695-2702.
157. P. Liu, W.-T. Chang, X.-Y. Liang, J. Wang and Y.-X. Li, *Catalysis Communications*, 2016, **76**, 42-45.

Chapter 2: Methodology and Experimental

2.1 Methodology

The main aim of this thesis has been to improve the selectivity of nickel-based catalysts for furfural hydrogenation. This has required careful catalyst preparation and reactor testing, as well as the use of advanced characterisation techniques with model colloidal nanoparticle catalysts to elucidate structure-activity relationships. The various techniques that have been employed to prepare and analyse the catalysts are discussed below.

2.1.1 Powder X-ray diffraction (pXRD)

pXRD is a widely used technique to study solid materials including catalysts and can elucidate information on the bulk phase or phases present in a material. X-ray diffraction works on the basis of Bragg's Law (see Figure 8 and Equation 1[1]), since at certain incident angles of radiation, specific to the phase and components of the material being studied, the conditions of Bragg's Law are met and constructive interference occurs.[1] Assuming the detector is also at a suitable angle, this will result in a signal being detected. pXRD is an effective technique since X-rays have a wavelength on the Ångstrom scale of atomic lattice spacings as well as energies that allow penetration into solids.

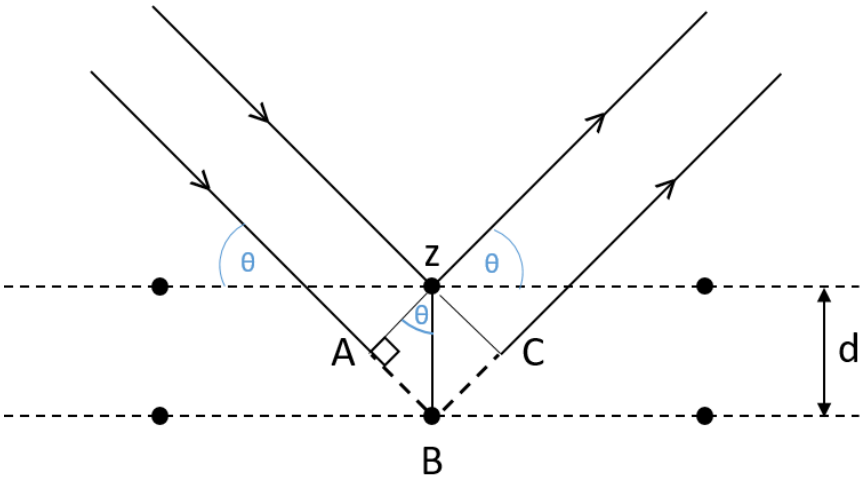

Figure 8: Schematic representing the basis of Bragg's Law[2]

$$n\lambda = 2d\sin(\theta)$$

where n = an integer, λ = wavelength of radiation, d = lattice spacing and θ = angle of incidence

Equation 1

Not only can pXRD provide information on the phases present in the material, the information obtained can be used to estimate the average crystallite size using the Scherrer equation (Equation 2).[3] The crystallite sizes obtained using this method can only be considered an estimate, since, for example, the dimensionless shape factor, *K*, is often assumed to be around 0.9, but this value varies with the shape of the crystallite. It can be seen from the Scherrer equation that smaller crystallites will lead to larger full width at half maximum (FWHM) values and therefore broader signals. This can mean that very small crystallites can sometimes have such broad signals that the error associated with determining the FWHM value is fairly large due to the low intensity of the signal. This is often true for supported catalyst materials where small metal nanoparticles are highly desirable. Additionally, these materials often have low metal loadings that can result in lower intensity reflections from available sample sizes, further complicating the analysis of the data. The 2θ value of the chosen reflection also has an effect on the amount of broadening observed since 2θ varies as cos(θ) in the Scherrer equation and so larger angles will result in increased broadening. Therefore, the choice of reflection used for analysis is important, since the broadening effect will be more noticeable at larger 2θ values. In samples where the crystallites are larger, this normally means larger 2θ values will give the best result. However, with smaller crystallites, like those found in many supported catalysts, the broadening is already significant. This means it may not be possible to use larger 2θ values since the reflections may become too broad to accurately measure the FWHM.

$$\beta(2\theta) = \frac{K\lambda}{L\cos(\theta)}$$

where β*(2*θ*) = peak width (FWHM) of reflection at angle 2*θ *in radians, K = dimensionless shape factor (~0.9),* λ *= wavelength of radiation in nm, L = average crystallite size in nm and* θ *= angle of reflection in radians*

Equation 2

Whilst the Scherrer equation can produce a rough estimate of the average crystallite size, many factors that are not often considered, or hard to estimate, can affect the results.[4] Therefore, Rietveld refinements are often employed to obtain more reliable average crystallite sizes, as well as a significant amount of additional information such as the lattice parameters and the space group of the material. A Rietveld refinement uses a least squares approach to minimise the difference between the values for a calculated pattern and those of the experimentally data.[5] In order to produce a suitable calculated pattern, various factors have to be included such as the expected structure of the material (*e.g.* lattice parameters, space group), instrumental parameters and

sample height.[5] Rietveld refinements of data presented in this thesis were performed by Prof. John Evans, a collaborator in this project, using TOPAS academic.

2.1.2 Transmission electron microscopy (TEM)

Unlike conventional optical microscopy, which uses the interaction of light with a sample to obtain an image, electron microscopy uses the interactions of an electron beam with a sample. The typical wavelength of an electron beam is around 5 orders of magnitude smaller than the wavelength of light.[6] Only objects that are larger than the wavelength of the illumination source can be observed and so the resolution of electron microscopy is much greater than the resolution of optical microscopes, allowing nanometre sized objects to be imaged. Whilst optical microscopes use carefully shaped glass lenses to focus the light, electron microscopes rely on magnetic fields to focus an electron beam. When a sample is exposed to an electron beam, the electrons collide with the electrons in the sample, resulting in elastic or inelastic scattering. Inelastic scattering can also lead to additional processes, such as the emission of an electron or electromagnetic radiation. These collisions can result in a deviation of the electrons' paths and electrons can be back-scattered, forward scattered or remain in the sample due to the absorption of energy by the sample. In transmission electron microscopy, it is the forward scattered transmitted electrons, as well as those that did not interact with the sample, that are detected. The detector, which in modern models is typically a charge coupled device (CCD) or complementary metal oxide semiconductor (CMOS) camera, then measures the number density of transmitted electrons at an image plane formed by an objective lens. Since TEM measures transmitted electrons and the mean free path of electrons is small, it is important that the sample thickness is also small, typically less than 100 nm.

2.1.3 Scanning-transmission electron microscopy (STEM)

STEM, as the title suggests, consists of aspects of both conventional scanning electron microscopy (SEM) and TEM.[7] Like in the case of SEM, a beam of electrons is focused using a series of lenses to form a focussed convergent beam (often referred to as the probe) at the surface of the sample. This probe can then be moved over the sample in a raster pattern to produce an image (see Figure 9). In comparison to conventional SEM, a thin sample (<100 nm) is used for STEM analysis and so it is the transmitted electrons that are detected.

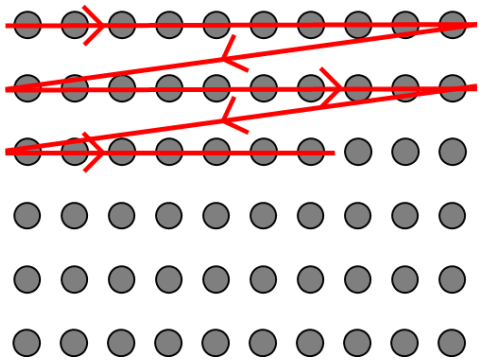

Figure 9: Schematic representation of an electron probe moving across a sample in a raster pattern to create an image

Typically, there are two detectors used for STEM; a bright field detector and a high angle annular dark field (HAADF) detector. The HAADF detector measures the total signal of scattered electrons with angles between a certain internal and external radius (hence the description of 'annular'). The detector measures high-angle elastic scattering which makes it highly sensitivity to atomic number. This sensitivity is a key benefit of ADF detectors since it means that it is possible to get good contrast between elements with different atomic numbers. Another particularly useful aspect of operating in STEM mode rather than TEM mode, is that since the electron beam is focussed to a spot on the sample surface, it is possible to obtain energy dispersive X-ray (EDX) spectra of a specified point on the image. This means that it is possible to probe the elemental composition of specific particles or specific areas of a particle. Additionally, it is possible to create elemental maps of selected areas of interest. The more extensive elemental analysis possible in STEM mode is particularly useful in the analysis of small bimetallic nanoparticles (such as those prepared in this report) since it provides confirmation that bimetallic particles have been formed, which is not possible with bulk elemental analysis.

2.1.4 Diffuse reflectance infrared Fourier transform spectroscopy (DRIFTS)

Diffusely reflected light can be defined as reflected light where the angle of incidence is not equal to the angle of reflection, as opposed to specular reflection where they are equal.[8] Specular reflection is generally associated with the reflection from polished surfaces whereas diffuse reflection often occurs with powdered samples. Figure 10 illustrates the main types of reflection that can occur with a sample consisting of small grains.[8] The two types of Fresnel reflection both contribute to the signal but contain minimal information with respect to the grains of material present since they are not transmitted through any sample grains. The Kubelka-Munk diffuse reflectance transmits through at least one grain of sample (as well as reflecting off of others) and so contains information on the species present in the sample. It is therefore this type of reflectance that allows the production of a DRIFT spectrum. The removal of contributions from specular Fresnel

reflectance is possible with the correct instrumentation (*e.g.* exclude radiation from the plane of incidence of the incident radiation), however contributions from diffuse Fresnel reflectance can generally only be reduced rather than removed altogether. This is done by ensuring the grain size is small which increases the amount of incident radiation will transmit through a sample grain. The situation with adsorbed surface species, such as CO in the present study, is slightly more complicated, as Fresnel reflections have angular and polarisation selection rules associated with them, but light reflected at the surface of a grain of material can in some cases result in the correct geometry to result in absorption of the infrared light.

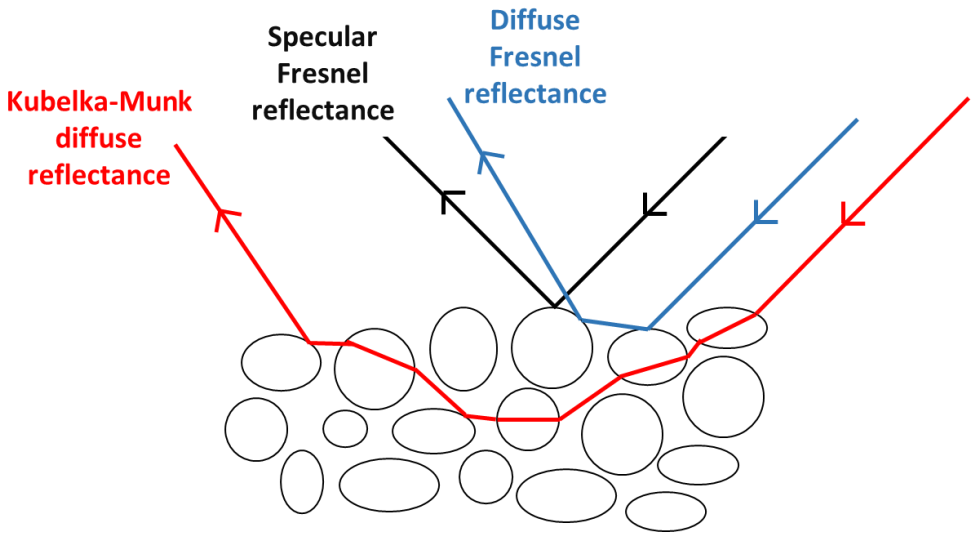

Figure 10: Schematic representation of the types of reflectance expected with a powdered sample during exposure to radiation during DRIFTS, adapted from Mitchell[8]

Quantitative analysis of DRIFTS data is complex, since there is not a linear relation between the intensity of a band and the concentration of the species in the sample.[8, 9] The most commonly used expression is the Kubelka-Munk equation, which is a simplified model based on the limiting case of an infinitely thick sample (see Equation 3).

$$f(R_\infty) = \frac{(1 - R_\infty)^2}{2R_\infty} = \frac{k}{s}$$

where R_∞ is the absolute reflectance of an infinitely thick sample, k is the absorption coefficient and s is the scattering coefficient.

Equation 3

Based on the Beer-Lambert law, the absorption coefficient can be expressed as shown in Equation 4.

$$k = 2.303\varepsilon c$$

where ε is the extinction coefficient and c is the sample concentration.

Equation 4

Combining Equation 3 and Equation 4 gives an expression that, if *s* is assumed to be an intrinsic property of the sample and therefore constant, varies directly with sample concentration (see Equation 5). This allows for semi-quantitative analysis of DRIFTS data. However, for measuring surface adsorbates, except where there is absorbance of most of the infrared light by the sample, experiments suggest absorbance to provide a more quantitative measure of concentration in practice.[10] For this reason, Kubelka Monk units have not been used in this report. It must also be remembered that DRIFTS is at best semi-quantitative.

$$f(R_\infty) = \frac{2.303\varepsilon c}{s}$$

Equation 5

One of the most common uses for DRIFTS with respect to heterogeneous catalysis with metal-based catalysts is CO-DRIFTS. This involves first exposing the catalyst to CO which binds to the surfaces of the metal particles. The CO can bind to sites in different ways depending on the type of site; linearly in the case of corner or edge sites and bridging in the case of the flat surface. The different ways in which the CO interacts with the surface results in shifts in the wavenumber of the carbonyl peak due to differences in the extent of π-backbonding (see Figure 11). This is important for catalysis since corner, edge and flat surface sites have different extents of coordination to other atoms, which results in corner and edge sites having higher energies than sites on the flat surface. Therefore, in structure sensitive reactions, this generally translates to edge and corner sites being more reactive than those on the flat surface.[11] Additionally, the adsorption geometry of reactants and/or products on these sites, which often plays a major role in determining selectivity, may be different.

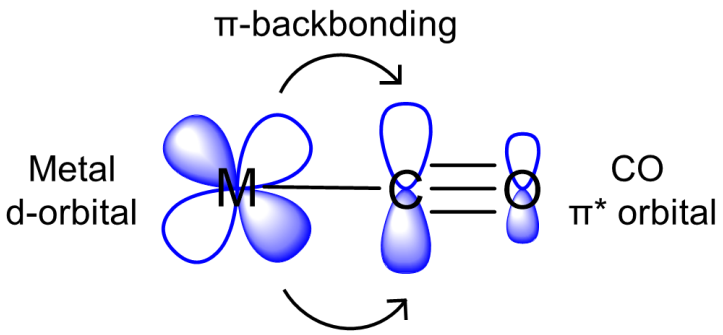

Figure 11: Representation of the orbitals involved in π-backbonding when CO interacts with a metal

The ratio of corner/edge sites to flat surface sites becomes increasingly important with the addition of a second metal to a catalyst since it could indicate the position(s) that the second metal substitutes. This is especially true if the aim of introducing a second metal is to target a specific type of surface site. For instance, the effect of Re on the surface of a Pd-based catalysts ($RePd/Al_2O_3$) was investigated using CO-DRIFTS.[12] The authors report that the introduction of Re consistently led to an increase in the ratio of linear to bridging CO. Therefore, in this case, the Re is not selectively substituting the edge/corner sites and is instead more generally disrupting the surface of the Pd metal particles. The authors then suggest, in combination with other analytical techniques, that the superior activity and selectivity of the Re-doped catalysts was as a consequence of the close contact of Re clusters with the Pd particles.

2.1.5 Gas chromatography – flame ionisation detector (GC-FID)

Gas chromatography is a technique that is used to separate mixtures of volatile chemicals for further analysis and/or quantitative detection.[13] The ease at which quantitative detection is possible using GC is often considered one of the merits of this technique. A GC operates by introducing a mixture of chemicals and rapidly heating them in the presence of an inert carrier gas, typically helium or hydrogen. This leads to the volatilisation of the sample before being introduced to the GC column. The GC column is typically a long metal tube with the inner surface coated in a thin layer of stationary phase such as polymer or inert solid supports. The GC column is kept inside an oven that can be temperature programmed to aid optimisation of peak separation as molecules pass through the column. The molecules interact with the stationary phase to different degrees depending on the functional groups in the molecule, which affects the retention time of the molecule (the time at which the chemical elutes from the column). Other factors can also affect the retention time of a molecule such as the boiling point. There are a variety of potential detectors that can be used to quantify the molecules exiting the column, including flame ionisation detectors (FIDs; Figure 12). FIDs operate by combustion of the organic molecules that exit from the column.

This combustion process results in the formation of ions. A voltage is applied between the flame jet and the nearby collector plates to create a potential difference between them such that ions move from the flame jet to the collector plates producing a current. This current is measured and is the signal output for the detector. It is important to note however that different molecules will have different response factors based on the ease with which they burn and the number of ions they produce during combustion. These response factors can be estimated by Equation 6 and Equation 7[14] since the response factors can be related to chemical make-up of the molecule. However, direct calibrations are almost always carried out to ensure reliable results.

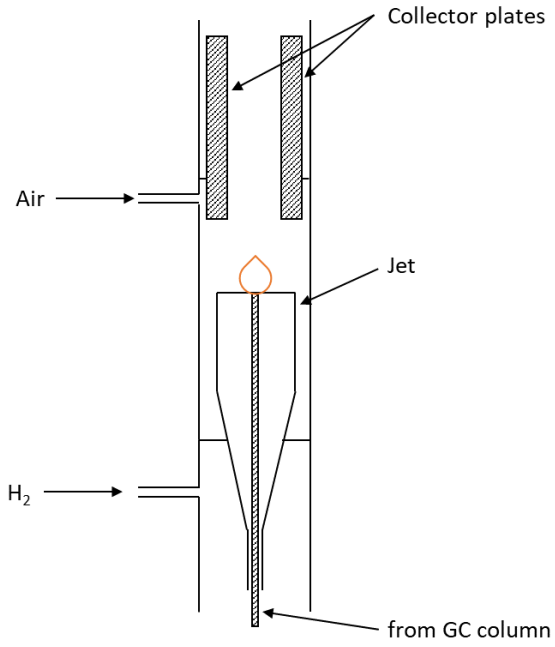

Figure 12: Simplified schematic of an FID detector, adapted from Rood[13]

$$MRF = -0.071 + 8.57 \times 10^{-4} \Delta H_{Comb}^{MF} + 0.127 n_{Benz}$$

Equation 6

$$\Delta H_{Comb}^{MF} = 11.06 + 103.57 n_C + 21.85 n_H - 48.18 n_O + 7.46 n_N + 74.67 n_S$$
$$-23.57 n_F - 27.44 n_{Cl} - 11.90 n_{Br} - 2.04 n_I$$

where MRF = molar response factor and n_x = number of atoms (e.g. C, H, O etc.) or fragments (e.g. Benz = benzene rings)

Equation 7

2.1.6 Gas chromatography – mass spectrometry (GC-MS)

As discussed above, GC-FID allows for the separation and quantification of compounds in a mixture. However, for the identification of products, GC-MS is more suitable since the GC separated compounds are passed through to a mass spectrometer. The mass spectrometer operates by first ionising the molecules, typically by electron impact (EI) ionisation in the case of GC-MS.[15] The produced ions are then separated by their mass-to-charge ratios (m/z) before reaching a detector. Unless using specialist techniques, most ions produced will only be singly charged, therefore the m/z ratio usually corresponds to the mass of an ion. During ionisation using EI, fragmentation of the molecules normally occurs due to the large amount of energy transferred to the molecules during the ionisation process. The fragmentation pattern produced can often give information about the original molecule and, in combination with other information from the mass spectrum such as the molecular ion, the identity of the molecule can normally be determined.

2.1.7 Inductively coupled plasma – optical emission spectroscopy/mass spectrometry (ICP-OES/ICP-MS)

ICP-OES is a commonly used analytical technique to determine elemental compositions and is applicable to a variety of elements. ICP relies on a plasma to transfer energy to a sample that leads to atomisation, ionisation and electronic excitation of atoms within the sample.[16] A plasma can be defined as a gas that is ionised, but that is overall neutral, containing equal numbers of positively and negatively charged particles. An argon plasma is used in ICP-OES as it has many useful properties such as a high ionisation energy and chemical inertness, therefore producing a simple emission spectrum and ensuring the argon ions do not form stable compounds with the element being analysed. When the atoms excited by the plasma return from these excited states to lower energy states, electromagnetic radiation is emitted. Optical emission spectroscopy can then separate the radiation emitted by wavelength, with specific elements (and their corresponding individual electronic transitions) appearing as spectral lines. The intensity of these lines can be related to the concentration of the element in the sample. ICP-OES instruments typically have detection limits of parts per billion (ppb), however ICP-MS instruments have a lower detection limit of parts per trillion (ppt)[17, 18] and so ICP-MS is often used to quantify the concentration of elements in very dilute samples. In ICP-MS systems, the ions produced from the sample in the plasma are transferred to a quadrupole mass analyser, which separates the ions present by their mass-to-charge ratios (m/z), and the number of these ions can then be determined (typically in counts per second) at the detector.[17, 19] The counts can then be correlated to a sample concentration after suitable instrument calibration.

One important point, particularly relevant for the analysis of supported metal catalysts, is that samples for ICP must be in the solution state. This is due to the fact that the sample is introduced to the plasma *via* a nebuliser, commonly an ultrasonic nebuliser. This device produces a fine mist of solution particles (an aerosol), however, it is not able to operate with solids or suspensions. Therefore, in order to analyse the metal content of these solid materials, the metals have to be removed from the support through a process commonly referred to as digestion. This typically involves heating the sample in concentrated acid or a mix of acids to dissolve the metal, thereby producing a solvated sample suitable for analysis.

2.1.8 Solid state nuclear magnetic resonance spectroscopy (SS NMR)

NMR is an analytical technique that can provide information on the structure and composition of molecules present in a sample, which can often help to identify them. NMR involves placing a sample in a magnetic field (B_0), which, if the nuclei has a non-zero spin, leads to a magnetic moment that is nearly aligned along the same axis as the magnetic field, in either the parallel or anti-parallel direction.[20] The parallel direction is a lower energy state than the anti-parallel direction, and so the population of the spins in the parallel direction is higher. This leads to a net magnetisation along the same axis and in the same direction as the magnetic field. By applying a pulse of radio frequency, the net magnetisation can be moved into the xy plane (Figure 13).[20] Relaxation back to the z-axis is recorded as a free induction decay (FID) and, by carrying out a Fourier transform of the FID, a typical NMR spectrum is produced.

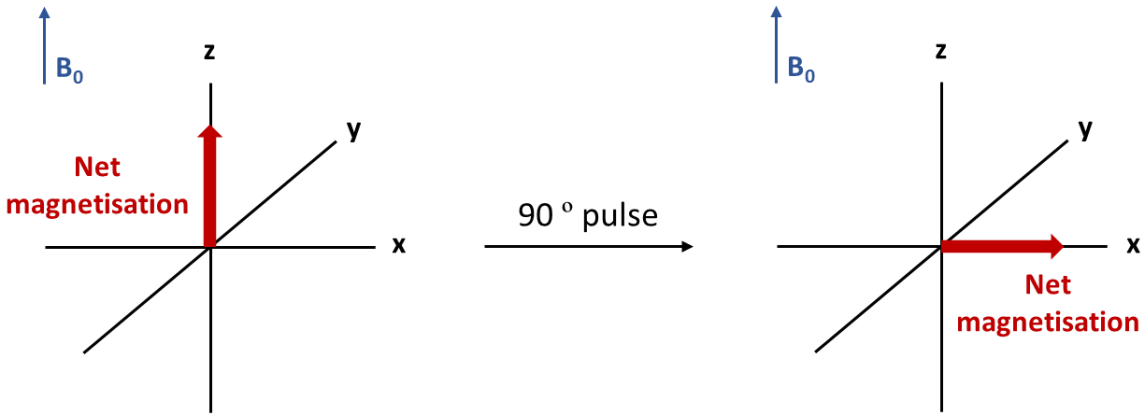

Figure 13: An example of the net magnetisation during an NMR experiment, adapted from Günther[20]

Carrying out NMR experiments of materials in the solid state, as opposed to the solution state, creates a variety of additional challenges. These challenges mainly arise from the fact that the orientation of molecules in solids is mostly fixed, whereas in solutions the molecules are rapidly tumbling.[21] Therefore, whilst in solution state NMR any values that depend on orientation are

averaged out, this is not the case for solid state experiments. There are three important and common techniques used in SS NMR that help alleviate some of the problems caused by fixed orientations, which are high power proton decoupling (HPPD), magic angle spinning (MAS) and cross polarisation (CP).[21]

The dipolar interactions between different atoms (*e.g.* ^{1}H and ^{15}N, or ^{1}H and ^{13}C) can lead to significant line broadening, especially with compounds that contain a large number of protons. This can be overcome using HPPD, which eliminates both the scalar and dipolar coupling and therefore helps with achieving narrower peaks.[21]

Another key source of line broadening in SS NMR is shielding anisotropy, in which nuclei in different crystallites, and therefore with different orientations with respect to the magnetic field, will have slightly different chemical shifts. All internal NMR interactions have a dependence on orientation when in a magnetic field as described by Equation 8.[21]

$$\frac{1}{2}(3\cos^2\theta - 1)$$

Equation 8

If the solid sample is rapidly rotated at a certain angle, β, with respect to the applied magnetic field, Equation 8 can be expressed as shown in Equation 9.[21]

$$\langle\frac{1}{2}(3\cos^2\theta - 1)\rangle = \frac{1}{2}(3\cos^2\beta - 1) \times \frac{1}{2}(3\cos^2\Theta - 1)$$

where Θ is the angle between a molecular level direction (e.g. interatomic distance) and the axis of rotation.

Equation 9

If β is set to 54.44 °, then cosβ is equal to 1/√3 which means the equation goes to zero and any effects from the anisotropy disappear, leading to a significant reduction in peak broadness.[21] Rapid rotation at this angle had such a dramatic impact on the broadness of the peaks that it was referred to as the 'magic angle', hence the technique was named magic angle spinning (MAS).

Cross polarisation involves the transfer of magnetisation from abundant nuclei (*e.g.* ^{1}H) to a dilute nuclei with the same spin of 1/2 (*e.g.* ^{13}C).[21] CP does not impact peak broadness unlike HPPD and MAS, however it has other benefits, with the main two being shorter relaxation times and an increase in signal intensity. In solids, the relaxation times for dilute spins (*e.g.* ^{13}C) tend to be long, which means significantly longer pulse sequences and therefore longer experiment times to achieve

a good signal to noise ratio. In cross-polarisation experiments, the magnetisation originates from the abundant nuclei (typically ^{1}H), and so the relaxation time depends on the recovery of the ^{1}H magnetisation, and not the relaxation of the dilute nucleus. The time required to recover the ^{1}H magnetisation is significantly shorter than the relaxation time of the dilute nucleus, and so it is possible to significantly reduce the experimental time required to achieve good signal to noise ratios. Additionally, due to differences in the equilibrium populations for the abundant and dilute nuclei, there is an increase in signal intensity. As an example, the maximum for ^{13}C is a factor of around 4, however this does depend significantly on the efficiency of the magnetisation transfer and the cross polarisation process in general.[21] This increase in signal again leads to a reduction in the amount of experimental time required to achieve spectra with good signal to noise ratios.

Overall, whilst the spectra obtained from solid state experiments are generally of lower resolution and can take longer to acquire than solution state equivalents, the techniques discussed above mean that it is possible to obtain useful spectra from solid samples.

2.1.9 Temperature programmed reduction/oxidation (TPR/TPO)

TPR is a characterisation technique commonly employed in the context of metal or metal oxide based catalysis to investigate the reduction processes that occur when the catalyst or pre-catalyst is heated at a constant rate in a reducing atmosphere (typically H_2, although CO is used in some cases).[22] A detector such as a thermal conductivity detector (TCD) is used to indicate when gas consumption occurs during the heating process, allowing the reduction temperature to be established. Additionally, careful calibration of the detector allows the consumption of the reducing gas to be quantified, which, when related to the number of moles of metal present in the sample, can provide additional information about the reduction process or processes that are occurring.

TPO is very similar to TPR, with the key difference being that TPO experiments are carried out in an oxidising atmosphere (*e.g.* oxygen) whereas TPR experiments are carried out in a reducing atmosphere. TPO is frequently employed to gain information on the oxidation processes that occur for metal or metal oxide catalysts, however, in the context of this thesis, the focus will be on its use for coke characterisation.

Many catalysts experience deactivation due to the formation of carbon deposits that, directly or indirectly, block access to active sites. This process is known as coking. In order to investigate the nature of the coke species present, spent catalysts are often analysed by TPO, since it can provide useful information about the coke including the type/morphology,[23, 24] the amount and, in some cases with detailed experiments and analysis, the location of the coke.[25]

Brown *et al.*[26] proposed the mechanism for coke combustion shown below in Figure 14, where -C_f corresponds to a free carbon site available for the chemisorption of oxygen and -C(O) and -C(O_2) correspond to dissociated and undissociated surface oxides respectively. Initially, oxygen is adsorbed onto a free site on the carbon surface (1), followed by re-arrangement to a more stable surface species resulting in the release of CO (2). The more stable surface species can then desorb to form additional CO (3) or react with additional oxygen resulting in the release of CO_2 (4). Additionally, the undissociated surface oxide, as formed in reaction (1), can desorb forming CO_2 (5). The authors also discuss some likely reasons for the changes in the TPO spectra of coked catalysts from different reactions, in comparison to charcoal. They suggested that the key reasons were the interactions between the coke and the catalyst (support and/or metal) particularly at low coverages of coke, a difference between the activation energy of coke combustion for coke in the pores and on the external surface of the catalyst and differences in the coke morphology and/or chemical species present leading to variability in the chemical reactivity.[26] Hence, TPO can be used to investigate various aspects of the coke present on catalysts.

$$—C_f + O_2 \longrightarrow —C(O_2) \quad (1)$$

$$—C(O_2) + —C_f \longrightarrow —C(O) + CO \quad (2)$$

$$—C(O) \longrightarrow CO \quad (3)$$

$$—C_f + O_2 \xrightarrow{—C(O)} CO_2 \quad (4)$$

$$—C(O_2) \longrightarrow CO_2 \quad (5)$$

Figure 14: Proposed mechanism for the combustion of coke[26]

2.1.10 X-ray photoelectron spectroscopy

XPS is a technique that can be used to determine the surface composition of different materials, including elemental composition and the oxidation states of the elements present.[27, 28] In XPS experiments, the sample is exposed to an X-ray source which provides the energy required to emit electrons from atoms in the material. By measuring the kinetic energy of these emitted electrons, it is possible to determine the binding energy of the electrons using Equation 10 shown below.[27] A typical XPS spectrum is then produced by plotting binding energy against intensity. Importantly, only those electrons that are coming from atoms near the surface of the material will escape and reach the detector, meaning that XPS is a surface sensitive technique.

$$E_K = h\nu - (E_B - \phi)$$

where E_K is the kinetic energy, $h\nu$ is the energy of the incident photons (where h is Plank's constant and ν is the frequency), E_B is the binding energy and Φ is the work function.

Equation 10

In order to measure the kinetic energy of the emitted electrons, it is important that the system is under ultra-high vacuum (UHV), since if gas molecules are present, the electrons would interact with the gas molecules, resulting in an attenuation of the photoelectron intensity observed. The requirement of UHV results in significant limitations, in particular for catalysis, since it means that in most cases, it is not possible to study the surface of a catalyst under reaction conditions. Therefore, instruments have been developed for near-ambient pressure XPS (NAP-XPS) experiments, where small amounts of gaseous molecules (typically up to around 25 mbar) can be present. One example of such an instrument is the near-ambient pressure end station of the B07 beamline at Diamond Light Source.[29] In this instrument, the ability to record spectra under near-ambient conditions is achieved by placing a small aperture (typically less than 1 mm diameter) very close to the sample. The aperture then connects to a differential pumping system that incrementally reduces the pressure before the photoelectrons reach the detector, which is under UHV (see Figure 15).[29] Although NAP-XPS is a relatively newly developed technique, it has been employed to study a variety of samples relevant to those discussed in this thesis, including bimetallic nanoparticles *e.g.* CoPt nanoparticles studied under reducing conditions[30] or CuNi/CuCo nanoparticles studied under reducing and oxidising conditions.[31]

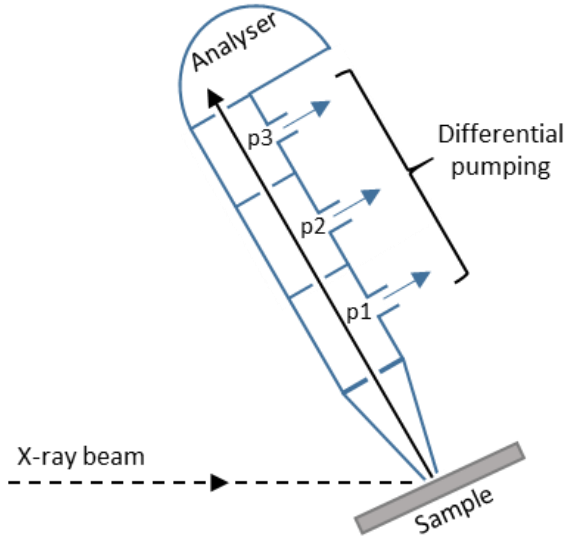

Figure 15: Schematic representation of a typical NAP-XPS set up[29]

The background chosen for XP spectra is important when carrying out quantitative analysis, as this can have a significant impact on the results, particularly the peak areas. Some of the more common backgrounds employed include the Shirley background and the Tougaard background and so these models will be discussed in further detail here.[32]

The Shirley background was first described in 1972 to allow for the detailed analysis of gold XP spectra.[33] The model accounts for step changes in the background over the energy range of the peak by assuming that the background at any specific binding energy is proportional to the integrated intensity of the peak at higher kinetic energies.[32] As briefly mentioned in the original paper by Shirley,[33] an iterative approach may be required to reduce the errors associated with the fact that the area of the peak, as used to calculate the Shirley background, is initially determined based on a linear background rather than the Shirley background. Therefore, an iterative Shirley background is frequently employed.

Tougaard and Sigmund proposed a background for XP spectra, known as the Tougaard background, based on contributions to the background from the extrinsic inelastic scattering of higher kinetic energy electrons.[34] This background is calculated based on the electron energy loss function and, by taking into account a variety of inelastic scattering events, the background was found to extend over a relatively large energy range.[32] Whilst this method can act as a good background model at energies higher than around 50 eV above the binding energy, it has been suggested that it is not as successful at accounting for the step changes often observed in the near-peak region.[35]

Other important considerations when carrying out quantitative analysis of XPS data are the inelastic mean free path (IMFP) of the electrons at the chosen kinetic energy, the cross section of the elements and, if carrying out experiments at near-ambient pressure, the extent of signal attenuation due to the presence of the gas molecules. The IMFP can be roughly estimated for most materials using a universal curve, as described by the equations detailed in a paper by Seah and Dench.[36] The cross sections of the elements being studied at the selected energies can be determined based on the work by Yeh and Lindau[37] who calculated the cross sections of a large number of elements at a variety of different energies. The extent of signal attenuation due to the presence of gas molecules in near-ambient pressure experiments is largely based on the instrument used to carry out the experiments and so cannot be universally calculated. Correction factors for signal attenuation due to the presence of gases for the NAP-XPS experiments discussed in this thesis can be estimated using the data reported by Held *et. al.,*[29] which details relevant the data for the instrument used.

2.1.11 Nanoparticle synthesis via chemical reduction

In comparison to the metal nanoparticles formed using incipient wetness techniques, forming nanoparticles as a colloidal solution *via* chemical reduction and subsequently loading onto oxide supports allows for the production of more well-defined particles with a monodisperse particle size distribution. Less variation in particle size and, for bimetallic materials, metal distribution, can make the interpretation of catalytic and/or analytical data easier, since it should lead to simplified data. The formation of nanoparticles using the solution-phase chemical-reduction method is not definitively understood, however the most commonly reported and likely mechanisms for nucleation, growth and ripening are discussed below.

2.1.11.1 Classical nucleation theory

Classical nucleation theory (CNT) was first developed in the 1920s and 30s to describe the process of particle formation in general[38-40] and is now a common model used to explain nanoparticle formation.[41, 42] In general, it describes the nucleation of a new phase (*e.g.* liquid from a vapour or solid from a melt or solution) and so can be applied to nanoparticle synthesis to describe the nucleation of metal atoms from a solution to form solid metal nanoparticles. In the case of nanoparticle synthesis, a metal salt pre-cursor is normally used, and so the first step in the synthesis requires reduction of the metal salt to form metal(0) atoms. The next stage is then nucleation to form small clusters of atoms. The change in Gibbs free energy (ΔG) associated with this nucleation (assuming homogeneous nucleation and spherical particles) can be expressed as shown in Equation 11.[41]

$$\Delta G = \frac{-4\pi r^3}{3v} kTlnS + 4\pi r^2 \sigma$$

where r is the radius of a spherical nucleus, v is the volume of a single atom/molecule, k is the Boltzmann constant, T is the temperature, S is the vapour supersaturation ratio and σ is the specific surface energy of the interface between the nucleus and the surrounding vapour.

Equation 11

The first term, corresponding to a decrease in free energy due to the phase transition during nucleation (bulk energy), and the second term, corresponding to an increase in free energy due to surface formation (interfacial energy), depend on the radius of the nucleus in opposing manners.[42] As a result, a maximum ΔG will be reached at a certain radius (see Figure 16). This radius is known as the radius of critical nucleus (r*) since it corresponds to a minimum in the probability of nucleus

formation and so, for a nucleus that has r = r*, the further addition of atoms/molecules leads to decreasing free energy and therefore increasing probability of formation.

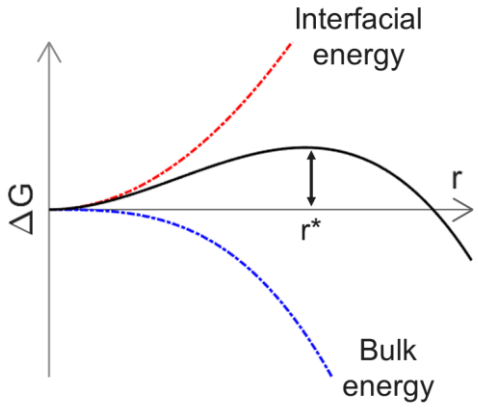

Figure 16: The dependence of Gibbs free energy on the radius of the nucleus based on classical nucleation theory

2.1.11.2 LaMer's nucleation and growth theory

LaMer's theory was based on CNT and introduced the concept of separate nucleation and growth stages.[43, 44] As the monomer concentration (typically metal(0) atoms in the case of metal nanoparticles) increases, the solution will reach a critical supersaturation value (C_s) where nucleation is possible, but there is not enough energy to overcome the energy barrier (*i.e.* the energy required to form nuclei with r = r*; Figure 16). As the concentration of monomers continues to increase, the solution will then reach the minimum supersaturation value (C_{min}) where there is enough energy to overcome the energy barrier, resulting in rapid, homogeneous nucleation, termed 'burst nucleation' (see Figure 17). This burst nucleation leads to a rapid decrease in the concentration of monomer in the solution, bringing the supersaturation value down below C_{min} and therefore resulting in an end to the nucleation stage. The system then enters the growth stage, where any additional monomer is added to the particles *via* diffusion to the particle surface.[45] Once the concentration of the monomer drops below the C_s value, then the particle can no longer grow *via* diffusion of the monomers to the particle surface and so the ripening stage begins.[46] The most applicable ripening mechanisms are discussed below.

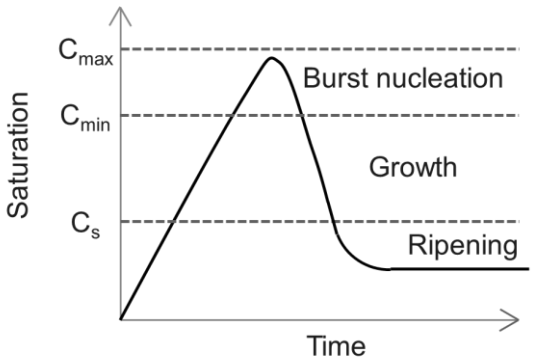

Figure 17: Schematic representation of the variation of monomer saturation with time according to LaMer's nucleation and growth theory, adapted from Polte[45] and Sorensen *et al.*[46]

2.1.11.3 Ostwald ripening

Ostwald ripening, which was first described over 100 years ago[47], is a process that leads to increasing average particle size. Smaller particles in the suspension, over time, re-dissolve into the solution and, in turn, the larger particles grow (see Figure 18).[48] The decreasing number of smaller particles, which have a high surface area to volume ratio, and the growth of larger particles, which lowers their surface area to volume ratio further, results in a decrease in the total surface area of the system. This decrease in total surface area corresponds to a decrease in the total free energy of the system and therefore acts as the thermodynamic driving force (as seen in Figure 16 where, once nucleation has occurred, increasing particle size results in decreasing free energy). There have been many proposed quantitative models reported to describe Ostwald ripening[48], however it is outside the scope of this thesis to discuss them in detail.

Figure 18: Schematic representation of Ostwald ripening

2.1.11.4 Digestive ripening

Digestive ripening essentially follows the opposite process to Ostwald ripening and is likely relevant to the nanoparticle syntheses in this report due to the small size of the nanoparticles produced by this method (~4 nm) and the presence of long chain amine and/or phosphine capping agents.[46] It is an important mechanism since it can offer some explanation for the formation of a narrow size distribution around an equilibrium particle size. Larger particles become smaller and smaller particles become larger, eventually converging at an equilibrium size, as opposed to Ostwald ripening where particles will continue to grow and an equilibrium size will not be reached. The reasoning behind this mechanism is not well understood,[46, 49-53] although it has been hypothesised

that it could be explained by employing a modified version of Equation 11 to account for a more realistic particle shape (polygonal rather than spherical). Rather than just terms for bulk and surface (inter-facial) sites, edge and corner sites also have to be considered (with dimensionalities of 1 and 0 respectively).[46] Therefore, the change in free energy can be given by a generalised expression, Equation 12.

$$\Delta G = a_3 r^3 + a_2 r^2 + a_1 r + a_0$$

Equation 12

Since the edge sites have a first-order dependence on particle radius, this term can have an impact on the free energy when *r* is low, as shown in Figure 19 where there is a minimum in the free energy. The radius at which this minimum occurs is then the equilibrium particle radius, r_{eq}. However, this does rely on the edge term being negative, which is somewhat unexpected since the surface term is positive due to the increase in surface free energy as the surface becomes larger, and so, following similar logic, it would be expected that the edge site term would also be positive. Therefore, a key flaw with this model is that there is no definitive explanation for the edge term being negative, although the authors do suggest that it may be related to the presence of adsorbed ligands on the surface (*e.g.* amine or phosphine capping agents).[46]

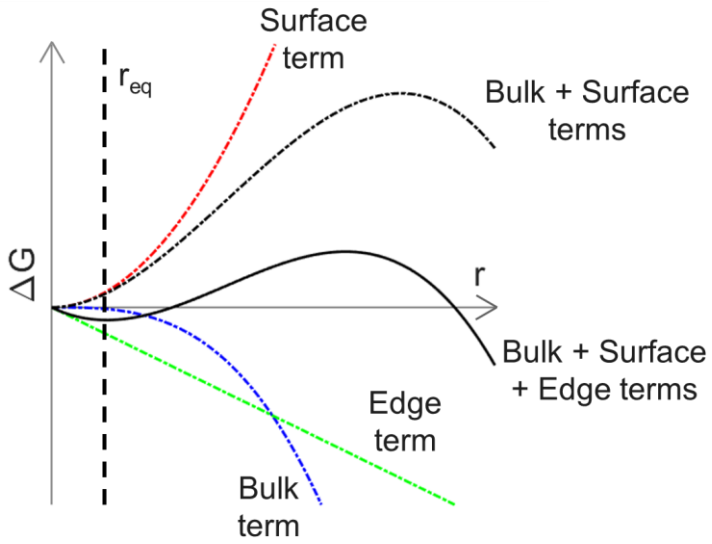

Figure 19: The dependence of Gibbs free energy on the radius of the nucleus comparing the results from digestive ripening and classical nucleation theory

Chikan and Kelly[54] explored the role of the capping agent during the synthesis of nanoparticles, in relation to digestive ripening. They proposed that the interaction of these ligands with the surface of the particles is the source of the minimum in free energy required to form an equilibrium particle

size. The binding of a ligand to the surface is energetically favourable and so it will have a negative contribution to the total free energy of the system. This offsets the increase in free energy resulting from increasing surface area and results in a minimum in the free energy. The radius at which this minimum occurs is then the equilibrium particle radius. The value of the equilibrium radius is dependent on the binding energy of the chosen ligand, with ligands that bind more strongly resulting in smaller particles. The authors backed up the key role of the ligand in digestive ripening by producing MoS_2 nanoparticles, from previously synthesised polydisperse samples, with a particle size of 3.5 nm or 8 nm dependent on the ligand used (I^- or SH^- respectively). Therefore, the ligand is likely playing a key role in the digestive ripening mechanism, although as stated previously, this complex process is still generally regarded as not well understood.

2.2 Experimental

2.2.1 Materials and general methods

Deionised water was obtained from a Purite Neptune and had a resistivity ≤18.2 MΩ. All gases were obtained from BOC and had a minimum purity of 99.99 %. The gases were further purified and dried using zeolite and activated carbon filters. The silica and titania catalyst supports were obtained from commercial sources: Cab-O-Sil M5 silica (CABOT) and P25 titania (Evonik). The ceria support, SBA-15 and KIT-6 silica were all synthesised in-house using the standard procedures detailed below. $Ni(NO_3)_2.6H_2O$, ethanol (HPLC grade), acetone (HPLC grade), n-hexane (HPLC grade), oleylamine (80 – 90 % C_{18}), oleic acid (~70 % oleic acid), furfuryl alcohol (98 %), tetrahydrofuran (99.5 %) and dichloromethane (analytical grade) were purchased from Fisher Scientific. Furfural (99 %), cerium nitrate hexahydrate (99%), heptane (HPLC grade), 1,2-dichlorobenzene (99 %), tetraethyl orthosilicate (98 %), Pluronic 123 (average M_n ~ 5800), borane *tert*-butylamine complex (97 %), 1-octadecene (90 %), diphenyl ether (99 %) and Na_2CO_3 (99.5 - 100.5 %) were purchased from Sigma Aldrich. Sn(II) 2-ethylhexanoate (96 %), $Ni(acac)_2$ (95 %) and $SnCl_2.2H_2O$ (98 %) were purchased from Alfa Aesar. 3-(trimethoxysilyl)propyl methacrylate (>98 %) was purchased from TCI. Dibenzyl ether (99 %) was purchased from Acros organics. 1-Butanol (99.4+ %) was purchased from Fluorochem. Tri-n-octylphosphine (97 %) was purchased from STREM chemicals and transferred under nitrogen flow to a Schlenk flask for storage. The furfural was purified *via* vacuum distillation from Na_2CO_3 before use.[55] The furfuryl alcohol was used as received, unless specifically stated that it was vacuum distilled from Na_2CO_3 before use. All other compounds were used as received. Unless stated otherwise, a Sorvall Legend centrifuge with 50 mL centrifuge tubes was used for all centrifugation.

2.2.2 Incipient wetness impregnation (IWI) catalysts

2.2.2.1 Estimation of the apparent pore volume of supports

Cab-O-Sil M5 silica (~0.6 g) was dried in a vacuum oven for around 4 hours at 120 °C. UHP water was added dropwise to a known mass of the dried silica, and a vortex mixer was used frequently to ensure an even dispersion of the water. Once the silica was seen to be macroscopically wet, observed as agglomeration, the pores were assumed to be filled. The mass (and therefore volume) of water added was measured, and this was used to calculate the approximate apparent pore volume of the silica. An analogous procedure was carried out for the other supports used for IWI catalysts (mesoporous CeO_2, TiO_2 and KIT-6).

2.2.2.2 Preparation of supported $Ni(NO_3)_2$ catalysts via IWI

To prepare a nominally 5 wt. % Ni/SiO_2 catalyst, the silica (Cab-O-Sil) was first dried for a minimum of 4 h in a vacuum oven at 120 °C. The dried silica (4.10 g) was placed in a round bottom flask or conical flask. $Ni(NO_3)_2.6H_2O$ (1.07 g) was dissolved in deionised water (12.7 mL) (as determined by the pore volume of the support). The $Ni(NO_3)_2.6H_2O$ solution was added dropwise to the silica with frequent mixing using a vortex mixer to ensure an even distribution. The impregnated silica was then dried overnight in an oven at 120 °C and then further dried in a vacuum oven for a minimum of 4 h at 120 °C. The nominally 5 wt. % Ni/TiO_2 and Ni/CeO_2 catalysts were prepared in an analogous manner (Ni/TiO_2: P25 titania (dried) 0.5048 g, $Ni(NO_3)_2.6H_2O$ 0.1348 g, deionised water 0.55 mL; Ni/CeO_2: mesoporous ceria (dried) 0.1324 g, $Ni(NO_3)_2.6H_2O$ 0.0355 g, deionised water 0.1 mL).

2.2.2.3 Ex situ reduction of IWI catalysts

In order to prepare samples for analysis (*e.g.* TEM or pXRD) or prior to impregnation with the Sn precursor (during the successive impregnation procedure detailed below in Section 2.2.2.4), the nickel nitrate impregnated samples had to be reduced. (Note: before catalysis, all samples were reduced *in situ* and so *ex situ* reduction was not necessary in these cases). Samples were placed into a quartz tube (either $1/8^{th}$ or 1/2 inch ID dependent on mass of catalyst used - typically around 80 mg for $1/8^{th}$ inch tube or 1 – 2 g for 1/2 inch tube). The tube contained a quartz wool plug that supported the catalyst, and when using the larger 1/2 inch tube, a second piece of glass wool was placed at the top of the catalyst bed to ensure it remained approximately level when turned horizontal. The tube was then placed inside a horizontal tube furnace. A K-type thermocouple was attached to the outside of the quartz tube using wire, ensuring that the end of the thermocouple was level with the position in the furnace of the centre of the catalyst bed. This thermocouple was used to provide feedback for an Omega CN7500 PID temperature controller that controlled the

temperature inside the tube furnace. Gases were supplied to the set up using computer controlled MKS G-series mass flow controllers (MFCs). The gases were passed through filters comprising of activated carbon and zeolite sieves to remove hydrocarbon impurities and/or water prior to entering the MFCs. The quartz tubes were attached to the gas supply *via* Ultra-Torr vacuum fittings (Swagelok). Catalyst reduction (for all samples except the titania supported catalyst) was carried out in 30 mL min^{-1} of hydrogen by heating to 500 °C at a rate of 15 °C min^{-1} and holding at 500 °C for 2 h before cooling to room temperature. The titania supported catalyst was reduced at the lower temperature of 300 °C but all other parameters remained the same as used for the other catalysts (lowering the reduction temperature to 300 °C gave an approximately three-fold more active catalyst, but did not significantly affect selectivity, likely due to strong metal support interaction (SMSI) effects reducing access to the nickel).[56] All reduced catalysts were stored in air prior to and during characterisation (TEM/pXRD), as well as prior to and during impregnation with tin in the successive impregnation method (Section 2.2.2.4), unless specifically stated otherwise.

2.2.2.4 Preparation of Sn-doped Ni/SiO_2 catalysts via successive IWI

To prepare a nominally 1.5 wt. % Sn-5 wt. % Ni/SiO_2 catalyst (denoted 1.5Sn-Ni/SiO_2 throughout this thesis), the $Ni(NO_3)_2$/SiO_2 pre-catalyst prepared as in Section 2.2.2.2 was reduced under the conditions outlined in Section 2.2.2.3. The reduced Ni/SiO_2 catalyst (1.6772 g) was weighed into a vial. $SnCl_2.2H_2O$ (0.0485 g; 0.2150 mmol) was weighed out and then dissolved in 4.5 mL of acetone. The $SnCl_2.2H_2O$ solution was added dropwise to the catalyst with frequent mixing using a vortex mixer to ensure an even distribution. The impregnated catalyst was dried for at least 6 hours in an oven at 120 °C, before being further dried in a vacuum oven overnight at 120 °C. The dried impregnated catalyst was then reduced under the conditions outlined Section 2.2.2.3. Initially, these catalysts were then washed with 5 x 15 mL portions of UHP water. However, it was found that this was not necessary since the chlorine had already been removed from the catalyst, likely during the reduction step (Section 5.5.1 in Chapter 5). A nominally 0.25 wt. % Sn-5 wt. % Ni/SiO_2 catalyst (denoted 0.25Sn-Ni/SiO_2 throughout this thesis) was prepared using a similar method, however the mass of the tin salt required was too small to be accurately weighed. Therefore $SnCl_2.2H_2O$ (0.0442 g, 0.1959 mmol) was dissolved in 25 mL of acetone and then 5 mL of this solution was added to the reduced Ni/SiO_2 (1.8692 g) dropwise with frequent mixing using a vortex mixer to ensure an even distribution. Apart from this small deviation, the procedure was analogous to the other sample.

2.2.3 Preparation of mesoporous supports

2.2.3.1 Synthesis of KIT-6 silica

The KIT-6 silica was prepared following the method outlined by Pirez *et al.*[57] P123 (6.0 g) was added to a mixture of deionised water (217 mL) and concentrated HCl (11.8 g) in a polypropylene bottle. The obtained mixture was stirred at 35 °C until homogeneous. 1-Butanol (6.0 g) was then added to the mixture and it was stirred at 35 °C for 1 h. Tetraethyl orthosilicate (TEOS) (12.9 g) was added and the mixture was continuously stirred at 35 °C for 24 h before aging at 100 °C for a further 24 h. The solid product was isolated by filtration whilst hot and without washing, and then dried at 100 °C for 24 h. The dried product was calcined in static air to remove the template material by heating it to 550 °C at a rate of 1 °C min^{-1} and holding it at 550 °C for 6 h.

2.2.3.2 Synthesis of mesoporous ceria

The mesoporous ceria was prepared based on methods outlined by Bruce *et al.*[58] and Tuysuz *et al.*[59] $Ce(NO_3)_3{\cdot}6H_2O$ (1.5 g) was dissolved in ethanol (20 mL), followed by the addition of KIT-6 silica (1 g). The mixture was stirred at room temperature until a nearly dry powder was obtained (~36 h). Then the sample was calcined by heating in static air to 500 °C at a rate of 1 °C min^{-1} and kept at 500 °C for 6 h. To remove the KIT-6 silica template, the resulting sample was added to 2 M NaOH (20 mL) in a polypropylene bottle and heated to 70 °C for around 24 h. The resulting mixture was centrifuged at 8000 rpm for 10 min to separate the solid. The solid was then added to another portion of 2 M NaOH (20 mL) in a polypropylene bottle. The mixture was sonicated to disperse the solid before being heated to 90 °C in static air for ~24 h. The sample was then separated *via* centrifugation at 8000 rpm for 10 min. The solid was washed 3 times with deionised water and then dried at 60 °C overnight.

2.2.3.3 Synthesis of SBA-15 silica

The SBA-15 silica was prepared by the method outlined by Somorjai *et al.*[60] Note: the SBA-15 silica was synthesised by a summer student (Rob Welsh). P123 (8 g) was added to deionised water (60 mL) and HCl (2 M, 240 mL) in a polypropylene bottle and stirred at 45 °C for 30 min. TEOS (17 g) was then added and the solution was stirred at 45 °C for 20 h. The solution was then aged at 100 °C for 24 h without stirring. The resulting material was filtered and washed with ethanol and deionised water. Then the product was calcined in static air to remove the template material by heating it to 550 °C at a rate of 1 °C min^{-1} and holding it at 550 °C for 4 h.

2.2.3.4 Synthesis of 3-(trimethoxysilyl)propyl methacrylate-grafted SBA-15

SBA-15 (~1 g) was dried at 120 °C in an oven overnight. Oven-dried SBA-15 (1 g) was added to a dried Schlenk tube and placed under vacuum using a Schlenk line. The sample was heated to 125 °C under vacuum overnight using an oil bath. The sample was then cooled to room temperature and back-filled with nitrogen. Dry toluene (75 mL) and 3-(trimethoxysilyl)propyl methacrylate (50 µL) were added to the sample. The solution was left stirring for 24 h under nitrogen. The sample was isolated by filtration (under air) and washed twice with toluene (2 x 15 mL), then twice with hexane (2 x 15 mL) and finally twice with methanol (2 x 15 mL). The sample was then left to dry at room temperature for around 2 days before being dried in a vacuum oven at room temperature for 2 h. The silane content was quantified by CHN analysis.

2.2.4 Synthesis of colloidal nanoparticles via chemical reduction

2.2.4.1 Synthesis of Ni nanoparticles (~4 nm)

These nanoparticles were prepared using a method outlined by Metin *et al.*[61] A 3-necked round bottom flask with a condenser was evacuated/backfilled with nitrogen three times. All glassware was dried in an oven at 120 ^{o}C overnight before use and was assembled whilst still hot to prevent water deposition. Then, $Ni(acac)_2$ (257mg, $8.17x10^{-4}$ mol), oleylamine (15 mL, $4.55x10^{-2}$ mol), and oleic acid (0.32 mL, $1.01x10^{-3}$mol) was added to the flask under a stream of nitrogen. The formed solution was heated to 110 °C while stirring over 20 min, and was kept at 110 °C for 1 h. The temperature was controlled using a PID controlled isomantle with feedback from a K-type thermocouple immersed in the reaction solution. Then, the solution was cooled down to 90 °C. Borane *tert*-butylamine complex (264 mg, $3.03x10^{-3}$ mol) and oleylamine (2 mL, $6.07x10^{-3}$mol) was added to a second 3-necked round bottom flask under nitrogen and stirred for around 1 h until dissolved. This solution was injected into the flask containing the $Ni(acac)_2$. The solution was kept at 90 °C for 1 h before rapidly cooling it to room temperature using an ice bath. Once the nanoparticle solution had reached room temperature, the reaction was exposed to air. The nanoparticle product was precipitated using the anti-solvent ethanol (~30 mL). The mixture was centrifuged at 8000 rpm for 10 min and then the supernatant was decanted. The particles were washed by first re-dispersing the precipitate in the smallest amount of hexane possible (~4 mL). The resulting solution was concentrated by evaporating some of the hexane until only a small amount remained (<1 mL), followed by the addition of the anti-solvent ethanol (~30 mL) to precipitate the nanoparticles. Finally, the mixture was centrifuged at 8000 rpm for 10 min and the supernatant was decanted. This washing process was performed a further 3 times. The particles were then dispersed in hexane (20 or 25 mL) for storage.

2.2.4.2 Synthesis of co-addition SnNi nanoparticles (~4 nm)

The co-addition Sn-Ni nanoparticles were prepared in an analogous method to that of the nickel nanoparticles (see Section 2.2.4.1), with the exceptions of adding tin (II) 2-ethylhexanoate (0.1076 mL, 2.12 x 10^{-4} mol) at the same point that $Ni(acac)_2$ was introduced and increased amounts of oleylamine (20 mL, 6.07 x 10^{-2} mol) and oleic acid (0.43 mL, 1.34 x 10^{-3} mol) were used.

2.2.4.3 Synthesis of sequential addition SnNi nanoparticles (~ 4 nm)

A 3-necked round bottom flask with a condenser was evacuated/backfilled with nitrogen three times. All glassware was dried in an oven at 120 ^{o}C overnight before use and was assembled whilst still hot to prevent water deposition. Then, $Ni(acac)_2$ (257 mg , 8.17x10^{-4} mol), oleylamine (20 mL, 6.07 x 10^{-2} mol), and oleic acid (0.43 mL, 1.34 x 10^{-3} mol) was added to the flask under a stream of nitrogen. The formed solution was heated to 110 °C while stirring in 20 min, and was kept at 110 °C for 1 h. The temperature was controlled using a PID controlled isomantle with feedback from a K-type thermocouple immersed in the reaction solution. The solution was cooled down to 90 °C. Borane *tert*-butylamine complex (264 mg, 3.03x10^{-3} mol) and oleylamine (2 mL, 6.07x10^{-3} mol) was added to a second 3-necked round bottom flask under nitrogen and stirred for around 1 h until dissolved. This solution was then injected into the flask containing the $Ni(acac)_2$ and the solution was kept at 90 °C for 1 h. Tin (II) 2-ethylhexanoate (0.1076 mL, 2.12 x 10^{-4} mol) and heptane (5 mL) were added to a third 3-necked round bottom flask under nitrogen and briefly stirred to ensure a homogeneous solution. This solution was injected into the nickel nanoparticle solution using a syringe pump at a rate of 0.333 mL min^{-1} to ensure slow, controlled addition. Once the addition of the tin reagent was complete, the solution was rapidly cooled to room temperature using an ice bath. Once the nanoparticle solution had reached room temperature, the reaction was exposed to air. The nanoparticle product was then precipitated using the anti-solvent ethanol (~30 mL). The mixture was centrifuged at 8000 rpm for 10 min and then the supernatant was decanted. The particles were washed by first re-dispersing the precipitate in the smallest amount of hexane possible (~4 mL). Then solution was concentrated by evaporating some of the hexane until only a small amount remained (<1 mL), followed by the addition of the anti-solvent ethanol (~30 mL) to precipitate the nanoparticles. Finally, the mixture was centrifuged at 8000 rpm for 10 min and the supernatant was decanted. This washing process was performed a further 3 times. The particles were dispersed in hexane (20 or 25 mL) for storage.

2.2.4.4 Synthesis of Ni nanoparticles (~12 nm; amorphous)

These nanoparticles were prepared using a method outlined by Mézailles *et al.*[62] A 3-necked round bottom flask with a condenser was evacuated/backfilled with nitrogen three times. All glassware was dried in an oven at 120 °C overnight before use and was assembled whilst still hot to prevent water deposition. $Ni(acac)_2$ (500 mg, 1.95 mmol), oleylamine (4 eq., 2.6 mL, 7.8 mmol), tri-n-octylphosphine (4 eq., 3.5 mL, 7.8 mmol) and 1-octadecene (0.8 mL) were added to the flask under a flow of nitrogen. The mixture was heated to 100 °C and maintained at this temperature until bubbling stopped (to degass the solution) and was then heated to 210 °C in around 20 min and kept at 210 °C for 2 h. The temperatures were controlled using a PID controlled isomantle with feedback from a K-type thermocouple immersed in the reaction solution. Once the reaction mixture had been held at reaction temperature for the appropriate length of time, it was cooled to 80 °C before being rapidly cooled to room temperature using an ice bath. Once the nanoparticle solution had reached room temperature, the reaction was exposed to air. The nanoparticle product was then precipitated using the antisolvent acetone (around 30 mL, HPLC grade). The mixture was centrifuged at 8000 r.p.m. for 10 min., then the supernatant was decanted. In order to wash the particles, the precipitate was re-dispersed in the smallest amount of hexane possible (around 4 mL, HPLC grade). The solution was then concentrated by evaporating some of the hexane until only a small amount remained (<1 mL). Then the anti-solvent acetone (around 45 mL, HPLC grade) was added to precipitate the nanoparticles. The mixture was centrifuged at 8000 r.p.m. for 10 min. and the supernatant was decanted. This washing process will be performed a further 3 times. The particles were dispersed hexane (around 20 mL, HPLC grade) for storage.

2.2.4.5 Synthesis of sequential addition SnNi nanoparticles (~12 nm; amorphous)

A 3-necked round bottom flask with a condenser was evacuated/backfilled with nitrogen three times. All glassware will be dried in an oven at 120 °C overnight before use and will be assembled whilst still hot to prevent water deposition. $Ni(acac)_2$ (500 mg, 1.95 mmol), oleylamine (4 eq., 2.6 mL, 7.8 mmol), tri-n-octylphosphine (4 eq., 3.5 mL, 7.8 mmol) and 1-octadecene (0.8 mL) were added to the flask under a flow of nitrogen. The mixture was heated to 100 °C and maintained at this temperature until bubbling stopped (to degass the solution) and was then heated to 210 °C in around 20 min and kept at 210 °C for 2 h. The temperatures were controlled using a PID controlled isomantle with feedback from a K-type thermocouple immersed in the reaction solution. A second flask 3-necked round bottom flask was evacuated/backfilled with nitrogen 3 times. A solution of Sn(II) 2-ethylhexanoate (31 µL, 0.096 mmol) in 1-octadecene (5 mL) was prepared. At the end of the 2 h reaction time, the Sn-containing solution was injected into the reaction flask at

a rate of 1.14 mL min^{-1} using a syringe pump. The reaction mixture was then cooled to 80 °C before being rapidly cooled to room temperature using an ice bath. Once the nanoparticle solution had reached room temperature, the reaction was exposed to air. The nanoparticle product was then precipitated using the antisolvent acetone (around 30 mL, HPLC grade). The mixture was centrifuged at 8000 r.p.m. for 10 min, then the supernatant was decanted. In order to wash the particles, the precipitate was re-dispersed in the smallest amount of hexane possible (around 4 mL, HPLC grade). The solution was then concentrated by evaporating some of the hexane until only a small amount remained (<1mL). Then the anti-solvent acetone (around 45 mL, HPLC grade) was added to precipitate the nanoparticles. The mixture was centrifuged at 8000 r.p.m. for 10 min. and the supernatant was decanted. This washing process will be performed a further 3 times. The particles were dispersed hexane (around 20 mL, HPLC grade) for storage. This procedure gave nanoparticles with a nominal Sn:Ni ratio of around 1:20. Nanoparticles with other Sn:Ni ratios were prepared in an analogous manner, with the amount of Sn(II) 2-ethylhexanoate varied to give the appropriate Sn:Ni ratio (Sn:Ni 1:50: 12 µL (0.037 mmol) of Sn(II) 2-ethylhexanoate, 2 mL of 1-octadecene, flow rate of 1.14 mL min^{-1}). Nanoparticles with Sn:Ni ratio of around 1:3 were prepared by using an excess of Sn(II) 2-ethylhexanoate (459 µL, 1.42 mmol) dissolved in 5 mL of 1-octadecene and added at a rate of 0.171 mL min^{-1}. It is suspected that the additional Sn is present in the supernatant/insoluble particles.

2.2.4.6a Synthesis of Ni nanoparticles (~16 nm; amorphous)

These nanoparticles were prepared using a method outlined by Emmerling *et al.*[63] A 3-necked round bottom flask was evacuated/backfilled with nitrogen three times. All glassware was dried in an oven at 120 °C overnight before use and will be assembled whilst still hot to prevent water deposition. $Ni(acac)_2$ (65 mg, 0.253 mmol), oleylamine (10 eq., 0.83 mL, 2.53 mmol), and diphenyl ether (8.9 mL) were added to the flask under a stream of nitrogen (total reaction volume of ~10 mL). Nitrogen was bubbled through the solution for around 2 min to degass before the mixture was heated to 100 °C and held at that temperature for 10 min. Tri-n-octylphosphine (2 eq., 0.23 mL, 0.506 mmol) was added and then nitrogen was bubbled through the solution for 2 min to degass. The solution was then heated to 220 °C (in around 20 mins) and was kept at 220 °C for 2 h. The temperature was controlled using a PID controlled isomantle with feedback from a K-type thermocouple immersed in the reaction solution. Once the reaction was complete, it was allowed to cool to 80 °C, before being placed in an ice bath to rapidly cool to room temperature. Once the nanoparticle solution had reached room temperature, the reaction was exposed to air. The nanoparticle product was precipitated using the antisolvent acetone (around 30 mL, HPLC grade). The mixture was centrifuged at 8000 r.p.m. for 10 min, then the supernatant was decanted. In order

to wash the particles, the precipitate was re-dispersed in the smallest amount of hexane possible (around 4 mL, HPLC grade). The solution was then concentrated by evaporating some of the hexane until only a small amount remained (<1mL). The anti-solvent acetone (around 30 mL, HPLC grade) was added to precipitate the nanoparticles. The mixture was centrifuged at 8000 r.p.m. for 10 min and the supernatant was decanted. This washing process was performed a further 3 times. The particles were then dispersed hexane (around 20 mL, HPLC grade) for storage.

2.2.4.6b Synthesis of Ni nanoparticles (~16 nm; polycrystalline)

These nanoparticles were prepared using a method outlined by Emmerling *et al.*[63] A 3-necked round bottom flask was evacuated/backfilled with nitrogen three times. All glassware was dried in an oven at 120 ^{o}C overnight before use and will be assembled whilst still hot to prevent water deposition. $Ni(acac)_2$ (65 mg, 0.253 mmol), oleylamine (10 eq., 0.83 mL, 2.53 mmol), and dibenzyl ether (3.9 mL) were added to the flask under a stream of nitrogen (total reaction volume of ~5 mL). Nitrogen was bubbled through the solution for around 2 min to degass before the mixture was heated to 100 °C and held at that temperature for 10 min. Tri-n-octylphosphine (2 eq., 0.23 mL, 0.506 mmol) was added and then nitrogen was bubbled through the solution for 2 min to degass. The solution was then heated to 220 °C (in around 20 mins) and was kept at 220 °C for 2 h. The temperature was controlled using a PID controlled isomantle with feedback from a K-type thermocouple immersed in the reaction solution. Once the reaction was complete, it was allowed to cool to 80 °C, before being placed in an ice bath to rapidly cool to room temperature. Once the nanoparticle solution had reached room temperature, the reaction was exposed to air. The nanoparticle product was precipitated using the antisolvent acetone (around 30 mL, HPLC grade). The mixture was centrifuged at 8000 r.p.m. for 10 min, then the supernatant was decanted. In order to wash the particles, the precipitate was re-dispersed in the smallest amount of hexane possible (around 4 mL, HPLC grade). The solution was then concentrated by evaporating some of the hexane until only a small amount remained (<1mL). The anti-solvent acetone (around 30 mL, HPLC grade) was added to precipitate the nanoparticles. The mixture was centrifuged at 8000 r.p.m. for 10 min and the supernatant was decanted. This washing process was performed a further 3 times. The particles were then dispersed hexane (around 20 mL, HPLC grade) for storage.

2.2.4.7 Synthesis of sequential addition SnNi nanoparticles (~16 nm; polycrystalline)

A 3-necked round bottom flask was evacuated/backfilled with nitrogen three times. All glassware was dried in an oven at 120 ^{o}C overnight before use and will be assembled whilst still hot to prevent water deposition. $Ni(acac)_2$ (65 mg, 0.253 mmol), oleylamine (10 eq., 0.83 mL, 2.53 mmol), and dibenzyl ether (3.9 mL) were added to the flask under a stream of nitrogen. Nitrogen was bubbled

through the solution for around 2 min to degass before the mixture was heated to 100 °C and held at that temperature for 10 min. Tri-n-octylphosphine (2 eq., 0.23 mL, 0.506 mmol) was added and then nitrogen was bubbled through the solution for 2 min to degass. The solution was then heated to 220 °C (in around 20 mins) and was kept at 220 °C for 2 h. The temperature was controlled using a PID controlled isomantle with feedback from a K-type thermocouple immersed in the reaction solution. A second flask 3-necked round bottom flask was evacuated/backfilled with nitrogen 3 times. A solution of Sn(II) 2-ethylhexanoate (12 µL, 0.037 mmol) in dibenzyl ether (3 mL) was prepared and nitrogen was bubbled through the solution for 2 mins to degass. At the end of the 2 h reaction time, the 1 mL of the Sn-containing solution was injected into the reaction flask at a rate of 1.71 mL min^{-1} using a syringe pump. The reaction mixture was then cooled to 80 °C in air before being rapidly cooled to room temperature using an ice bath. Once the nanoparticle solution had reached room temperature, the reaction was exposed to air. The nanoparticle product was precipitated using the antisolvent acetone (around 30 mL, HPLC grade). The mixture was centrifuged at 8000 r.p.m. for 10 min, then the supernatant was decanted. In order to wash the particles, the precipitate was re-dispersed in the smallest amount of hexane possible (around 4 mL, HPLC grade). The solution was then concentrated by evaporating some of the hexane until only a small amount remained (<1mL). The anti-solvent acetone (around 30 mL, HPLC grade) was added to precipitate the nanoparticles. The mixture was centrifuged at 8000 r.p.m. for 10 min and the supernatant was decanted. This washing process was performed a further 3 times. The particles were then dispersed hexane (around 20 mL, HPLC grade) for storage. Nanoparticles with a molar Sn:Ni ratio of 1:50 were prepared in an analogous manner, with the amount of Sn(II) 2-ethylhexanoate varied to give the appropriate Sn:Ni ratio (injected 0.4 mL of a solution that consists of 12 µL (0.037 mmol) of Sn(II) 2-ethylhexanoate in 3 mL of dibenzyl ether using a syringe pump with a flow rate of 1.71 mL min^{-1}).

2.2.4.8 Synthesis of Ni nanoparticles using a seeded growth method

A 3-necked round bottom flask was evacuated/backfilled with nitrogen three times. All glassware was dried in an oven at 120 ^{o}C overnight before use and was assembled whilst still hot to prevent water deposition. $Ni(acac)_2$ (1028mg , 3.27 mmol), oleylamine (15 mL, 45.5 mmol), and oleic acid (1.28 mL, 4.04 mol) were added to the flask under a stream of nitrogen. At room temperature, the mixture was a solid, and so the reaction mixture was first heated to 70 ^{o}C in order to form a solution, and then heated to 110 ^{o}C in 11 min and kept at 110 ^{o}C overnight before it was cooled to room temperature. The temperatures were controlled using a PID controlled isomantle with feedback from a K-type thermocouple immersed in the reaction solution. A 3-necked round bottom flask will be evacuated/backfilled with nitrogen three times, then $Ni(acac)_2$ (257 mg , 0.817 mmol),

oleylamine (15 mL, 45.5 mmol), and oleic acid (0.32 mL, 1.01 mmol) was added to the flask under a stream of nitrogen. The solution was heated to 110 ^{o}C whilst stirring in 20 min and was kept at 110 ^{o}C for 1 h. Then, the solution was cooled down to 90 ^{o}C. Another 3-necked round bottom flask was evacuated/backfilled with nitrogen three times and a solution of borane *tert*-butylamine complex (264 mg, 3.03x10^{-3}mol) dissolved in Oleylamine (2 mL, 6.07x10^{-3}mol) was prepared and stirred for around 1 h to ensure homogeneity, after which it was injected into the reaction solution. The reaction was kept at 90 ^{o}C for an hour. Another 3-necked round bottom flask was evacuated/backfilled with nitrogen three times and a solution of borane *tert*-butylamine (BTB) complex (1056 mg, 1.21x10^{-2} mol) dissolved in Oleylamine (16.3 mL, 4.95 x10^{-2} mol) was prepared and stirred for around 1 h to ensure homogeneity. The $Ni(acac)_2$ solution that was stirred overnight and the BTB/oleylamine solution was co-fed into the reaction flask using a dual syringe pump at a rate of 0.1358 mL min^{-1} (~ 2 h injection time). Once the addition was complete, the reaction was then rapidly cooled to room temperature using an ice bath. Once the nanoparticle solution had reached room temperature, the reaction was exposed to air. The nanoparticle product was then split into 3 centrifuge tubes and precipitated using the antisolvent ethanol (around 100 mL split between the 3 centrifuge tubes, ≥99%, Sigma-Aldrich). The mixture was centrifuged at 8000 r.p.m. for 10 minutes and then the supernatant was decanted. In order to wash the particles, the precipitate was redispersed in the smallest amount of hexane possible (around 4 mL, 95%, Fischer-Scientific). The solution was concentrated by evaporating some of the hexane until only a small amount remained (<1mL). The anti-solvent ethanol (around 30 mL, ≥99%, Sigma-Aldrich) was added to precipitate the nano-particles. The mixture was centrifuged at 8000 r.p.m. for 10 minutes and then the supernatant was decanted. This washing process was performed a further 3 times. The particles were then dispersed hexane (around 20 mL, ≥99%, Sigma-Aldrich) for storage.

2.2.5 Preparation of supported nanoparticle catalysts

2.2.5.1 Impregnation of nanoparticles onto KIT-6 support

KIT-6 (~0.2 g) was dried at 120 °C in an oven overnight. Oven-dried KIT-6 (0.2 g) was added to a dried Schlenk tube and placed under vacuum using a Schlenk line. The sample was heated to 120 °C under vacuum overnight using an oil bath. The sample was then cooled to room temperature and back-filled with nitrogen. Under nitrogen flow, the KIT-6 was covered with hexane (~4 mL). The mixture was then exposed to air and all subsequent procedures were carried out in air. The mixture was sonicated for around 5 min until it was homogeneous. The solution of small nickel nanoparticles in hexane (as prepared in Section 2.2.4.1) was also sonicated for around 5 min, before a portion (10 mL - the required volume to prepare a nominally 5 wt. % Ni catalyst) was added to the KIT-

6/hexane mixture. The resultant mixture was sonicated for 1 h, before the solid was isolated *via* centrifugation (8000 rpm, 10 min). The solid was washed by adding 20 v/v % ethanol in acetone (15 mL) and then centrifuging the mixture at 8000 rpm for 10 min to separate the solid. This was repeated a further 6 times before the sample was dried in an oven at 70 °C for 2.5 d. The other nanoparticles were impregnated in an analogous method with the amounts of pre-cursor varied accordingly to achieve nominally 5 wt. % Ni catalysts (Typical masses are listed here, however it should be noted that the masses varied slightly between different batches of the same catalyst; co-addition small Sn-Ni nanoparticles: oven dried KIT-6 (0.35 g), nanoparticle/hexane solution (14.1 mL); sequential addition small Sn-Ni nanoparticles: oven dried KIT-6 (0.44 g), nanoparticle/hexane solution (15.8 mL); larger amorphous Ni nanoparticles: oven dried KIT-6 (0.47 g), nanoparticle/hexane solution (7.7 mL); larger amorphous SnNi nanoparticles (Sn:Ni ratio of 1:20): oven dried KIT-6 (0.49 g), nanoparticle/hexane solution (7.9 mL); larger amorphous SnNi nanoparticles (Sn:Ni ratio of 1:50): oven dried KIT-6 (0.49 g), nanoparticle/hexane solution (8.1 mL); larger crystalline Ni nanoparticles: oven dried KIT-6 (0.19 g), nanoparticle/hexane solution (16.2 mL); larger crystalline SnNi nanoparticles (Sn:Ni ratio of 1:20): oven dried KIT-6 (0.19 g), nanoparticle/hexane solution (16.4 mL); larger crystalline SnNi nanoparticles (Sn:Ni ratio of 1:50): oven dried KIT-6 (0.19 g), nanoparticle/hexane solution (16.2 mL)).

2.2.5.2 Treatment of Ni nanoparticles (~4 nm) supported on KIT-6 with ozone

A sample of the Ni nano/KIT-6 material (0.033 g) was added to a quartz tube supported by glass wool. The quartz tube was connected to a Triogen LAB2B ozone generator which was supplied with oxygen at a rate of 2 L min^{-1}. The ozone generator was then started and the top portion of the catalyst bed turned from dark grey to black within <1 min of ozone exposure. The catalyst was exposed to the ozone for around 1 h at which point around a quarter of the bed was black (see Figure 20). The bed was then shaken slightly to mix the sample and then exposed to ozone for a further hour. Then bed was then shaken for a third time and exposed to ozone for a further 5 min, by which point it most of the sample was black.

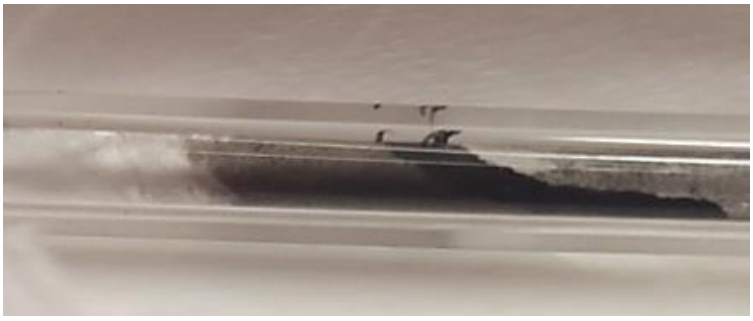

Figure 20: Ni nano/KIT-6 after around 1 h of treatment with ozone

2.2.6 Furfural hydrogenation

2.2.6.1 Vacuum distillation of furfural

Furfural (100 mL) was added to a round bottom flask, followed by ~7 wt. % Na_2CO_3 (8.12 g) to neutralise any acidic components such as 2-furoic acid.[55] A standard vacuum distillation set-up was used, with the addition of a fractionation column (~15 cm in length) since a substantial amount of bumping occurred during the distillation. The flask that contained the crude furfural was heated to around 100 °C using an oil bath and the pressure in the set-up was reduced to around 40 Torr, however the pressure gauge continually mal-functioned when exposed to the reaction set-up and so the exact pressure at which the distillation occurred is not known. The pressure in the set-up was reduced gradually in steps until the distillation occurred at a steady rate. A clear liquid (originally dark brown/black) was obtained and transferred to a Schlenk flask under nitrogen. The Schlenk flask was then wrapped in aluminium foil to limit exposure to light and placed in the freezer for storage.

2.2.6.2 Vapour phase furfural hydrogenation

A schematic representation of the reactor used for vapour-phase furfural hydrogenation is depicted in Figure 21. Furfural hydrogenation was carried out in a fixed bed reactor, consisting of a 1/4 inch outer diameter stainless steel tube that sat inside a vertical tube furnace. Gases were delivered by computer controlled MKS mass flow controllers. Unreduced catalyst (10 – 120 mg as necessary to obtain comparable / desired catalyst activities) was added to the reactor tube supported by a glass rod and glass wool. The IWI catalysts (excluding the titania supported catalyst) were reduced *in situ* in 30 mL min^{-1} of hydrogen by heating to 500 °C at a rate of 15 °C min^{-1} and holding at 500 °C for 2 h before cooling to the reaction temperature of 180 °C. The nanoparticle catalysts, Ni/TiO_2 and the copper chromite catalyst required lower reduction temperatures and were heated to 300 °C (still at a rate of 15 °C min^{-1}) under the same hydrogen flow (30 mL min^{-1}) but held at 300 °C for varying amounts of time (2 h for the nanoparticle catalysts, 3 h for Ni/TiO_2 and 4 h for copper chromite) before cooling to the reaction temperature of 180 °C. The conditions for the activation of the nanoparticle catalysts were chosen based on TPR analysis, the conditions for copper chromite were taken from literature protocols,[64] and the conditions for Ni/TiO_2 were established experimentally, since lowering the reduction temperature to 300 °C gave an approximately three-fold more active catalyst.

During furfural hydrogenation, the hydrogen flow rate was increased to 70 mL min^{-1} and distilled furfural was supplied at a rate of 0.0138 mL min^{-1} using a syringe pump (World Precision

Instruments, molar H_2:furfural ratio 19:1). The furfural and hydrogen passed into a vaporiser, which consisted of a stainless steel ConFlat full nipple containing glass beads for heat transfer and was heated to 170 °C using heat tapes, as monitored by a K-type thermocouple positioned on the vaporizer. All tubing/components after the vaporizer were heat traced (160 – 220 °C) to prevent condensation. The catalyst bed was kept at 180 °C during reaction, with temperature feedback provided by a K-type internal thermocouple that sat just above the catalyst bed. Typical runs lasted around 16 h. Online sampling of the reactor effluent was achieved by connecting the exit to a six-way Vici-Valco sampling valve, before venting *via* a cold trap. The samples from the valve were injected into a Hewlett Packard HP5890 gas chromatograph (GC) with a flame ionisation detector (FID), equipped with a SGE BP5 30 m column (ID: 0.53 mm; film thickness: 1 μm). Samples were collected automatically (around 5 h^{-1}) and analysed using the GC-FID (Oven temperature programme: 4 min at 60 °C, then heated to 140 °C (heating rate of 20 °C min^{-1}) and held at 140 °C for 1 min). Calibrations of the FID sensitivity factors and GC retention times were conducted by initially identifying products from the cold trap after reaction using an off-line GC-MS and then injecting commercial samples of the identified products into the online GC to calculate FID sensitivity factors and confirm retention times. Selectivity was calculated as the fraction: (moles of a given product) / (moles of all detected products) and expressed as a percentage. Selectivity was seen to be stable after the first few hours in all cases (even though conversion decreased during a run), therefore data was averaged over a period from ~5 -10 h time on stream (TOS) to obtain the most accurate values possible for smaller components in the product mixture. To obtain results for consistent conversion profiles conversion at 5 h TOS were targeted to be ~25% (and were all within the range 5-40%). Given that no strong selectivity variations were seen over time as catalysts deactivated across this conversion range, this eliminated the possibility that variations in selectivity seen were the result of obtaining measurements at substantially different conversions, or from catalysts experiencing different mass transport regimes. Conversion was calculated as the fraction: (moles of all products detected)/(initial moles of furfural). The mass balance was seen to be close to unity within experimental sensitivity and reproducibility (overall < 10%), although as discussed in several later chapters, some deposition of carbonaceous materials must be occurring. Errors shown are based on 4 repeat measurements of a typical sample (the standard error in the mean for the Ni/SiO_2 sample as this was reproduced 4 times to get an estimate of reproducibility, or standard error in this typical sample, where applied to samples repeated a smaller number of times).

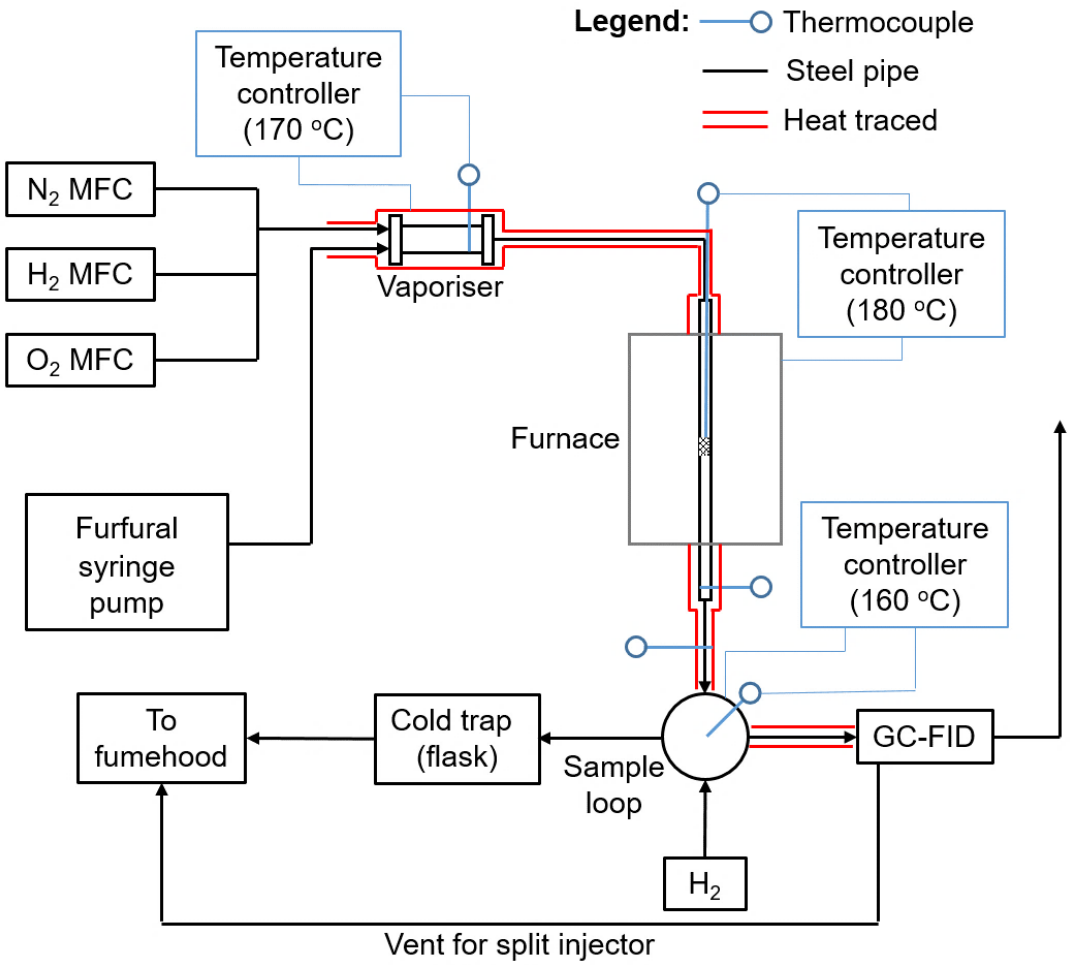

Figure 21: Schematic representation of the reactor set-up used for vapour-phase furfural hydrogenation

2.2.7 Characterisation techniques

2.2.7.1 TPR

A schematic representation of the TPR set-up is shown in Figure 22. Impregnated catalyst (50 mg) was added to a quartz tube, supported with quartz wool, placed inside a tube furnace and connected to gas lines *via* Ultra-torr type fittings. Gas flows were set to 10 mL min^{-1} of hydrogen and 40 mL min^{-1} of nitrogen. The outlet of the quartz tube was connected to a calcium chloride column to remove water before the gases were analysed with a homebuilt thermal conductivity detector (TCD). The hydrogen amount represented by TPR peaks was calibrated by TPR of known masses of CuO diluted in SiC ($CuO + H_2 \rightarrow Cu + H_2O$; 3 different masses, each run in duplicate).

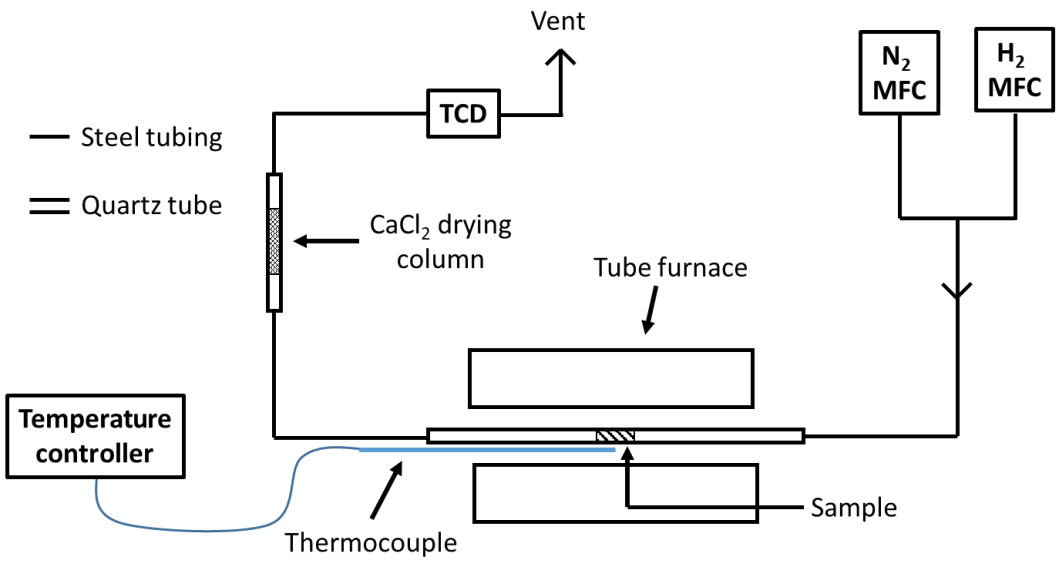

Figure 22: Schematic representation of a typical TPR set-up (MFC: mass flow controller)

2.2.7.2 pXRD

For supported metal catalysts, pXRD patterns were acquired using a Bruker AXS D8 Advance diffractometer, fitted with a Lynxeye Soller PSD detector and controlled by Diffrac and XRD commander software. Samples were placed on a low background silicon sample holder (silicon wafer (100)-cut off orientation 9 ° towards (001), Sil'tronix Silicon Techniologies, mounted in a plastic puck). Copper $K\alpha_1$ (λ = 1.5406 Å) and $K\alpha_2$ (λ = 1.5444 Å) radiation was used. Patterns were recorded with a 2θ range of 10 – 90 ° and a typical scan lasted ~110 min. All samples were reduced prior to analysis, however they were exposed to air before and during analysis.

For unsupported nanoparticles, 5 - 10 mL of the nanoparticles dispersed in hexane (depending on the concentration of the nanoparticle solution) was deposited onto a low background silicon wafer by drop-casting. The silicon wafer was mounted in a plastic puck using white tack before collecting pXRD patterns. The pXRD patterns were acquired using the same instrument and radiation as used for the supported catalysts discussed above. Patterns were recorded with a 2θ range of 10 – 140 ° and a typical scan lasted ~90 min.

The Scherrer equation was used to estimate crystallite sizes for several samples. MATLAB was used to apply an exponential background to the section of the data in the 2θ range of 23 – 50 ° and fit a Gaussian function to the Ni (111) reflection at 44.5 °. This gave the full width at half maximum (FWHM) of the reflection, permitting crude estimation of the crystallite size using the Scherrer equation (Equation 2).

Rietveld refinements were carried out by Prof. John Evans, a collaborator in this project, using TOPAS academic.

2.2.7.3 ICP-OES/ICP-MS

For supported samples, the digestion was carried out by boiling a small amount of catalyst (typically ~20 mg) in around 3 mL of aqua regia (3:1 v/v conc. HCl: conc. HNO_3) at 80 °C for 1 h. For unsupported nanoparticle samples, the desired volume of nanoparticles dissolved in hexane was added to a boiling tube and heated to evaporate the hexane (50 – 70 °C depending on the volume of sample). Once the hexane had evaporated, the tubes were left to cool to room temperature, around 3 mL of aqua regia (3:1 v/v conc. HCl: conc. HNO_3) was added and then the samples were digested by heating them to 80 °C for 1 h.

After digestion was complete and the solutions were at room temperature, they were diluted with deionised water using volumetric flasks to achieve a solution with the appropriate metal concentration (Ni: 80 mg L^{-1} or 8 mg L^{-1}; Sn: 8 mg L^{-1} or 0.08 mg L^{-1}). Controls were prepared from the water-soluble salt precursor $Ni(NO_3)_2.6H_2O$ for Ni and $SnCl_2.2H_2O$ (soluble low concentration acidic solutions), and used to confirm the absence of any significant deviations on a given run. The required amount of the salt was dissolved and diluted in aqua regia and deionised water, ensuring both the metal and acid concentrations matched that of the digested samples. All samples were prepared in duplicate.

Initially, a Jobin Yvon Horiba Ultima 2 instrument was used to carry out the ICP-OES analysis, however, due to the instrument breaking, a Thermo iCAP 6000 series instrument was used for later measurements (from November 2019). Both instruments had a cyclonic spray chamber and a concentric nebuliser, however the Jobin Yvon Horiba Ultima 2 instrument had a radial torch and the Thermo iCAP 6000 series instrument had a vertical torch. The nickel content was determined from the emission line at 231.604 nm and the tin content was determined from the emission line at 242.949 nm. The instrument was calibrated before the samples were measured using commercial Ni and Sn calibration standards of known metal content.

The tin content of the crystalline tin-nickel nanoparticles (prepared with TOP) had to be determined using a more sensitive instrument (ICP-MS) due to the requirement of low concentration solutions (the synthesis method used lower amounts of precursors and the Sn:Ni ratios of 1:20 and 1:50 were also very low). For these samples, analysis was carried out at Leeds University using a Thermo Scientific iCAPQc ICP-MS.

2.2.7.4 XRF

A PANalytical Epsilon 1 benchtop X-ray fluorescence (XRF) instrument was used for XRF. Around 0.5 g of sample was placed into a 35 mm sample cup with a 4 µm thick polypropylene film forming the bottom of the cup. The sample was flattened to ensure it covered the polypropylene film evenly, since this acted as the window through which the sample was exposed to the radiation. The X-ray source was a 50 kV thin-walled Ag anode X-ray tube. The instrument was not user-calibrated for chlorine, however the instrument was calibrated by the manufacturer. Therefore, whilst there is increased uncertainty in the reliability of the results reported, it is likely that they are a reasonable estimate. Additionally, the sample analysed was compared to a sample suspected to contain a high level of chlorine to confirm a difference was observable.

2.2.7.5 CHN

An Exeter Analytical CE440 Elemental Analyser was used for CHN analysis. Static combustion of the sample (typically 3- 7 mg) contained within a tin cup was carried out in pure oxygen using a horizontal furnace. The instrument was calibrated with acetanilide before each set of samples.

2.2.7.6 BET

The BET surface area of ceria was measured by nitrogen adsorption and desorption at 77 K using a Micromeritics ASAP 2020 volumetric adsorption analyzer. Samples were degassed at 350 °C (ramp rate: 10 °C min^{-1}) for 4 h under dynamic vacuum before analysis. P/P_0 values between 0.05-0.25 were used in the BET calculation for evaluation of the surface area.

2.2.7.7 DRIFTS

DRIFTS measurements were carried out using a Nicolet iS10 FTIR spectrometer, fitted with a Praying Mantis diffuse reflection accessory. Samples were analysed for 32 scans with a resolution of 0.5 cm^{-1}. Spent catalyst samples were diluted in KBr (10 mg sample; 400 mg KBr) by grinding the sample and diluent together using a pestle and mortar until homogeneous. Samples were typically backgrounded against the relevant catalyst support diluted in KBr (10 mg support; 400 mg KBr). For the spent nickel powder spectra, pre-reaction nickel powder diluted in KBr was used as the background. Silane-grafted SBA-15 was analysed without dilution and backgrounded on SBA-15 that was also not diluted in KBr. To qualitatively visualise the DRIFTS data, the spectra were plotted in transmittance.

2.2.7.8 CO-DRIFTS

The DRIFTS spectra in this section were also obtained using a Nicolet iS10 FTIR spectrometer, fitted with a Praying Mantis diffuse reflection accessory. Samples were analysed for 32 scans with a resolution of 0.5 cm^{-1}. The CO-DRIFTS was carried out using an in-house developed cell. The development of the cell is detailed in Appendix 4, however a brief description of the cell will be included here for clarity. Figure 23 shows an image of the DRIFTS cell used for CO-DRIFTS experiments and a schematic representation of the window sealing mechanism. The cell has two beds, one for sample and one for the reference material, that are separated by two gratings with glass wool in the middle, to allow an even gas flow through the sample/reference material without any mixing. Gases were introduced to the cell through 1/8th inch pipe, sealed to the cell using JB weld and attached to ball valves using standard Swagelok joints. In future experiments, this cell is expected to be able to operate at temperature and so a thermocouple was inserted into the sample bed, so that sample temperature can be closely monitored. A seal around the thermocouple entrance was also made using JB weld. A seal was also required between the cell and the KBr window, which was achieved by screwing the window down onto an O-ring using a metal ring (Figure 23b).

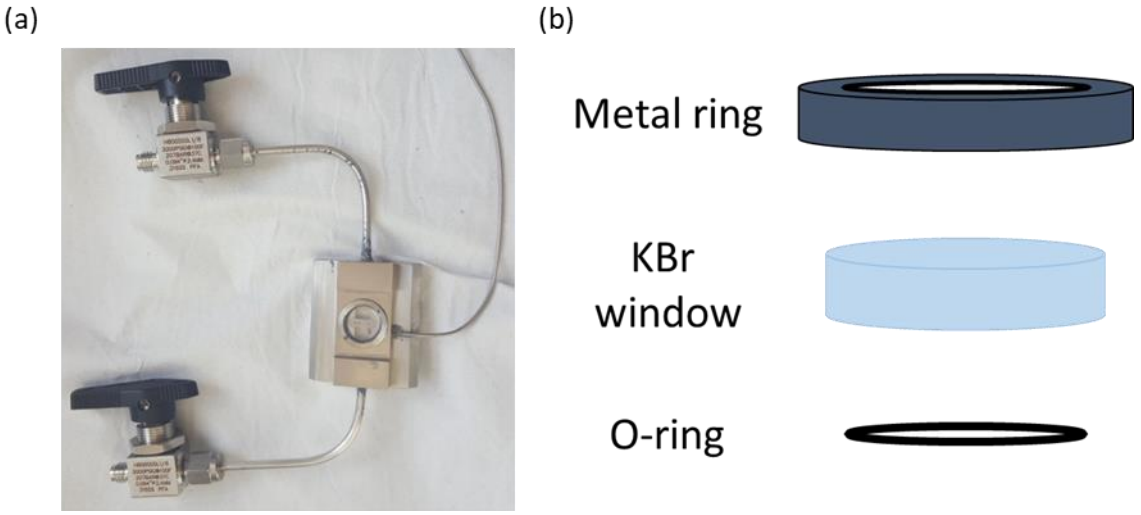

Figure 23: The in-house developed cell used for CO-DRIFTS experiments (a) image of the cell and (b) schematic representation of the window sealing mechanism

Since the heating capabilities of the cell have yet to be developed, the catalysts had to be reduced prior to loading them into the cell. This was carried out using the setup described in Section 2.2.2.3, with some minor modification to allow the sample to be transferred to a glovebox without any exposure to oxygen. The cell was filled and sealed in the glovebox to prevent oxidation of the catalyst. Spectra were then taken of both the catalyst and reference material prior to CO-exposure.

The CO exposure was carried out using the set up shown in Figure 24. Gases were supplied using MKS G-series MFCs controlled using a computer program. A gas line was vented with Ar and, with an Ar flow of 12 mL min^{-1}, attached to the T-joint with the ball vale open to the oil bubbler. At this point the gas flow was changed to 10 mL min^{-1} of CO. The ball joints to the DRIFTS cell were opened and then the ball joint to the oil bubbler was closed to prevent any gas by-passing the cell. The sample and reference were exposed to the CO for ~30 minutes before the gas was changed back to 12 mL min^{-1} Ar in order to vent the system. After venting the cell for ~30 mins, the cell was sealed and the gas flows were stopped. Spectra were then taken of the catalyst and reference material. To qualitatively visualise the DRIFTS data, the spectra were plotted in transmittance, however for quantitative analysis, absorbance (strictly, pseudo-absorbance in the case of DRIFTS) was used.

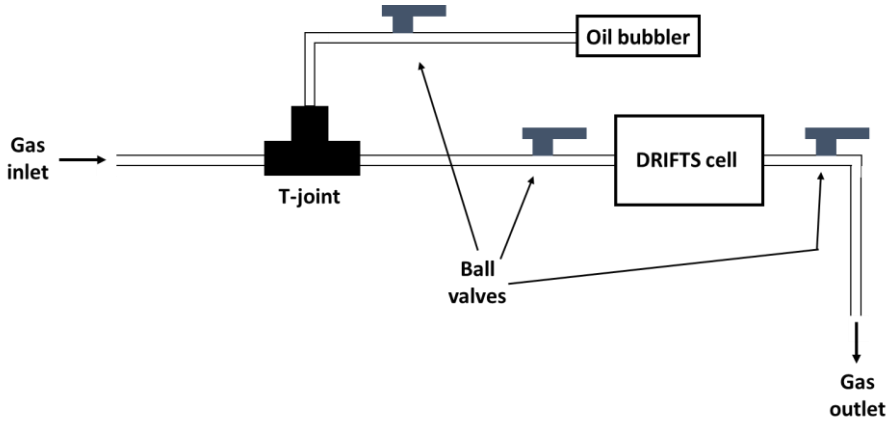

Figure 24: Schematic of the method of CO exposure

2.2.7.9 Soxhlet extraction for coke analysis by GC-MS

Spent catalyst (10 mg) was placed into an extraction thimble. Dichloromethane (DCM) (100 mL) was used as the extraction solvent. DCM was refluxed in the Soxhlet extraction apparatus for around 2.5 days. The resulting solution was concentrated under reduced pressure and then dissolved in a minimal volume of DCM (<0.5 mL). This sample, along with a sample of DCM for reference were analysed by gas chromatography-mass spectrometry (GC-MS). GC-MS analysis was carried out using a Shimadzu QP2010-Ultra with a Rxi-5Sil MS 10 m column (column ID: 0.15 mm; column film thickness: 0.15 µm; oven temperature program: 30 °C for 1 min, heat to 300 °C at a rate of 50 °C min^{-1} and hold at 300 °C for 5 min).

For the reference sample, furfuryl alcohol had to be purified by vacuum distillation. Furfuryl alcohol (5 mL) was added to a round bottom flask, followed by ~7 wt. % Na_2CO_3 (0.40 g) to neutralise any acidic components. A standard vacuum distillation set-up was used, with the addition of a fractionation column (~15 cm in length). The flask that contained the crude furfuryl alcohol was

heated to around 100 °C using an oil bath and the pressure in the set-up was reduced gradually in steps until the distillation occurred at a steady rate (around 1.4 Torr). A clear liquid (originally dark orange/brown) was obtained and transferred to a Schlenk flask under nitrogen. The Schlenk flask was then wrapped in aluminium foil to limit exposure to light and placed in the freezer for storage.

2.2.7.10 GC-MS

Samples were prepared by diluting the sample in dichloromethane (DCM) or 1,2-dichlorobenzene (DCB) to achieve a solution where each component had a concentration of around 1 mg mL^{-1}.

A Shimadzu QP2010-Ultra fitted with an Rxi-17Si MS 10 m column (inner diameter: 0.15 mm; film thickness: 0.15 µm) was used for the GC-MS experiments. Electron impact (EI) ionisation was carried out at 70 eV and the working mass range was 35 – 650 u.

Data was analysed using MestreNova software, before being exported and plotted in Matlab. Mass spectra were compared to those in the National Institute for Standards and Technology Chemistry WebBook database.[64]

2.2.7.11 TEM/STEM

Supported samples and copper chromite were dispersed in ethanol by sonication and unsupported nanoparticles were diluted in hexane by sonication, before the samples were deposited onto 300 mesh copper grids with a carbon film (EM Resolutions). The grids for the unsupported nanoparticles were dried in a vacuum oven at 80 °C for a minimum of 4 h after deposition. Supported samples and the nanoparticles were reduced prior to analysis however they were exposed to air before analysis.

TEM imaging was carried out using a JEOL 2100F FEG microscope with a Schottky field emitter at 200 keV. Initial images (up until March 2020) were obtained using a Gatan Orius camera (Charge coupled device (CCD)). The camera was then updated to a Gatan Rio 16 camera (complementary metal oxide semiconductor (CMOS)), which was used to obtain all subsequent images. At least 6 areas were sampled in order to ensure the images selected were representative of the sample. To obtain particle size distributions, a total of at least 100 particles were measured from at least 6 six different TEM grid areas.

STEM imaging and EDX analysis (including elemental mapping) of the IWI catalysts was carried out using the same microscope used for TEM, with the addition of a JEOL HAADF/dark field photomultiplier tube (PMT) and Gatan ADF/bright field PMT (imaging carried out at 200 keV). All other STEM imaging and EDX analysis was carried out by Dr. Nicole Hondow at Leeds University

using an FEI Titan3 Themis 300 (imaging carried out at 300 keV) with a Gatan OneView 4K CMOS digital camera (for TEM imaging), multiple HAADF/ADF/BF STEM detectors and an FEI Super-X 4-detector EDX system. In order to get more reliable EDX data, it was necessary to plasma clean the samples prior to analysis.

2.2.7.12 SS NMR

CP/MAS ^{13}C NMR spectra were acquired at 100.63 MHz using a Bruker Avance III HD spectrometer and 4 mm (outer diameter) probe. Spectra were acquired at a spin rate of 10 kHz. Cross-polarisation (CP) was carried out using TOSS spinning sideband suppression, a 0.5 ms contact time and a recycle delay of 1 s. Carbon spectral referencing was relative to neat tetramethylsilane, carried out by setting the high-frequency signal from an external sample of adamantane to 38.5 ppm.

2.2.7.13 TGA/TPO

A Perkin Elmer TGA 8000 was used for TGA/TPO analysis of small quantities of post-reaction sample. Samples were heated from room temperature at a rate of 5 °C min^{-1} or 2 °C min^{-1} as indicated in flowing air for the spent silica samples and spent Ni/SiO_2 catalyst respectively.

2.2.7.14 NAP-XPS

NAP-XPS experiments were performed at beamline B07, Diamond Light Source, Oxfordshire, UK. Details of the NAP-XPS apparatus and B07 beamline are described elsewhere.[29] Samples were prepared by drop-casting the nanoparticles onto silicon wafers from solutions of the nanoparticles dissolved in hexane. Spectra were recorded with photon energies of 1100 eV and 1490 eV or 1650 eV for Ni 2p, 700 eV and 1100 eV or 1300 eV for Sn 3d, 550 eV and 1100 eV for P 2p and 1100 eV for O 1s, N 1s, Si 2p and C 1s. The samples were analysed using higher and lower photon energies to allow for analysis at different sample depths and the photon energies were selected so that, where possible, the kinetic energies were approximately equal. Beam induced damage was checked for by recording regular survey scans (typically after a scan set was complete) and in most samples, no detectable beam damage was observed. However, occasionally, some minor beam induced damage was observed and when this was the case, the beam was moved to a different spot on the sample and any effected scans were repeated. The binding energy was calibrated using the Fermi edge of nickel for spectra where the Fermi energy was clearly defined (*i.e.* where the sample was metallic). In oxidised samples (where the Fermi edge was poorly defined), the binding energy correction was assumed to be similar to the correction determined for the reduced sample at the same photon energy and, where possible, verified by the shift in the O 1s peak, assuming that the main peak corresponded to oxygen as part of SiO_2 (present on the surface of the silicon

wafer). After subtraction of a Shirley background, the integral areas of the peaks were used to determine the molar ratios of the different elements. Attenuation of the signal due to the presence of different gases and transmission corrections were accounted for based on data reported elsewhere for the instrument[29] and cross sections for the chosen elements were extrapolated from data reported by Yeh and Lindau.[37]

2.3 References

1. W. H. Bragg and W. L. Bragg, 1913, **88**, 428-438.
2. R. Prins, A. Wang and X. Li, *Introduction to Heterogeneous Catalysis*, World Scientific Publishing, London, 2016.
3. A. L. Patterson, *Physical Review*, 1939, **56**, 978-982.
4. J. S. J. Hargreaves, *Catalysis, Structure & Reactivity*, 2016, **2**, 33-37.
5. H. Rietveld, *Journal of Applied Crystallography*, 1969, **2**, 65-71.
6. I. M. Watt, *The Principles and Practice of Electron Microscopy*, Cambridge University Press, Cambridge, 2 edn., 1997.
7. P. D. Nellist, in *Springer Handbook of Microscopy*, eds. P. W. Hawkes and J. C. H. Spence, Springer International Publishing, Cham, 2019, DOI: 10.1007/978-3-030-00069-1_2, pp. 2-2.
8. M. B. Mitchell, in *Structure-Property Relations in Polymers*, American Chemical Society, 1993, vol. 236, ch. 13, pp. 351-375.
9. T. Armaroli, T. Bécue and S. Gautier, *Oil & Gas Science and Technology - Rev. IFP*, 2004, **59**, 215-237.
10. J. Sirita, S. Phanichphant and F. C. Meunier, *Analytical Chemistry*, 2007, **79**, 3912-3918.
11. G. A. Somorjai and Y. Li, *Introduction to surface chemistry and catalysis*, Wiley, Hoboken, N.J., 2010.
12. S. T. Thompson and H. H. Lamb, *ACS Catalysis*, 2016, **6**, 7438-7447.
13. D. Rood, *A practical guide to the care, maintenance, and troubleshooting of capillary gas chromatographic systems*, Wiley-VCH, Weinheim; New York, 1999.
14. J.-Y. de Saint Laumer, E. Cicchetti, P. Merle, J. Egger and A. Chaintreau, *Analytical Chemistry*, 2010, **82**, 6457-6462.
15. D. H. Williams and I. Fleming, *Spectroscopic methods in organic chemistry*, McGraw-Hill Education, Berkshire, 6 edn., 2008.
16. L. Balcaen, M. J. Baxter, J. A. Caruso, J. M. Cook, H. M. Crews, E. H. Evans, A. Fisher, M. Foulkes, H. R. Hansen, G. M. Hieftje, S. J. Hill, J.-M. Mermet, D. L. Miles, C. O'Connor, G. O'Connor, S. A. Pergantis, P. Robb, B. B. M. Sadi, J. R. Shann, B. L. Sharp, K. L. Sutton, P. Taylor, F. Vanhaecke and A. P. Vonderheide, *Inductively Coupled Plasma Spectroscopy and its Applications*, Blackwell Publishing, Oxford, 2 edn., 2007.
17. M. F. Al-Hakkani, *SN Applied Sciences*, 2019, **1**, 791.
18. G. Tyler and S. Jobin Yvon, *ICP Optical Emission Spectroscopy Technical Note*, 1995, **5**.
19. S. C. Wilschefski and M. R. Baxter, *Clin Biochem Rev*, 2019, **40**, 115-133.
20. H. Günther, *NMR Spectroscopy : Basic Principles, Concepts and Applications in Chemistry*, John Wiley & Sons, Incorporated, Somerset, GERMANY, 2013.
21. D. C. Apperley, R. K. Harris and P. Hodgkinson, *Solid-state NMR : basic principles & practice*, New York : Momentum Press, New York, N.Y., 2012.
22. C. Pirola, F. Galli and G. S. Patience, *The Canadian Journal of Chemical Engineering*, 2018, **96**, 2317-2320.
23. B. Sánchez, M. S. Gross, B. D. Costa and C. A. Querini, *Applied Catalysis A: General*, 2009, **364**, 35-41.
24. D. González, O. Altin, S. Eser and A. B. Garcia, *Materials Chemistry and Physics*, 2007, **101**, 137-141.
25. X. Xian, C. Ran, C. Nai, P. Yang, S. Zhao and L. Dong, *Applied Catalysis A: General*, 2017, **547**, 37-51.
26. C. Le Minh, R. A. Jones, I. E. Craven and T. C. Brown, *Energy & Fuels*, 1997, **11**, 463-469.
27. G. Held, in *Spectroscopic Properties of Inorganic and Organometallic Compounds: Techniques, Materials and Applications, Volume 42*, The Royal Society of Chemistry, 2012, vol. 42, pp. 1-33.

28. S. Hüfner, S. Schmidt and F. Reinert, *Nuclear Instruments and Methods in Physics Research Section A: Accelerators, Spectrometers, Detectors and Associated Equipment*, 2005, **547**, 8-23.
29. G. Held, F. Venturini, D. C. Grinter, P. Ferrer, R. Arrigo, L. Deacon, W. Quevedo Garzon, K. Roy, A. Large, C. Stephens, A. Watts, P. Larkin, M. Hand, H. Wang, L. Pratt, J. J. Mudd, T. Richardson, S. Patel, M. Hillman and S. Scott, *Journal of Synchrotron Radiation*, 2020, **27**, 1153-1166.
30. S. Alayoglu, S. K. Beaumont, F. Zheng, V. V. Pushkarev, H. Zheng, V. Iablokov, Z. Liu, J. Guo, N. Kruse and G. A. Somorjai, Topics in Catalysis, 2011, 54, 778.
31. S. K. Beaumont, S. Alayoglu, V. V. Pushkarev, Z. Liu, N. Kruse and G. A. Somorjai, Faraday Discussions, 2013, 162, 31-44.
32. M. H. Engelhard, D. R. Baer, A. Herrera-Gomez and P. M. A. Sherwood, *Journal of Vacuum Science & Technology A*, 2020, **38**, 063203.
33. D. A. Shirley, *Physical Review B*, 1972, **5**, 4709-4714.
34. S. Tougaard and P. Sigmund, *Physical Review B*, 1982, **25**, 4452-4466.
35. A. Herrera-Gomez, D. Cabrera-German, A. D. Dutoi, M. Vazquez-Lepe, S. Aguirre-Tostado, P. Pianetta, D. Nordlund, O. Cortazar-Martinez, A. Torres-Ochoa, O. Ceballos-Sanchez and L. Gomez-Muñoz, *Surface and Interface Analysis*, 2018, **50**, 246-252.
36. M. P. Seah and W. A. Dench, *Surface and Interface Analysis*, 1979, **1**, 2-11.
37. J. J. Yeh and I. Lindau, *Atomic Data and Nuclear Data Tables*, 1985, **32**, 1-155.
38. M. Volmer and A. Weber, *Z. Phys. Chem.*, 1926, **119U**, 277.
39. R. Becker and W. Döring, *Annalen der Physik*, 1935, **416**, 719-752.
40. J. Frenkel, *The Journal of Chemical Physics*, 1939, **7**, 538-547.
41. S. Karthika, T. K. Radhakrishnan and P. Kalaichelvi, *Crystal Growth & Design*, 2016, **16**, 6663-6681.
42. N. T. K. Thanh, N. Maclean and S. Mahiddine, *Chemical Reviews*, 2014, **114**, 7610-7630.
43. V. K. LaMer and R. H. Dinegar, *Journal of the American Chemical Society*, 1950, **72**, 4847-4854.
44. V. K. LaMer, *Industrial & Engineering Chemistry*, 1952, **44**, 1270-1277.
45. J. Polte, *CrystEngComm*, 2015, **17**, 6809-6830.
46. K. J. Klabunde, C. M. Sorensen, S. I. Stoeva, B. L. V. Prasad, A. B. Smetana and X.-M. Lin, in *Metal Nanoclusters in Catalysis and Materials Science*, eds. B. Corain, G. Schmid and N. Toshima, Elsevier, Amsterdam, 2008, DOI: https://doi.org/10.1016/B978-044453057-8.50013-1, pp. 233-249.
47. W. Ostwald, *Z. Phys. Chem.*, 1900, **34U**, 495.
48. A. Baldan, *Journal of Materials Science*, 2002, **37**, 2171-2202.
49. J. Jeong, N. Kim, M.-G. Kim and W. Kim, *Chemistry of Materials*, 2016, **28**, 172-179.
50. S. B. Kalidindi and B. R. Jagirdar, *Inorganic Chemistry*, 2009, **48**, 4524-4529.
51. S. P. Bhaskar, M. Vijayan and B. R. Jagirdar, *The Journal of Physical Chemistry C*, 2014, **118**, 18214-18225.
52. N. Arora, B. R. Jagirdar and K. J. Klabunde, *Journal of Alloys and Compounds*, 2014, **610**, 35-44.
53. J. A. Manzanares, P. Peljo and H. H. Girault, *The Journal of Physical Chemistry C*, 2017, **121**, 13405-13411.
54. V. Chikan and D. F. Kelley, *The Journal of Physical Chemistry B*, 2002, **106**, 3794-3804.
55. W. L. F. Armarego and C. Chai, in *Purification of Laboratory Chemicals*, Butterworth-Heinemann, Boston, 7 edn., 2013, p. 442.
56. S. J. Tauster, S. C. Fung and R. L. Garten, *Journal of the American Chemical Society*, 1978, **100**, 170-175.
57. C. Pirez, J.-M. Caderon, J.-P. Dacquin, A. F. Lee and K. Wilson, *ACS Catalysis*, 2012, **2**, 1607-1614.

58. Y. Ren, Z. Ma, L. Qian, S. Dai, H. He and P. G. Bruce, *Catalysis Letters*, 2009, **131**, 146-154.
59. X. Deng, K. Chen and H. Tüysüz, *Chemistry of Materials*, 2017, **29**, 40-52.
60. V. V. Pushkarev, K. An, S. Alayoglu, S. K. Beaumont and G. A. Somorjai, *Journal of Catalysis*, 2012, **292**, 64-72.
61. Ö. Metin, V. Mazumder, S. Özkar and S. Sun, *Journal of the American Chemical Society*, 2010, **132**, 1468-1469.
62. S. Carenco, C. Boissière, L. Nicole, C. Sanchez, P. Le Floch and N. Mézailles, *Chemistry of Materials*, 2010, **22**, 1340-1349.
63. M. Heilmann, H. Kulla, C. Prinz, R. Bienert, U. Reinholz, A. Guilherme Buzanich and F. Emmerling, *Nanomaterials*, 2020, **10**, 713.
64. R. Rao, A. Dandekar, R. T. K. Baker and M. A. Vannice, *Journal of Catalysis*, 1997, **171**, 406-419.
65. NIST Chemistry WebBook, https://webbook.nist.gov/chemistry/).

Chapter 3: Incipient wetness impregnated nickel catalysts as furfural hydrogenation catalysts: performance evaluation, characterisation and study of deactivation by carbon containing species

Nickel-based catalysts are effective for a variety of hydrogenation reactions, as well as more complex reactions such as steam reforming.[1, 2] However, the high activity of these catalysts can often mean they are prone to rapid deactivation, typically due to coke formation.[3-5] Nickel and modified-nickel catalysts have been explored for both liquid-phase[6-15] and vapour-phase[16-20] furfural hydrogenation but were commonly found to have low selectivity or exhibit deactivation. This chapter benchmark's the chemistry of furfural hydrogenation on nickel incipient wetness catalysts, comparing them to the current industry standard, copper chromite. The activity, selectivity and deactivation profiles of these catalysts have been determined and compared. The role of the support and the nature of the carbonaceous deposits, which likely account for the rapid deactivation, have also been discussed in detail. Understanding the baseline behaviour of nickel catalysts allows for the development and rational design of improved catalysts for this important bio-refinery transformation.

3.1 Optimisation of the furfural hydrogenation reactor

Optimisation of the fixed-bed reactor used to carry out furfural hydrogenation was crucial for obtaining consistent results. Vapour-phase furfural hydrogenation is a somewhat challenging reaction due to the propensity of the reactant to polymerise, which led to frequent blockages and inconsistent catalytic results. The blockages that occurred did so at the furfural inlet to the vaporiser (Figure 25) and, since it was thought that these blockages were likely related to the issues with inconsistency, optimisation of the vaporiser set-up was anticipated to be key to improving the reactor.

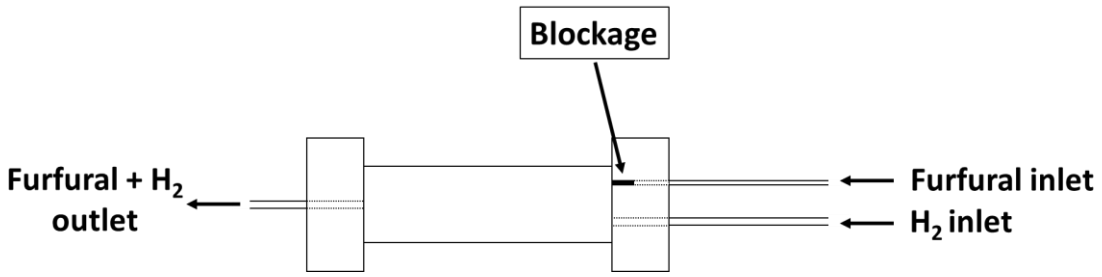

Figure 25: Schematic representation of the initial vaporiser set-up, illustrating the position where the blockages occurred

Therefore, during troubleshooting, there was a focus on vaporiser optimisation, however many other variables were also altered in order to ensure that other issues were not missed. The most effective changes that were made are described below:

(i) Vacuum distillation of furfural - purification of furfural by vacuum distillation to a colourless liquid (as well as appropriate post-purification storage at -18 ^{o}C under N_2 and kept away from light) was found to significantly improve reactor consistency. The discolouration of furfural *via* a yellow to a brown/black liquor results from highly conjugated oligomeric impurities, which form due to hydrogen abstraction by oxygen acting as a diradical.[21] Even though these are thought to be present at << 1%, incorrect storage or the absence of purification resulted in more frequent blockages of the reactor, inconsistent catalytic results and more rapid catalyst deactivation.

(ii) Heating of the vaporiser – the addition of a jacket allowed the vaporiser to be wrapped with heat tape more evenly, ensuring consistent heating with a reduced chance of hotspots. Additionally, the position of the thermocouple was moved to near the furfural inlet pipe, to ensure this part, which was typically where the blockages occurred, was at the correct temperature. The temperature of the vaporiser was also lowered from 190 ^{o}C to 170 ^{o}C to help lower the rate of furfural polymerisation.

(iii) Modification of the furfural inlet to the vaporiser - the original furfural inlet pipe (stainless steel 1/16th inch pipe) was replaced with a section of PTFE pipe that feeds through a section of 1/4th inch stainless steel pipe into the vaporiser (Figure 26). This configuration means that if a blockage were to occur, only one plastic ferrule joint would have to be disconnected to remove the section of PTFE pipe. The blocked section could then be simply cut off before re-attaching the PTFE pipe, with the whole process taking <5 min. Whilst the purpose of this modification was to reduce the time required to clear a blockage, it also, somewhat inadvertently, stopped the blockages forming at all. In the ~1.5 years (at time of writing) since the modification was implemented, no blockages have occurred, however with the previous configuration, blockages typically occurred every 2-4 weeks. The updated configuration therefore massively improved the efficiency and consistency of the reactor, eliminating the problems associated with frequent blockages.

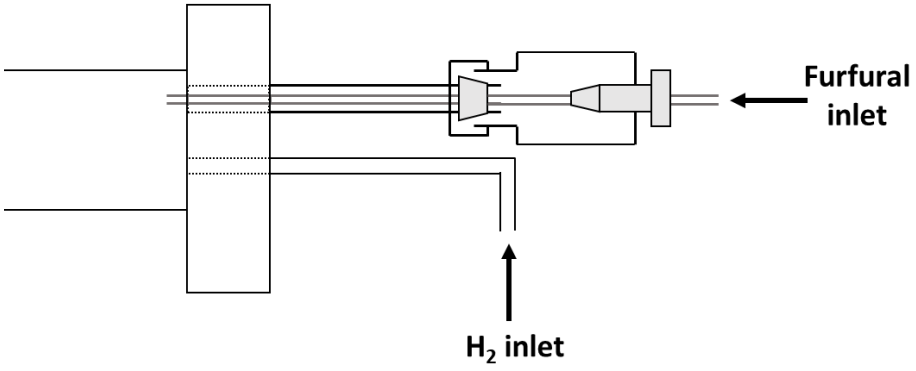

Figure 26: Schematic representation of the updated vaporiser inlet configuration

3.2 Synthesis and Characterisation of the Ni/SiO_2 IWI catalyst

Incipient wetness impregnation is a widely employed and relatively simple technique for the preparation of nickel-based catalysts. Therefore, it is used here to prepare series of catalysts to benchmark the performance of nickel-based catalysts for furfural hydrogenation.

3.2.1 Characterisation of the catalyst

The catalyst was prepared using the $Ni(NO_3)_2.6H_2O$ salt and had a target nickel loading of 5 wt. %. ICP-OES analysis showed that the nickel loading was 4.82 wt. % which is in good agreement with the target loading. Since the nickel precursor was a Ni(II) salt, the catalyst had to be reduced prior to use. Typically, activation of nickel nitrate catalysts involves calcination to NiO followed by reduction to nickel metal, however in a report by Nakagawa *et al.*[17], direct reduction of $Ni(NO_3)_2/SiO_2$ catalysts, without an initial calcination step, showed superior activity. This calcination-free approach was adopted for the incipient wetness catalysts discussed in this chapter. In order to study this reduction process further, TPR was carried out (Figure 27). The reduction of the silica-supported catalyst resulted in two peaks; a sharp peak centred at 263 ^oC and broad shoulder centred at 304 ^oC. The peaks were deconvoluted as shown in Figure 27b, with the areas found to correspond to 0.91 (± 0.04) and 0.98 (± 0.08) H_2 molecules per nickel atom for the lower temperature and higher temperature peak, respectively. This suggests a two-step reduction process since each of the peaks correspond to around 1 mol of H_2 consumed per mol of nickel and is consistent with previous literature that reports a two-step reduction process as shown Scheme 1.[17, 22] Whilst not to the same extent as reported in other papers,[17] it should be noted that the lower temperature peak, corresponding to nitrate reduction, is slightly sub-stoichiometric. This lower than expected consumption of H_2 can be explained by the formation of basic nitrate species such

as $Ni(NO_3)_2.2Ni(OH)_2$ which can form during the drying of impregnated catalysts.[22] (Note: the calibration for the TCD detector used in these TPR experiments is detailed in Appendix 2).

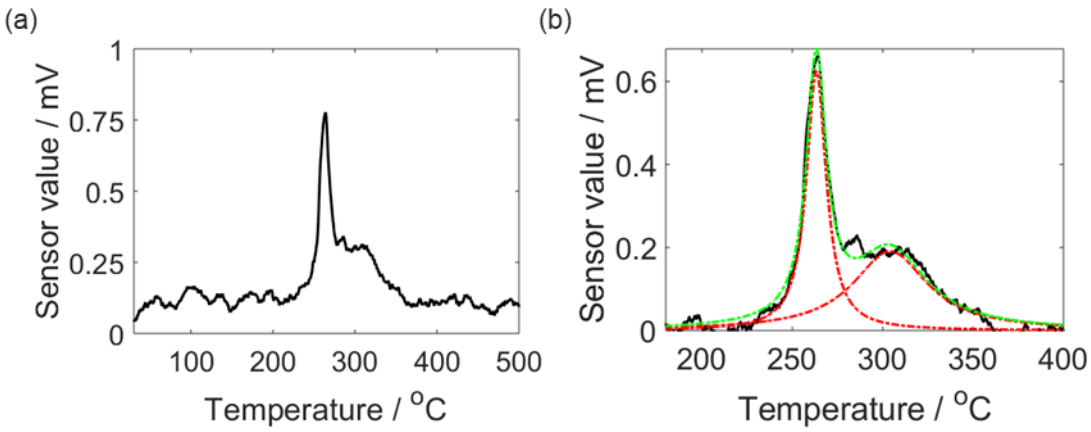

Figure 27: (a) TPR profile showing the consumption of hydrogen for $Ni(NO_3)_2$ impregnated silica, and (b) showing a deconvolution of the data, which has two clear components (20 v/v % H_2 in N_2, total gas flow rate 50 mL min^{-1}, heating rate 5 °C min^{-1})

$$Ni(NO_3)_2 + H_2 \longrightarrow NiO + 2NO_2 + H_2O$$

$$NiO + H_2 \longrightarrow Ni + H_2O$$

Scheme 1: Reactions steps occurring during a 2-step reduction process for $Ni(NO_3)_2$ to nickel metal

The pXRD pattern of the silica-supported catalyst after reduction showed the presence of nickel metal reflections (see Figure 28). The Scherrer equation was used to estimate the average crystallite size, based on the Ni(111) reflection, to be 7 ± 1 nm. TEM was also used to analyse the post-reduction silica-supported catalyst (see Figure 29). Whilst distinguishing the support from the metal particles can be challenging due to poor contrast, especially for smaller particles, a rough particle size distribution is provided below. There was a broad distribution of particle sizes, with the average particle found to be 7 ± 6 nm, which is in good agreement with the results from the pXRD data. However, it should be noted that in both pXRD and TEM, larger particles are likely to be favoured, since pXRD provides a volume average and in TEM, smaller particles are harder to distinguish from the support compared to larger particles.

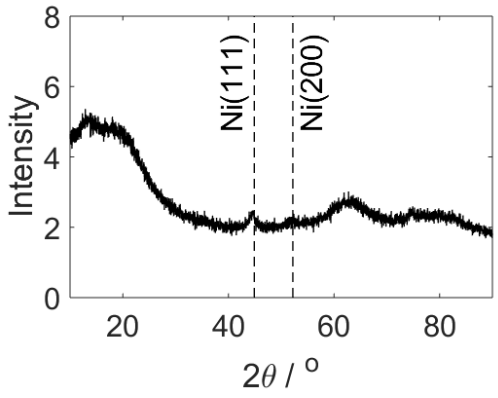

Figure 28: pXRD pattern of post-reduction Ni/SiO_2 sample, the positions of metallic f.c.c. nickel reflections are marked by the vertical dashed lines

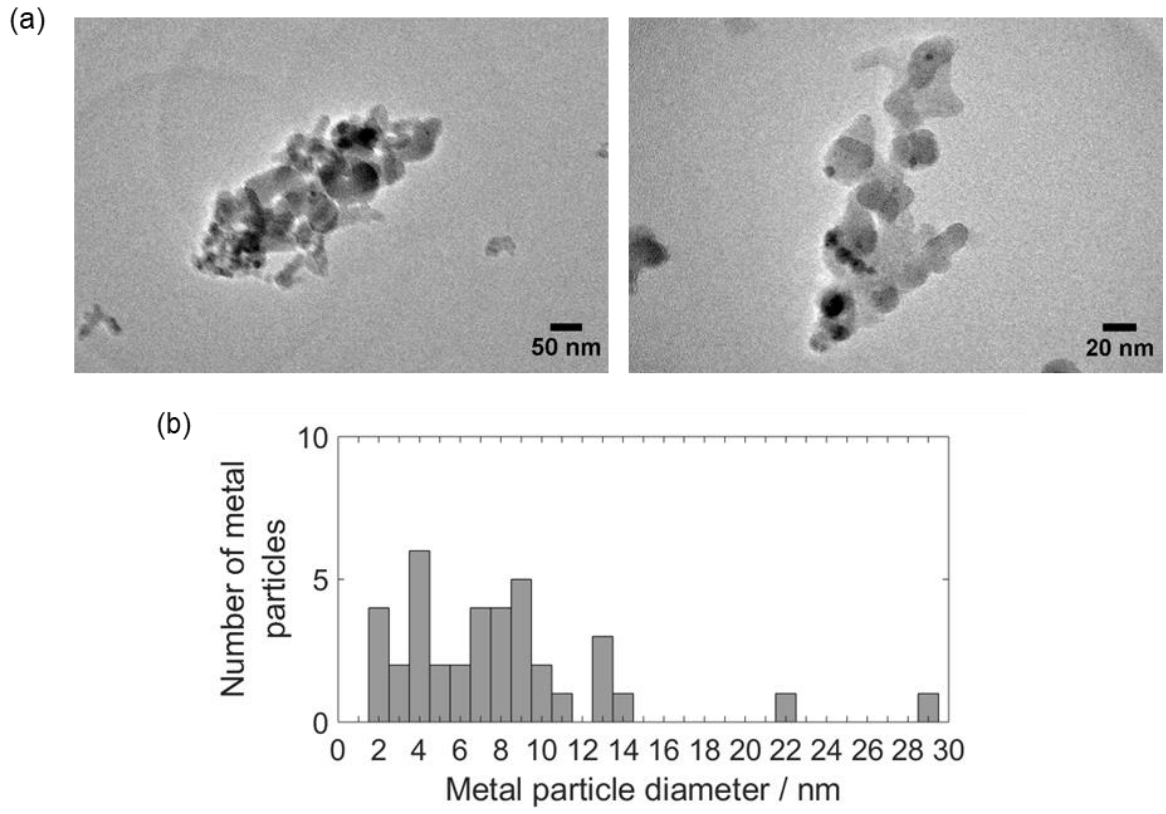

Figure 29: (a) TEM images of post-reduction Ni/SiO_2 and (b) corresponding particle size distribution

3.2.2 Furfural hydrogenation with Ni/SiO_2

The Ni/SiO_2 catalyst was evaluated for furfural hydrogenation, with the results displayed in Figure 30. The catalytic performance was evaluated at both low and high conversion by varying the mass of catalyst used. The catalyst exhibited similar selectivity at both low (37 % at 5 h TOS) and high (82 % at 5 h TOS) conversion (see Figure 30), with around a 50 % selectivity to the desired furfuryl alcohol product. A range of by-products were produced, including significant quantities of furan,

which is produced by decarbonylation. Therefore, the nickel catalyst not only carries out hydrogenation reactions, but also decarbonylation, which contributes to the fairly poor selectivity achieved by this catalyst. From the low conversion data (where mass transport and/or equilibrium effects are less significant) the intrinsic mass activity was found to be 622 ± 192 $mmol_{(prod)}\ g_{(cat)}^{-1}\ h^{-1}$ after 1 h time on stream (TOS). However, as seen from Figure 30c, moderately rapid deactivation occurred, and so after 5 h TOS the mass activity had almost halved to 329 ± 109 $mmol_{(prod)}\ g_{(cat)}^{-1}\ h^{-1}$. If the deactivation is fitted to a rate equation that assumes simple 1st order kinetics (to minimise the effect of the time the first reaction sample is taken), then a deactivation rate constant can be calculated (in this case 0.16 ± 0.02 h^{-1}). Determination of a deactivation rate constant is useful when comparing different catalysts and so will be used throughout this thesis. The rapid deactivation is likely to be due to either sintering or coking, or a combination of both, and this is explored in detail in Section 3.5.

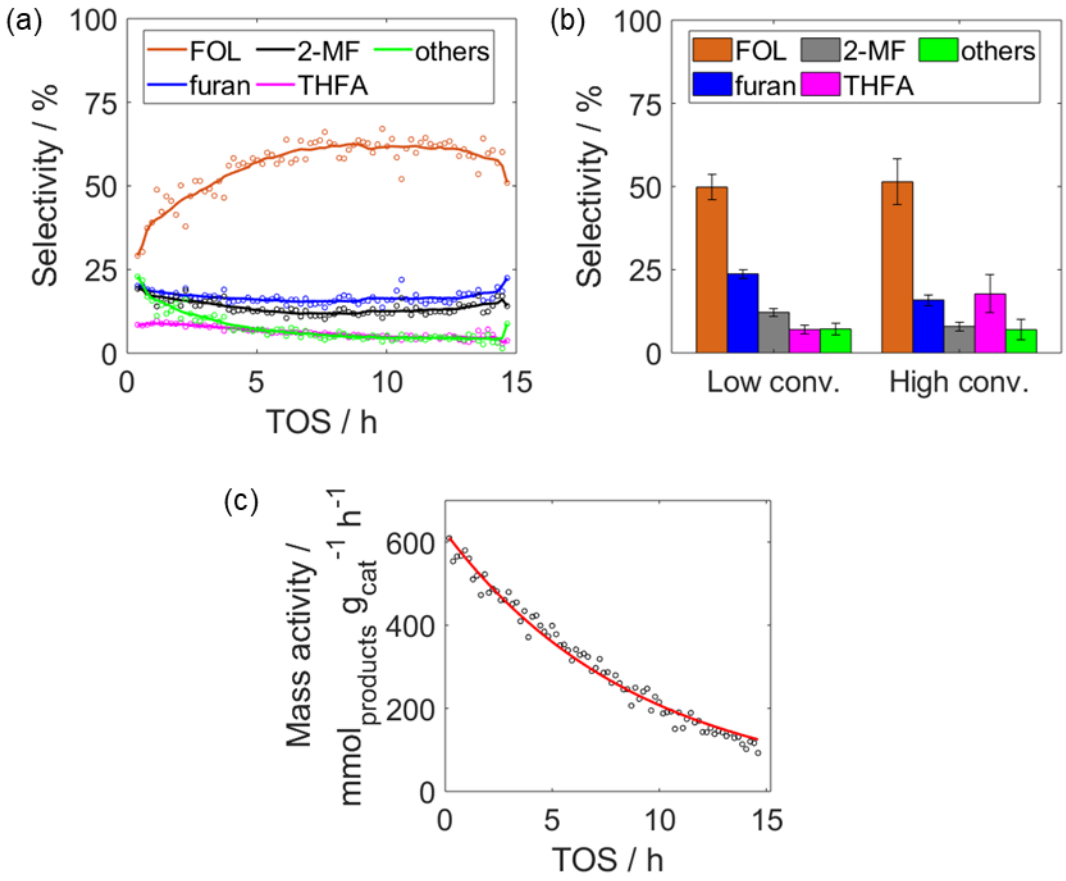

Figure 30: (a) An example of selectivity for Ni/SiO_2 as a function of time on stream (TOS) at low conversion (37 % at 5 h TOS), (b) Comparison of low (37 % at 5 h TOS) and high conversion (82 % at 5 h TOS) Ni/SiO_2 average selectivity under stable operation and (c) deactivation profile showing mass activity as a function of time on stream for Ni/SiO_2 under low conversion conditions. Low and high conversions were achieved by varying the mass of catalyst used. Errors shown are based on repeat measurements of a typical sample as indicated in the experimental section. Key to product abbreviations: FOL=furfuryl alcohol, 2-MF=2-methyl furan, furan=furan, THFA=tetrahydrofurfuryl alcohol, others are predominantly butanal, 1-butanol, 2-methyl tetrahydrofuran and tetrahydrofuran.

3.3 Comparison of Ni/SiO_2 to copper chromite

Copper chromite is the current standard industrial catalyst for furfural hydrogenation and therefore acts as an important comparison. A sample of commercially available copper chromite was obtained for this purpose.

3.3.1 Characterisation of copper chromite

Figure 31 shows a TEM image of a typical particle of the as received copper chromite catalyst. The reduction process of the copper chromite catalyst was also explored using TPR (see Figure 32). Whilst the reduction conditions for the copper chromite catalyst were chosen based on literature protocols,[23] it was important to confirm that these conditions were appropriate. There were two peaks, a sharp one centred at 191 °C and a broad shoulder centred at 213 °C. Notably, the reduction

process is complete by around 260 °C, meaning that the reported reduction conditions used (4 h at 300 °C) are able to reduce the catalyst. The presence of two peaks suggests that there are different copper species present in the catalyst. The peak at 191 °C is likely due to the reduction of CuO to Cu metal.[24] The peak areas were determined by deconvoluting the data (Figure 32b) and the peak at 191 °C was found to correspond to 0.77 (± 0.01) H_2 molecules per copper atom. The reduction process of CuO occurs as described in Scheme 2 and consumes one mole of H_2 per mole of copper. The presence of the second peak at 213 °C suggests that there is a second copper species being reduced, likely copper in a spinel form.[24] The broadness of the peak meant that small adjustments to the background resulted in significant changes in the peak area, and so it was not possible to accurately determine the hydrogen consumption of the second peak.

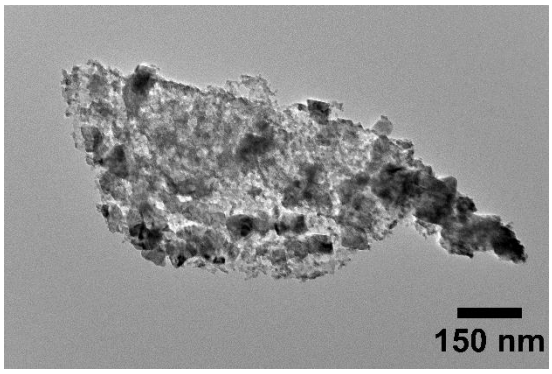

Figure 31: Typical TEM image of the as received copper chromite catalyst

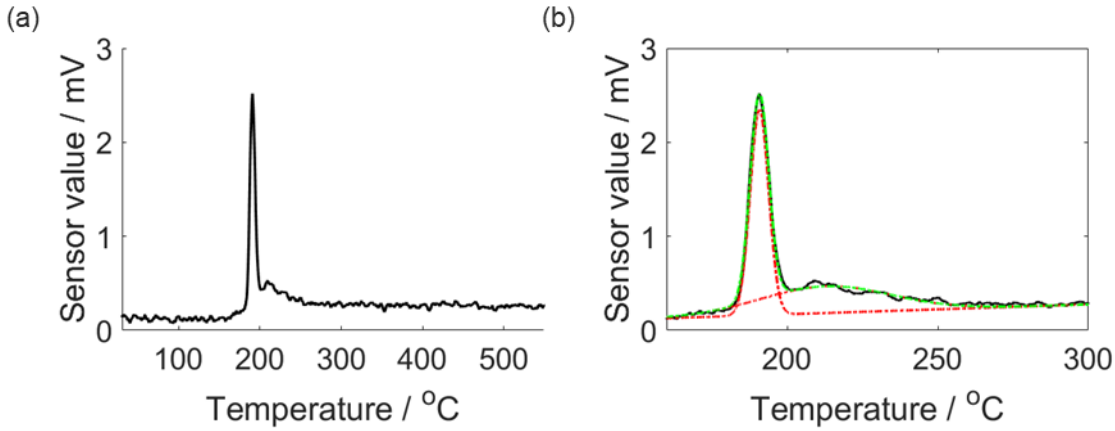

Figure 32: (a) TPR profile showing the consumption of hydrogen for copper chromite and (b) showing a deconvolution of the data, which has two clear components (20 v/v % H_2 in N_2, total gas flow rate 50 mL min^{-1}, heating rate 5 °C min^{-1}).

$$CuO + H_2 \longrightarrow Cu + H_2O$$

Scheme 2: Reduction process of copper oxide

3.3.2 Furfural hydrogenation using copper chromite

The copper chromite catalyst was received as a powder and so was initially loaded into the reactor in this form. However, it was noticed that there was a significant increase in the inconsistency of the furfural GC peak. Running the reactor with a silica blank gave consistent furfural peaks, suggesting that the issue was related to the copper chromite catalyst, not the reactor. Since copper chromite has a low surface area/porosity and was a fairly fine powder, it was thought that the issue could be related to an increased back pressure from the catalyst bed. Therefore, a sample was prepared by pelleting a portion of the catalyst and then lightly crushing the pellet so that larger catalyst particles could be loaded into the reactor, which should lead to a decreased back pressure. When this catalyst was evaluated for furfural hydrogenation, the furfural GC peak consistency significantly improved, confirming that a higher back pressure had likely caused the issue.

The results for furfural hydrogenation using the powdered and crushed pellet versions of the copper chromite catalyst are shown in Figure 33. The results were generally comparable, however there were some differences; the selectivity to furfuryl alcohol was decreased by around 8 % and both the mass activity and deactivation rate constant were roughly halved. This is likely due to changes in mass transport and diffusion due to the larger catalyst particles in the crushed pellet catalyst.

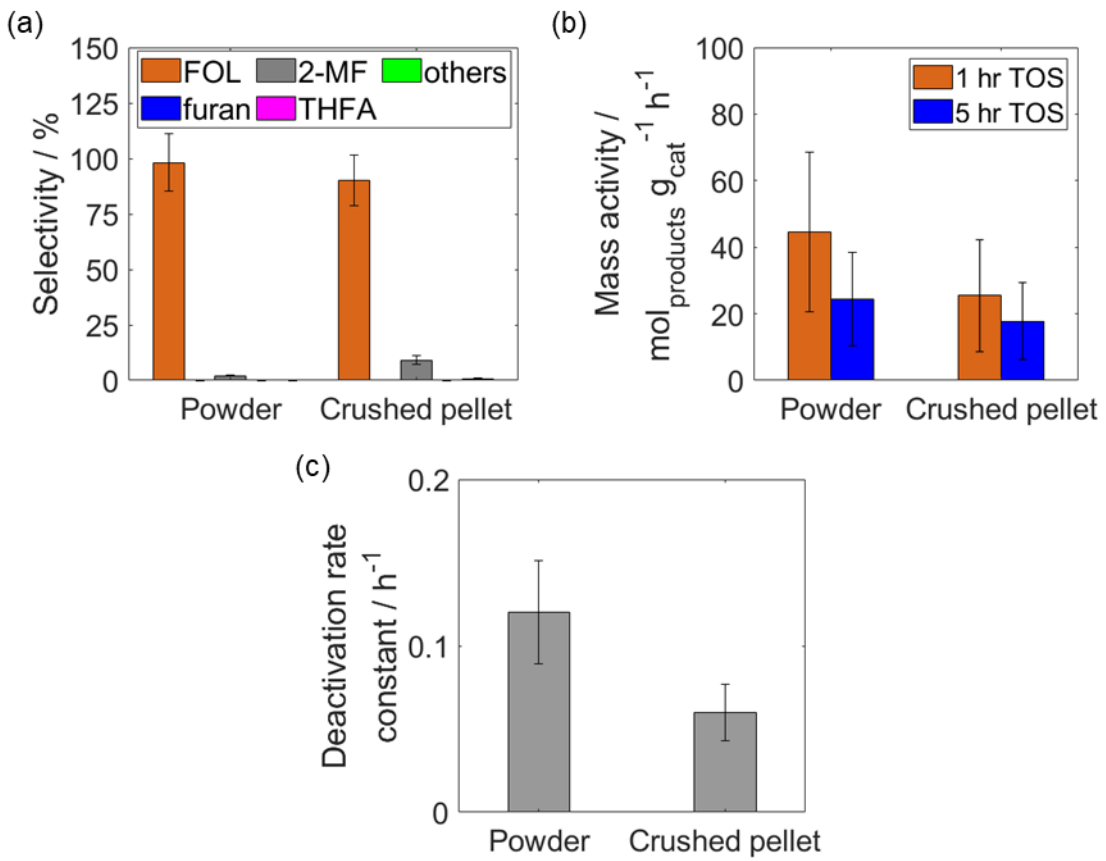

Figure 33: Comparison of the as received powdered copper chromite catalyst and the lightly crushed pelleted version during furfural hydrogenation (a) Average selectivity under stable operation; (b) Mass activity after 1 and 5 hrs TOS; (c) Deactivation rate constants. Errors shown are based on repeat measurements of a typical sample as indicated in the experimental section. Key to product abbreviations: FOL=furfuryl alcohol, 2-MF=2-methyl furan, furan=furan, THFA=tetrahydrofurfuryl alcohol, others are predominantly butanal, 1-butanol, 2-mtheyl tetrahydrofuran and tetrahydrofuran.

Since consistent results were achieved with the crushed pellet catalyst, these results were compared to the Ni/SiO_2 IWI catalyst (Figure 34). The copper chromite catalyst had a mass activity that was an order of magnitude lower than the Ni/SiO_2 catalyst, despite the fact that the copper chromite catalyst contains around 40 wt. % copper whereas the nickel catalyst contains only around 5 wt. % nickel.

Copper chromite was found to be 90 % selective to furfuryl alcohol, with small amounts of 2-methylfuran as a minor side product (see Figure 34), in contrast to the Ni/SiO_2 catalyst, which had a selectivity of ~50 % to furfuryl alcohol and formed a range of by-products including furan which had a selectivity of around 20 %. Decarbonylation leads to the formation of furan, and so whilst this appears to be a significant competing reaction for the nickel catalyst, it does not occur with the copper chromite catalyst. This accounts for a significant portion of the improved selectivity of the copper chromite catalyst.

The copper chromite catalyst exhibited moderately rapid deactivation and had a deactivation rate constant that was broadly comparable to that of the nickel catalyst. Since it is generally thought that copper chromite catalysts have good stability, as seen in a range of other reactions,[25] it was somewhat unexpected for the catalyst to rapidly deactivate at a similar rate to the nickel catalyst. However, the deactivation of copper chromite in this reaction has been highlighted by others.[26, 27]

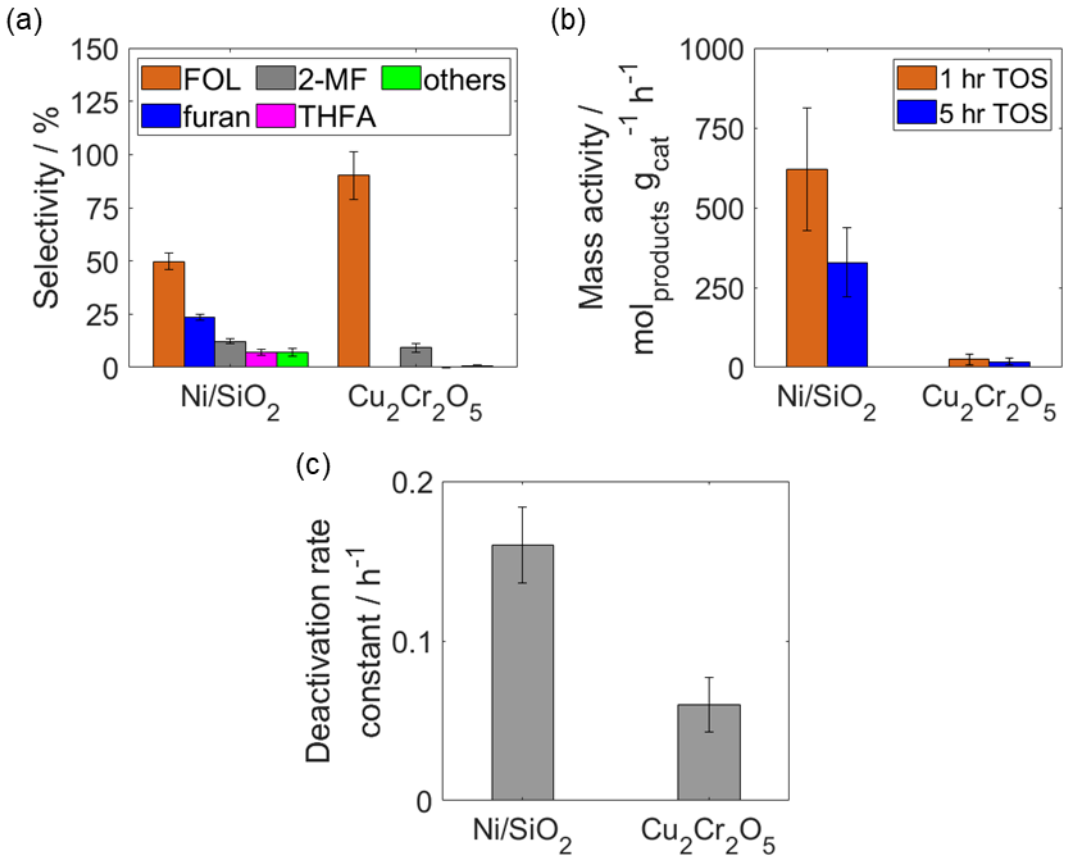

Figure 34: Comparison of Ni/SiO_2 and copper chromite (crushed pellet) during furfural hydrogenation (a) Average selectivity under stable operation; (b) Mass activity after 1 and 5 hrs TOS; (c) Deactivation rate constants. Errors shown are based on repeat measurements of a typical sample as indicated in the experimental section. Key to product abbreviations: FOL=furfuryl alcohol, 2-MF=2-methyl furan, furan=furan, THFA=tetrahydrofurfuryl alcohol, others are predominantly butanal, 1-butanol, 2-mtheyl tetrahydrofuran and tetrahydrofuran.

3.4 The role of the support for nickel incipient wetness catalysts

The use of silica supports, whose surfaces contain acidic silanol groups, raises the possibility that these sites can catalyse unwanted side reactions that contribute to the deactivation seen above. Specifically, furfural and furfuryl alcohol polymerisation can be acid catalysed, which may promote

coke formation. To address this question, two further catalysts were prepared in an analogous manner on two non-acidic supports: titania and ceria.

3.4.1 Characterisation of the catalysts

Whilst the point of the experiment was to explore the impact of support acid sites, it was important to consider the exposed surface area of the support if this was responsible for unwanted side reactions. A commercial TiO_2 powder with slightly lower surface area was used, but for CeO_2, it was found necessary to prepare a mesoporous ceria to obtain a material of comparable surface area to the silica. Their BET surface areas are reported in Table 5.

Table 5: BET surface areas of the different supports; [a]value obtained from specification documentation provided by the supplier

Support	**BET surface area / $m^2\ g^{-1}$**
Cab-O-Sil M5 silica	200[a]
Aeroxide P25 titania	35 – 65[a]
Mesoporous ceria (prepared in-house)	152

It is generally known that silica is weakly acidic due to the presence of hydroxyl groups on the surface of the support, however, in order to demonstrate this, the acidity of the supports was assessed using a simple Hammett indicator test. Methyl red was chosen as a suitable indicator; in a solution above pH 6.2, it appears as yellow, changing to orange and then red once at pH 4.2 (pKa 4.8). The results of the test are show in Figure 35, where it can be seen that the indicator, which forms an orange solution in toluene, changed to a darker orange with ceria, a light pink with titania and a distinct magenta/red colour with silica. Therefore, as expected, the acidity of the supports is as follows: SiO_2>TiO_2>CeO_2. It should also be noted that when methyl yellow was used as the indicator (pKa 3.3), none of the supports produced a colour change, confirming that the acid sites present are fairly weak.

Figure 35: Photograph showing the colour change on exposure of different oxide supports to and adsorption of the Hammett indicator methyl red in toluene solution: silica (left); titania (middle); ceria (right)

ICP-OES analysis was used to confirm the catalysts had close to the nominal 5 wt. % nickel loading targeted, with the results displayed in Table 6.

Table 6: The nickel loading of the incipient wetness catalysts, based on ICP-OES data. Duplicate samples were digested/analysed and the error based on the standard deviation of those results

Catalyst	Ni wt. %
Ni/SiO_2	4.82 ± 0.05
Ni/TiO_2	6.1 ± 0.3
Ni/CeO_2	6.0 ± 0.5

The TPR data (Figure 36) for the titania- and ceria-supported samples were notably different to that of the silica-supported sample discussed previously in this chapter, since significantly larger peaks were obtained that were not able to be reliably deconvoluted. This meant that for both the titania- and ceria-supported samples, the total area of the peak, rather than the individual components, was used to determine the H_2 consumption. For the titania-supported sample, greater than 2 equivalents of H_2 were consumed during reduction, which is likely explained by the reducibility of the support (TiO_2 to TiO_x). This is also likely responsible for the different peak shape compared to the silica-supported sample. Ceria is also a reducible support as it can form Ce_2O_3. This resulted in a very large peak, corresponding to almost 8 equivalents of hydrogen. The reducibility of both the titania and ceria supports unfortunately meant that the underlying nickel reduction process was masked. However, all of the catalysts reduced at similar temperatures to the Ni/SiO_2 catalyst and so the standard reduction conditions used previously should also be suitable for these materials.

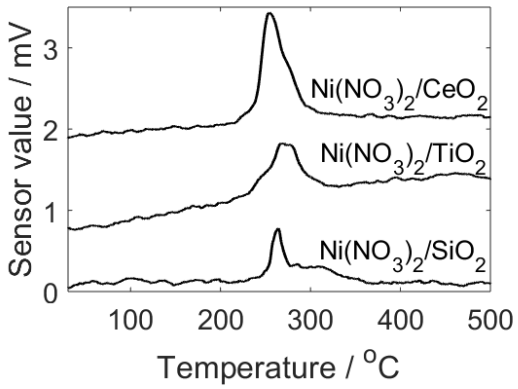

Figure 36: TPR traces for $Ni(NO_3)_2$ impregnated silica, titania and ceria

TEM images were taken for post-reduction Ni/CeO_2 and Ni/TiO_2, however, as seen in the example image of Ni/CeO_2 (Figure 37), it was difficult to distinguish between the support and the metal particles due to poor contrast.

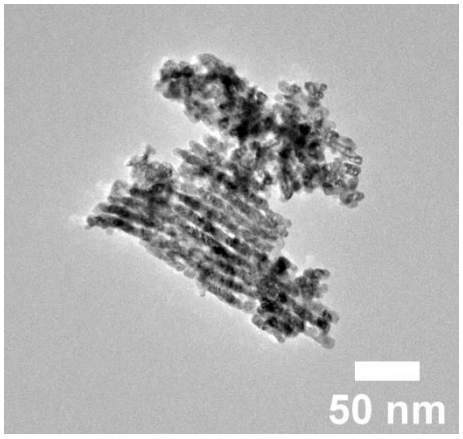

Figure 37: TEM image of post-reduction Ni/CeO_2

3.4.2 Comparison of the support during furfural hydrogenation

The effect of the support was then evaluated by carrying out furfural hydrogenation. When the titania supported catalyst was reduced at the standard temperature of 500 °C and then used to carry out furfural hydrogenation, the mass activity was found to be low, likely due to strong metal support interaction (SMSI) effects reducing access to the nickel.[28] Therefore, to limit these SMSI effects, the reduction temperature of the titania supported catalyst was lowered to 300 °C. Whilst the selectivity and deactivation rate were not significantly affected, the mass activity was around 3 times higher than the catalyst reduced at 500 °C (see Figure 38).

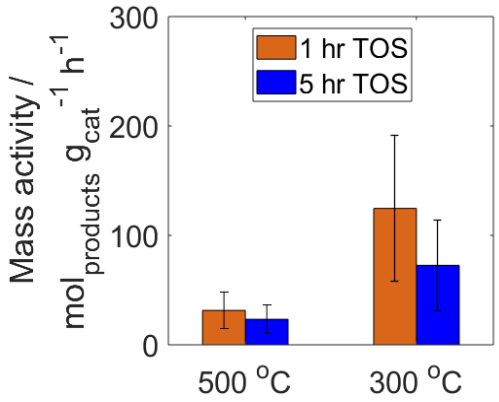

Figure 38: Mass activity at 1 and 5 h TOS for Ni/TiO_2 reduced at 500 °C and 300 °C

The results from furfural hydrogenation with the SiO_2, TiO_2 and CeO_2 supported catalysts are displayed in Figure 39. As seen in Figure 39a, changing the support did not have a significant effect on the selectivity, implying that the selectivity is predominantly controlled by the metal. The deactivation rate constants were also fairly similar (Figure 39b), suggesting the hypothesis that weakly acidic sites present on the SiO_2 support promoted furfural/furfuryl alcohol polymerisation, and therefore increased deactivation, is incorrect or the effect is insignificant. The TiO_2 supported

sample does appear to have a slightly lower deactivation rate constant, however this may be within error or else is only a small difference. The mass activity (Figure 39c) of the titania and ceria supported catalysts was lower than that of the silica supported catalyst, but this could easily result from particle size effects and was unimportant from the point of view of understanding deactivation, so was not investigated further. The key observation is that the slightly acidic silanol groups on the silica support are not a significant factor in catalyst deactivation.

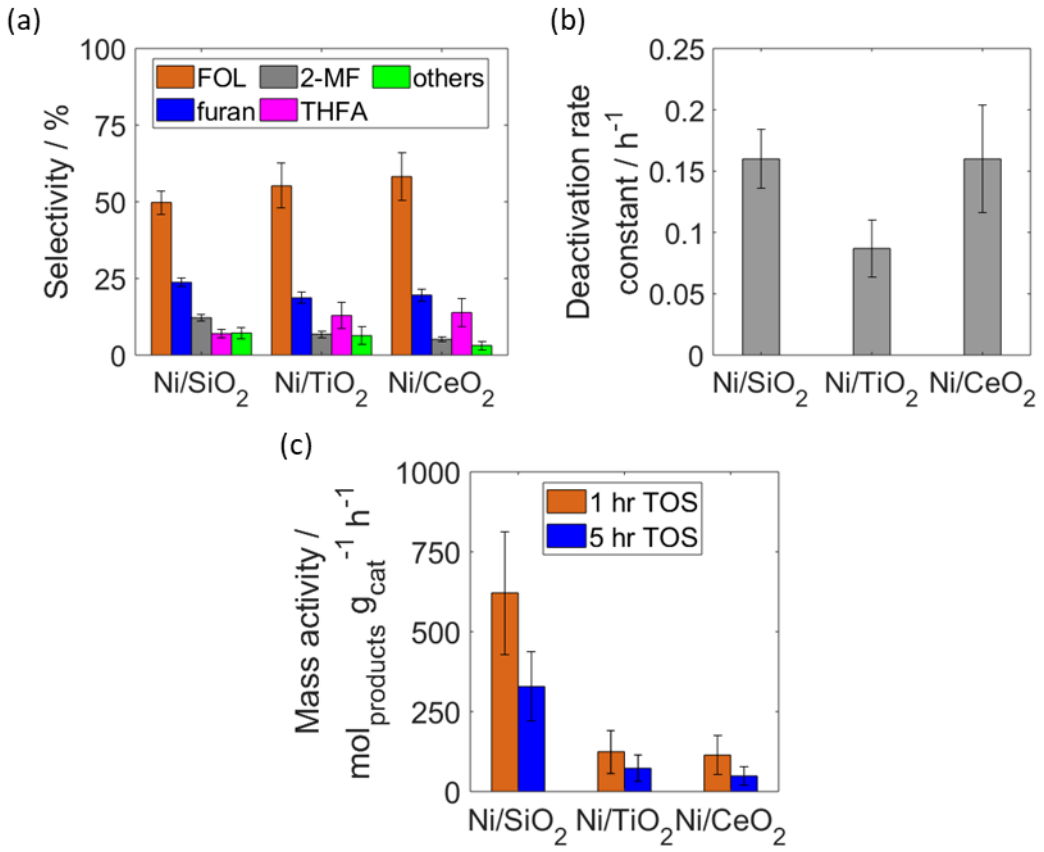

Figure 39: Comparison of different supports during furfural hydrogenation (a) Average selectivity under steady operation; (b) Deactivation rate constants; (c) Mass activities at 1 and 5 h TOS. Errors shown are based on repeat measurements of a typical sample as indicated in the experimental section.

3.5 Catalyst Deactivation

All of the catalysts tested, including copper chromite, exhibited rapid deactivation therefore it was important to understand the reasons for this deactivation. The deactivation is likely to result from either sintering or coking. The pXRD pattern in Figure 40 is for the post-reaction Ni/SiO_2 catalyst. The pattern is very similar to the pre-reaction catalyst with only a slight narrowing of the Ni(111) reflection corresponding to an estimated average crystallite size of 10 nm. Assuming spherical particles, this increase in particle size would, at most, correspond to a decrease in surface area of

50 %, however the activity decreases by an order of magnitude. Therefore, this small increase in particle size would not alone account for the deactivation.

TEM imaging of the post-reaction catalyst (Figure 41a) was also consistent with minimal sintering. The average particle size was found to be 4 ± 3 nm, with the particle size distribution compared to the pre-reaction catalyst shown in Figure 41b. This average particle size is actually smaller than that obtained for the pre-reaction catalyst (7 ± 6 nm). There are a number of potential explanations that could account, or partially account, for this change, including:

i) Upgraded TEM camera – the pre-reaction catalyst was imaged using the old TEM camera that produced poorer quality images and made it more difficult to reliably distinguish small metal particles from the support. Whereas the post-reaction catalyst was imaged using the new, improved camera that was able to produce higher quality images that made it easier to distinguish the smaller particles. Unfortunately, due to the timing of these results it was not possible to obtain comparable images on the same sample with both cameras.

ii) Oxidation – the smaller metal particles would be expected to oxidise more easily. Therefore, in the pre-reaction catalyst (reduction only), any smaller metal particles present may become oxidised when exposed to air during sample preparation and storage. Since small metal particles are already challenging to distinguish from the support, oxidation may make this impossible. However, as discussed below, significant coking appears to occur during furfural hydrogenation. This means that the metal particles in the post-reaction catalyst will likely be covered with carbonaceous deposits, which may offer some protection against oxidation. If so, this may mean the smaller particles remain in the metallic state and are therefore more easily distinguishable.

iii) Metal migration – it is possible that during reaction, the metal migrates across the support, resulting in the formation of some smaller metal particles. This seems unlikely unless the increased net surface area of smaller particles can be strongly stabilised in some way, as the converse (Ostwald ripening) typically occurs when metal is mobile on surfaces, so as to minimise energetically unfavourable surface free energy.

The average particle size of the spent catalyst by TEM is also significantly smaller than that estimated by pXRD, however this is likely due to the fact that pXRD produces a volume average, and so smaller particles contribute less to the average particle size compared to TEM which is a

number average. Overall, the key result from TEM and pXRD characterisation is that sintering alone cannot account for the rapid deactivation of the catalysts.

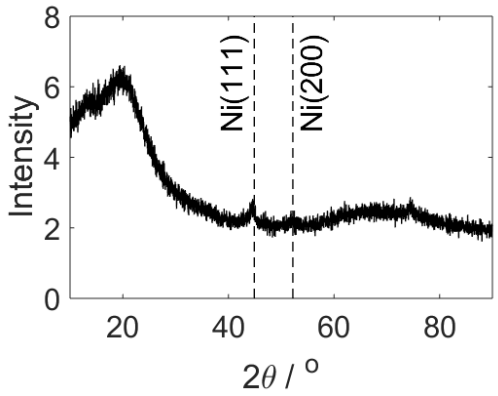

Figure 40: pXRD pattern of post-reaction Ni/SiO_2 sample, the positions of metallic f.c.c. nickel reflections are marked by the vertical dashed lines

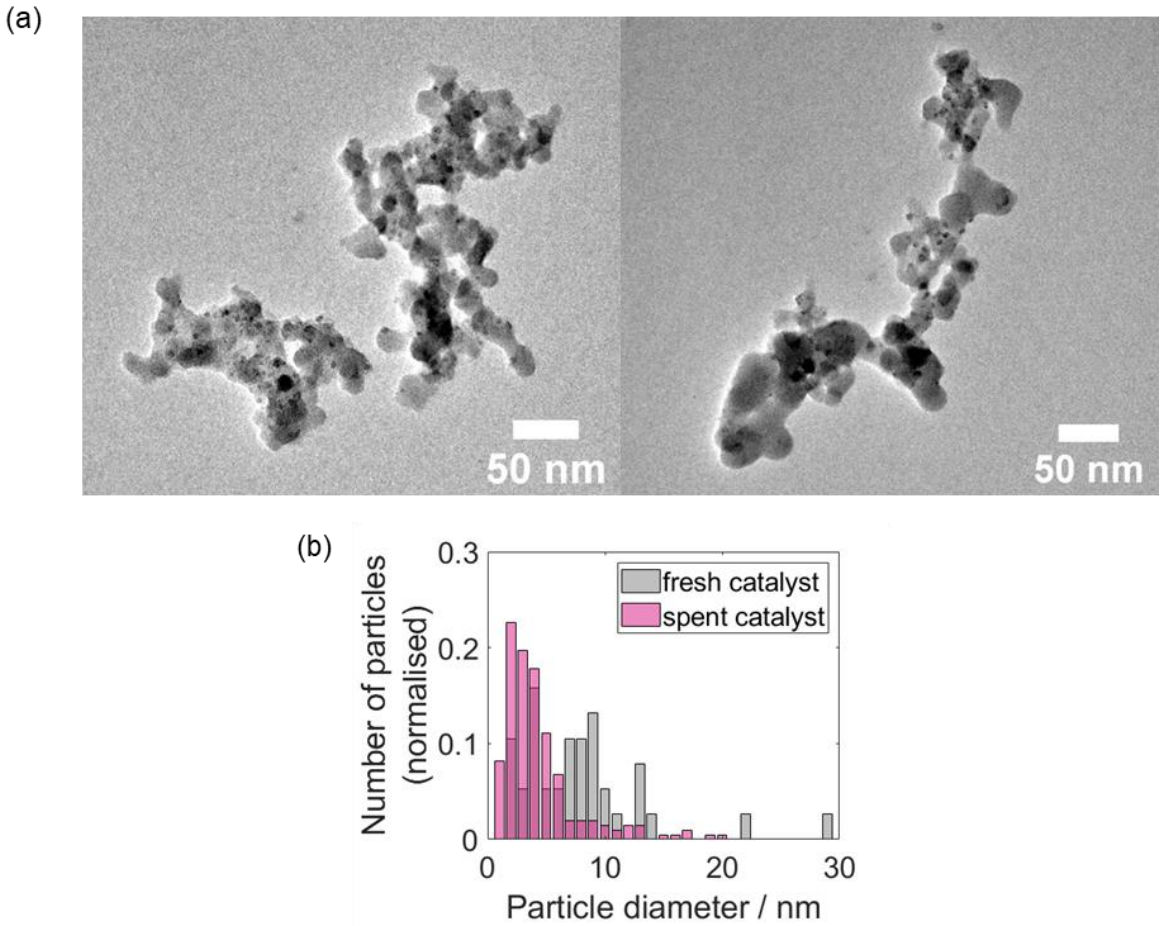

Figure 41: (a) TEM images of post-reaction Ni/SiO_2 and (b) particle size distribution for the pre-reaction Ni/SiO_2 ('fresh') catalyst and the post-reaction Ni/SiO_2 ('spent') catalyst

Another likely source of deactivation is coking, and so this was investigated by carrying out TPO analysis (Table 7). There was significant carbon deposition on the spent Ni/SiO_2 catalyst, with a mass loss of around 30 wt. % by 500 ^oC. Contributions to coking from the support were also investigated by carrying out TPO analysis on silica that was exposed to either furfural or furfuryl alcohol under standard reaction conditions (180 °C, 70 mL min^{-1} H_2). Both samples of silica (furfural-SiO_2 and furfuryl alcohol-SiO_2) exhibited a mass loss, however the mass loss was significantly lower than for the spent Ni/SiO_2 catalyst (<15 wt. % vs. 30 wt. %). The copper chromite catalyst also had a mass loss, however it was significantly less than the other samples (spent Ni/SiO_2, furfural-SiO_2 and furfuryl alcohol-SiO_2) at only 1.3 wt. %. The lower mass loss for the copper chromite catalyst is likely due to the low surface area of the catalyst compared to the other catalysts that were supported on high surface area supports.

Table 7: The mass losses from TPO data for silica exposed to furfural or furfuryl alcohol under standard reaction conditions and spent catalysts (Ni/SiO_2 and copper chromite). Mass loss that occurred before 200 °C is likely due to water loss and was therefore excluded. A small mass gain for copper chromite (likely due to copper oxidation) was observed at around 200 °C and so the mass loss for this sample was determined from temperatures above 320 °C to exclude this feature

Sample	**wt. % loss**
Furfural-SiO_2	9.5
Furfuryl alcohol-SiO_2	10
Spent Ni/SiO_2	30
Spent copper chromite	1.3

In order to further understand the coking occurring on these catalysts, differential mass loss analysis of the TPO data was carried out (Figure 42). Both the spent Ni/SiO_2 catalyst and the spent SiO_2 samples had a peak at around 300 ^oC, however the spent Ni/SiO_2 catalyst had a second peak at around 450 ^oC. This means that in the presence of nickel, a second coke species is forming, and so whilst SiO_2 does appear to contribute to coke formation, nickel is also playing a significant role in the coking process.

Consideration of the spatial volume of coke present on the catalysts can also provide some useful information on the type of coke forming on the catalysts. The volume of the nickel metal can be roughly estimated as 5×10^{-3} cm^3 g_{cat}^{-1} (assuming spherical particles with a density equivalent to bulk nickel metal and crystallites the size of those observed by pXRD). Assuming the coke is present as hydrocarbons (density ~1 g cm^{-3}) or graphitic carbon (density 2.3 g cm^{-3}), then a 15 wt. % loss (roughly the weight loss associated with both the peak at ~300 ^oC and ~450 ^oC) gives a coke:Ni

volume ratio of ~30:1 or ~15:1 respectively. The coke:Ni volume ratio can be instructive when considering the type of deactivation occurring, which can be generally classified as either site blocking, encapsulation or pore blocking.[29] When the coke:Ni volume is large, as in this case, then encapsulation and/or pore blocking are likely to be occurring.

Additionally, the coke:Ni volume ratio can aid in the interpretation of the differential mass loss spectra. Since the majority of the coke will not be directly on the surface of nickel particles, we can reasonably assume that nickel will not significantly contribute to the decomposition of coke species during the TPO experiment. Therefore, the peaks in the differential mass loss spectra can be assigned based on literature TPO analysis of polymer-silica composites. The peak at around 300 ^{o}C, seen in both the spent Ni/SiO_2 and spent SiO_2 samples, is consistent with that seen for low coverages of poly(furfuryl alcohol) on MCM-41 during TGA experiments carried out in air.[30] The same study also investigated a sample that had higher coverages of poly(furfuryl alcohol) on MCM-41 and found that this resulted in a second higher temperature peak centred at around 480 ^{o}C. It is unclear what the origin of this higher temperature peak is in the case of poly(furfuryl alcohol), however the temperature range is consistent with long chain hydrocarbons such low density polyethylene (both alone or as a silica-composite).[31] For the Ni/SiO_2 catalyst discussed in this chapter, the presence of the ~450 ^{o}C peak can be attributed to a different coke species from the lower temperature peak since the spent SiO_2 samples did not exhibit this feature. Metal oxide and metal/metal oxide catalysts at low temperatures (<200 ^{o}C) have been found to mainly produce coke consisting of components from rearrangement and condensation reactions of the reactants and products, as opposed to the formation of poly(aromatics), which occurs at higher temperatures (>350 ^{o}C).[32] During furfural hydrogenation with the Ni/SiO_2 catalyst, the presence of both Ni and H_2 is likely to lead to additional reactions such as hydrogenation, deoxygenation or dehydration. The acid-catalysed formation of polymers from the reactant and products likely results in the lower temperature peak at 300 ^{o}C, which is present both with and without nickel. Whilst these polymers may possibly also contribute to the higher temperature peak at 450 ^{o}C, this peak is likely due to the formation of long chain hydrocarbons species ('poly-ethylene like') that result from the dehydration of the initially formed polymers of furfural or furfuryl alcohol.

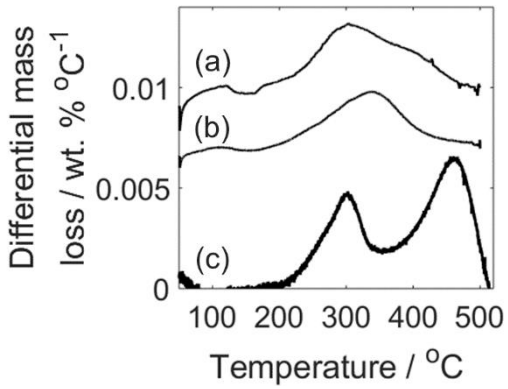

Figure 42: Differential mass loss during TGA in flowing air of (a) silica exposed under reaction conditions to furfural (5 °C min^{-1}); (b) silica exposed under reaction conditions to furfuryl alcohol (5 °C min^{-1}); (c) spent Ni/SiO_2 (2°C min^{-1})

To further investigate the nature of the coke species present, Soxhlet extraction of any soluble species from the post-reaction catalysts was carried out, followed by analysis of the extracted species by GC-MS. A sample of spent Ni/SiO_2 catalyst was analysed using this method. The extraction solution had to be concentrated to ensure that the extracted species were at an appropriate concentration for GC-MS analysis. It should be noted that after concentrating the solution, a trace insoluble residue remained on the flask and so could not be analysed. Several of the peaks in the GC trace corresponded to long chain hydrocarbons, identified by the distinctive mass spectra that have regular spacings of one methylene unit between peaks (see example spectrum shown in Figure 43a). Some of the long chain hydrocarbon peaks were able to be identified from their parent ions including $C_{21}H_{44}$, $C_{22}H_{46}$, $C_{23}H_{48}$ and $C_{24}H_{50}$. Figure 43b shows the mass spectrum of a lower retention time peak with fragments at 155, 139, 99, 57, and 41 m/z. Although a definitive assignment cannot be made (as several combinations of fragments fit the data) the dominant m/z = 155 and 99 features (and absence of m/z = 71 implying this isn't a linear hydrocarbon fragment) indicate the likelihood of this belonging to either ring opened furanic oligomers or hydrogenated linear oligomers of furfuryl alcohol. Possible fragments are shown in Figure 43c. A wide range of such structures have been proposed for furfuryl alcohol oligomers formed over acidic solids such as Al_2O_3 or WO_3.[33, 34]

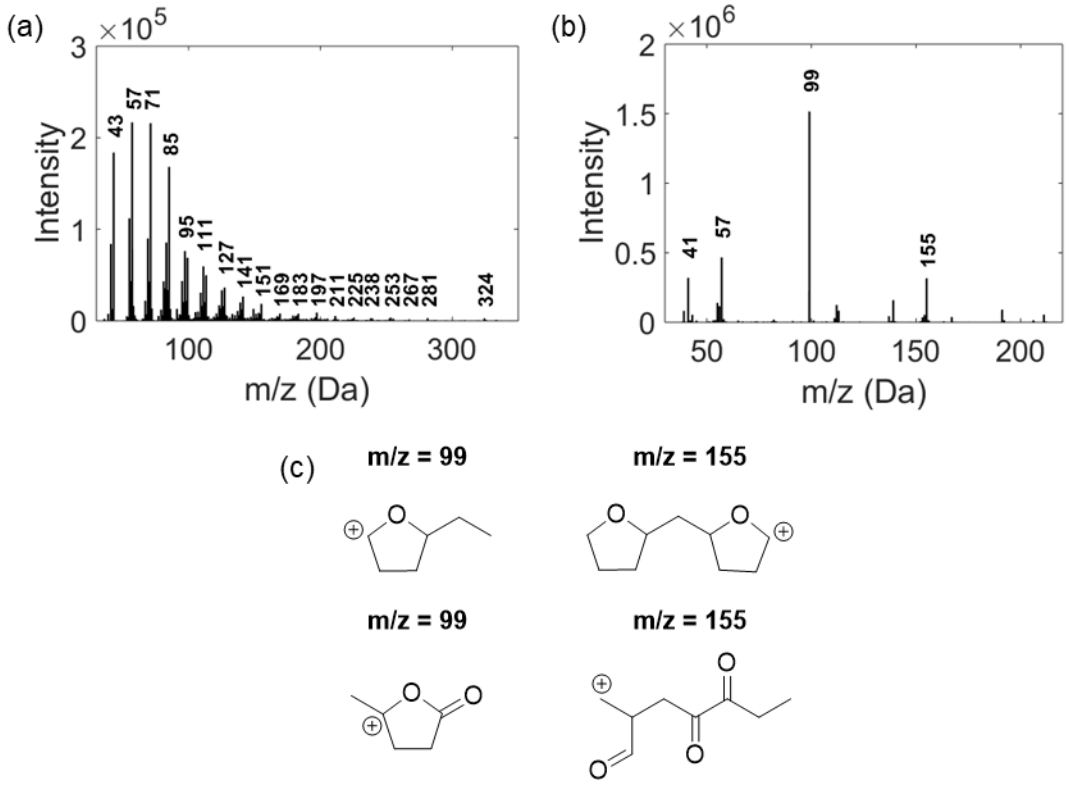

Figure 43: GC-MS mass spectra (m/z 35-350) of species extracted from spent Ni/SiO_2 catalyst using a Soxhlet extraction: (a) example of a mass spectrum of a long chain hydrocarbon (consistent with tricosane; $C_{23}H_{48}$); (b) mass spectrum of lower retention time peak attributed to hydrogenated furanic or ring opened furanic oligomers, (c) possible hydrogenated components of short chain furanic oligomers contributing to the spectrum in (b).

Since Soxhlet extraction involves refluxing the solvent (in this case DCM), it was important to rule out the possibility of the reflux itself leading to the formation of furfuryl alcohol oligomers or other similar compounds. Therefore, an experiment was carried out where a small amount of furfuryl alcohol (which would be equivalent to a catalyst having a ~29 wt. % loading of furfuryl alcohol) was added to DCM and then left to reflux using the Soxhlet apparatus for the same time as a typical experiment, but with no Soxhlet thimble or spent catalyst. The GC trace (Figure 44a) shows one main peak and two significantly smaller peaks. The mass spectrum of the main peak matches furfuryl alcohol as expected (Figure 44b). The mass spectrum of one of the smaller peaks is shown in Figure 44c and appears to potentially be a side-product that formed during the vacuum distillation of furfuryl alcohol from sodium carbonate (Figure 44d). It can be concluded from this experiment that the Soxhlet extraction procedure does not lead to the formation of furfuryl alcohol oligomers or other species in significant quantities, and therefore, any species found during the Soxhlet extraction of spent catalysts can be attributed to carbonaceous deposits that formed on the catalysts during furfural hydrogenation.

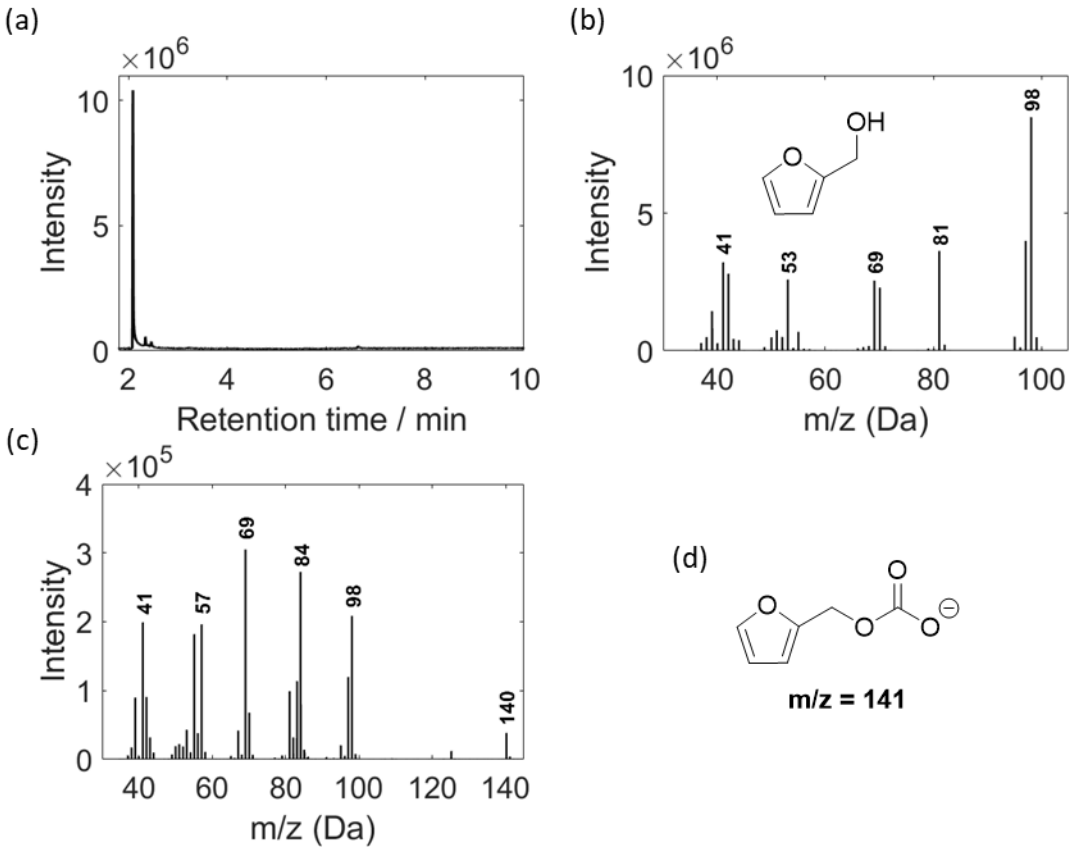

Figure 44: (a) GC spectrum of a blank Soxhlet extraction (no catalyst or thimble included) where distilled furfuryl alcohol was added to the DCM, (b) GS-MS mass spectrum (m/z 35-350) of the main peak in the GC spectrum corresponding to furfuryl alcohol, (c) GC-MS mass spectrum (m/z 35-350) of a possible furfuryl alcohol impurity, (d) possible structure of the furfuryl alcohol impurity corresponding to the mass spectrum in (c)

Since coking appears to be playing a significant role in deactivation, the nature of the carbon deposits was investigated further using DRIFTS. In order to distinguish between species present on the support and species present on the metal, the silica and a sample of nickel powder were exposed to furfural, furfuryl alcohol or products under standard furfural hydrogenation conditions. The DRIFT spectra of the nickel powder samples contained no significant peaks, likely due to the low surface area of the material. However, there were several peaks observed for the silica samples (Figure 45). The peaks observed in the spectrum of silica exposed to furfural matched well with the reference furfural spectrum, with only some small shifts in peak position, likely due to interactions with the support or oligomerisation. The spectrum for silica exposed to furfuryl alcohol contained similar infrared bands to those observed in the spent Ni/SiO_2 catalyst, with two very broad peaks in the 1350 – 2000 cm^{-1} region and four weak peaks in the C-H region (2800-3000 cm^{-1}). Therefore, one of the coke species present is likely related to furfuryl alcohol or its oligomers. The furfuryl alcohol reference spectrum generally has weak signals, however there is a sharp peak at 1504 cm^{-1} which has been assigned as C=C stretching.[35] This sharper signal was not present in either the silica

exposed to furfuryl alcohol or the spent Ni/SiO_2, perhaps due to interaction of furfuryl alcohol with the silica or oligomerisation. Some examples of furfuryl alcohol polymers are shown in Figure 46, although other versions such as cross-linked polymers are known.[34]

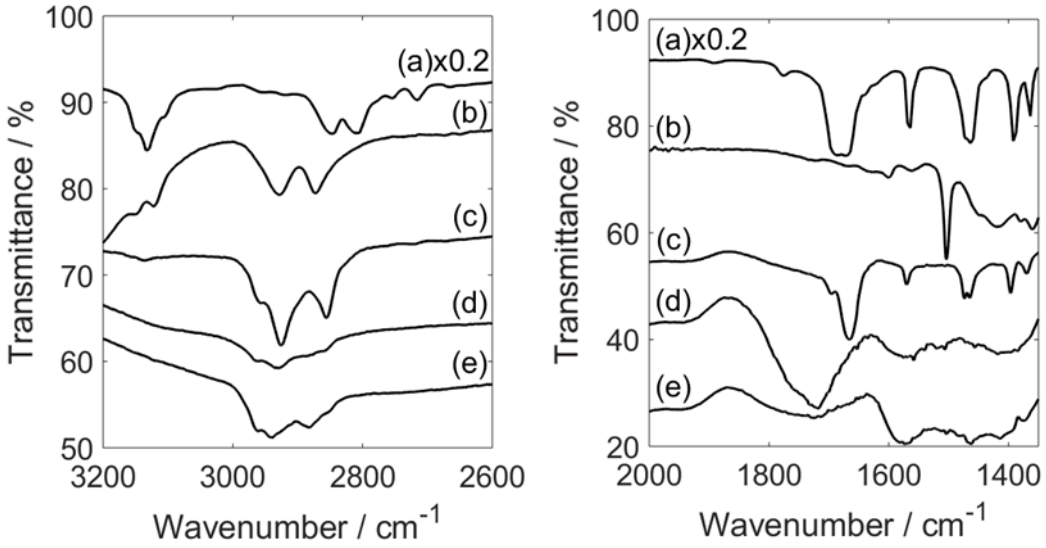

Figure 45: Infrared spectra showing (3200-2600 cm-1 left, 2000-1350 cm-1 right): (a) Furfural reference spectrum,[36] multiplied by 0.2 for comparison (b) Furfuryl alcohol reference spectrum (ATR); (c) Silica exposed to furfural (DRIFTS); (d) Silica exposed to furfuryl alcohol (DRIFTS); (e) spent Ni/SiO2 catalyst (DRIFTS). Spectra (b-e) offset vertically for clarity. For (c) and (d) furfural or furfural alcohol were fed into the reactor under otherwise standard catalyst testing conditions with only the support rather than a catalyst present.

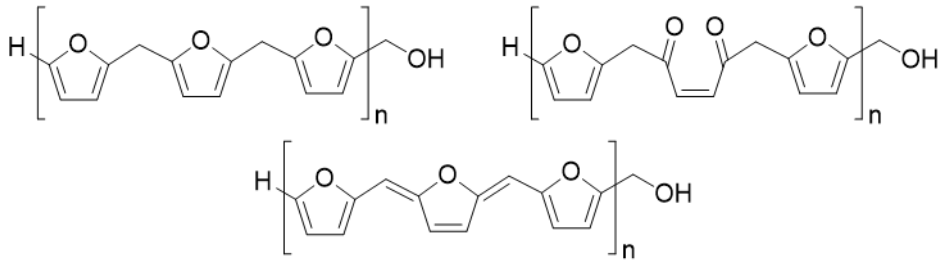

Figure 46: Examples of possible furfuryl alcohol polymers[34]

Changing the support to titania and ceria did not have a significant effect on the peaks observed in the DRIFT spectra (see Figure 47), suggesting that similar coke species are present in all catalysts and that these species are likely related to furfuryl alcohol. The similarity across all supports fits with the fact that changing the support had little effect on the selectivity and deactivation of the catalysts. If the finding by infrared that the main species seen are furfuryl alcohol-like is considered relative to the TPO and GC-MS data above, it must be remembered that the presence of long chain hydrocarbons is hard to see by infrared, with the only distinguishing features likely to be in the same region as the C-H stretches already seen. Furthermore, if the more deoxygenated coke forms

in the pores around the nickel it may be less evenly distributed than the oligomers formed over silica alone, which in turn may make the long-chain hydrocarbons less readily probed during DRIFTS measurements that result from light reflecting off multiple surfaces in the sample.[37] An overall model for deactivation therefore likely involves both condensation to form oligomers and polymers of the product (and perhaps reactant), followed by Ni catalysed hydrogenation and dehydration to produce deoxygenated coke. The volume of coke is sufficient to encapsulate the nickel or block access *via* the pores of the silica and gradually results in a large fractional loss of activity over ~10 h TOS.

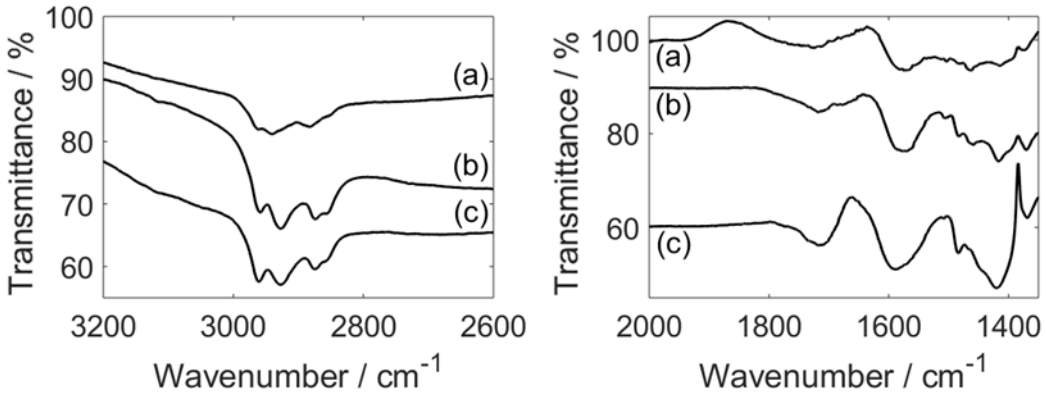

Figure 47: DRIFT spectra (3200-2600 cm-1 left, 2000-1350 cm-1 right); (a) spent Ni/SiO2; (b) spent Ni/TiO2; (c) spent Ni/CeO2. Spectra offset for vertically clarity

The spent copper chromite sample had much weaker bands in the infrared spectrum (Figure 48), which is consistent with the lower mass loss in the TPO experiment and is attributable to the lower surface area of the catalyst compared to the supported catalysts. The infrared spectra show bands in the C-H stretching region (~2850-3000 cm^{-1}), although with slight differences from the nickel samples. This potentially suggests that different oligomeric species are formed as the dominant carbon containing products, which is feasible given the change of catalyst, but their presence again supports the formation of hydrocarbons as well as purely carbonaceous coke.

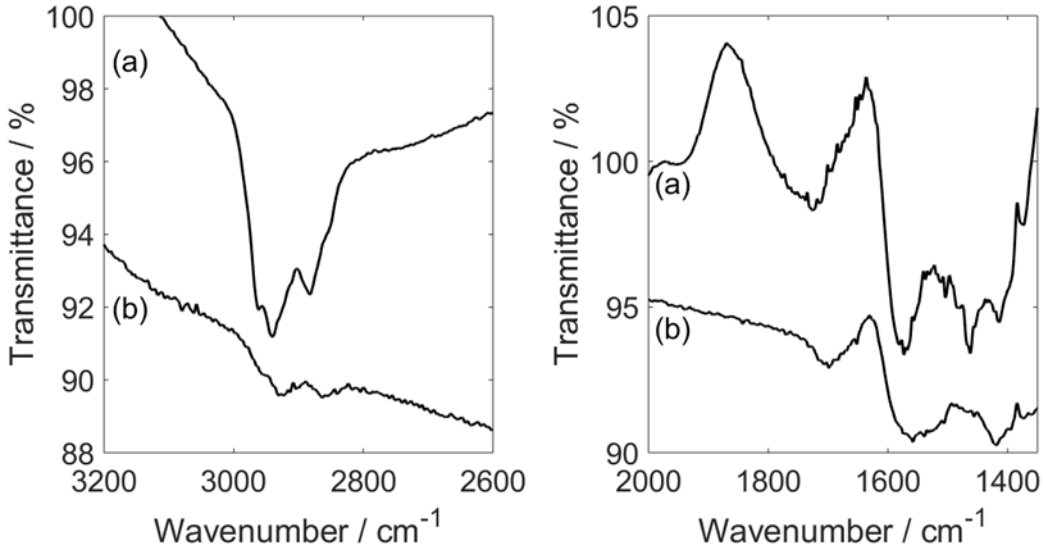

Figure 48: DRIFT spectra (3200-2600 cm^{-1} left, 2000-1350 cm^{-1} right); (a) spent Ni/SiO_2; (b) spent copper chromite. Spectra offset for vertically clarity

3.6 Conclusions

In summary, supported nickel catalysts were found to produce furfuryl alcohol as the dominant product with a selectivity of ~50% during vapour phase furfural hydrogenation. The Ni/SiO_2 IWI catalyst was seen to be significantly more active than copper chromite but exhibited much poorer selectivity when tested under comparable conditions. The deactivation behaviours of Ni/SiO_2 and copper chromite were found to be relatively similar as a function of time on stream. Ni/TiO_2 and Ni/CeO_2 exhibited similar deactivation profiles, indicating that acidic sites on the catalyst support are not strongly implicated in the deactivation occurring. pXRD analysis of the Ni/SiO_2 catalyst before and after reaction indicated that sintering was not a significant cause of the rapid deactivation observed. TPO, infrared and solvent extraction of spent catalysts provided evidence that deactivation is likely the result of the gradual formation of oligomeric/polymeric forms of the product (or reactant) and their deoxygenation to hydrocarbons. Overall, the high activity seen points to the potential for developing new catalysts based on nickel for furfural hydrogenation, and two important areas for further work, which will be explored in later chapters, have been identified: (1) tuning the selectivity of the nickel, potentially by introducing a second metal, and (2) preventing the oligomerisation and deoxygenation steps that result in deactivation by coking of the catalyst.

3.7 References

1. F. Besenbacher, I. Chorkendorff, B. S. Clausen, B. Hammer, A. M. Molenbroek, J. K. Nørskov and I. Stensgaard, *Science*, 1998, **279**, 1913.
2. J. R. Rostrup-Nielsen, J. Sehested and J. K. Nørskov, *Adv. Catal.*, 2002, **47**, 65-139.
3. R. A. van Santen and H. W. Niemantsverdriet, *Chemical kinetics and catalysis*, Springer US, New York, 1995.
4. H. S. Bengaard, J. K. Norskov, J. Sehested, B. S. Clausen, L. P. Nielsen, A. M. Molenbroek and J. R. Rostrup-Nielsen, *J. Catal.*, 2002, **209**, 365-384.
5. A. R. McFarlane, I. P. Silverwood, E. L. Norris, R. M. Ormerod, C. D. Frost, S. F. Parker and D. Lennon, *Chem. Phys.*, 2013, **427**, 54-60.
6. W. B. Gong, C. Chen, H. M. Zhang, Y. Zhang, Y. X. Zhang, G. Z. Wang and H. J. Zhao, *Mol. Catal.*, 2017, **429**, 51-59.
7. A. O'Driscoll, J. J. Leahy and T. Curtin, *Catal. Today*, 2017, **279**, 194-201.
8. S. Y. Sang, Y. Wang, W. Zhu and G. M. Xiao, *Res. Chem. Intermed.*, 2017, **43**, 1179-1195.
9. Y. Su, C. Chen, X. Zhu, Y. Zhang, W. Gong, H. Zhang, H. Zhao and G. Wang, *Dalton Transactions*, 2017, **46**, 6358-6365.
10. W. Gong, C. Chen, H. Zhang, G. Wang and H. Zhao, *Catalysis Science & Technology*, 2018, **8**, 5506-5514.
11. Y. Xu, S. Qiu, J. Long, C. Wang, J. Chang, J. Tan, Q. Liu, L. Ma, T. Wang and Q. Zhang, *RSC Adv.*, 2015, **5**, 91190-91195.
12. S. Srivastava, G. C. Jadeja and J. Parikh, *J. Mol. Catal. A: Chem.*, 2017, **426**, 244-256.
13. P. Jia, X. Lan, X. Li and T. Wang, *ACS Sustainable Chemistry & Engineering*, 2018, **6**, 13287-13295.
14. Rodiansono, M. D. Astuti, D. R. Mujiyanti, U. T. Santoso and S. Shimazu, *Molecular Catalysis*, 2018, **445**, 52-60.
15. V. Vetere, A. B. Merlo, J. F. Ruggera and M. L. Casella, *Journal of the Brazilian Chemical Society*, 2010, **21**, 914-920.
16. M. Manikandan, A. K. Venugopal, K. Prabu, R. K. Jha and R. Thirumalaiswamy, *J. Mol. Catal. A: Chem.*, 2016, **417**, 153-162.
17. Y. Nakagawa, H. Nakazawa, H. Watanabe and K. Tomishige, *ChemCatChem*, 2012, **4**, 1791-1797.
18. T. P. Sulmonetti, S. H. Pang, M. T. Claure, S. Lee, D. A. Cullen, P. K. Agrawal and C. W. Jones, *Appl. Catal., A*, 2016, **517**, 187-195.
19. V. R. Madduluri, K. K. Mandari, V. Velpula, M. Varkolu, S. R. R. Kamaraju and M. Kang, *Fuel*, 2020, **261**.
20. D. Vargas-Hernández, J. M. Rubio-Caballero, R. Moreno-Tost, J. M. Mérida-Robles, J. Santamaría-González, A. Jiménez-López, M. A. Pérez-Cruz, R. Hernández-Huesca and P. Maireles-Torres, *Mod. Res. Catal.*, 2016, **05**, 85-94.
21. K. J. Zeitsch, *The chemistry and technology of furfural and its many by-products*, Elselvier Science, Amersterdam, The Netherlands, 1 edn., 2000.
22. C. Louis, Z. X. Cheng and M. Che, *The Journal of Physical Chemistry*, 1993, **97**, 5703-5712.
23. R. Rao, A. Dandekar, R. T. K. Baker and M. A. Vannice, *Journal of Catalysis*, 1997, **171**, 406-419.
24. I. I. Simentsova, A. V. Khasin, L. P. Davydova and T. M. Yurieva, *Reaction Kinetics and Catalysis Letters*, 2004, **82**, 355-361.
25. E. Santacesaria, G. Carotenuto, R. Tesser and M. Di Serio, *Chem. Eng. J. (Lausanne)*, 2012, **179**, 209-220.
26. H. Zhang, C. Canlas, A. Jeremy Kropf, J. W. Elam, J. A. Dumesic and C. L. Marshall, *Journal of Catalysis*, 2015, **326**, 172-181.

27. D. Liu, D. Zemlyanov, T. Wu, R. J. Lobo-Lapidus, J. A. Dumesic, J. T. Miller and C. L. Marshall, *Journal of Catalysis*, 2013, **299**, 336-345.
28. S. J. Tauster, S. C. Fung and R. L. Garten, *Journal of the American Chemical Society*, 1978, **100**, 170-175.
29. C. H. Bartholomew, *Applied Catalysis A: General*, 2001, **212**, 17-60.
30. R. Janus, A. Wach, P. Kuśtrowski, B. Dudek, M. Drozdek, A. M. Silvestre-Albero, F. Rodríguez-Reinoso and P. Cool, *Langmuir*, 2013, **29**, 3045-3053.
31. H. Sertchook, H. Elimelech, C. Makarov, R. Khalfin, Y. Cohen, M. Shuster, F. Babonneau and D. Avnir, *Journal of the American Chemical Society*, 2007, **129**, 98-108.
32. M. Guisnet and P. Magnoux, *Applied Catalysis A: General*, 2001, **212**, 83-96.
33. E. M. Wewerka, *Journal of Polymer Science Part A-1: Polymer Chemistry*, 1971, **9**, 2703-2715.
34. G. Tondi, N. Cefarin, T. Sepperer, F. D'Amico, R. J. F. Berger, M. Musso, G. Birarda, A. Reyer, T. Schnabel and L. Vaccari, *Polymers*, **11**, 2126.
35. C. Araujo-Andrade, A. Gómez-Zavaglia, I. D. Reva and R. Fausto, *J. Phys. Chem. A*, 2012, **116**, 2352-2365.
36. W. E. Wallace and NIST Mass Spectrometry Data Center, in *NIST Chemistry WebBook, NIST Standard Reference Database Number 69*, eds. P. J. Linstrom and W. G. Mallard, National Institute of Standards and Technology, Gaithersburg MD, Accessed May 23, 2020, DOI: https://doi.org/10.18434/T4D303, ch. Infrared Spectra.
37. T. Armaroli, T. Bécue and S. Gautier, *Oil Gas Sci. Technol.*, 2004, **59**, 215-237.

Chapter 4: Synthesis of nickel, tin-nickel and nickel phosphide colloidal nanoparticles

In the previous chapter, incipient wetness nickel catalysts were prepared and evaluated for furfural hydrogenation. Whilst incipient wetness impregnation is a widely used and simple technique for preparing supported nickel catalysts, the catalysts produced often have broad particle size distributions. Additionally, for bi-metallic catalysts, which will be explored for furfural hydrogenation in later chapters, the distribution of the metals may also be heterogeneous. This can make analysis more challenging, particularly when using advanced characterisation techniques such as XAS or NAP-XPS. Therefore, in order to produce more homogeneous catalysts, colloidal nanoparticles have been synthesised. Small nickel and tin-nickel monodisperse nanoparticles (~4 nm) have been prepared using a phosphine-free method, however larger versions of these nanoparticles (10 - 15 nm) required the use of a phosphine capping agent. The importance of the synthetic conditions employed during the syntheses that use a phosphine capping agent has been demonstrated, with effects on the structure, composition and morphology of the resulting nanoparticles considered.

4.1 Synthesis of small (~4 nm) colloidal nickel and tin-nickel nanoparticles

The synthesis of small colloidal nanoparticles using oleylamine as a capping agent and a borane-amine complex as a reducing agent was first described by Metin *et al.*[1] and has become a popular synthetic method for colloidal nickel nanoparticles since it produces small (~4 nm) nanoparticles with a narrow size distribution. This synthetic method has therefore been adopted here to produce small nickel nanoparticles, as well as adapted to produce small tin-nickel bimetallic nanoparticles.

4.1.1 Synthesis of small nickel nanoparticles

The main aim of synthesising colloidal nanoparticles was to produce model catalysts that were more uniform in terms of their particle size and composition, which should allow the impact of tin on catalysis to be understood in greater detail (*e.g.* by identifying clear structure-activity relationships). However, it is important to also synthesise monometallic nickel nanoparticles to act as an appropriate reference. Figure 49 shows a TEM image of the monometallic nickel nanoparticles and the corresponding size distribution. The average particle size was found to be 4.3 ± 0.6 nm, which is a fairly narrow size distribution and indicates good uniformity. These results are relatively consistent with Metin *et al.*[1] who reported an average particle size of 3.2 ± 0.2 nm using the same

synthetic conditions, however the nanoparticles produced in this report have a slightly larger particle size and a slightly broader particle size distribution. The authors did note that lowering the borane tributyl amine (BTrB) to nickel ratio from 3 to 1 led to small increases in particle size (3.2 nm to 5.4 nm by altering the BTrB:Ni ratio from 3 to 1) and slightly broader particle size distributions. Borane tert-butylamine (BTB, used in this work) is only weakly soluble in oleylamine and a small volume (2 mL) was used to dissolve the BTB, a potential explanation for the small differences in both particle size and distribution could be that not all of the BTB was dissolved and therefore injected into the reaction mixture, slightly lowering the BTB:Ni ratio.

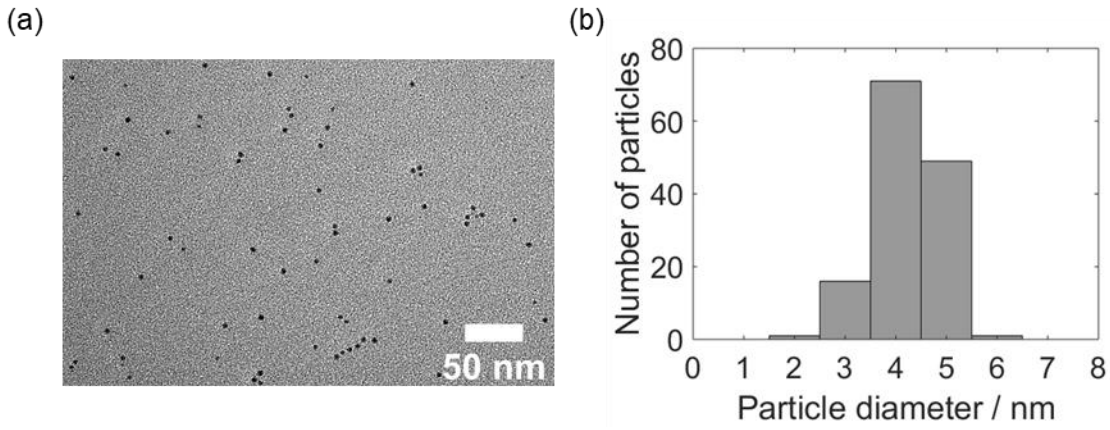

Figure 49: TEM image of the nickel nanoparticles (left) and the corresponding particle size distribution (right)

The percentage yields and, where relevant, Ni:Sn molar ratios for the nanoparticles synthesised in this chapter are reported in Table 8. The yield for the nickel nanoparticles synthesised in this section ('small Ni nanoparticles') was found to be 36.9 ± 0.9 %. This yield, although seemingly fairly low, is typical of colloidal nanoparticle syntheses. However, for our purposes it is considered acceptable since the purpose here is to produce a model catalyst and it easily provides enough nickel nanoparticles to make a suitable quantity of supported catalyst for testing and analysis.

Table 8: The yields and Sn:Ni ratios of the colloidal nanoparticles synthesised in this chapter, based on ICP-OES or ICP-MS analysis. ICP analysis, including digesting of samples, was carried out in duplicate to ensure consistency and allow errors to be determined. [a]Although the sample was sealed in a vial with a taped lid, some of the hexane evaporated over the time between synthesis and ICP analysis, resulting in a yield of >100 %, however the nickel yield is expected to be similar to other samples prepared using this synthetic method (~ 90 %). [b]the error was estimated based on the error in a similar sample (crystalline larger SnNi (1:50) nanoparticles) since there was an issue with the instrument when the duplicate sample was run (it was not possible to repeat the analysis due to the small amount of sample produced in this reaction, of which a significant portion was required for catalytic testing).

Sample	**Yield / % (based on Ni)**	**Nominal Ni/Sn molar ratio**	**Experimental Ni/Sn molar ratio**
Small Ni nanoparticles	36.9 ± 0.9	N/A	N/A
Small SnNi nanoparticles – co-addition method	56.2 ± 0.3	3	3.3 ± 0.2
Small SnNi nanoparticles – sequential addition method	13.9 ± 0.6	3	2.9 ± 0.1
Amorphous larger Ni nanoparticles	68.4 ± 0.9	N/A	N/A
Amorphous larger SnNi (1:3) nanoparticles	35.5 ± 0.5	3	4.19 ± 0.08
Amorphous larger SnNi (1:20) nanoparticles	74 ± 1	20	18.1 ± 0.7
Amorphous larger SnNi (1:50) nanoparticles	68.8 ± 0.6	50	33.6 ± 0.7
Crystalline larger Ni nanoparticles	— [a]	N/A	N/A
Crystalline larger SnNi (1:20) nanoparticles	92.7 ± 0.9[b]	20	23.6 ± 0.5
Crystalline larger SnNi (1:50) nanoparticles	91.6 ± 0.8	50	56.7 ± 0.7

4.1.2 Synthesis of small tin-nickel nanoparticles via the co-addition method

In order to synthesise bimetallic tin-nickel nanoparticles, the method used for the synthesis for the nickel nanoparticles was modified. There are two main ways in which this could be done; the addition of a Sn(II) precursor at the same time that the Ni(II) precursor was added or first forming the nickel nanoparticles before adding the Sn(II) precursor (see Figure 50). These synthetic routes

are described as the co-addition method and the sequential addition method respectively. The SnNi bimetallic nanoparticles prepared using the co-addition method are discussed in this section.

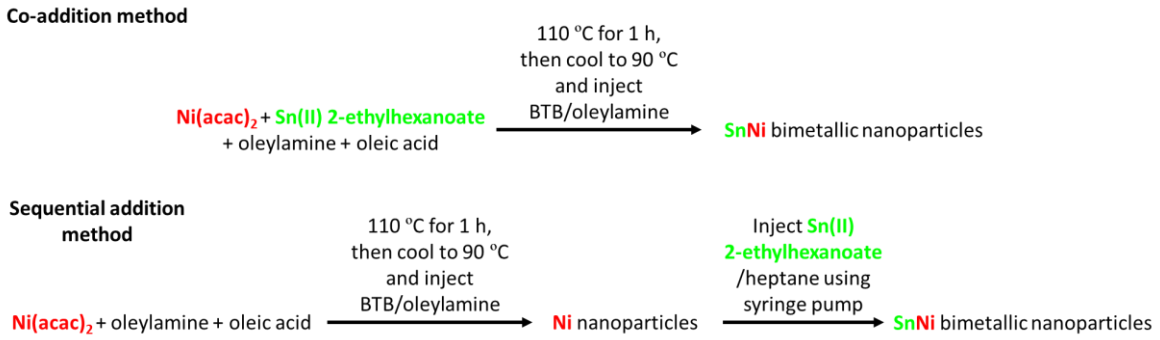

Figure 50: Reaction schemes illustrating the differences between the co-addition and sequential addition synthesis methods for the SnNi bimetallic nanoparticles

Figure 51 shows a TEM image of the nanoparticles and the corresponding particle size distribution. The average particle size was found to be 4.4 ± 1.3 nm, which is very similar to the nickel monometallic nanoparticles, but with a broader particle size distribution. This may indicate that the presence of the Sn(II) precursor during reduction is leading to less a uniform nucleation and growth of the nanoparticles.

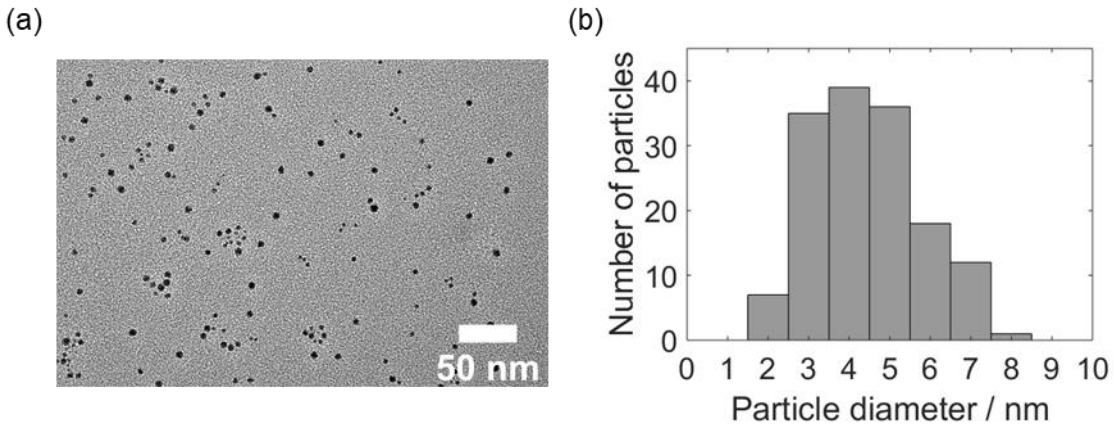

Figure 51: (a) TEM image and (b) particle size distribution for the co-addition SnNi particles

The yield of the reaction, determined by ICP-OES, was found to be 56.2 ± 0.3 % with respect to nickel (Table 8), which is a reasonable yield and actually slightly higher than the analogous nickel only reaction. The nanoparticles were synthesised with a nominal Ni:Sn molar ratio of 3:1 and ICP-OES analysis confirmed that the Ni/Sn molar ratio (3.3 ± 0.2) was very close to the targeted ratio (Table 8).

4.1.3 Synthesis of small tin-nickel nanoparticles via the sequential addition method

Since it was thought that the presence of the Sn(II) precursor during the reduction step may be detrimental to obtaining a narrow particle size distribution, bimetallic nanoparticles were then prepared using the sequential addition method. It was thought that this method may also lead to a more narrow distribution of Ni:Sn molar ratios, as the Sn(II) reagent will be slowly added using a syringe pump (2.6 $mg_{(Sn)}$ min^{-1}) and so should be evenly added to the already formed nickel nanoparticles. Slow addition of the Sn(II) precursor is necessary to ensure that the concentration will remain below that required for nucleation, since this will result in the addition of tin to existing nickel nanoparticles rather than the formation of new tin nanoparticles.[2] Figure 52 shows a TEM image of the SnNi nanoparticles prepared using the sequential addition method, as well as the corresponding particle size distribution. The average particle size was found to be 4.4 ± 0.8 nm which means the nanoparticles are of a similar size to both the monometallic nickel and bimetallic SnNi co-addition method nanoparticles. However, the particle size distribution is narrower than the bimetallic nanoparticles prepared using the co-addition method and is much more similar to that obtained for the monometallic nickel nanoparticles. This confirms that the presence of the Sn(II) precursor during the reduction, nucleation and growth of the nanoparticles is leading to a broadened particle size distribution. ICP-OES analysis revealed the nanoparticles had a lower yield of 13.9 ± 0.6 %. However, since these nanoparticles have been synthesised to act as a model catalyst and the yield still provided enough material to make a reasonable mass of catalyst for testing and analysis, the low yield was deemed acceptable. The nanoparticles were prepared with a nominal Ni:Sn molar ratio of 3:1, and ICP-OES analysis confirmed the nanoparticles had a Ni/Sn ratio of 2.9 ± 0.1, which is very close to the targeted ratio (see Table 8).

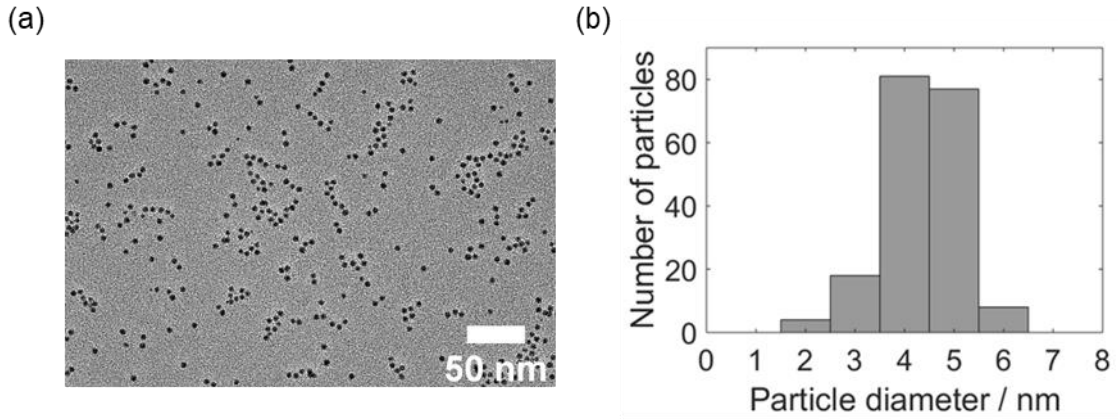

Figure 52: (a) TEM image and (b) particle size distribution for the sequential addition SnNi particles

High resolution TEM (HRTEM) imaging of the nanoparticles revealed that the nanoparticles had a polycrystalline structure, with an example image shown in Figure 53a. The d-spacings were determined by carrying out a fast Fourier transform (FFT) of the image of the nanoparticle and were found to be 0.20 nm and 0.21 nm which correspond to Ni(111) and NiO(200) respectively (Figure 53b). Therefore, the crystalline regions of the as made nanoparticles appear to remain as nickel metal or nickel oxide, with nothing to suggest significant tin incorporation. This could be consistent with the formation of core-shell nanoparticles, where the centre is nickel metal and the surface consists of a tin-containing phase. The tin is present in relatively low amounts, and so it is reasonable to assume it would not be possible to see this phase in TEM images, especially since the nanoparticles are small and therefore already challenging to image. Alternatively, the tin phase could be amorphous and therefore not produce any lattice fringes. The formation of core-shell nanoparticles would fit with the synthetic method used since nickel nanoparticles are first formed before tin is added, therefore it is reasonable to hypothesise that the tin would be added to the surface of the nickel nanoparticles and not necessarily be incorporated into the nickel centre.

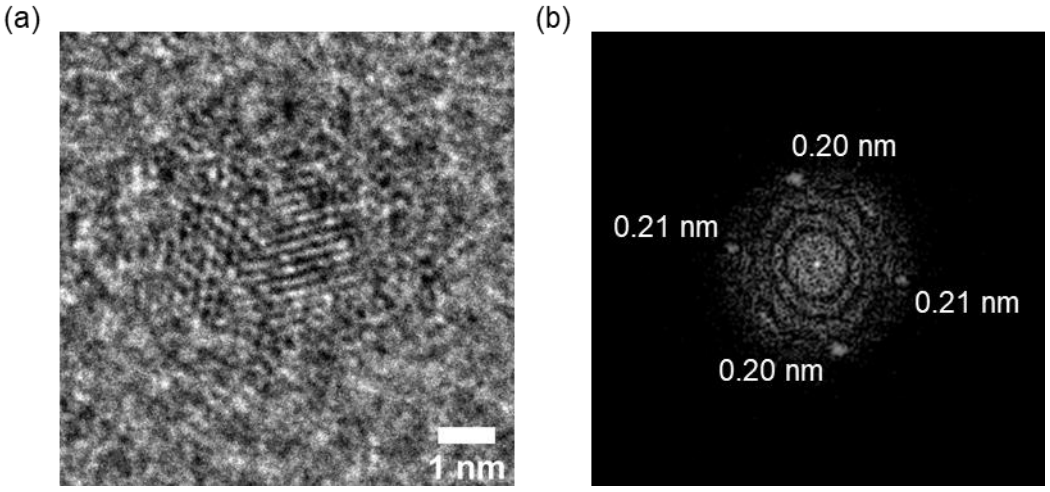

Figure 53: (a) HRTEM image of a SnNi sequ. add. nanoparticle and (b) FFT of the HRTEM image of the nanoparticle shown in (a)

Figure 54 shows the pXRD patterns of the as prepared and reduced (at 300 °C and 350 °C) SnNi sequential addition nanoparticles. The pattern for the as prepared nanoparticles contains broad reflections, suggesting the particles are mostly amorphous or consist of very small crystallite sizes, which is consistent with the TEM images where the visible crystalline regions are limited to around 1 – 2 nm, despite the nanoparticles being around 4 nm in size. After reduction at 300 °C (the pre-treatment used before catalytic reactions in later chapters), there is the introduction of some sharper reflections, in particular at around 42.3 °. Higher temperature reduction (350 °C) produces a very similar pattern, but with slightly sharper reflections. The reflections at 42.3 °, 71.8 ° and 86.8,

as well as a weak reflection at around 48.6 ° fit well with the expected reflections for cubic Ni_3Sn (auricupride structure).[3] The stoichiometry of this structure is consistent with the Ni:Sn molar ratio as determined by ICP analysis, and is also similar to the Ni-Sn phase observed by pXRD in the IWI catalysts (Chapter 5). Whilst Ni_3Sn appears to fit well with several of the reflections, there are still some unaccounted for broader reflections. The unaccounted for reflections do not fit well with any expected structures (*e.g.* metallic nickel or tin, nickel-tin alloys, nickel and/or tin oxides, nickel and/or tin phosphides, nickel and/or tin carbides), however the reflections may roughly correspond to NiO. At this stage, it is hard to make a definitive assignment, however other nanoparticle samples (discussed later in this chapter) were found to contain nickel oxide after similar treatments. Additionally, whilst the samples were reduced prior to analysis and kept under inert atmosphere until around 30 minutes prior to analysis, they were exposed to air immediately prior to analysis and during analysis, which could lead to oxidation. HAADF-STEM imaging of the as prepared nanoparticles (discussed below and shown in Figure 56) revealed likely surface oxidation of the nanoparticles, so it does appear that these nanoparticles are susceptible to oxidation.

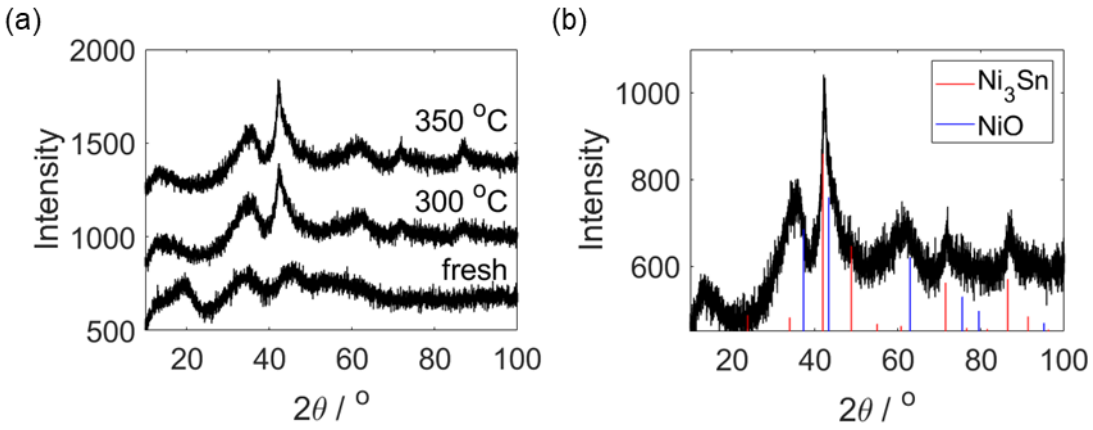

Figure 54: (a) pXRD patterns of SnNi sequential addition nanoparticles for the as prepared ('fresh') nanoparticles and after reduction at 300 °C and 350 °C and (b) the nanoparticles after reduction at 350 °C compared to reference patterns of Ni_3Sn (cubic, auricupride structure) and NiO.

Whilst ICP-OES can provide the bulk molar ratio of Ni:Sn, it should be noted that it does not provide the elemental composition of individual nanoparticles. Therefore, there is the potential for there to be significant variation in the ratios of individual nanoparticles, with the most extreme situation being the formation of separate monometallic nickel and tin nanoparticles. Therefore, to confirm that bimetallic SnNi nanoparticles have been successfully synthesised, and to obtain a distribution of Ni:Sn molar ratios, a particle specific technique, such as STEM-EDX, is required.

STEM-EDX is distinct from EDX analysis whilst operating in TEM mode. In TEM mode, it is only possible to obtain an EDX spectrum of the whole field of view, which means that the spectrum will

provide the average Ni:Sn ratio of all nanoparticles in the field of view. Therefore, TEM-EDX, like with ICP analysis, can only provide a bulk Ni:Sn ratio. In STEM mode, the electron beam is concentrated to a point on the surface of the sample, and so it is possible to obtain an EDX spectrum of a specific point in the field of view and therefore of an individual nanoparticle. Consequently, STEM-EDX analysis permits confirmation of the formation of SnNi bimetallic nanoparticles and provides a distribution of Ni:Sn ratios.

Figure 55 shows the distribution of Ni:Sn molar ratios based on STEM-EDX analysis of individual nanoparticles prepared *via* the sequential addition method. The average Ni/Sn molar ratio was found to be 2.5 ± 0.9 and is close to the average determined by ICP analysis (2.9 ± 0.1), although the distribution is broader, as may be expected since ICP is a bulk technique that would average variations between individual nanoparticles. It should be noted that the data reported here are for a sample that was plasma cleaned prior to analysis. A set of data that was acquired without plasma cleaning was found to exhibit a lower Ni:Sn molar ratio, however organic contaminants (*e.g.* capping agent) were thought to be interfering with measurement (see experimental).

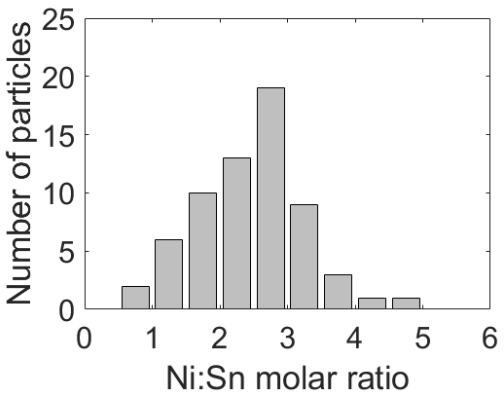

Figure 55: The distribution of Ni:Sn molar ratios for the small SnNi nanoparticles, as determined by STEM-EDX analysis of individual nanoparticles

STEM imaging can also be useful for obtaining more detailed images, since a high angle annular dark field (HAADF) camera can be used, which provides higher contrast. The increased contrast is illustrated in Figure 56a, where it can be seen that the nanoparticles have a core-shell structure, likely due to oxidation of the surface of the nanoparticles since they were exposed to air during sample storage.

Additionally, whilst operating the microscope in STEM mode, it is possible to use EDX analysis to obtain elemental maps, which show the distribution of the chosen elements across the nanoparticles. STEM-EDX analysis was used to obtain elemental maps of the nanoparticles produced here and it can be seen that both nickel and tin are present in the nanoparticles (Figure

56b). However, due to the small size of the nanoparticles, the resolution was not high enough to obtain maps with sufficient detail to see the distribution of the metals within the nanoparticles.

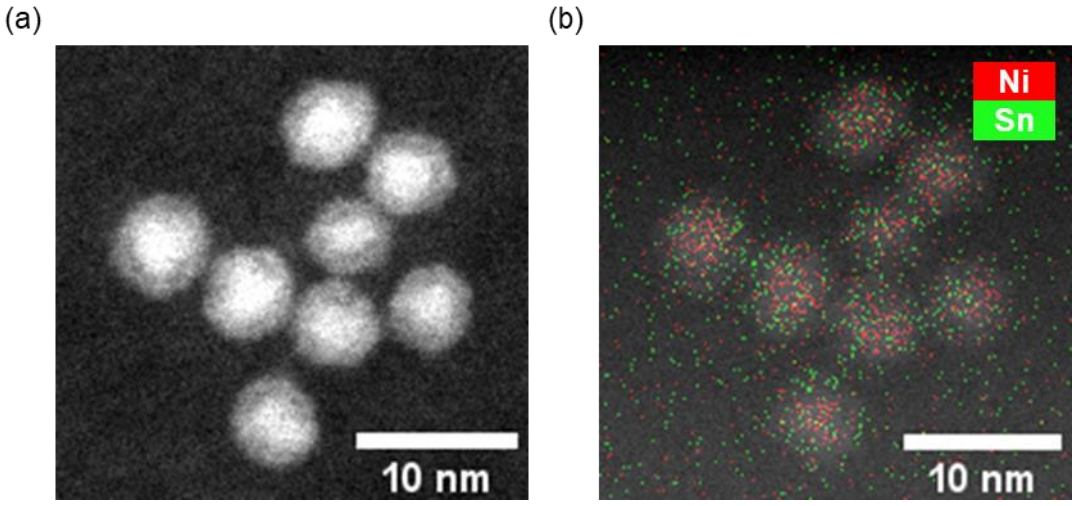

Figure 56: (a) HAADF-STEM image of the sequential addition SnNi nanoparticles and (b) elemental mapping

The SnNi sequential addition nanoparticles were also analysed using near ambient pressure X-ray photoelectron spectroscopy (NAP-XPS), with the results shown in Figure 57. The Ni 2p spectra (Figure 57a and b) were recorded at 1100 eV and 1490 eV to probe different depths into the nanoparticles (kinetic energies (KE) of around 200 eV and 600 eV, corresponding to inelastic mean free paths (IMFP) of roughly 0.77 nm and 1.3 nm respectively[4]). The spectra for the as synthesised nanoparticles (room temperature, high vacuum) both have very little signal, which is likely due to the presence of large quantities of capping agent (or synthesis agents including entrained solvent) on the surface of the nanoparticles. Heating the sample to 300 °C in 1 mbar of H_2 (to mimic the conditions of the reduction step carried out prior to catalysis), results in the appearance of a peak at around 852.6 eV, which corresponds to the Ni $2p_{3/2}$ peak for nickel metal.[5] The corresponding Ni $2p_{1/2}$ peak (not shown in the figure) was also observed at around 869.8 eV. Heating the sample in hydrogen is likely to result in the removal of some capping agent, as seen by the significant decrease in the C 1s signal (Figure 57e) and the disappearance of the weak N 1s peak (Figure 57d). This confirms that it is the presence of capping agent that is preventing any signal from nickel in the as prepared nanoparticles. The sample was then cooled to 180 °C, still in 1 mbar of H_2, to mimic the temperature at which catalysis is carried out and it can be seen that the nickel remains metallic.

The Sn 3d spectra (Figure 57c and d) were recorded at two photon energies that resulted in kinetic energies, and therefore IMFP's, similar to that obtained for the nickel spectra (photon energies of 700 eV and 1100 eV to give KE's of roughly 200 eV and 600 eV). The more surface sensitive spectrum for the as prepared nanoparticles (room temperature, high vacuum) does not contain any

peaks, which is consistent with the results of the nickel spectra and is again likely due to the presence of large amounts of capping agent. However, in the spectrum recorded at higher kinetic energy, there are two weak peaks present at 486.7 eV and 495.2 eV, which correspond to the Sn $3d_{5/2}$ and Sn $3d_{3/2}$ peaks of oxidised tin (SnO_2) respectively.[5] This provides an additional explanation for the absence of nickel in both the lower and higher kinetic energy spectra; tin is coating the surface of the as prepared nanoparticles and so in combination with large amounts of capping agent, it is not possible to get any significant nickel signal. The presence of a tin-based surface would fit well with the synthesis method employed since it involves the formation of nickel nanoparticle seeds followed by the addition of a tin precursor, which is expected to deposit on the nickel to form an overlayer. Additionally, the presence of an oxidised surface is consistent with the HAADF-STEM imaging which also evidenced oxidation of the surface of the nanoparticles.

Heating the sample to 300 °C in 1 mbar of H_2 results in strong peaks in both the lower and higher kinetic energy spectra, with the main peaks centred at 484.7 eV and 493.1 eV corresponding to the Sn $3d_{5/2}$ and Sn $3d_{3/2}$ peaks for metallic tin.[5] However, especially in the lower kinetic energy, more surface sensitive spectrum, there is a significant tail on the higher binding energy side of the peak, suggesting that some oxide remains on the surface of nanoparticles and that the tin is not fully reduced. Cooling the sample to 180 °C in 1 mbar of H_2 results in an increase in the shoulder that corresponds to oxidised tin. Since the sample was kept under reducing conditions (1 mbar H_2), it is unclear as to the source of the oxygen. It is important to note that the standard reaction conditions have a significantly higher amount of hydrogen present (~1000 mbar vs 1 mbar), so it is unclear whether the oxidation observed here would still occur. However, this does highlight the ease at which the tin can be oxidised and suggests that it may be particularly susceptible to oxidation.

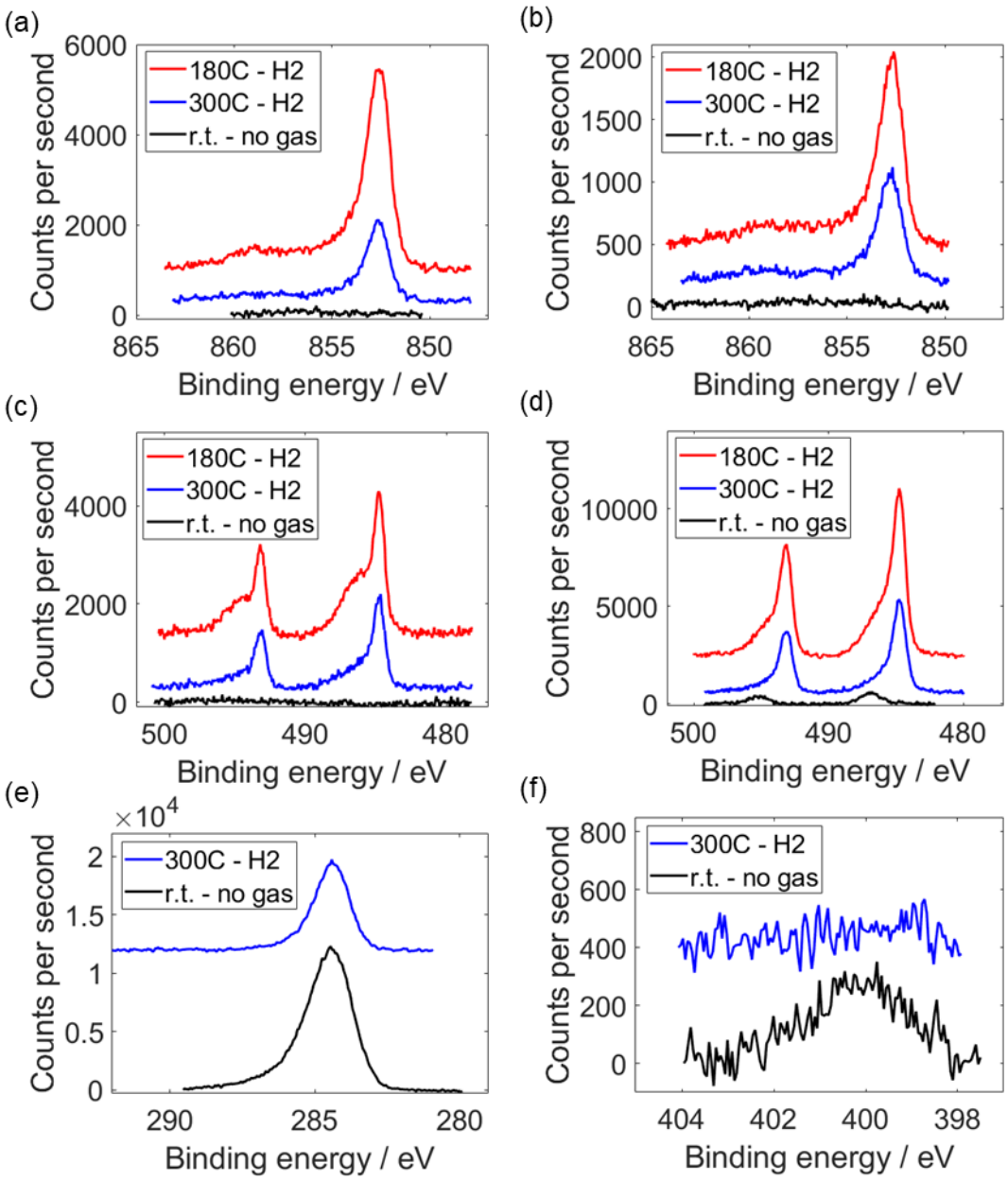

Figure 57: NAP-XP spectra of the SnNi sequential addition nanoparticles deposited on a silicon wafer recorded at room temperature under high vacuum ('r.t. – no gas'), at 300 °C under 1 mbar of H_2 ('300C – H2') and at 180 °C under 1 mbar of H_2 ('180C – H2'); (a) Ni 2p spectra recorded with a photon energy (E_{ph}) of 1100 eV (kinetic energy (KE) of 250 eV), (b) Ni 2p spectra recorded with a E_{ph} of 1490 eV (KE of 640 eV), (c) Sn 3d spectra recorded with a E_{ph} of 700 eV (KE of 220 eV), (d) Sn 3d spectra recorded with a E_{ph} of 1100 eV (KE of 620 eV), (e) C 1s spectra recorded at 1100 eV and (f) N 1s spectra recorded at 1100 eV. Binding energy was corrected as described in the experimental section (Chapter 2).

The Ni:Sn ratios were then determined by comparing the corrected peak areas of similar kinetic energy spectra. At 300 °C in 1 mbar of H_2, the most surface sensitive measurement reveals a Ni:Sn molar ratio of around 3:1, which then increases to around 4:1 when the sample is cooled to 180 °C. For the higher kinetic energy spectra, a significantly higher amount of tin is found at both 300 °C and 180 °C, with a Ni:Sn molar ratio of around 0.4 found in both cases. This indicates that the top

surface of the nanoparticles consists of a nickel rich Sn-Ni phase, which is then followed by a section of the nanoparticle that consists almost entirely of tin. HRTEM images suggest the centre 1 – 2 nm of the nanoparticles consists of nickel or nickel oxide, and so the core of the nanoparticles is then likely to consist of mostly nickel. A representation of the proposed structure for the nanoparticles based on these results is shown in Figure 58.

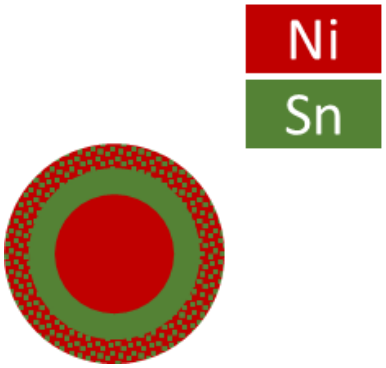

Figure 58: A representation of the proposed structure for the SnNi sequential addition nanoparticles after reduction at 300 °C and at the temperature at which catalysis is carried out (180 °C) based on the NAP-XPS results, with nickel shown in red and tin shown in green

4.2 Synthesis of larger (~10 nm) colloidal nickel nanoparticles without a phosphine capping agent

The nanoparticles synthesised in Section 4.1 were all ~4 nm in size, which meant that analysis by key techniques (*e.g.* TEM/STEM, pXRD) was challenging. Since the purpose of synthesising the colloidal nanoparticles was to be able to analyse them in greater detail, the smaller nanoparticles were not ideal candidates. Therefore, the synthesis of larger analogues was attempted. The synthesis of larger nickel nanoparticles with a narrow particle size distribution typically requires the use of sulfur or, more commonly, phosphorus containing capping agents, with tri-*n*-octylphosphine (TOP) frequently used in the literature.[6-8] However, both sulfur and phosphorus will interact strongly with the surface of the nanoparticles, and so may impact catalysis or even lead to complete inactivity. Additionally, phosphorus incorporation has been noted when using TOP as a capping agent.[9-14] Therefore, for this work it was hoped the use of phosphorus or sulfur containing capping agents could be avoided. The synthesis of larger nickel nanoparticles (~8 nm) with only an amine capping agent was reported by Hensen *et al.*[15] using a seeded growth based method. However, even under the optimised conditions, there was clear evidence of a broader than desirable particle size distribution, which could lead to difficulties achieving an even addition of tin given the differing sizes of the preformed nickel nanoparticles. Whilst this seeded growth method led to a broader distribution of particle sizes than ideal, it did show some promise and identified that one of the key

reasons for improved results in their optimised synthesis was the rapid decomposition of the additional nickel precursor, which they achieved by heating to 220 °C. Here, an alternative seeded growth approach was attempted where additional nickel precursor will be co-fed with additional reducing agent into a solution of preformed nickel seeds in attempt to rapidly reduce the nickel precursor as it is added to the solution and so achieve even addition to the seeds.

4.2.1 Synthesis of larger nickel nanoparticles via seeded growth with the addition of a Ni(II) pre-cursor ($Ni(acac)_2$)

The seeds for the larger nanoparticles were formed by carrying out the reaction described in Section 4.1.1, which leads to the formation of nickel nanoparticles that have a size of ~4 nm. The additional nickel was added to the seeds using a $Ni(acac)_2$ based pre-cursor. $Ni(acac)_2$ is not soluble in oleylamine/oleic acid at room temperature, however it has been found that by heating this mixture at 110 ^{o}C overnight, the nickel pre-cursor remains soluble once it is cooled to room temperature. Whilst the exact complex or species that forms during the overnight reaction is unknown, it is likely that the oleylamine/oleic acid is interacting with the $Ni(acac)_2$ to form a new species, since a variety of species are known to form under similar conditions with $Pd(acac)_2$ and $Pt(acac)_2$.[16, 17] Since the nickel pre-cursor was in the Ni(II) oxidation state and needed to be reduced in order to be added to the seeds as nickel metal, a solution of BTB in oleylamine was co-fed with the Ni pre-cursor into the seed reaction mixture. Figure 59a and b show a typical TEM image of the nanoparticles formed during this reaction and the corresponding particle size distribution. The average particle size was found to be 6 ± 2 nm, however the particle size distribution obtained was bimodal and when compared to the nanoparticle size distribution obtained for a typical seed reaction (Figure 59c), it is clear that nanoparticles the size of nickel seeds are present, alongside a set of larger nickel nanoparticles. This suggests that along with a seeded growth-based mechanism, there is some nucleation of the additional nickel precursor, which is leading to the formation of new nanoparticles. Therefore, a seeded growth mechanism is unlikely to be a viable option for synthesising larger nickel nanoparticles.

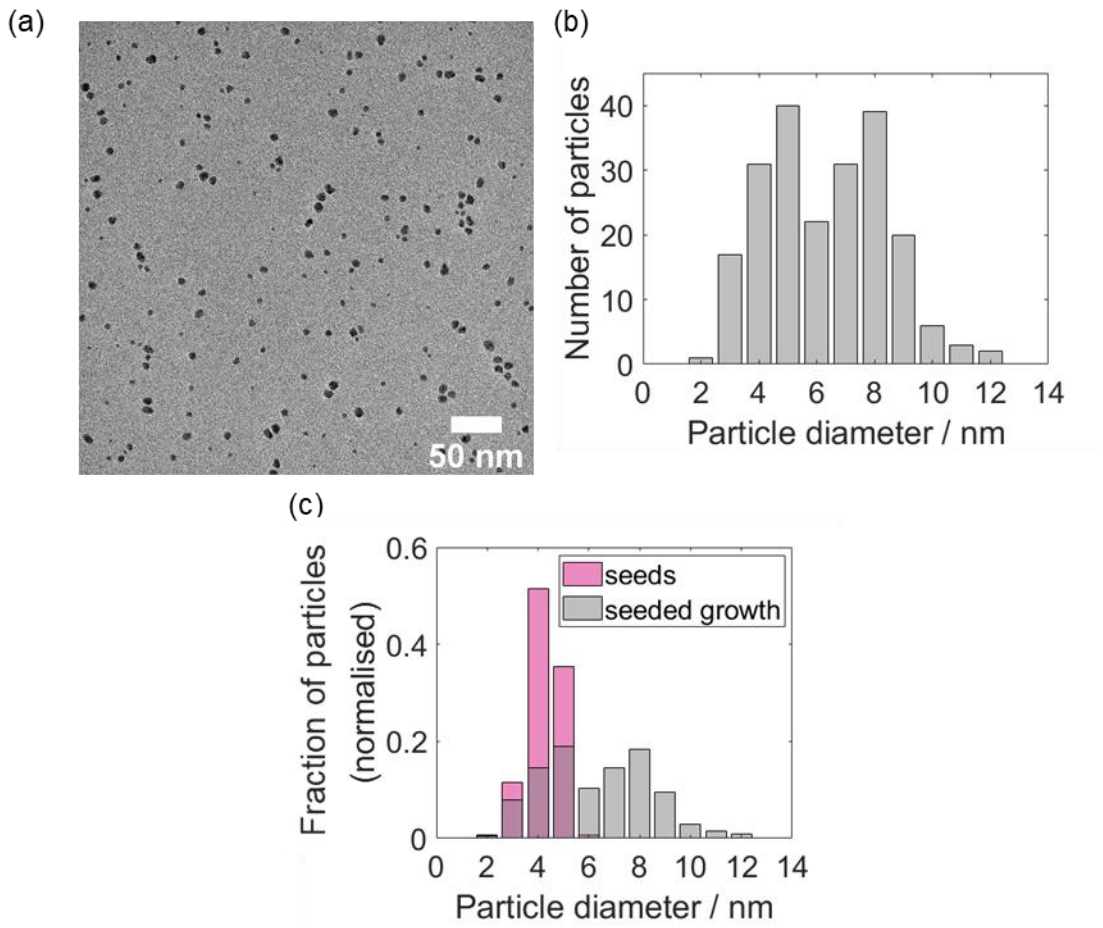

Figure 59: (a) TEM image of the seeded growth nickel nanoparticles, (b) the corresponding particle size distribution and (c) a comparison of the particle size distribution of the nickel nanoparticle seeds to the particle size distribution of the seeded growth nickel nanoparticles. The number of particles were normalised in (c) to facilitate comparison of the distributions.

4.3 Synthesis of larger colloidal nickel and tin-nickel nanoparticles (~10 – 15 nm) using a phosphine capping agent

Whilst it is desirable to synthesise larger nickel nanoparticles without the use of a phosphine capping agent, as discussed above, this has so far been unsuccessful, therefore, larger nickel nanoparticles were prepared based on a synthesis reported by Mézailles *et al.*[7] that used TOP as a capping agent. A reaction temperature of 210 °C, rather than the 220 °C reported in the paper, was employed, since the reaction was found to bump excessively at temperatures higher than 210 °C.

4.3.1 Synthesis of larger nickel nanoparticles (amorphous)

The yield of the reaction (68.4 ± 0.9 %), as determined by ICP-OES, was found to be significantly higher than the reaction for the small nickel nanoparticles, which had a yield of <40 %. TEM was then used to characterise the nanoparticle size and size distribution (Figure 60). The nanoparticles

had a narrow size distribution, with an average particle size of 11.6 ± 1.3 nm. This particle size is slightly lower than that obtained by Mézailles *et al.*[7] who reported an average particle size of 15 ± 1 nm under similar conditions (but this could be due to the small change in temperature). The particle size distributions were consistent and narrow.

HRTEM imaging of the nanoparticles (Figure 60c) revealed some important information; the nanoparticles were amorphous, not crystalline. Whilst the authors did not provide a pXRD pattern or HRTEM image of the nanoparticles produced with the same synthetic conditions used here, they did provide a pXRD pattern that corresponded to crystalline nickel metal for a different set of nanoparticles. Crucially, the nanoparticles for which the authors reported this pXRD pattern, were produced with a significantly lower TOP:Ni ratio (0.8 eq. of TOP compared to 4 eq. of TOP). The TOP:Ni ratio has been found to play a significant role in the extent of phosphorus incorporation during nickel nanoparticle synthesis, with higher amounts of TOP leading to the production of amorphous nickel phosphide nanoparticles.[7, 9-11] Therefore, the amorphous morphology of the nanoparticles produced here is likely explained by the formation of an amorphous nickel phosphide phase and also suggests significant quantities of phosphorus have been incorporated into the nanoparticles.

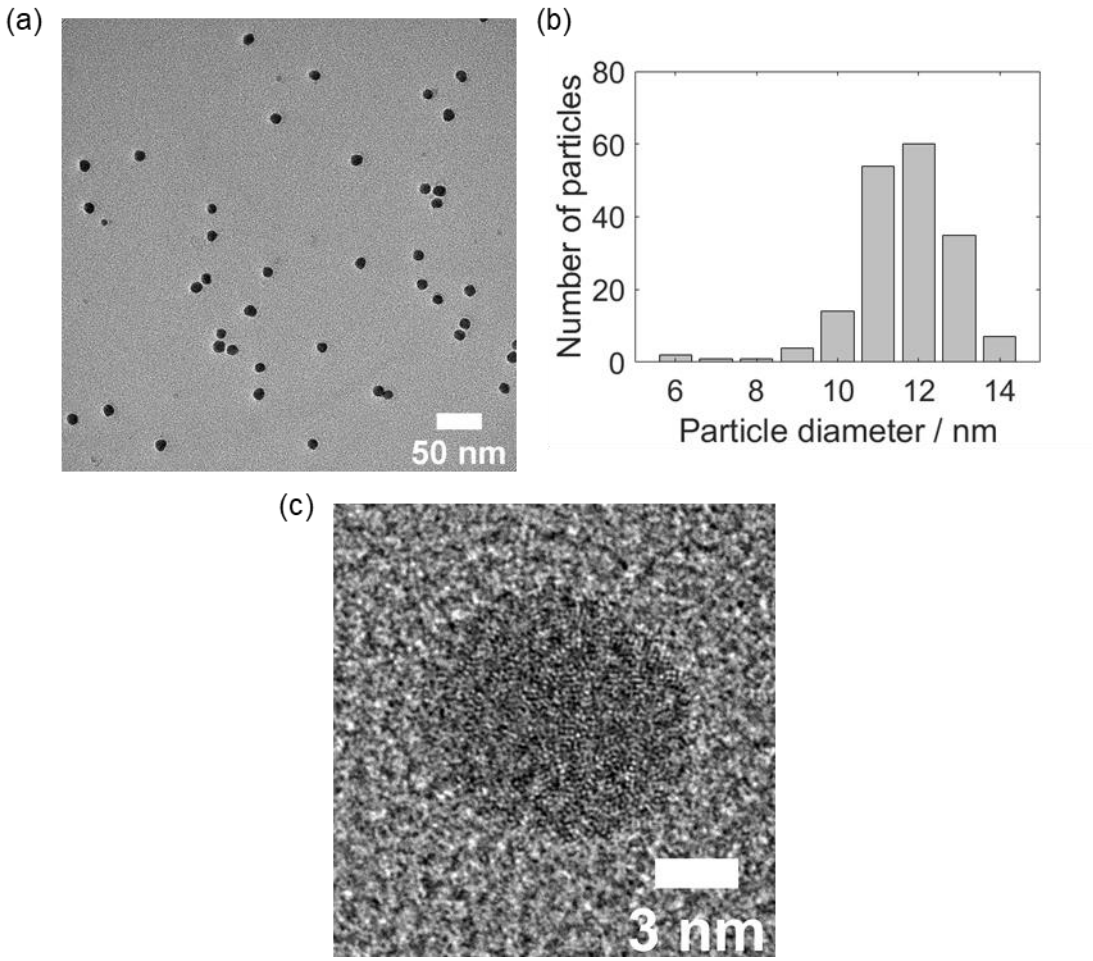

Figure 60: (a) TEM image of the larger amorphous nickel nanoparticles, (b) the corresponding particle size distribution and (c) a HRTEM image illustrating the amorphous structure of the nanoparticles

The structure and composition of the nanoparticles was further investigated using pXRD (Figure 61). The pattern for the as prepared nanoparticles contained one broad reflection centred at around 45 °. The broadness of the reflection is indicative of a poorly crystalline structure, which is consistent with the HRTEM images of these nanoparticles that also showed an amorphous structure. Additionally, the position of the reflection, in combination with the broadness, fits well with the pattern reported in the literature for amorphous nickel phosphide nanoparticles prepared using similar methods.[9, 10] Reduction of the nanoparticles at 300 °C resulted in the introduction of several additional reflections as well as slightly sharper reflections. The slight sharpening of the reflections suggests some small regions of crystallinity have formed upon reduction, however since the reflections are still relatively broad, it suggests only partial crystallisation and very small regions of crystallinity. The reflections observed in the pattern for the reduced nanoparticles fit well with Ni_2P and NiO (Figure 61b). Although the sample was reduced, it was exposed to air immediately prior to and during measurement which may provide an explanation for the presence of oxidised nickel. The presence of Ni_2P fits well with the fact that this synthesis appears to result in significant

phosphorus incorporation, such that the as synthesised nanoparticles are amorphous nickel phosphide. Reduction of these nanoparticles has then led to the amorphous nickel phosphide partially crystallising to form Ni_2P.

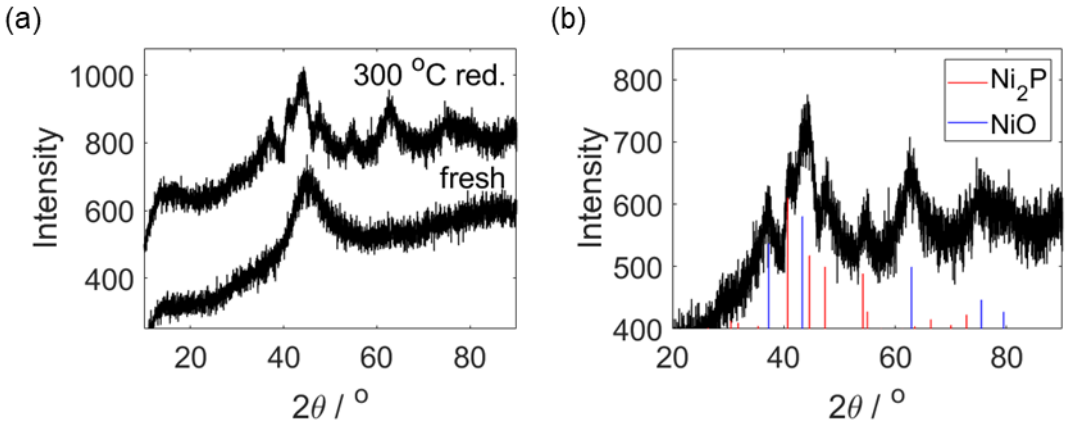

Figure 61: (a) pXRD patterns for the as prepared ('fresh') amorphous nickel phosphide nanoparticles after deposition onto a silicon wafer, as well as after reduction at 300 °C and (b) a comparison of the pattern for the nanoparticles after reduction at 300 °C to reference patterns for Ni_2P (red)[18] and NiO (blue).[19] The patterns are vertically offset for clarity.

The amorphous nickel phosphide nanoparticles were then analysed using NAP-XPS (Figure 62). The Ni 2p spectra (Figure 62a and b) were recorded with photon energies of 1100 eV and 1650 eV (KE's of ~200 eV and 800 eV respectively). The lower kinetic energy spectrum for the as synthesised nanoparticles (room temperature, high vacuum) contains two main peaks; a weak peak at 852.4 eV and a stronger peak at 855.8 eV. The peak at 852.4 eV fits well with the Ni $2p_{3/2}$ peak for metallic nickel,[5] indicating that the surface of the as prepared nanoparticles does contain some amount of metallic nickel. It should also be noted that despite a small charge transfer from nickel to phosphorus in nickel phosphide materials, this typically does not result in an observable of shift of the peak compared to metallic nickel.[20-22] The assignment of the larger peak at 855.6 eV is less certain and frequently debated in the literature. It is often assigned to Ni^{3+} species,[23, 24] possibly as part of a structure such as Ni_2O_3, however it has also been proposed to correspond to lattice distortions that form due to vacancies in nickel oxide[25] or nickel hydroxide species.[26] Marcu *et al.*[27] found that increasing amounts of phosphorus on the surface of nickel oxide particles corresponded to an increase in the intensity of a peak at 855.6 eV, suggesting the presence of phosphorus is promoting the formation of this species. Ultimately, the presence of this peak, along with the fact that it is relatively strong compared to the metallic nickel peak in the lower kinetic energy spectrum, suggests a significant portion of the surface is higher oxidation state nickel in the as prepared nanoparticles. In the higher kinetic energy Ni 2p spectrum, the Ni $2p_{3/2}$ peak at 852.6 eV which corresponds to metallic nickel, or $Ni^{\delta+}$ as part of nickel phosphide, is significantly stronger compared

to the Ni $2p_{3/2}$ peak at around 855.8 eV that corresponds to oxidised nickel species. This indicates that it is only the top surface that has significant oxidation, and that the bulk of the nanoparticles remain as nickel metal or nickel phosphide.

The sample was then heated to 300 °C in 1 mbar of hydrogen to mimic the conditions used in the reduction step carried out prior to catalysis. In both the lower and higher kinetic energy spectra, this results in an increase of the peak corresponding to metallic nickel or $Ni^{\delta+}$ compared to the peak that corresponds to oxidised nickel. However, particularly for the lower kinetic energy spectrum, the peak corresponding to oxidised nickel species does still remain and so the surface is not fully reduced. The sample was then cooled to 180 °C, still in 1 mbar of H_2, since this is the temperature at which catalysis is carried out, and in both the lower and higher kinetic energy spectra, there are no significant changes in the extent of reduction.

The P 2p spectra (Figure 62c and d) were also recorded with different photon energies to probe different depths into the nanoparticles (photon energies of 550 eV and 1100 eV corresponding to KE's of ~400 eV and ~1000 eV respectively). The lower kinetic energy spectrum for the as prepared nanoparticles (room temperature, high vacuum) contains two main peaks; one centred at 133 eV and one at 129.3 eV. The P $2p_{3/2}$ and P $2p_{1/2}$ peaks are only separated by around 0.84 eV,[5] meaning that they commonly overlap and that it is likely that the two peaks observed here actually consist of contributions from both the P $2p_{3/2}$ and P $2p_{1/2}$ peaks. The higher binding energy peak at around 133 eV has been previously assigned as phosphorus as part of the TOP capping agent interacting with surface of the nanoparticles, whereas the lower binding energy peak at 129.3 eV was assigned as $P^{\delta-}$ species as part of nickel phosphide.[28] This therefore confirms the presence of nickel phosphide on the surface of the nanoparticles. The higher kinetic energy spectrum contains the same two peaks, however there is a significant increase in the intensity of the phosphide peak when compared to the intensity of the capping agent peak, which is consistent with the formation of amorphous nickel phosphide nanoparticles. If the bulk of the nanoparticles consists of nickel phosphide and TOP is only on the surface of the nanoparticles, then probing deeper into the nanoparticles would result in an increase in the amount of phosphide species observed when compared to the capping agent.

Heating the sample to 300 °C in 1 mbar of H_2, followed by subsequent cooling to 180 °C, had little effect on any of the P 2p spectra, apart from slight increases in the intensity of the phosphide peak compared to the capping agent. Possible explanations for this slight increase include the heating of the sample resulting in increased phosphorus incorporation to the nanoparticles, migration of phosphorus from the bulk of the nanoparticles to the surface or a decrease in the amount of

capping agent present on the nanoparticles (which would attenuate the signals). The intensity of the C1s peak (Figure 62e) and the weak N1s peak (Figure 62f) remain relatively unaltered, which suggests that a decrease in capping agent can likely be ruled out as a possible explanation for the relative increase in the phosphide peak intensity. Carenco *et al*.[28] found that, in the presence of a Ni(111) surface, temperatures of as low as 150 °C were enough to decompose the phosphine capping agent used to prepare these nanoparticles (TOP), leading to phosphorus incorporation. Therefore, whilst migration of phosphorus from the bulk cannot be ruled out, additional phosphorus incorporation is likely to be occurring under the conditions employed here.

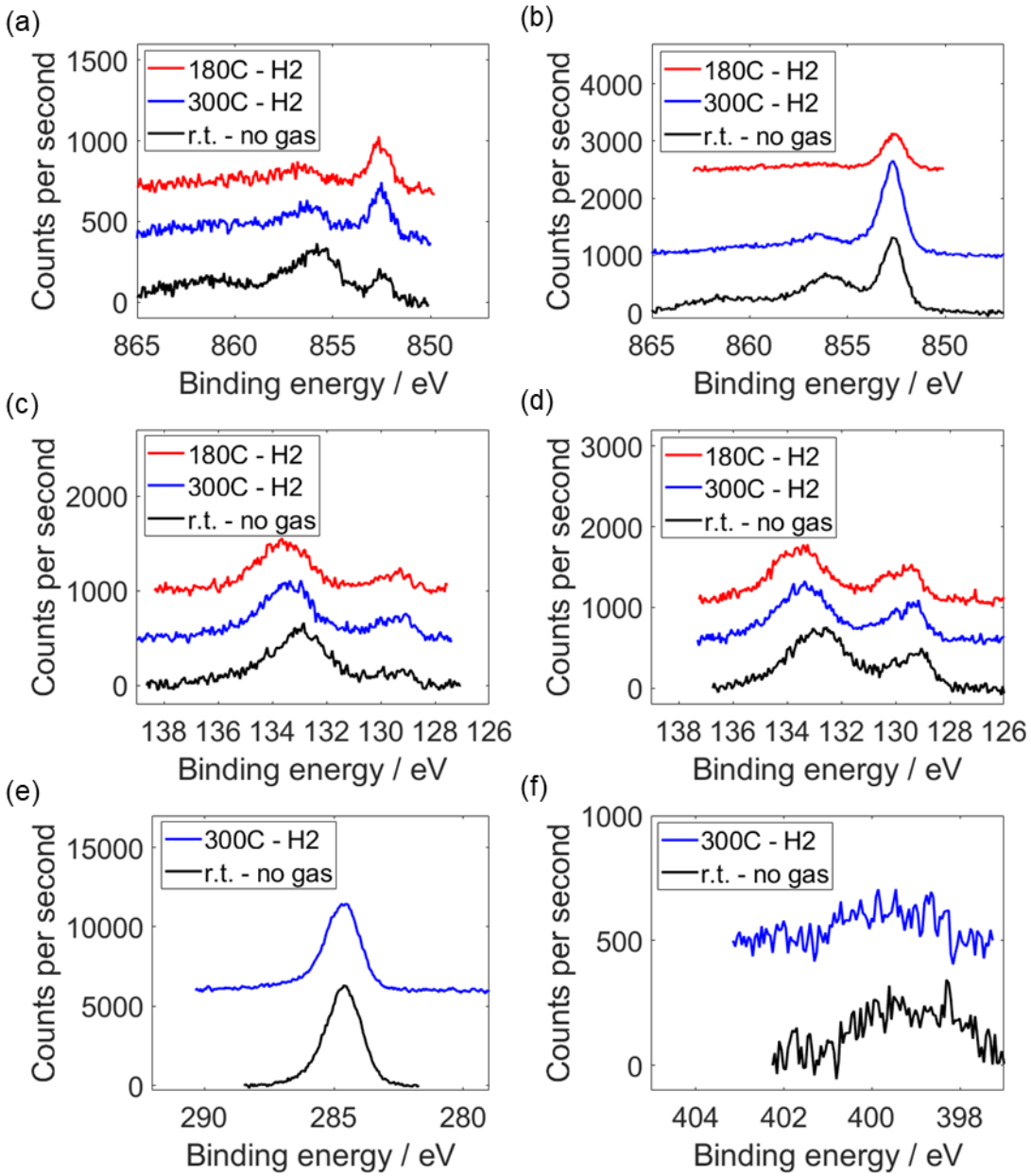

Figure 62: NAP-XP spectra of the amorphous nickel phosphide nanoparticles deposited on a silicon wafer recorded at room temperature under high vacuum ('r.t. – no gas'), at 300 °C under 1 mbar of H_2 ('300C – H2') and at 180 °C under 1 mbar of H_2 ('180C – H2'); (a) Ni 2p spectra recorded with a photon energy (E_{ph}) of 1100 eV (kinetic energy (KE) of 250 eV), (b) Ni 2p spectra recorded with a E_{ph} of 1490 eV (KE of 640 eV), (c) P 2p spectra recorded with a E_{ph} of 550 eV (KE of 420 eV) (d) P 2p spectra recorded with a E_{ph} of 1100 eV (KE of 970 eV) (e) C 1s spectra recorded at 1100 eV and (f) N 1s spectra recorded at 1100 eV. Binding energy was corrected as described in the experimental section (Chapter 2).

The presence of phosphorus in the nanoparticles was further investigated using Raman spectroscopy. Arrigo *et al.*[11] found that if there was enough phosphorus incorporation for the produced nanoparticles to form amorphous nickel phosphide, it was possible to detect a peak in the Raman spectrum at around 600 cm^{-1} that confirmed the presence of Ni-P bonds in the sample. Therefore, since amorphous nanoparticles were produced suggesting significant phosphorus

incorporation, the nanoparticles were analysed using Raman spectroscopy (see Figure 63). Unfortunately, the only signals detected in the region corresponded to peaks produced by the silicon wafer that the nanoparticles were deposited on. There are a number of possible explanations for the absence of the peak, such as the amount of phosphorus incorporation in the nanoparticles produced here is lower than that of Arrigo *et al.*[11] or the assignment of the peak at 600 cm^{-1} to Ni-P bonds is inaccurate since it was based on the Raman spectrum of $NiPS_3$ where the authors assign the peak at ~600 cm^{-1} to part of a doubly-degenerate pair of bands for the $\nu_d(PS_3)$ vibration.[29]

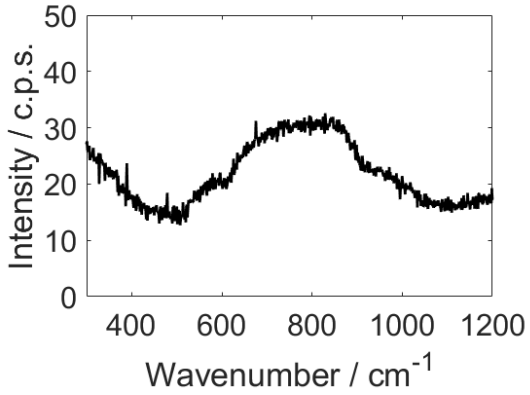

Figure 63: Raman spectrum of the amorphous nickel nanoparticles deposited on a silicon wafer for analysis.

4.3.2 Synthesis of larger amorphous tin-nickel nanoparticles

The incorporation of phosphorus into the nanoparticles is, as discussed above, likely to affect catalytic performance, and may also complicate structural analysis. However, as discussed in Chapter 6, these amorphous nanoparticles were still found to be active for furfural hydrogenation, so it was decided to continue with this synthetic route and modify the synthesis to produce Sn-doped nickel phosphide nanoparticles. The synthesis was carried out in a similar way to the sequential addition method described previously for the smaller SnNi bimetallic nanoparticles (Section 4.1.3), since that method was found to give a narrower particle size distribution than the co-addition method. Therefore, in this synthesis, the nickel phosphide nanoparticles were first formed by carrying out the standard reaction and then a solution of the Sn(II) precursor dissolved in 1-octadecene was added using a syringe pump. A Ni:Sn ratio of 3:1 was chosen to match the Ni:Sn ratios used for the smaller SnNi nanoparticles discussed in Section 4.1. ICP-OES analysis (Table 8) revealed the nanoparticles had a 35.5 ± 0.5 % yield and a Ni/Sn molar ratio of 4.19 ± 0.08 which is slightly higher than the targeted ratio, but acceptable for the intended purpose. A TEM image and the corresponding particle size distribution are shown in Figure 64. The average particle size was found to be 13.6 ± 1.4 nm, which means the nanoparticles have, as expected, a slightly larger

particle size than the nickel phosphide nanoparticles but maintain a narrow particle size distribution.

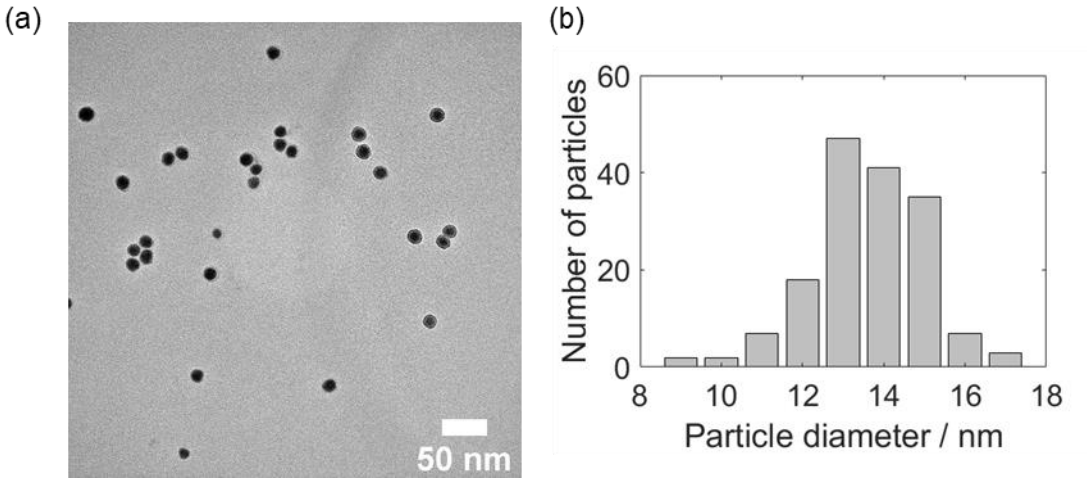

Figure 64: (a) TEM image of the larger SnNi (1:3) amorphous nanoparticles and (b) the corresponding particle size distribution

HAADF-STEM imaging of the nanoparticles revealed a core-shell structure, which was confirmed by STEM-EDX mapping and shows the nanoparticles have a nickel-based core and a tin-based shell (Figure 65). This fits well with the synthetic route chosen, since the nickel phosphide nanoparticles are first formed, followed by the addition of tin which is then deposited on the surface of the nickel phosphide nanoparticles. However, it should be noted that in the HAADF-STEM image, the core is brighter than the shell, which is not consistent with the shell consisting only of tin metal since tin is heavier than nickel and would appear brighter in the HAADF-STEM image. Therefore, the tin-based shell is likely to consist of either a tin oxide or phosphide.

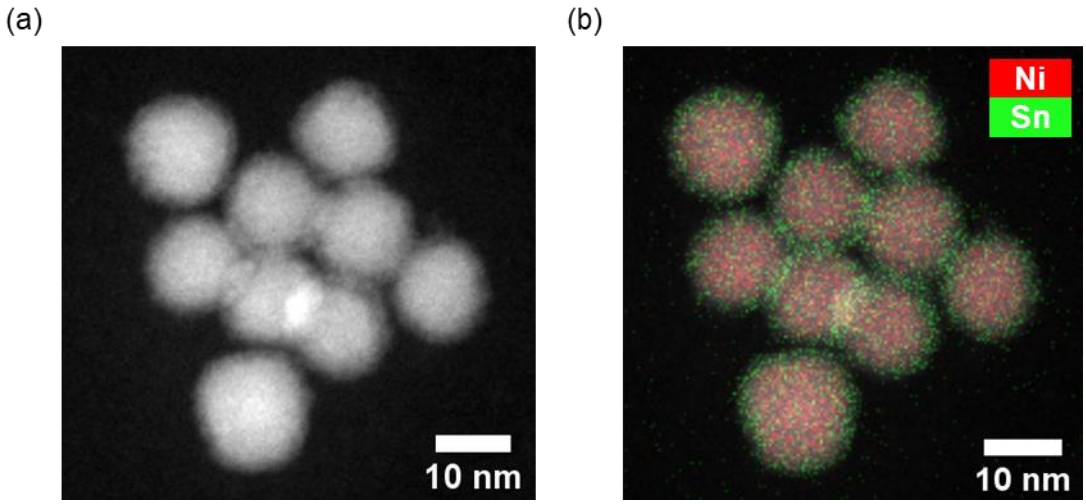

Figure 65: (a) HAADF-STEM image of the larger SnNi (1:3) amorphous nanoparticles and (b) elemental mapping

Figure 66a shows pXRD patterns for the as prepared nanoparticles as well as for nanoparticles after reduction at 300 °C and 400 °C. The pattern for the as prepared nanoparticles contains two broad reflections that appear at around 25 – 37 ° and 40 – 50 °, which confirms the poorly crystalline morphology of the nanoparticles and suggests that a substantial amount of phosphorus has been incorporated into the nanoparticles. The pattern for the nanoparticles that were reduced at 300 °C is very similar to the pattern of the as prepared sample, apart from the appearance of a slightly sharper reflection at 47.9 °, which suggests the sample is starting to crystallise. Increasing the reduction temperature to 400 °C produced a clear crystalline pattern. Several of the main reflections were found to fit well with Ni_3Sn_2, with the remaining key reflections tentatively assigned to $Ni_{10}SnP_3$ (see Figure 66b). A Rietveld refinement of the pattern for the nanoparticles reduced at 400 °C, based on Ni_3Sn_2 and $Ni_{10}SnP_3$, is shown in Figure 66c. The calculated pattern fits fairly well with experimental pattern, however there are some differences, particularly for the reflections that correspond to the $Ni_{10}SnP_3$ structure. This could be due to a variety of factors including small differences in the composition of the phase or effects due to strain caused by the small crystallite size of the phase. The Rietveld refinement estimated the sample composition to be 34 % Ni_3Sn_2 and 66 % $Ni_{10}SnP_3$. STEM-EDX mapping of the fresh nanoparticles showed a clear core-shell structure, with the centre composed of nickel and the shell consisting of a tin based phase. However, after reduction at 400 °C, both of the bulk phases identified by pXRD contained nickel and tin, which implies that reduction at 400 °C leads to the migration of tin from the surface to the bulk of the nanoparticles. Additionally, 66.0 % of the sample was composed of a phase that contained phosphorus ($Ni_{10}SnP_3$), which confirms that a significant amount of phosphorus is being incorporated into the nanoparticles. It should be noted however that prior to carrying out furfural hydrogenation, the catalyst is reduced at 300 °C and so the catalyst used for furfural hydrogenation is likely to be mostly amorphous, with some small crystalline regions. It should also be noted that, as discussed in Chapter 6, this catalyst was found to be inactive, and so the phases identified here may be inactive for furfural hydrogenation.

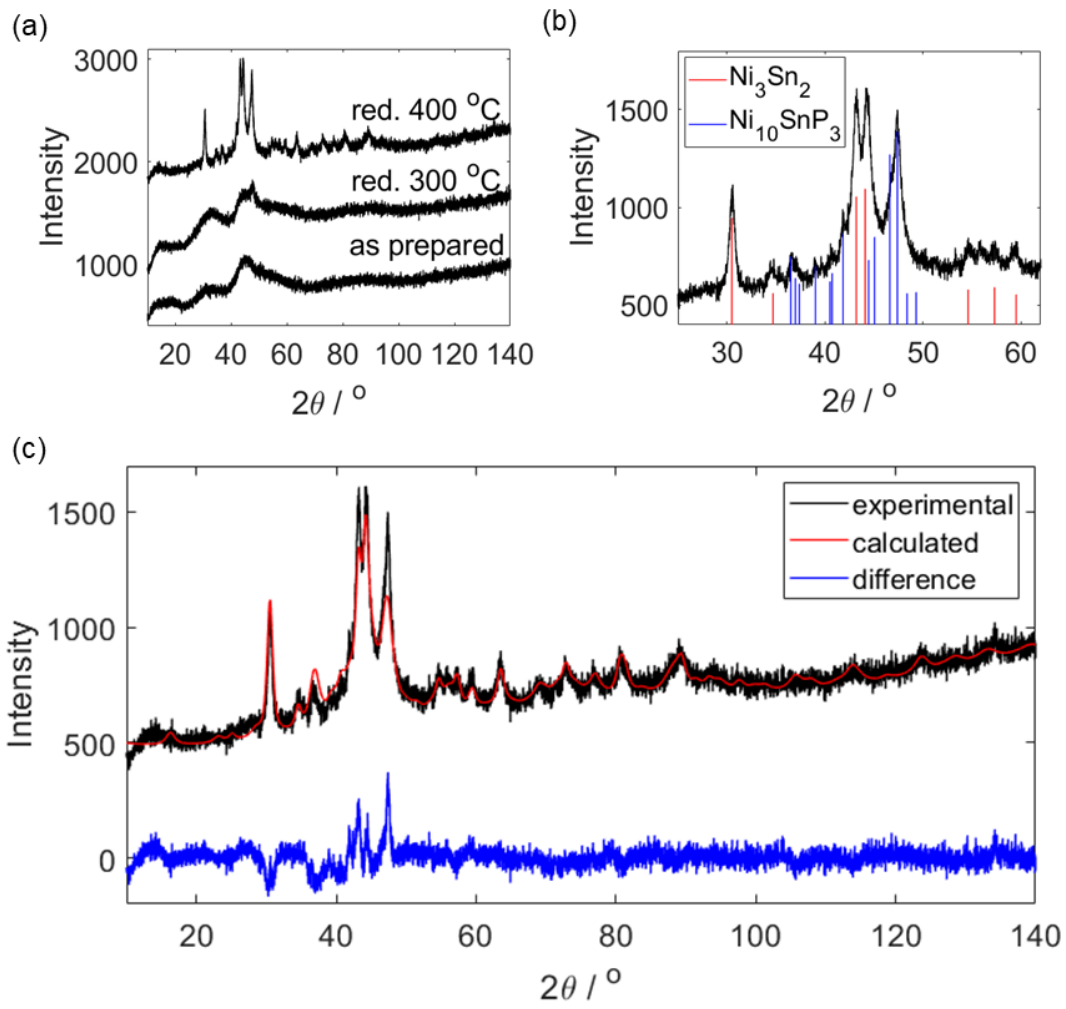

Figure 66: (a) pXRD of larger SnNi (1:3) amorphous nanoparticles; 'as prepared' refers to a sample where the nanoparticles were drop cast onto a silicon wafer, 'red. 300 °C' refers to a sample where the nanoparticles were reduced at 300 °C once deposited on the silicon wafer and 'red. 400 °C' refers to a sample where the nanoparticles were reduced at 400 °C once deposited on the silicon wafer. The data is vertically offset for clarity. (b) pXRD pattern of the nanoparticles reduced at 400 °C compared to reference patterns of Ni_3Sn_2 (red)[30] and $Ni_{10}SnP_3$ (blue).[31] (c) A Rietveld refinement of the pXRD pattern of the nanoparticles reduced at 400 °C, based on Ni_3Sn_2 and $Ni_{10}SnP_3$

Since the nanoparticles with a Ni:Sn ratio of 3:1 were found to be inactive for furfural hydrogenation, analogous nanoparticles were prepared with significantly lower amounts of tin (Ni:Sn molar ratios of 20:1 and 50:1). The nanoparticles with a nominal Ni:Sn molar ratio of 20:1 were found to have a yield (based on nickel) of 74 ± 1 % and a Ni/Sn molar ratio of 18.1 ± 0.7, which is close to the targeted ratio. Figure 67a and b show a TEM image and the particle size distribution for the nanoparticles prepared with a Ni:Sn ratio of 20:1. The nanoparticles were found to have an average particle size of 10.9 ± 1.2 nm, which is similar to the other nanoparticles prepared using this method. HRTEM imaging of the nanoparticles (Figure 67c) shows that the nanoparticles have an amorphous core with a polycrystalline shell. The amorphous core is consistent with the parent

nanoparticles forming amorphous nickel phosphide. The addition of Sn appears to lead to a crystalline phase forming on the surface of the nanoparticles, however considering the low tin loading in this sample (Ni:Sn molar ratio of 20:1), the thickness of the layer is inconsistent with a Sn only phase. Additionally, the centre of the nanoparticles is darker than the shell, which supports the prior suggestion that the outer layer is not consistent with a tin only phase as tin is heavier than nickel so should appear darker. In an attempt to identify the crystalline phase forming on the surface of the nanoparticles, a FFT of the image was carried out, with the result shown in Figure 67d. The d-spacing was found to be 0.21 nm, which fits well with NiO(200). FFT analysis of other HRTEM images of the nanoparticles commonly showed d-spacings of 0.21 nm and 0.24 nm (consistent with NiO(111)), and so the crystalline phase observed can reasonably be assigned as NiO. Therefore, the nanoparticles likely consist of an amorphous nickel phosphide core and a polycrystalline NiO shell and so does not suggest an answer to the question of where the Sn is located.

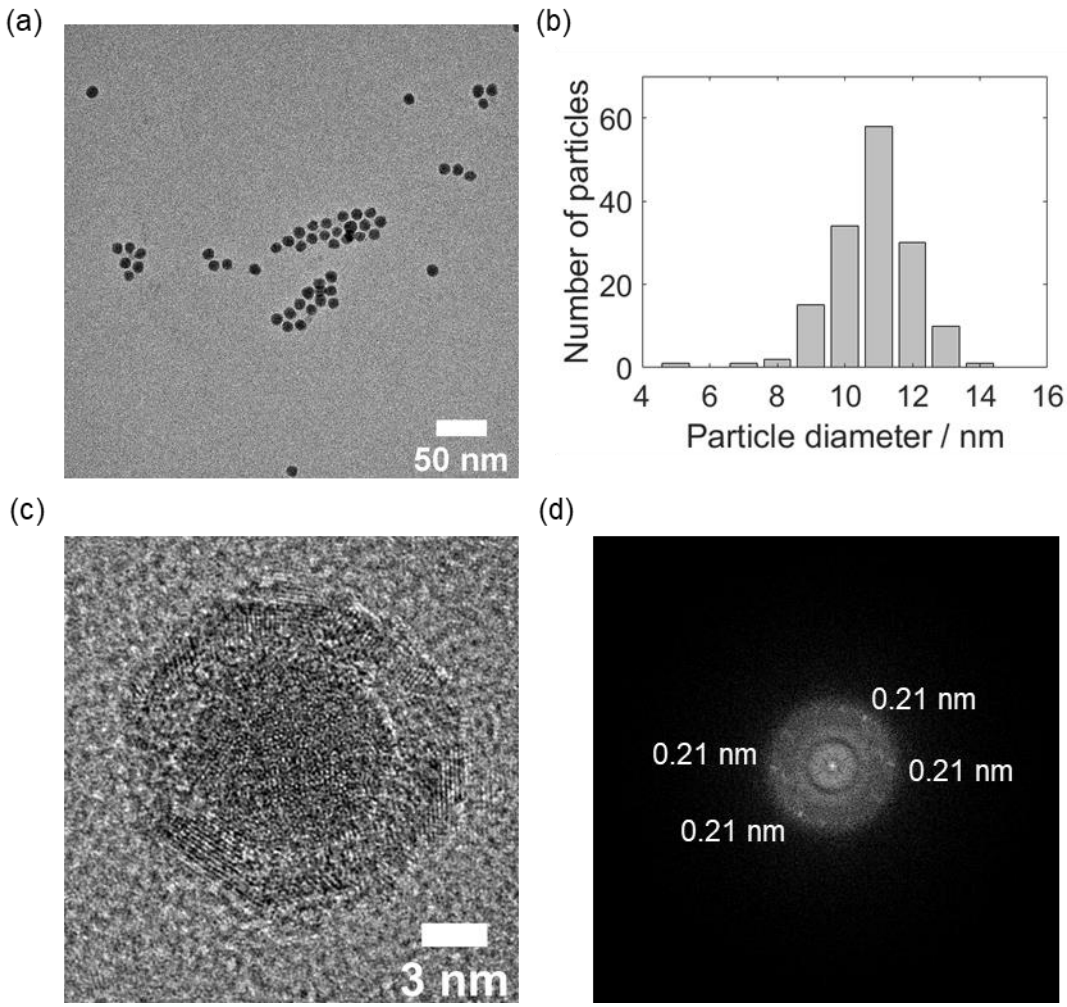

Figure 67: (a) TEM image of the larger SnNi (1:20) amorphous nanoparticles, (b) the corresponding particle size distribution, (c) a HRTEM image of the nanoparticles and (d) FFT of the image of the nanoparticle shown in (c)

HAADF-STEM imaging was consistent with the HRTEM imaging, showing the nanoparticles had a core-shell structure (Figure 68a). Elemental mapping was also carried using STEM-EDX (Figure 68b), however whilst it was clear that the nanoparticles contained both nickel and tin, the tin signal was too low to determine if it was sitting on the surface of the nanoparticles, like observed for the nanoparticles that had a Ni:Sn molar ratio of 3:1. However, since the nanoparticles were prepared in an analogous method, it is reasonable to assume that these nanoparticles when synthesized will also have a core composed of a nickel-based phase and shell composed of a tin-based phase.

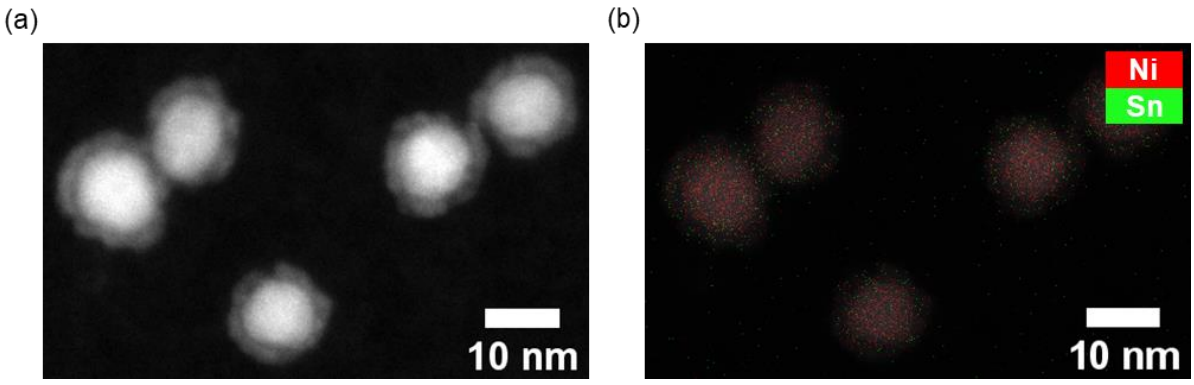

Figure 68: (a) HAADF-STEM image of the larger SnNi (1:20) amorphous nanoparticles and (b) elemental mapping

Figure 69 shows the pXRD patterns of the amorphous SnNi nanoparticles (Ni:Sn molar ratio of 20:1) after reduction at 300 °C and 400 °C. The pXRD pattern of the as prepared nanoparticles (*i.e.* drop cast onto the silicon wafer with no other treatment; pattern not shown here) contained a very broad reflection centred around 27 ° and some sharp reflections that corresponded to silicon (likely due to a defect in the silicon wafer). The broad reflection indicates that the as prepared nanoparticles are poorly crystalline, as expected based on the HRTEM images that indicate the nanoparticles consist of an amorphous core and a polycrystalline NiO shell. Reducing the nanoparticles at 300 °C led to the introduction of several reflections and these reflections sharpened after reduction at 400 °C. Most of the reflections fit well with those for NiO, however there is an unidentified reflection at around 48.9 °. Robinson *et al.*[10] also reported unidentified reflections at around 50 ° in the pXRD pattern of nickel nanoparticles prepared using TOP as a capping agent (although a higher reaction temperature of 350 °C was employed). These reflections were assigned to impurities. The fact that the main reflections in the patterns here correspond to NiO, despite reduction at either 300 °C or 400 °C, is likely due to the samples being exposed to air prior to and during analysis, resulting in oxidation. Although there are some unidentified phases present in the sample (*i.e.* the reflection at 48.9 °), it should be noted that there is no clear evidence for the formation of nickel phosphide species (no nickel phosphide structures were found to account for the reflection) unlike that seen for the nickel only nanoparticles prepared using this

method, which consisted of NiO and Ni_2P after reduction at 300 °C. This suggests that tin, even in the small quantities used in these nanoparticles, is either affecting the crystallisation of the nickel phosphide phase, leading to the segregation of nickel and phosphorus or altering the structure/composition of the nickel phosphide phase present. If the latter were true, this may explain presence of the reflection for the unidentified phase at around 48.9 °.

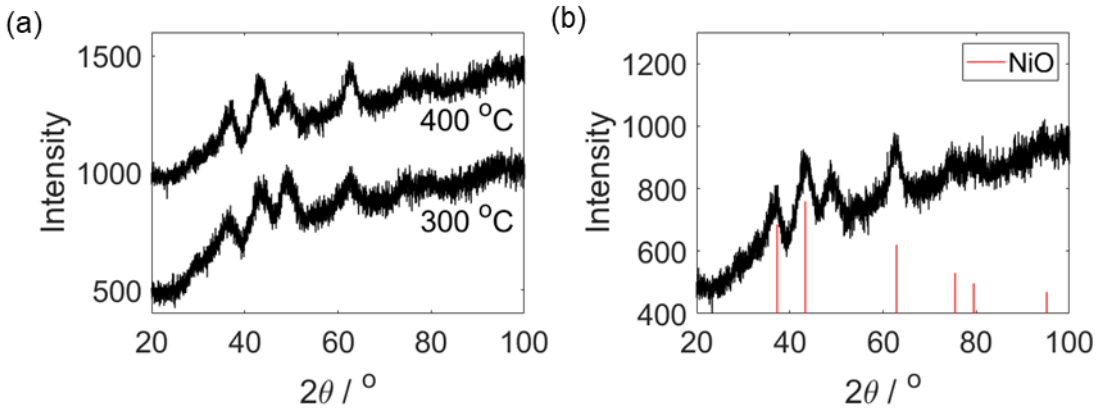

Figure 69: (a) pXRD of larger SnNi (1:*20*) amorphous nanoparticles*;* the nanoparticles were drop cast onto a silicon wafer and then reduced at 300 °C (‘ 300 °C’) and 400 °C (‘400 °C’). The patterns are vertically offset for clarity. (b) pXRD pattern of the nanoparticles reduced at 400 °C compared to a reference pattern of NiO.[19]

In order to further investigate the crystallinity of the nanoparticles after reduction at 300 °C, the nanoparticles were deposited onto a SiO_x grid, reduced at 300 °C and then imaged using TEM (Figure 70). Some of the nanoparticles formed large agglomerations and those that remained a similar size to the as prepared nanoparticles developed large shells encapsulating them. This encapsulation effect was not seen in subsequent work with the samples that had been supported on silica catalyst supports, and then heat treated, and so it was suspected this was due to some interaction of the grid with the nanoparticles during reduction. HRTEM images revealed that the nanoparticles were crystalline, which is in contrast to the pXRD results that showed the sample was mostly poorly crystalline after reduction at 300 °C. Carrying out FFT’s of the HRTEM images of the nanoparticles (Figure 70d) revealed the had nanoparticles had d-spacing’s that fitted well with those expected for Ni_2P ($Ni_2P(111)$ = 0.221 nm, $Ni_2P(201)$ = 0.203 nm and $Ni_2P(211)$ = 0.167 nm). However, only a small number of HRTEM images were able to be obtained since the grid was found to move back and forth fairly rapidly at higher magnifications, likely due to the fact that the grid was SiO_x based and so susceptible to beam damage. This, coupled with the encapsulation of the nanoparticles, means that the reliability of the data is likely lower.

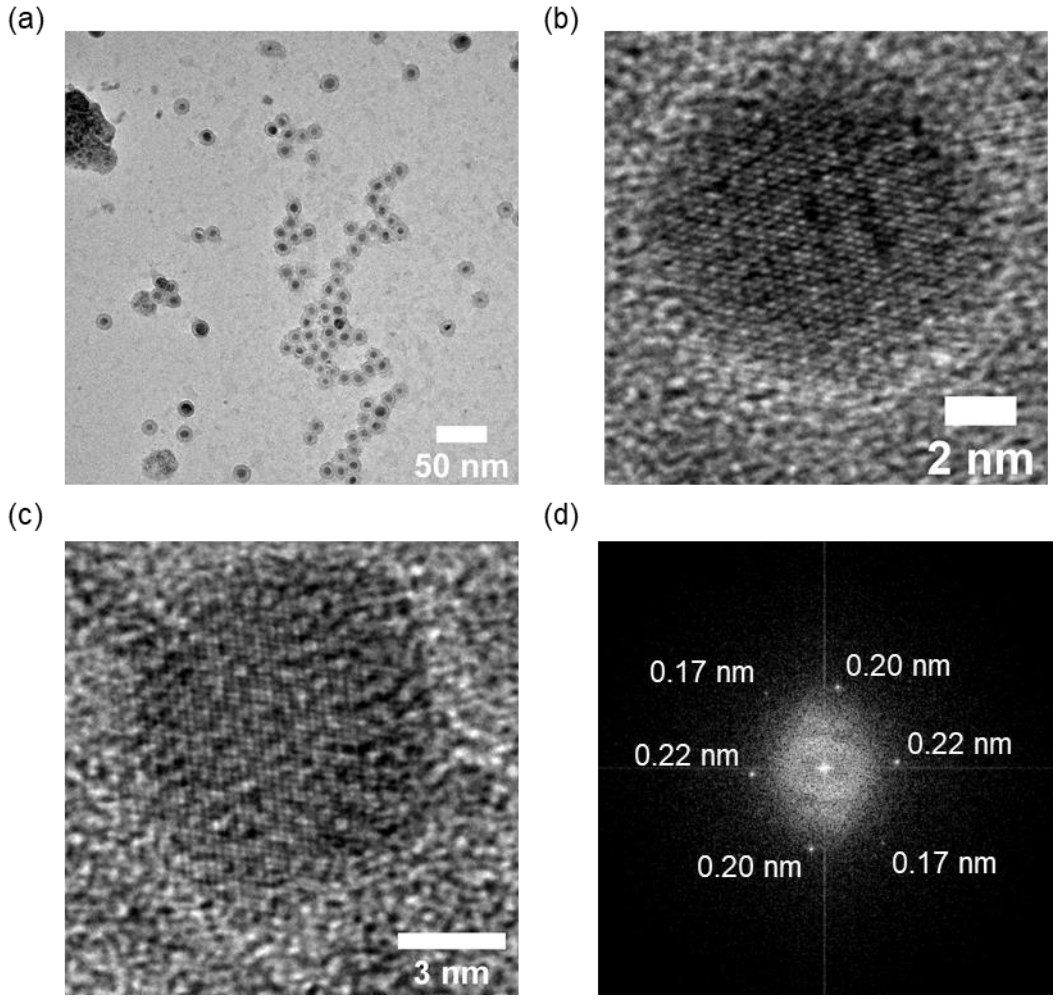

Figure 70: Larger SnNi (1:20) amorphous nanoparticles after reduction at 300 °C on a SiO_a/FORMVAR copper TEM grid; (a) TEM image, (b) and (c) HRTEM images and (d) FFT of the image of the nanoparticle shown in (c)

The amorphous SnNi nanoparticles (nominal molar Ni:Sn ratio of 20:1) were then further analysed using NAP-XPS (Figure 71). The Ni 2p spectra (Figure 71a and b) were recorded with photon energies of 1100 eV and 1650 eV in order to probe different depths into the nanoparticles (KE's of ~200 eV and ~800 eV respectively). The lower kinetic energy spectrum of the as prepared nanoparticles had a weak peak at 853.5 eV and a second weak peak at 856.7 eV. The first peak fits well with the Ni $2p_{3/2}$ peak for nickel oxide[5] and the second peak can be tentatively assigned as the Ni $2p_{3/2}$ peak for a Ni^{3+} species that is thought to correspond to oxidised nickel that forms in the presence of phosphorus.[27] The higher kinetic energy spectrum contains the same two peaks that are present in the lower kinetic energy spectrum, however the intensity of the peak that corresponds to standard nickel oxide is significantly more intense relative to the peak that corresponds to the nickel oxide species that forms in the presence of phosphorus. Therefore, unlike in the analogous nickel-only nanoparticles, the surface of the as prepared SnNi nanoparticles consists of only oxidised nickel species, suggesting that the presence of tin may be promoting the oxidation of nickel.

The sample was then heated to 300 °C in 1 mbar of H_2 to mimic the conditions employed during the reduction step prior to catalysis. In both the lower and higher kinetic energy spectra, this results in a strong peak at around 852.7 eV that corresponds to the Ni $2p_{3/2}$ peak for nickel metal[5] or $Ni^{\delta+}$ species as part of nickel phosphide.[20-22] However, in the lower kinetic energy, more surface sensitive spectrum, there is still a small contribution from oxidised nickel species, indicating that the surface is not fully reduced. The temperature was then lowered to 180 °C since this is the temperature at which catalysis is carried out and for both the lower and higher kinetic energy spectra it can be seen that there is no significant change in the extent of reduction.

The Sn 3d spectra (Figure 71c and d) were also recorded with different photon energies, such that the KE's would roughly match those used for the nickel spectra (photon energies of 700 eV and 1300 eV, which corresponds to KE's of ~200 eV and 800 eV). The spectra of the as prepared nanoparticles for both the lower and higher kinetic energy spectra contain two peaks at 487.3 eV and 495.7 eV. These binding energies fit with those expected for the $3d_{5/2}$ and $3d_{3/2}$ peaks for SnO_2.[5] However, the formation of tin phosphides, such as trigonal Sn_3P_4, results in Sn^{2+} and Sn^{4+} species that have very similar binding energies to those found for tin oxide.[32] Since these nanoparticles are synthesised using a phosphine capping agent and there was clear evidence of significant phosphorus incorporation in the analogous nickel-only nanoparticles, it is certainly a possibility that tin phosphides may be forming.

Heating the sample to 300 °C in 1 mbar of H_2 gave spectra, at both lower and higher energies, where the main peaks (487.3 eV and 495.7 eV) were consistent with those observed in the as prepared nanoparticles. However, small shoulders are now observed at 484.8 eV and 493.1 eV which are consistent with the $3d_{5/2}$ and $3d_{3/2}$ peaks for metallic tin.[5] This means that only a small portion of the tin present has been reduced to tin metal, with the large majority remaining as the Sn^{2+} and/or Sn^{4+} species identified in the as prepared nanoparticles. In the small phosphorus-free SnNi nanoparticles, it was observed that the tin was particularly susceptible to oxidation, however despite this susceptibility, at 300 °C the majority of the tin was present as metal. Whilst this does raise the possibility that the presence of phosphorus may be promoting the oxidation of tin further, the fact that so little tin is reduced means that if this the case, it must be a particularly strong effect and so other explanations should be considered. As discussed above, it is definitely possible that tin phosphides, such as trigonal Sn_3P_4, may form during synthesis, as well as, in this case, during heating to 300 °C in H_2. This type of tin phosphide would result in Sn^{2+} and Sn^{4+} species and the structure could be stable to reducing conditions, which would provide an explanation as to why the majority of the tin present is not reduced to metallic tin. Whilst it is not possible to definitively determine the cause for the resistance to reduction, the formation of tin phosphide may provide a

plausible explanation that fits well with the fact that a significant amount of phosphorus incorporation is known to occur with the synthesis method used for these nanoparticles. When the sample is then cooled to 180 °C, the spectra at both lower and higher kinetic energies remain fairly similar to those at 300 °C, apart from a slight decrease in the metallic tin peak relative to the oxidised tin/tin phosphide peak.

Initially, the P 2p spectra were obtained with a photon energy of 330 eV and 930 eV to match the kinetic energies used for the nickel and tin spectra. However, as can be seen with the spectra for the as prepared nanoparticles (room temperature, high vacuum), this resulted in very weak signals (Figure 71e and f), particularly for the lower kinetic energy spectrum. Therefore, for the remaining spectra, photon energies of 550 eV and 1100 eV were used. Whilst it is not possible to get much information from the lower kinetic energy spectrum for the as prepared nanoparticles, the higher kinetic energy spectrum does contain two peaks at 133.6 eV and 129.8 eV. As discussed previously, the P $2p_{3/2}$ and P $2p_{1/2}$ peaks are only separated by around 0.84 eV,[5] meaning that significant overlap typically occurs and that they often appear as one peak. Similar to that observed in the nickel-only equivalent of these nanoparticles, the peak at 133.6 eV can be assigned to the phosphine capping agent interacting with the surface and the lower kinetic energy peak at 129.8 eV can be assigned as phosphide, either due to the formation of nickel phosphide, tin phosphide or a combination of the two.[28] Heating the sample to 300 °C in 1 mbar of H_2 and subsequent cooling to 180 °C does not result in significant changes to the spectra recorded at both lower and higher kinetic energies.

Similar to the spectra obtained for the small phosphorus-free SnNi nanoparticles, heating the sample to 300 °C in H_2 results in a significant decrease in the C 1s peak (Figure 71g), as well as the disappearance of the weak N 1s peak (Figure 71h), indicating the removal of a significant amount of capping agent. This provides a good explanation for the weaker tin, and particularly nickel, signals for the as prepared nanoparticles when compared to the data obtained after the reduction step.

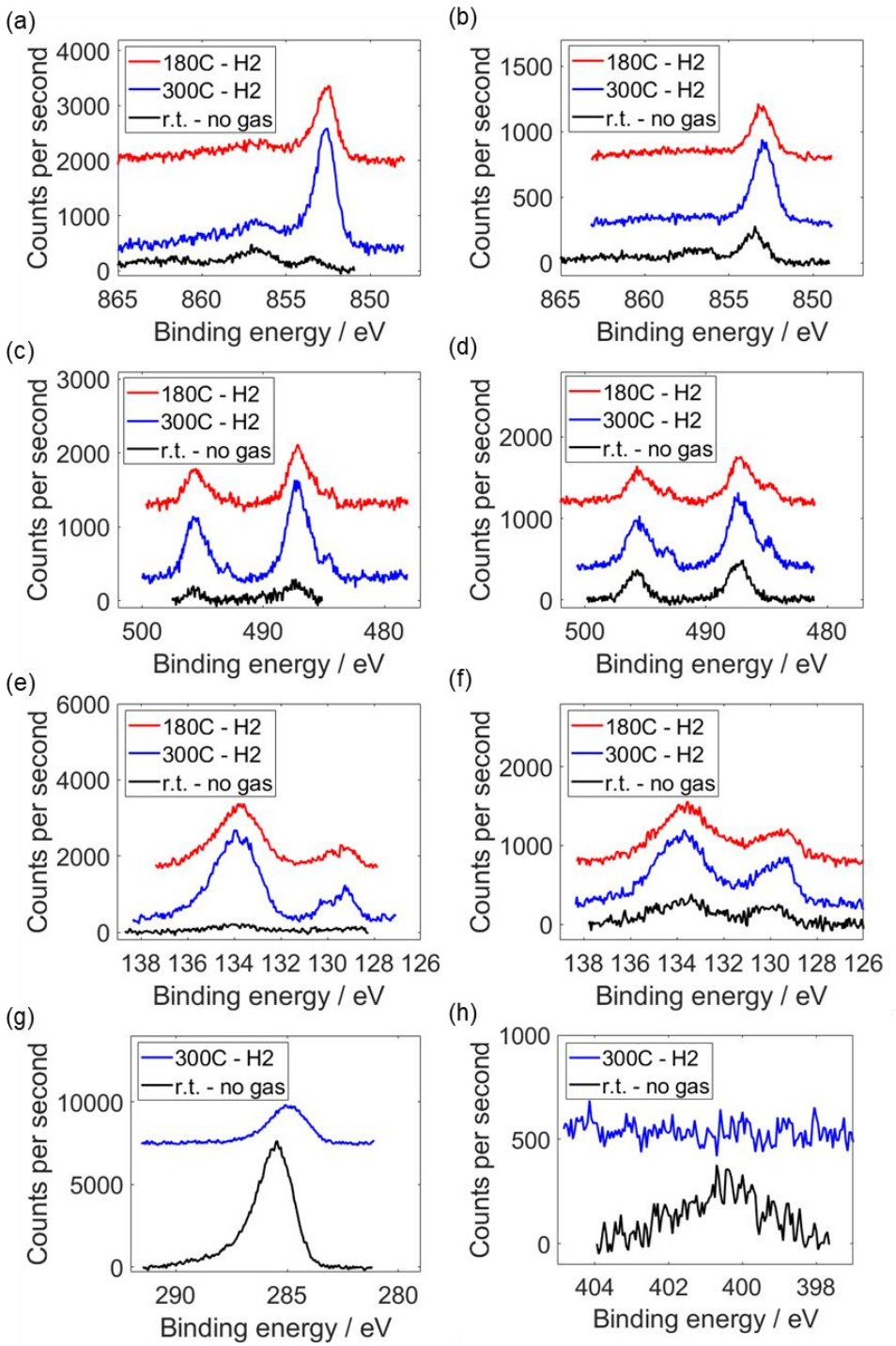

Figure 71: NAP-XP spectra of the amorphous SnNi nanoparticles (molar Ni:Sn ratio of 20*:1*) deposited on a silicon wafer recorded at room temperature under high vacuum ('r.t. – no gas'), at 300 °C under 1 mbar of H_2 ('300C – H2') and at 180 °C under 1 mbar of H_2 ('180C – H2'); (a) Ni 2p spectra recorded with a photon energy (E_{ph}) of 1100 eV (kinetic energy (KE) of 250 eV), (b) Ni 2p spectra recorded with a E_{ph} of 1490 eV (KE of 640 eV), (c) Sn 3d spectra recorded with a E_{ph} of 700 eV (KE of 220 eV), (d) Sn 3d spectra recorded with a E_{ph} of 1100 eV (KE of 620 eV), (e) P 2p spectra recorded at 330 eV for the r.t. spectrum and 550 eV for the higher temperature spectra (KEs of 200 eV and 420 eV respectively) (f) P 2p spectra recorded at 930 eV for the r.t. spectrum and 1100 eV for the higher temperature spectra (KEs of 800 eV and 970 eV respectively) (g) C 1s spectra recorded at 1100 eV and (h) N 1s spectra recorded at 1100 eV. Binding energy was corrected as described in the experimental section (Chapter 2).

The Ni:Sn molar ratios at different depths were then determined by comparing the corrected areas for the nickel and tin peaks from the spectra recorded with the lower and higher kinetic energies. The Ni:Sn molar ratio for the most surface sensitive measurement (KE of ~200 eV) after heating the sample to 300 °C in 1 mbar of H_2 was found to be around 3:1. Cooling the sample to 180 °C did not lead to any significant changes in the Ni:Sn molar ratio. The ratios obtained here are remarkably similar to those found for the small phosphorus-free SnNi nanoparticles, where the Ni:Sn ratios were found to be around 3:1 at 300 °C and around 4:1 at 180 °C. This provides a good explanation for the very similar furfuryl alcohol selectivity of these catalysts (discussed in later chapters), despite having very different bulk Ni:Sn molar ratios (around 3:1 for the small phosphorus-free version, and around 20:1 for the amorphous SnNi version).

The Ni:Sn ratio using the higher kinetic energy spectra (KE of ~800 eV) was found to be around 0.7:1 at 300 °C in 1 mbar of H_2, with a slight increase to around 0.8:1 after cooling to 180 °C. This indicates that whilst the top surface consists of a nickel-rich SnNi phase, there is a region below that is enriched with tin. As the total tin in the particle would correspond to only around 1 monolayer of atoms at the surface (slightly more in lower layers) the strength of the tin signal relative to nickel observed by XPS at the higher kinetic energy strongly points to all the tin being near the surface with a nickel overlayer (the calculation for the thickness of the Sn layer is detailed in Appendix 3). Again, this result is similar to that found for the small phosphorus-free SnNi nanoparticles. Although very different synthetic procedures were used to prepare the nanoparticles, the same methodology was used; nickel nanoparticles were first formed, followed by the addition of a tin precursor. This method may be expected to result in a layer of tin on the surface of the nickel nanoparticles, and so this fits well with the XPS results that indicate a tin-rich layer. Since these nanoparticles were amorphous, it was not possible to observe lattice fringed by HRTEM imaging. Therefore, this technique could not be used to determine whether tin was incorporated into the core of the nanoparticles. However, the addition of tin to the nanoparticles did result in the formation of a polycrystalline shell that was identified as nickel oxide and showed no identifiable contributions from tin. This implies it is likely that there is not any significant tin incorporation into the bulk of the nanoparticles in general and so the amorphous region likely consists of nickel phosphide. Therefore, after reduction at 300 °C and at catalytic temperatures, the nanoparticles likely have a structure similar to that shown in Figure 72, where the top surface consists of a nickel-rich SnNi layer, followed by region consisting almost entirely of tin-based species and then core consisting of nickel phosphide-based species.

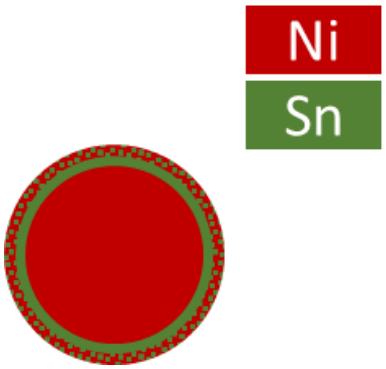

Figure 72: A representation of the proposed structure for the amorphous SnNi nanoparticles (nominal Ni:Sn molar ratio of 20*:1*) after reduction at 300 °C and at the temperature at which catalysis is carried out (180 °C) based on the NAP-XPS results, with nickel shown in red and tin shown in green

Nanoparticles with a nominal Ni:Sn ratio of 50:1 were also prepared using this method. The nanoparticles were found to have a yield (based on nickel) of 68.8 ± 0.6 % and a Ni/Sn molar ratio of 33.6 ± 0.7, which is significantly lower than the targeted ratio. This is likely because the targeted amount of tin in these nanoparticles is so low that small variations in the amount of tin added will lead to large differences in the Ni:Sn molar ratio. However, this ratio is still significantly higher than the previous nanoparticle sample that had a Ni/Sn molar ratio of ~18, and so the effect of differing tin contents can still be determined. Figure 73a and b show a TEM image and the corresponding particle size distribution, with the nanoparticles found to have an average particle size of 11.3 ± 1.6 nm. The average particle size and particle size distribution are consistent with the other nanoparticles prepared using this method. HRTEM imaging (Figure 73c) of the nanoparticles revealed they have a core-shell structure, with an amorphous core and a polycrystalline shell. The nanoparticles prepared using an analogous method but with a Ni:Sn ratio of 20:1 also had a core-shell structure, identified as a nickel phosphide core and polycrystalline NiO shell, and so it is likely that these nanoparticles are similar.

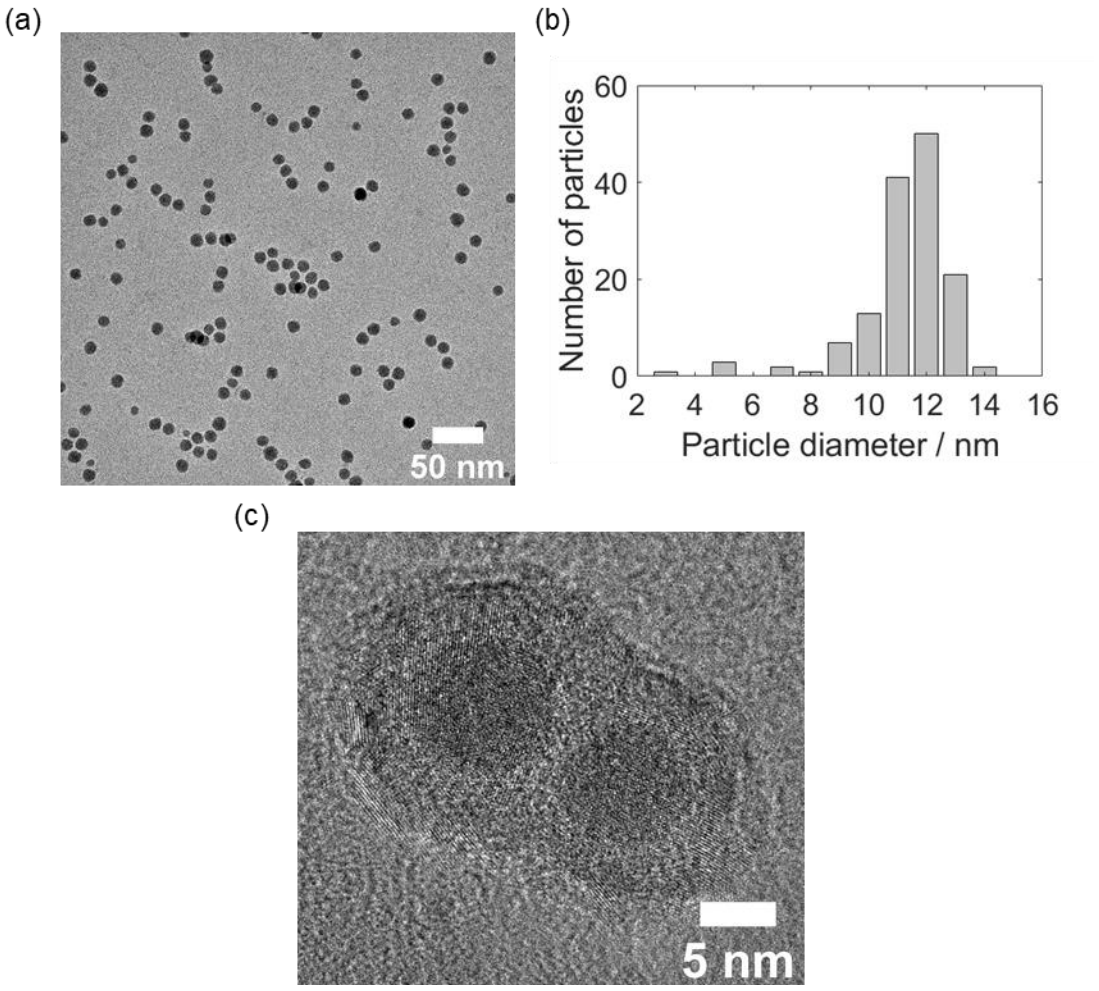

Figure 73: (a) TEM image of the larger SnNi (1:50) amorphous nanoparticles, (b) the corresponding particle size distribution and (c) a HRTEM image of the nanoparticles

HAADF-STEM imaging (Figure 74a) of the nanoparticles confirmed the core-shell structure of the nanoparticles observed by HRTEM. Elemental mapping using STEM-EDX was also carried out, however, like with the sample with a Ni:Sn molar ratio of 20:1, the tin signal was not strong enough to determine anything other than that the nanoparticles contain both nickel and tin as expected.

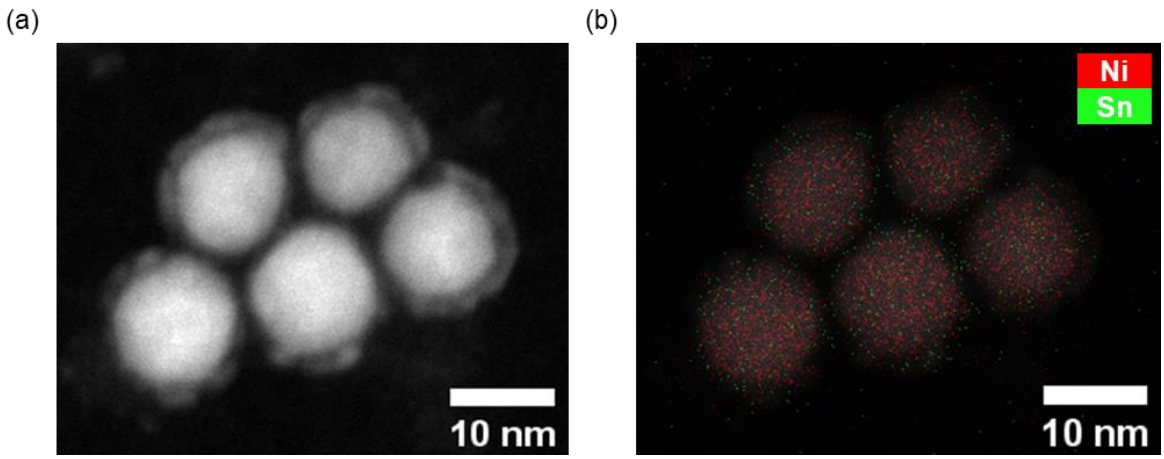

Figure 74: (a) HAADF-STEM image of the larger SnNi (1:50) amorphous nanoparticles and (b) elemental mapping

4.3.3 Synthesis of larger crystalline nickel nanoparticles

As discussed in Section 4.3.1, there is clear evidence that amorphous nanoparticles are produced using the synthetic method outlined by Mézailles *et al.*[7], which suggests significant amounts of phosphorus incorporation. Whilst phosphorus incorporation is likely to occur to some extent regardless of the synthetic conditions if TOP is used as a capping agent,[12] limiting this incorporation may help to minimise any effects of the phosphorus. Therefore, nanoparticles were prepared using a method based on that reported by Emmerling *et al.*[8], which used the lower TOP:Ni ratio of 2. Tracy *et al.*[9] showed that the P:Ni ratio, as well as reaction temperature, is key in determining the morphology, structure and composition of nickel nanoparticles prepared using TOP as a capping agent, with lower P:Ni ratios being claimed to favour the formation of nickel metal nanoparticles with less phosphorus incorporation. Therefore, the lower P:Ni ratio used in the synthesis outlined by Emmerling *et al.*[8] should favour the production of crystalline nickel metal nanoparticles with limited phosphorus incorporation.

Initially the reaction was carried out using diphenyl ether (DPE) as the solvent (the authors reported the use of dibenzyl ether (DBE), however the properties of DPE were thought to be similar enough to DBE that it could substituted) and a reaction volume of 10 mL. This reaction procedure was denoted DPE-10mL. Figure 75a and b show a TEM image of the nanoparticles and the corresponding particle size distribution. The nanoparticles were found to have an average particle size of 12.5 ± 0.9 nm, which is consistent with the particle size and distribution reported by Emmerling *et al.*[8] However, when HRTEM imaging was carried out, the nanoparticles were found to be amorphous (see Figure 75c). The fact that the nanoparticles were found to be amorphous suggests there was significant phosphorus incorporation leading to the formation of amorphous nickel phosphide nanoparticles, similar to those produced using the previous synthetic method.

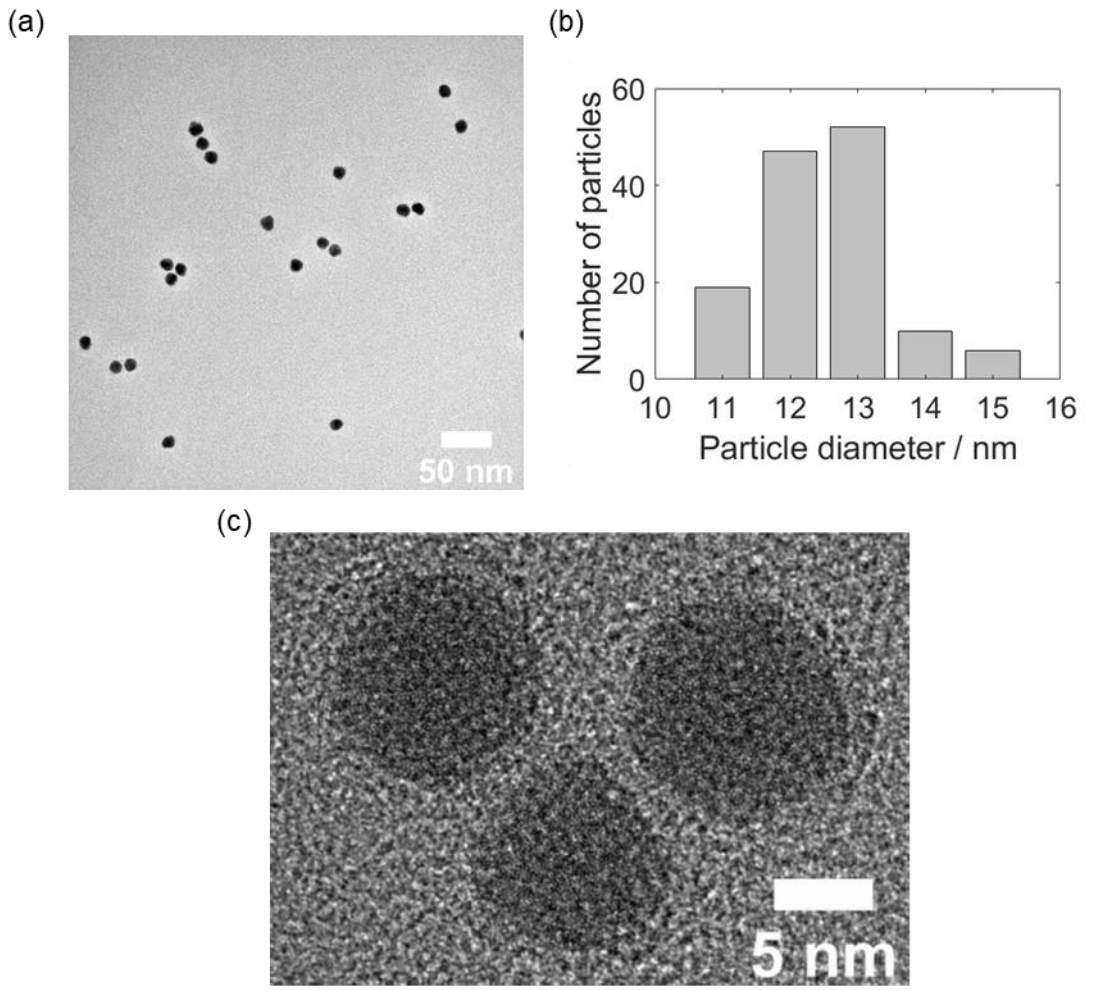

Figure 75: Nickel nanoparticles prepared using the DPE-10 mL synthetic route (a) TEM image, (b) the corresponding particle size distribution and (c) a HRTEM image of the nanoparticles

Since a different solvent was used to that reported in the procedure, it was then decided to repeat the reaction using DBE, the exact solvent reported in the literature procedure. Additionally, the authors reported carrying out the reaction with both a 10 mL and 5 mL reaction volume. In the previous synthesis, the reaction volume chosen was 10 mL, and so 5 mL was chosen for the second reaction since the reaction volume may also be impacting the results. This synthetic method was then denoted DBE-5mL. A TEM image and the particle size distribution for the nanoparticles can found in Figure 76a and b. The nanoparticles were found to have an average particle size of 15.2 ± 1.3 nm, which is slightly larger than the average particle size reported by Emmerling *et al.*[8], as well as that found for the nanoparticles produced using the DPE-10mL synthetic method, however the particle size distribution is still narrow. Importantly, HRTEM imaging of the nanoparticles (Figure 76c) revealed that the majority of the nanoparticles were polycrystalline, although there were a small minority of nanoparticles that appeared amorphous. Carrying out FFT's of the HRTEM images confirmed that the nanoparticles were mostly crystalline nickel metal, with

the nanoparticle shown in Figure 76c having d-spacings of 0.20 nm, 0.18 nm and 0.10 nm (Figure 76d), which fit with Ni(111), Ni(200) and Ni(222) respectively. A d-spacing of 0.21 nm was observed for one nanoparticle which fits better with NiO(200), indicating that in a limited number of nanoparticles, there may be some areas oxidation. Overall, the DBE-5mL synthetic method has been mostly successful, producing mostly crystalline nickel nanoparticles.

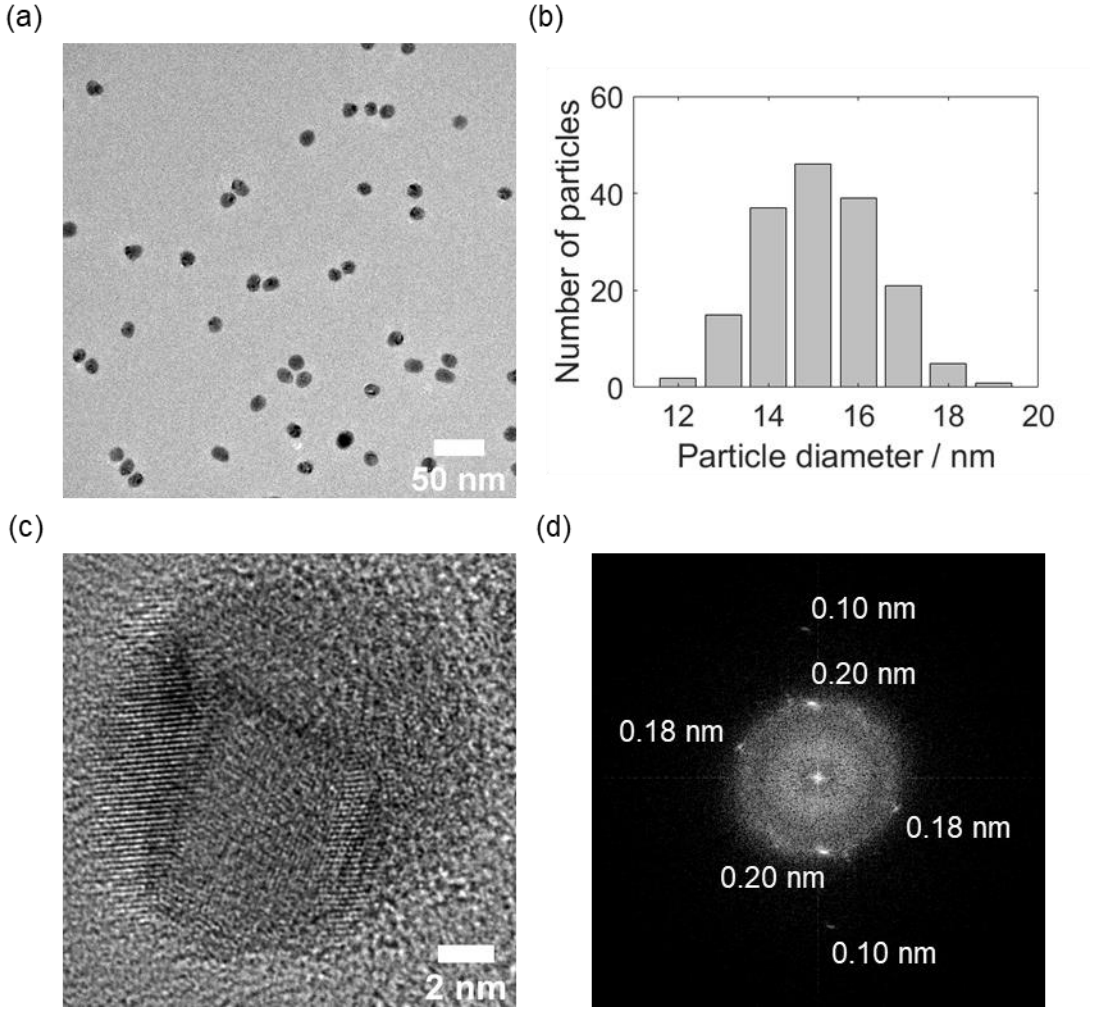

Figure 76: Nickel nanoparticles prepared using the DBE-5 mL synthetic route (a) TEM image, (b) the corresponding particle size distribution, (c) HRTEM images of a polycrystalline nanoparticle and (c) FFT of the nanoparticle in the HRTEM image shown in (c)

Further evidence that the nanoparticles were crystalline nickel metal came from pXRD analysis (Figure 77). Both the as prepared nanoparticles and those reduced at 300 ^{o}C had a pattern that corresponded to nickel metal, with the only difference being that the pattern after reduction at 300 ^{o}C had slightly sharper reflections, suggesting that there was a small increase in crystallite size. There is also no evidence of oxide in the as prepared or reduced patterns, indicating that the NiO identified from the HRTEM images is present in very low amounts or the crystallite size is very small.

The crystallite sizes of the nanoparticles were estimated by fitting Lorentzian peaks and then using the Scherrer equation. The as prepared nanoparticles were found to have an average crystallite size of 3.6 nm, whereas after reduction at 300 °C, the estimated crystallite size increased slightly to 4.7 nm. This is consistent with the reflections appearing visually slightly sharper after reduction, however, since the Scherrer equation only provides a rough estimate of the average crystallite size, the minimal increase observed may not be significant. However, the estimated crystallite sizes do confirm the polycrystalline morphology of the nanoparticles, since the average particle size determined by TEM is roughly 3 to 4 times larger than the average crystallite sizes calculated from the pXRD patterns.

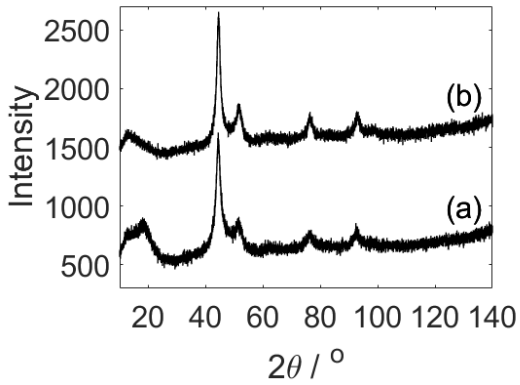

Figure 77: pXRD of the nickel nanoparticles prepared using the DBE-5 mL synthetic route; (a) as prepared nanoparticles deposited onto a silicon wafer and (b) the nanoparticles reduced at 300 °C whilst deposited on the silicon wafer. The data is vertically offset for clarity.

The crystalline nickel nanoparticles were investigated further using NAP-XPS (Figure 78). The Ni 2p spectra were obtained using photon energies of 1100 eV and 1650 eV (KE's of ~200 eV and ~800 eV respectively) in order to probe different depths into the nanoparticles. The lower kinetic energy spectrum for the as prepared nanoparticles (room temperature, high vacuum) contained two peaks, one at 856.1 eV and a second at 852.4 eV. The peak at 856.1 eV fits well with the Ni $2p_{3/2}$ peak for Ni^{3+} species found when nickel oxide is in the presence of phosphorus,[27] whereas the peak at 852.4 eV fits well with the Ni $2p_{3/2}$ peak for metallic nickel[5] or the $Ni^{\delta+}$ species found in nickel phosphide.[20-22] Since the peak for the $Ni^{\delta+}$ species associated with the formation of nickel phosphides does not result in a significant shift relative to nickel metal, it is not possible to determine from the nickel spectra alone whether phosphorus incorporation has occurred. The higher kinetic energy spectrum contains the same two peaks, however the amount of the metallic nickel/$Ni^{\delta+}$ species present is increased relative to the oxidised species. This indicates that only the surface of the nanoparticles is oxidised and that the bulk of the nanoparticles consists of nickel metal/nickel phosphide.

The sample was then heated to 300 °C in 1 mbar of H_2, which mimics the conditions used for the reduction step that is carried out prior to catalysis. The lower kinetic energy spectrum contains the same peaks seen in the as prepared nanoparticles, however there is significant increase in the intensity of the peak that corresponds to metallic nickel/nickel phosphide relative to the peak that corresponds to oxidised nickel. The presence of the small peak corresponding to oxidised nickel does however mean that, although only to a minimal extent, the surface of the nanoparticles has not been fully reduced. In the higher kinetic energy spectrum, there is a strong peak for nickel metal/nickel phosphide species and the peak for oxidised nickel species is no longer present, indicating that it is only the top surface that is partially reduced. Cooling the sample to 180 °C (the temperature at which catalysis is carried out) does not result in significant changes in the extent of reduction for both the lower and higher kinetic energy spectra.

The P 2p spectra (Figure 78) were also recorded with different photon energies (550 eV and 1100 eV corresponding to KE's of ~400 eV and 800 eV) in order to probe different depths into the nanoparticles. Both the lower and higher kinetic energy spectra have a main peak centred around 133 eV and a weaker peak, especially in the lower kinetic energy spectrum, at 129.6 eV. The energy difference between the $2p_{3/2}$ and $2p_{1/2}$ peaks for phosphorus is relatively low at around 0.84 eV,[5] meaning that significant overlap often occurs and that the two peaks frequently appear as one. The peak at around 133 eV then likely corresponds to the P $2p_{3/2}$ and P $2p_{1/2}$ peaks for the phosphine capping agent interacting with the nanoparticles and the peak at 129.6 eV likely corresponds to the P $2p_{3/2}$ and P $2p_{1/2}$ peaks for $P^{\delta-}$ species that form as part of nickel phosphide.[28] This provides clear evidence that despite the bulk structure of these nanoparticles being crystalline nickel metal, indicating minimal phosphorus incorporation, the surface of the nanoparticles does include nickel phosphide.

Heating the sample to 300 °C in 1 mbar of H_2 resulted in an increase in the intensity of the phosphide peak relative to the peak for the phosphine capping agent, especially in the higher kinetic energy spectrum. There are a number of possible explanations for this, such as the heating of the sample in H_2 resulting in the removal of capping agent, which would lower the amount of phosphine capping agent present on the sample. This explanation could be supported by the fact that there is a significant decrease in the C 1s signal after reduction at 300 °C (Figure 78e), although the disappearance of the weak N 1s signal (Figure 78f) also indicates that this could at least partially be accounted for by the loss of amine capping agent. Another potential explanation could be that heating the sample leads to increased phosphorus incorporation in the surface, due to decomposition of the phosphine capping agent, which is known to occur on Ni(111) metal surfaces at temperatures as low as 150 °C.[28] Finally, this could also be due to migration of phosphorus from

the bulk to surface during the reduction procedure. However, this seems unlikely since HRTEM imaging and pXRD revealed the bulk of these nanoparticles consisted of crystalline nickel metal, and so minimal, if any, phosphorus incorporation in the bulk would be expected. Lowering the temperature to 180 °C led to minimal changes in the phosphorus spectra at both lower and higher kinetic energies.

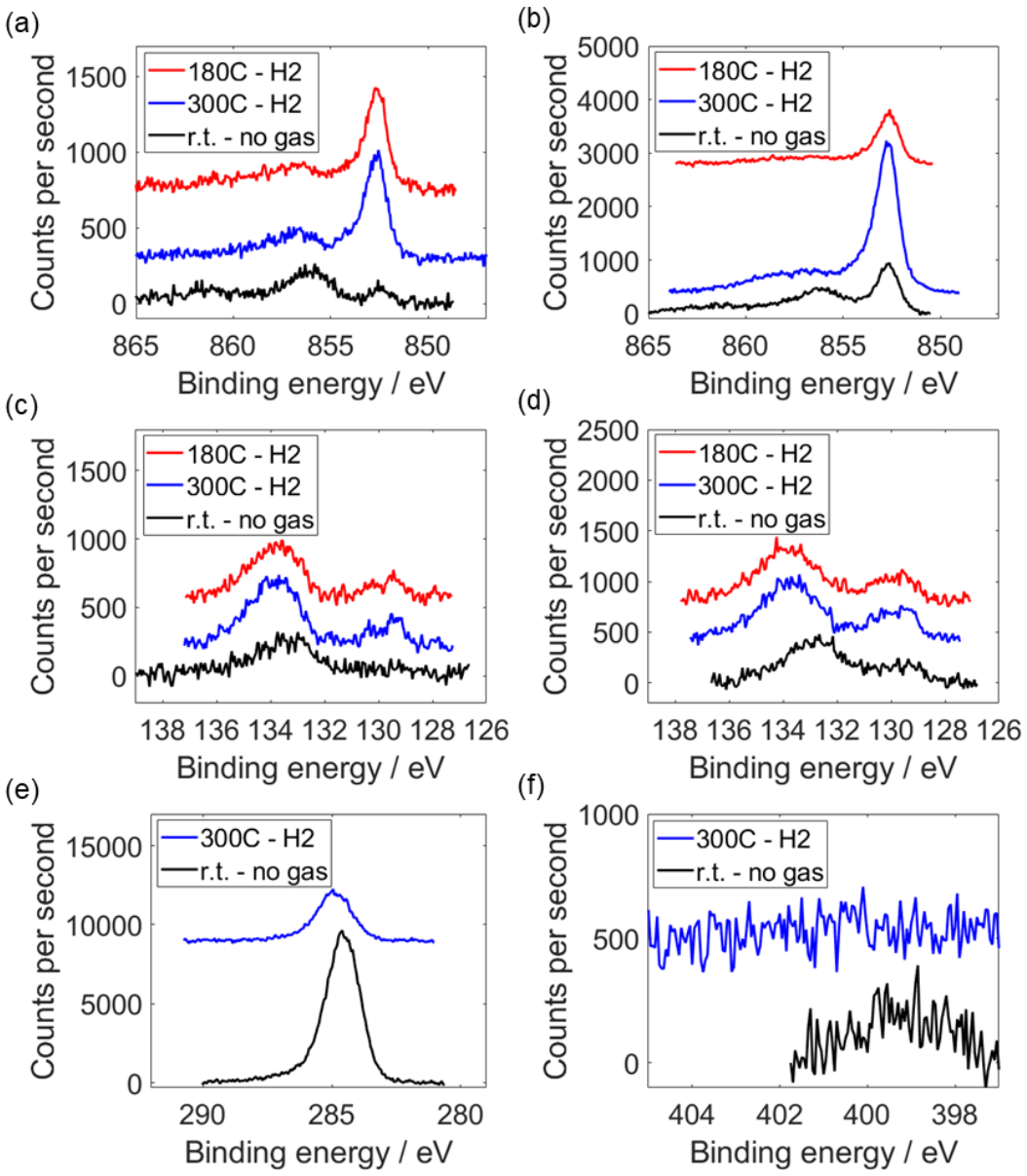

Figure 78: NAP-XP spectra of the crystalline nickel nanoparticles (prepared using TOP) deposited on a silicon wafer recorded at room temperature under high vacuum ('r.t. – no gas'), at 300 °C under 1 mbar of H_2 ('300C – H2') and at 180 °C under 1 mbar of H_2 ('180C – H2'); (a) Ni 2p spectra recorded with a photon energy (E_{ph}) of 1100 eV (kinetic energy (KE) of 250 eV), (b) Ni 2p spectra recorded with a E_{ph} of 1490 eV (KE of 640 eV), (c) P 2p spectra recorded with a E_{ph} of 550 eV (KE of 420 eV) (d) P 2p spectra recorded with a E_{ph} of 1100 eV (KE of 970 eV) (e) C 1s spectra recorded at 1100 eV and (f) N 1s spectra recorded at 1100 eV. Binding energy was corrected as described in the experimental section (Chapter 2).

It is instructive to compare the ratios of the peaks for phosphide and phosphine capping agent for the amorphous nickel phosphide nanoparticles and the crystalline nickel metal nanoparticles, in order to compare the extent of phosphide present (Figure 79). For the as prepared nanoparticles (room temperature, high vacuum), the ratio of phosphide to capping agent is similar for the lower kinetic energy, more surface sensitive data, however there is higher proportion of phosphide present in the amorphous nanoparticles for the higher kinetic energy data (Figure 79a). This is consistent with the fact that the bulk of the amorphous nanoparticles is nickel phosphide, whereas the bulk of the crystalline nanoparticles is nickel metal, since this suggests that the majority of phosphide is only present on the surface of the crystalline nanoparticles. Heating the sample to 300 °C in 1 mbar of H_2 results in a slight general increase in phosphide content relative to the amount of capping agent present, however again the ratio for the lower kinetic energy data is very similar for both sets of nanoparticles and is higher for the amorphous nanoparticles in the higher kinetic energy data. Finally, lowering the temperature has minimal effect on the phosphide to capping agent ratios for both sets of nanoparticles at both lower and higher kinetic energies. Ultimately, the similar ratios observed for the lower kinetic energy, more surface sensitive data provides a reasonable explanation for the fact that, as discussed in later chapters, both sets of nanoparticles were found to have an almost identical increase in furfuryl alcohol selectivity when compared to phosphorus-free nickel catalysts. Additionally, these results also confirm that the phosphorus incorporation is mostly limited to the surface of the crystalline nanoparticles but extends to the bulk for the amorphous nanoparticles, which is consistent with data on the bulk structures of the nanoparticles from HRTEM imaging and pXRD. Representations of the structures for the amorphous and crystalline nanoparticles are shown in Figure 80.

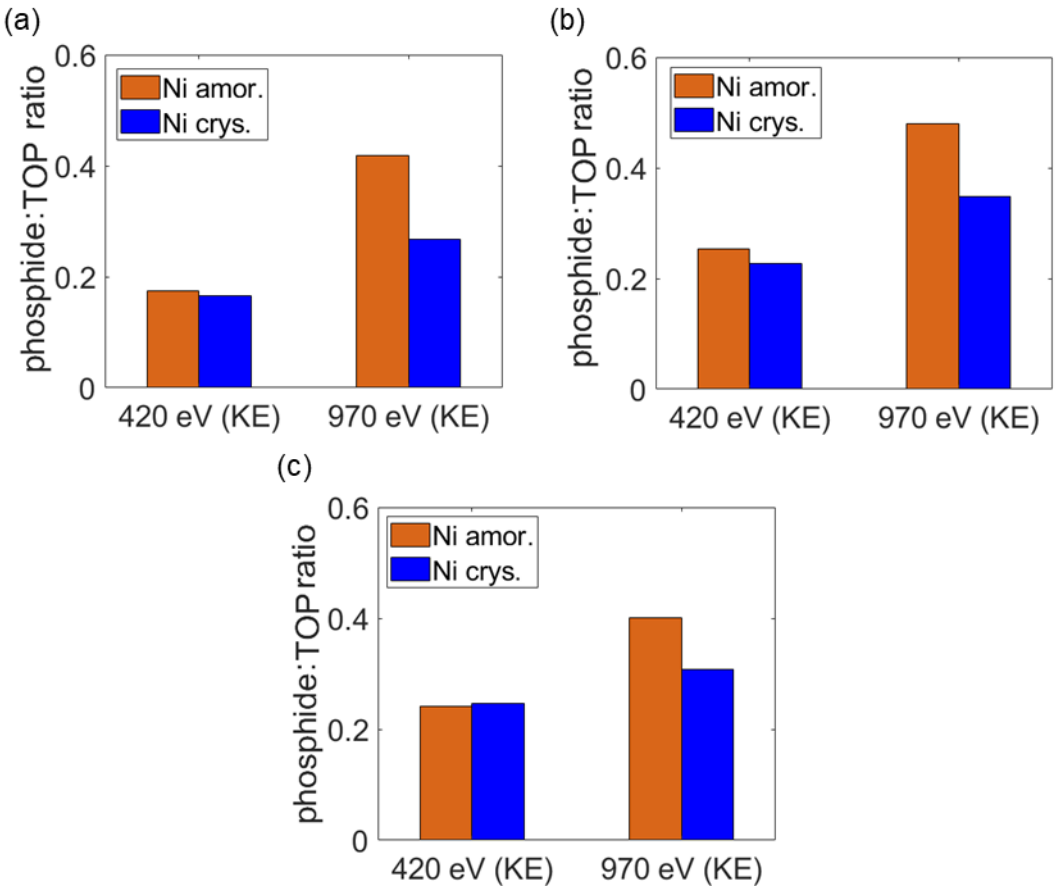

Figure 79: Comparison of the contribution to the P 2p XP spectra recorded at different kinetic energies (420 eV or 970 eV) for nickel phosphide and TOP capping agent for the amorphous nickel phosphide nanoparticles ('Ni amor.') and the crystalline nickel metal nanoparticles prepared using TOP ('Ni crys.'); (a) room temperature under high vacuum, (b) 300 °C under 1 mbar H_2 and (c) 180 °C under 1 mbar H_2

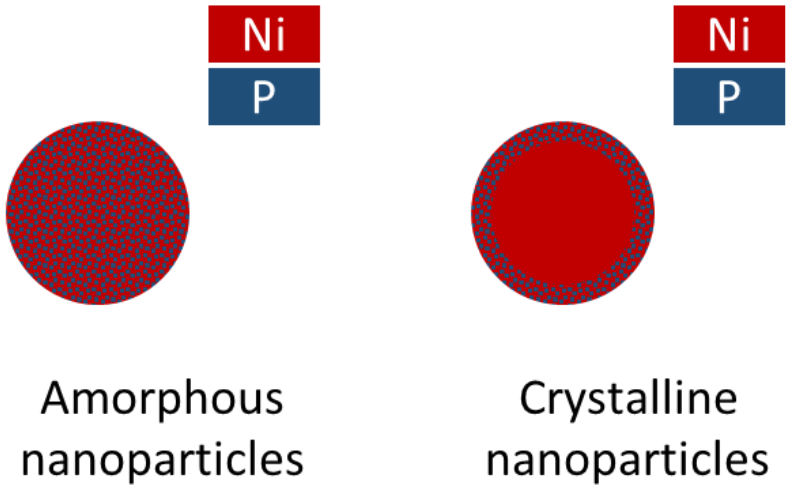

Figure 80: A representation of the proposed structure for the amorphous nickel phosphide nanoparticles and the crystalline nickel nanoparticles after reduction at 300 °C and at the temperature at which catalysis is carried out (180 °C) based on the NAP-XPS results, with nickel shown in red and phosphorus shown in blue

4.3.4 Synthesis of larger crystalline tin-nickel nanoparticles

Since the DBE-5mL synthetic method successfully produced crystalline nickel nanoparticles, the method was then modified to produce SnNi bimetallic nanoparticles. The bimetallic nanoparticles were prepared in a similar way to the sequential addition method discussed in Section 4.1.3, where the nickel nanoparticles are first synthesised followed by the addition of the Sn(II) precursor using a syringe pump. The Ni:Sn molar ratios were chosen as 20:1 and 50:1 to match the ratios chosen for the previously described amorphous nanoparticles. ICP-OES/ICP-MS analysis revealed the nanoparticles with a nominal Ni:Sn molar ratio of 20:1 had a yield of 92.7 ± 0.9 % (based on nickel) and a Ni/Sn molar ratio of 23.6 ± 0.5, which is relatively consistent with the targeted ratio (see Table 8). Figure 81a and b show a TEM image of the nanoparticles and the corresponding particle size distribution. The average particle size was found to be 15.7 ± 1.7 nm, which is consistent with the nickel only analogue of these nanoparticles. HRTEM imaging of the nanoparticles showed that they were polycrystalline and carrying out FFT's of the HRTEM images confirmed that the nanoparticles had *d*-spacings that were mostly consistent with nickel metal (Figure 81d), however, again, there were some *d*-spacings that corresponded to NiO (*e.g.* NiO(201) = 0.187 nm which fits with the *d*-spacing of 0.19 nm). Therefore, there does appear to be some limited oxidation of the nanoparticles, similar to that observed for the nickel only analogue.

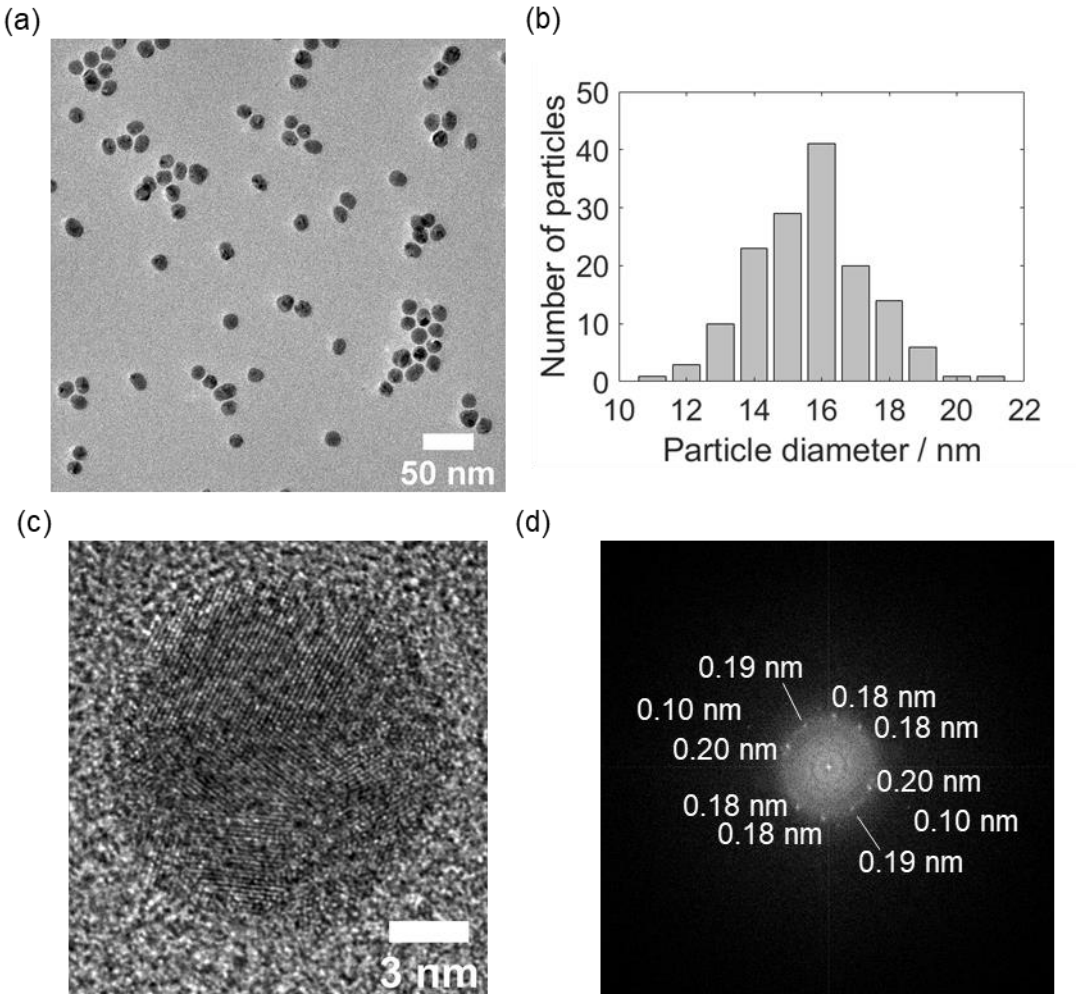

Figure 81: SnNi (1:20) nanoparticles prepared using the DBE-5 mL synthetic route (a) TEM image, (b) the corresponding particle size distribution, (c) HRTEM image of a polycrystalline nanoparticle and (d) FFT of the nanoparticle in the HRTEM image shown in (c)

The crystallinity of the nanoparticles was confirmed through pXRD (see Figure 82). The as prepared nanoparticles have a pattern that corresponds to nickel metal, which fits well with the TEM data. Like with the nickel only analogue, there is no evidence of NiO in the as prepared nanoparticles which indicates that the NiO is present in very low amounts or as very small crystallites. However, after reduction at 300 °C (and exposure to air at room temperature immediately before and during acquisition of the pXRD pattern), the sample is a mix of NiO and Ni metal. A plausible explanation could be that the reduction process is resulting in the removal of some capping agent, making the nanoparticles more susceptible to oxidation when exposed to air immediately prior to and during analysis.

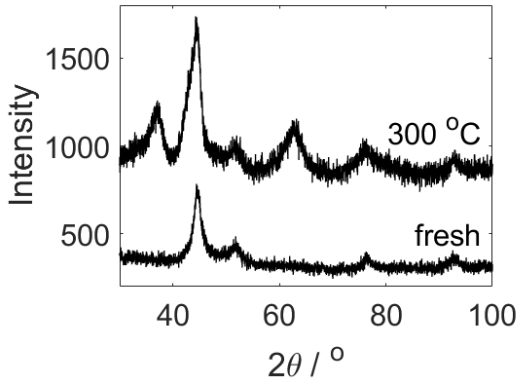

Figure 82: pXRD of the tin nickel nanoparticles with a Ni:Sn molar ratio of 20*:1* prepared using the DBE-5 mL synthetic route; (a) as prepared nanoparticles deposited onto a silicon wafer ('fresh') and (b) the nanoparticles reduced at 300 °C whilst deposited on the silicon wafer ('300 °C'). The data is vertically offset for clarity.

Nanoparticles were also prepared with a Ni:Sn molar ratio of 50:1. ICP-OES/ICP-MS revealed the yield of the reaction was 91.6 ± 0.8 % (based on nickel) and the Ni/Sn molar ratio was 56.7 ± 0.7, which is consistent with the targeted ratio. The nanoparticles were imaged using TEM, which was used to determine the particle size distribution (see Figure 83a and b). The average particle size was found to be 16.0 ± 1.3 nm, which is consistent with the other nanoparticles prepared using this method. These nanoparticles were also imaged using HRTEM, which showed that the nanoparticles had a polycrystalline morphology, again confirming that the addition of tin does not affect the crystallinity of the nanoparticles. Unfortunately, it was not possible to collect corresponding NAP-XPS data for the crystalline SnNi nanoparticle samples due to beamtime constraints and prioritisation of the amorphous nanoparticle sample with which more work had been conducted.

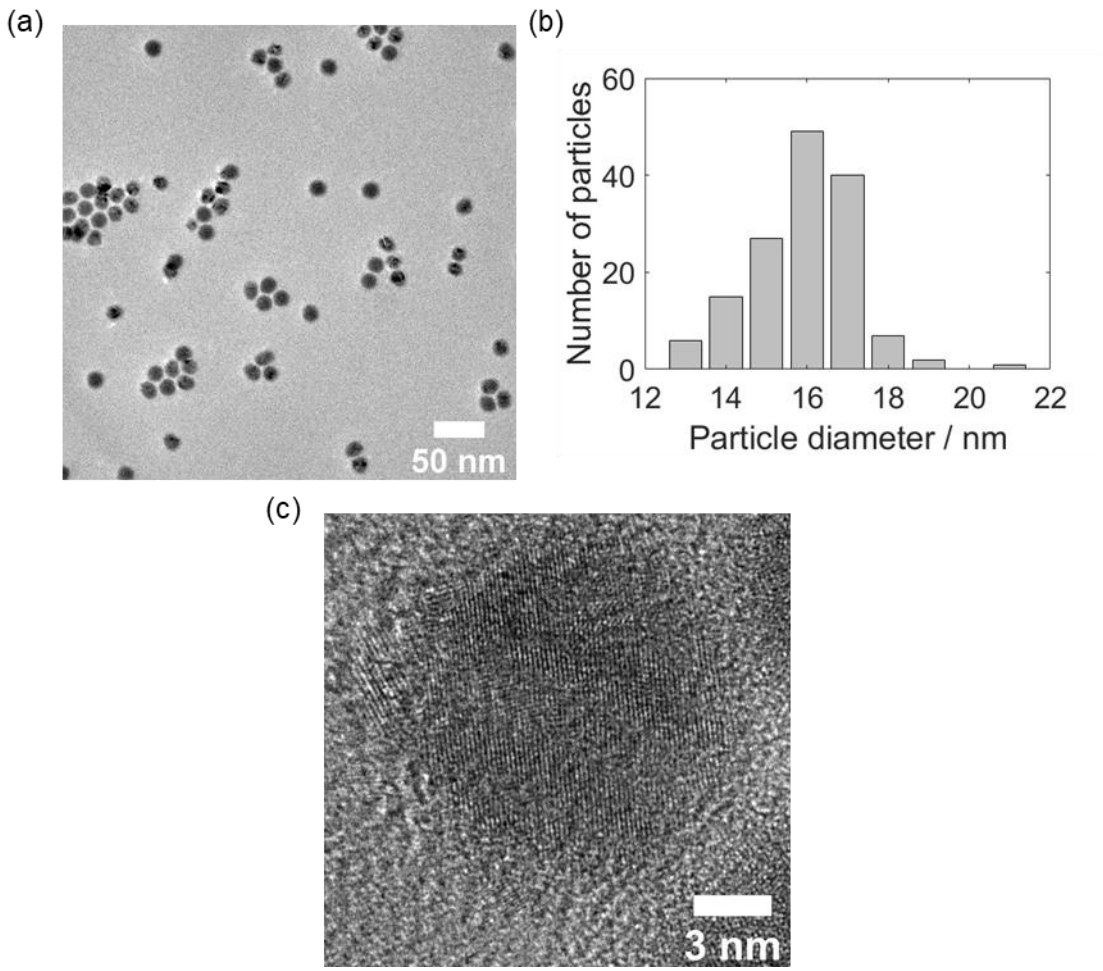

Figure 83: SnNi (1:50) nanoparticles prepared using the DBE-5 mL synthetic route (a) TEM image, (b) the corresponding particle size distribution and (c) HRTEM image showing a polycrystalline nanoparticle

4.4 Conclusions

Small (~4 nm) monometallic nickel and bimetallic SnNi colloidal nanoparticles have been successfully prepared with only the use of an amine capping agent. The nanoparticles were found to have a narrow size distribution and an acceptable distribution of Ni:Sn molar ratios, where relevant. NAP-XPS revealed the top surface of the nanoparticles consisted of a nickel-rich SnNi phase with a Ni:Sn ratio of ~3:1 (depending on the conditions), followed by a tin-rich layer and then a nickel-based core. Whilst the synthesis of larger nickel nanoparticles without the use of a phosphorus containing capping agent was attempted, this led to a bimodal distribution of particle sizes. Therefore, larger nickel nanoparticles (10 – 15 nm) had to be synthesised using a phosphine capping agent, TOP, which was found to lead to phosphorus incorporation into the surface of the nanoparticles regardless of the bulk structure (*i.e.* amorphous nickel phosphide or crystalline nickel metal). The larger nickel nanoparticles were successfully modified with differing amounts of tin in order to later study the effect of tin on furfural hydrogenation. NAP-XPS of the larger amorphous

SnNi nanoparticles revealed the nanoparticles had a similar structure to the small SnNi nanoparticles, with the top surface consisting of a SnNi phase with a Ni:Sn molar ratio of ~3:1, followed by a tin-rich layer and then a nickel-based core. Overall, a series of well-defined and uniform colloidal mono and bimetallic nanoparticles have been synthesised, which can act as model catalysts for furfural hydrogenation and should allow easier elucidation of complex structure-activity relationships.

4.5 References

1. Ö. Metin, V. Mazumder, S. Özkar and S. Sun, *Journal of the American Chemical Society*, 2010, **132**, 1468-1469.
2. S. M. Humphrey, M. E. Grass, S. E. Habas, K. Niesz, G. A. Somorjai and T. D. Tilley, *Nano Letters*, 2007, **7**, 785-790.
3. G. Poirier, J. D. Grice, R. Rowe, C. J. Stanley and L. s. Horváth, *The Canadian Mineralogist*, 2011, **49**, 651-656.
4. S. Tanuma, C. J. Powell and D. R. Penn, *Surface and Interface Analysis*, 1993, **20**, 77-89.
5. J. F. Moulder and J. Chastain, *Handbook of X-ray Photoelectron Spectroscopy: A Reference Book of Standard Spectra for Identification and Interpretation of XPS Data*, Physical Electronics Division, Perkin-Elmer Corporation, 1992.
6. Y. Chen, D.-L. Peng, D. Lin and X. Luo, *Nanotechnology*, 2007, **18**, 505703.
7. S. Carenco, C. Boissière, L. Nicole, C. Sanchez, P. Le Floch and N. Mézailles, *Chemistry of Materials*, 2010, **22**, 1340-1349.
8. M. Heilmann, H. Kulla, C. Prinz, R. Bienert, U. Reinholz, A. Guilherme Buzanich and F. Emmerling, *Nanomaterials*, 2020, **10**, 713.
9. J. Wang, A. C. Johnston-Peck and J. B. Tracy, *Chemistry of Materials*, 2009, **21**, 4462-4467.
10. L. M. Moreau, D.-H. Ha, H. Zhang, R. Hovden, D. A. Muller and R. D. Robinson, *Chemistry of Materials*, 2013, **25**, 2394-2403.
11. R. Arrigo, S. Gallarati, M. E. Schuster, J. M. Seymour, D. Gianolio, I. da Silva, J. Callison, H. Feng, J. E. Proctor, P. Ferrer, F. Venturini, D. Grinter and G. Held, *ChemCatChem*, 2020, **12**, 1491-1503.
12. L. M. Moreau, D.-H. Ha, C. R. Bealing, H. Zhang, R. G. Hennig and R. D. Robinson, *Nano Letters*, 2012, **12**, 4530-4539.
13. D. S. Sidhaye, T. Bala, S. Srinath, H. Srikanth, P. Poddar, M. Sastry and B. L. V. Prasad, *The Journal of Physical Chemistry C*, 2009, **113**, 3426-3429.
14. A. L. Abdelhady, M. A. Malik, P. O'Brien and F. Tuna, *The Journal of Physical Chemistry C*, 2012, **116**, 2253-2259.
15. W. L. Vrijburg, J. W. A. van Helden, A. J. F. van Hoof, H. Friedrich, E. Groeneveld, E. A. Pidko and E. J. M. Hensen, *Catalysis Science & Technology*, 2019, **9**, 2578-2591.
16. X. Yin, M. Shi, K. S. Kwok, H. Zhao, D. L. Gray, J. A. Bertke and H. Yang, *Nano Research*, 2018, **11**, 3442-3452.
17. X. Yin, M. Shi, J. Wu, Y.-T. Pan, D. L. Gray, J. A. Bertke and H. Yang, *Nano Letters*, 2017, **17**, 6146-6150.
18. R. Fruchart, A. Roger and J. P. Senateur, *Journal of Applied Physics*, 1969, **40**, 1250-1257.
19. S. Sasaki, K. Fujino, Tak, Eacute and Y. Uchi, *Proceedings of the Japan Academy, Series B*, 1979, **55**, 43-48.
20. Y. Pan, Y. Liu, J. Zhao, K. Yang, J. Liang, D. Liu, W. Hu, D. Liu, Y. Liu and C. Liu, *J. Mater. Chem. A*, 2015, **3**, 1656-1665.
21. G. Yun, Q. Guan and W. Li, *RSC Advances*, 2017, **7**, 8677-8687.
22. S. Fujita, K. Imagawa, S. Yamaguchi, J. Yamasaki, S. Yamazoe, T. Mizugaki and T. Mitsudome, *Scientific Reports*, 2021, **11**, 10673.
23. C. N. R. Rao, V. Vijayakrishnan, G. U. Kulkarni and M. K. Rajumon, *Applied Surface Science*, 1995, **84**, 285-289.
24. A. F. Carley, S. D. Jackson, M. W. Roberts and J. O'Shea, *Surface Science*, 2000, **454-456**, 141-146.
25. D. Alders, F. C. Voogt, T. Hibma and G. A. Sawatzky, *Physical Review B*, 1996, **54**, 7716-7719.
26. J. C. Vedrine, G. Hollinger and D. Tran Minh, *The Journal of Physical Chemistry*, 1978, **82**, 1515-1520.

27. Ş.-B. Ivan, I. Popescu, I. Fechete, F. Garin, V. I. Pârvulescu and I.-C. Marcu, *Catalysis Science & Technology*, 2016, **6**, 6953-6964.
28. S. Carenco, Z. Liu and M. Salmeron, *ChemCatChem*, 2017, **9**, 2318-2323.
29. H. Loboué, C. Guillot-Deudon, A. F. Popa, A. Lafond, B. Rebours, C. Pichon, T. Cseri, G. Berhault and C. Geantet, *Catalysis Today*, 2008, **130**, 63-68.
30. M. Ellner, *Journal of the Less Common Metals*, 1976, **48**, 21-52.
31. V. Keimes, H. M. Blume and A. Mewis, *Zeitschrift für anorganische und allgemeine Chemie*, 1999, **625**, 207-210.
32. V. Tallapally, R. J. A. Esteves, L. Nahar and I. U. Arachchige, *Chemistry of Materials*, 2016, **28**, 5406-5414.

Chapter 5: The effect of tin on nickel-based catalysts for furfural hydrogenation

Incipient wetness impregnation (IWI) nickel catalysts were shown to be highly active for furfural hydrogenation in Chapter 3. However, they were also found to only have a selectivity of around 50 % to furfuryl alcohol and suffer from rapid deactivation due to coking. Therefore, in order to improve the selectivity and/or stability of the nickel catalysts, tin was introduced as a dopant. In steam reforming, the introduction of Sn to nickel-based catalysts led to improvements in catalytic performance, particularly with regard to stability.[1] Whilst this a fairly different reaction, the premise of stabilising coordinatively unsaturated corner and edge sites, which may have different reactivity and stability, was thought to also likely be applicable to furfural hydrogenation. In fact, Peter *et al.*[2] found that for vapour-phase furfural hydrogenation, layered double hydroxide Ni-Sn/Al_2O_3 catalysts exhibited moderate improvements in furfuryl alcohol selectivity (up to ~75 %) when the alloy present was Ni_3Sn_4. However, the catalysts also had very low activities, despite the high reaction temperature of 280 °C. Ni-Sn based catalysts showed more significant improvements in furfuryl alcohol selectivity (<95 %) when the reaction was carried out in the liquid phase in batch reactors.[3-6] Whilst these reaction conditions are very different to those used in this thesis (the current work uses vapour-phase furfural, and a flow reactor), the addition of tin may still have beneficial effects on furfuryl alcohol selectivity. Therefore, in this chapter, Sn-doped nickel IWI catalysts and SnNi colloidal nanoparticle catalysts are evaluated for vapour-phase furfural hydrogenation.

5.1 Tin-doped nickel IWI catalysts for furfural hydrogenation

The initial tin-doped catalysts in the current study were prepared using successive IWI as a simple way of synthesising catalysts containing the two metals to determine the effect of tin on nickel catalysts for furfural hydrogenation. The following sections discuss the synthesis and characterisation of the IWI catalysts, catalytic performance and catalyst deactivation.

5.1.1 Synthesis and characterisation of tin-doped nickel IWI catalysts

The direct reduction of $Ni(NO_3)_2/SiO_2$, without calcination, has been shown to give superior activity elsewhere for furfural hydrogenation,[7] therefore this approach was adopted for the catalysts here without further investigation. The direct reduction process for $Ni(NO_3)_2/SiO_2$ catalysts was discussed in Chapter 3 and indicated a two-step reduction process whereby the nickel precursor was first reduced to NiO and then reduced to Ni metal in a second step. The reduced nickel catalyst was then impregnated with $SnCl_2$ and reduced under the same conditions as chosen for the

reduction of the nickel precursor in order to prevent the reduction procedure affecting the already formed nickel particles. There was some concern that the $SnCl_2$ precursor may result in significant quantities of chlorine remaining on the catalyst, however XRF analysis of the pre-reduction and post-reduction Sn-doped catalysts revealed very little remained on the catalysts after reduction (pre-reduction: 6500 ppm; post-reduction: 180 ppm; note ppm is by mass of catalyst). Two tin doped catalysts were prepared, one with a tin loading of 0.25 wt. % and a second with a higher tin loading of 1.5 wt. %, denoted as 0.25Sn-Ni/SiO_2 and 1.5Sn-Ni/SiO_2 respectively. The Ni loading for comparison with the Sn values is nominally 5 wt. % throughout.

Figure 84 shows TEM images of the post-reduction Ni/SiO_2 and 1.5Sn-Ni/SiO_2 IWI catalysts. Both catalysts were found to have a broad distribution of metal particle sizes, with the average particle found to be 7 ± 6 nm and 9 ± 4 nm for Ni/SiO_2 and 1.5Sn-Ni/SiO_2 respectively.

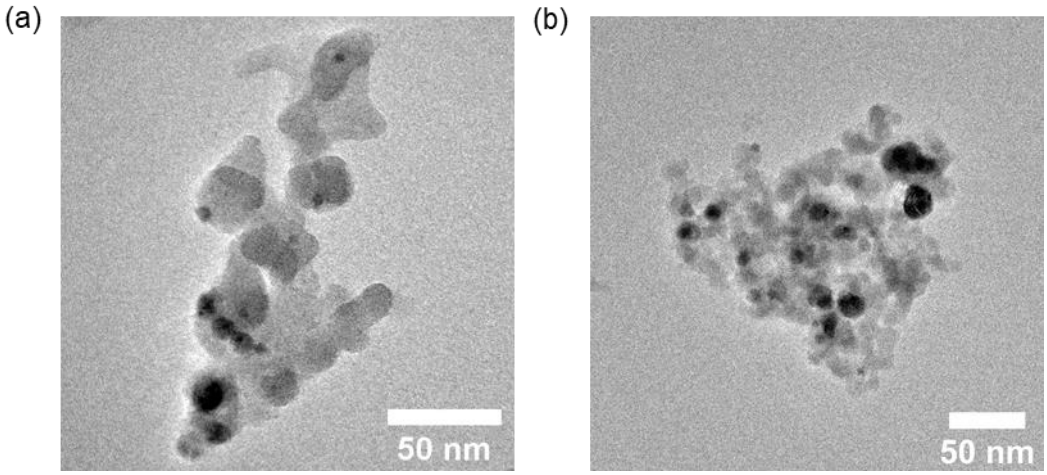

Figure 84: TEM images of (a) post-reduction Ni/SiO_2 IWI catalyst and (b) post-reduction Sn-Ni/SiO_2 IWI catalyst

The 1.5Sn-Ni/SiO_2 catalyst was also imaged using STEM. Figure 85 includes a high angle annular dark field (HAADF) image, a bright field (BF) image and elemental maps of nickel and tin produced using STEM-EDX analysis. The elemental mapping revealed that there was a very uneven distribution of tin across the nickel particles, with some nickel particles containing almost no tin. This means that correlating any effects of tin on catalysis may be challenging since some areas will behave like the nickel only catalyst, whilst others will be heavily tin doped.

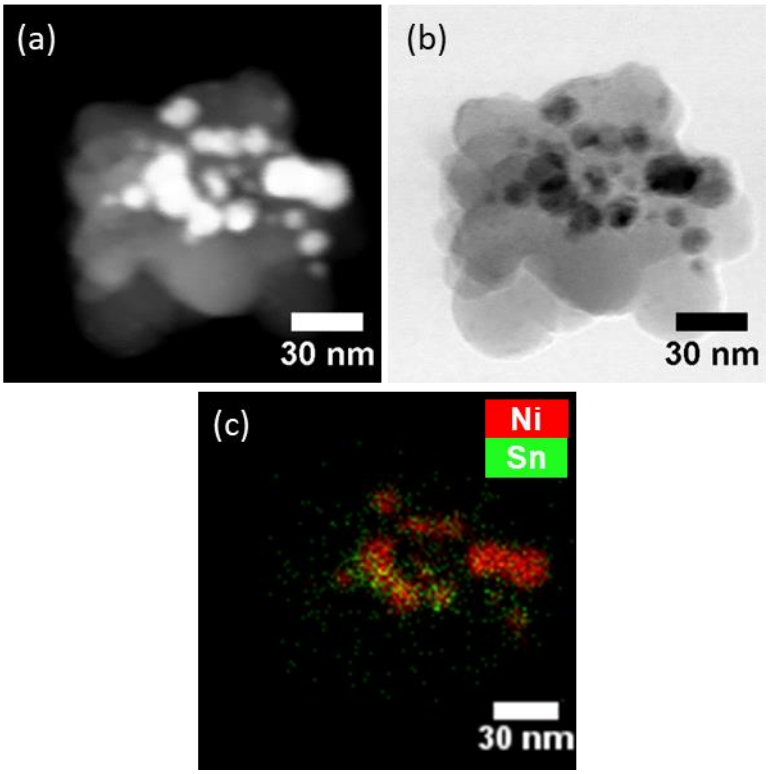

Figure 85: (a) HAADF-STEM image of 1.5Sn-Ni/SiO_2, (b) BF-STEM image of 1.5Sn-Ni/SiO_2 and (c) elemental map of Ni and Sn for the 1.5Sn-Ni/SiO_2 catalyst produced using STEM-EDX analysis

Further information on the structure and composition of the metal particles in the Sn-doped catalysts was obtained through pXRD analysis (Figure 86). All patterns contain a reflection at around 44.5 °, which corresponds to the Ni(111) reflection for metallic nickel, indicating all catalysts contain nickel metal. There were not any observable changes in the pattern for the 0.25Sn-Ni/SiO_2 catalyst compared to the nickel only catalyst, however when tin loading was increased to 1.5 wt. %, there was an additional reflection at 42.3 °. The resolution is too low to make a definitive assignment for this reflection, however it is reasonable to ascribe this to one of the two cubic forms of Ni_3Sn, which both have a reflection close to this angle.[8, 9]

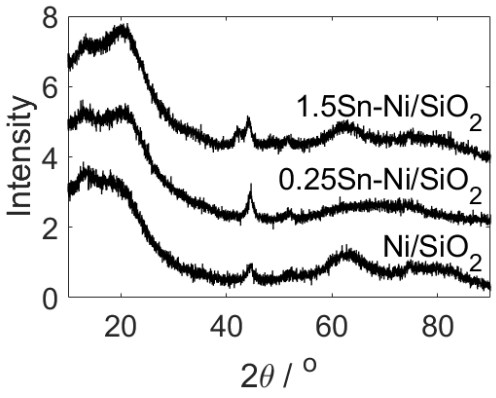

Figure 86: pXRD patterns for post-reduction Ni/SiO_2, 0.25Sn-Ni/SiO_2 and 1.5Sn-Ni/SiO_2 IWI catalysts; reduction procedure: samples were heated to 500 °C at a rate of 15 °C min^{-1} in 30 mL min^{-1} of H_2 and held at 500 °C for 2 h before cooling to room temperature. Samples were exposed to air prior to and during analysis. The data has been vertically offset for clarity.

In order to study the distribution of tin on the surface of the nanoparticles, the IWI catalysts were analysed using CO-DRIFTS (for details on the development of the cell used for this experiment, see Appendix 4). Figure 87a shows the spectra obtained for the nickel only catalyst (although supported on KIT-6 silica to allow for easier packing of the bed rather than the Cab-O-Sil silica, which is the standard silica used for IWI catalysts) and the 1.5Sn-Ni/SiO_2 catalyst. Both spectra contain two key peaks at around 2000 cm^{-1} and 1880 cm^{-1} that, for nickel catalysts, correspond to linear and bridging CO respectively.[10, 11] There is also a significant peak at around 1625 cm^{-1} in the spectrum of the Ni/KIT-6 catalyst which has previously been assigned as an absorbed carbonate species formed from CO interacting with support or NiO.[11] Since the surface area of the KIT-6 silica is around 3 to 4 times higher than that of the standard silica used for the IWI catalysts (Cab-O-Sil), the presence of the peak in the KIT-6 supported sample is likely related to the increased surface area of the support.

By plotting the data in absorbance (as required for quantitative analysis) and fitting Gaussian peaks to the bridging and linear CO peaks, the ratio of the two species present can be evaluated. The ratio of bridging to linear CO is slightly higher for the Ni/KIT-6 sample (1.36) than for the 1.5Sn-Ni/SiO_2 catalyst (1.24), however this difference is likely within the error of the peak fitting. A Ni/γ-Al_2O_3 catalyst prepared *via* IWI was reported to have a ratio of bridging to linear CO of 1.0,[12] which is roughly similar to the results found here for the Ni/KIT-6 catalyst (it should be noted that the authors[12] do not report the average metal particle size for the Ni//γ-Al_2O_3 catalyst, although broad metal reflections in the pXRD pattern may suggest the average size is roughly similar to the metal particles in the catalysts prepared here). The similar ratios of bridging to linear CO likely indicates that tin is occupying both corner/edge sites and sites on the flat surface. CO typically binds linearly on the edge and corner sites since there is enough space for a CO molecule to bind to every site,

whereas CO typically binds in bridging modes on flat surfaces (except at higher pressures of CO) since there is more crowding.[13] Therefore, if tin were to occupy edge/corner sites, then there would be a decrease in linearly bound CO. However, if tin were to occupy sites on the flat surface, then there would be an increase in linearly bound CO since there will be some nickel sites on the flat surface that are surrounded by tin resulting in linear CO binding. Therefore, if tin is occupying both types of site, then the effects on the amount of linearly bound CO would counteract themselves, resulting in similar bridging to linear CO ratios. Therefore, this could indicate that there is a relatively even distribution of tin on the surface of the nickel particles. However, there are other explanations worth consideration such as some segregation of nickel and tin or the reduction process resulting in the migration of tin from the surface of the nickel particles into bulk, such that there is minimal tin on the surface of the nickel particles.

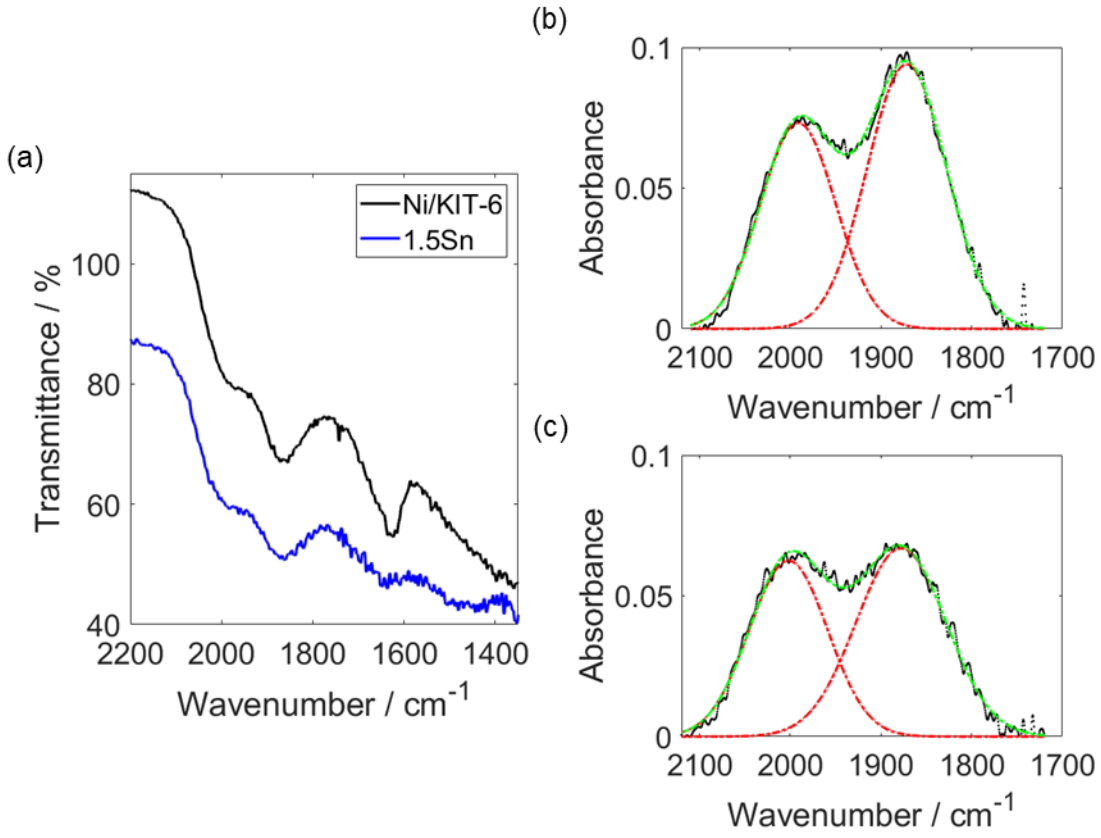

Figure 87: (a) CO-DRIFTS spectra of post-reduction Ni/KIT-6 and 1.5Sn-Ni/SiO_2 IWI catalysts (spectra are vertically offset for clarity), (b) fitted peaks for linear (~2000 cm^{-1}) and bridging (~1880 cm^{-1}) CO for Ni/KIT-6 and (c) fitted peaks for linear (~2000 cm^{-1}) and bridging (~1880 cm^{-1}) CO for 1.5Sn-Ni/SiO_2. For the fitted spectra (shown in (b) and (c)), the data was plotted in absorbance and a polynomial baseline was applied before Gaussian peaks were fitted. Reduction procedure: samples were heated to 500 °C at a rate of 15 °C min^{-1} in 30 mL min^{-1} of H_2 and held at 500 °C for 2 h before cooling to room temperature. Samples were transferred to a glovebox under inert conditions prior to being loaded and sealed in the cell.

Table 9: Positions of the linear and bridging CO peaks and the ratios of bridging to linear CO from CO-DRIFTS analysis of the IWI catalysts.

Catalyst	Position of linear peak / cm^{-1}	Position of bridging peak / cm^{-1}	Ratio of bridging to linear CO
Ni/KIT-6	1992	1872	1.36
1.5Sn-Ni/SiO_2	2002	1878	1.24

5.1.2 Tin-doped Ni/SiO_2 IWI catalysts for furfural hydrogenation

The IWI catalysts were then evaluated for furfural hydrogenation (Figure 88). The introduction of tin, even in low amounts (0.25 wt. %), led to an order of magnitude drop in mass activity. However, the introduction of a larger amount of tin (1.5 wt. %) caused a comparatively minor further decrease in mass activity. Therefore, once tin is present in the catalyst, even in small amounts, the addition of further tin does not appear to have a significant effect on mass activity. It should also be noted that the mass activity of copper chromite, the current standard industrial catalyst for this process, was previously found to be 23 $mmol_{prod}\ g_{cat}^{-1}\ h^{-1}$ after 5 h TOS (Chapter 3) which is fairly similar to the mass activities found for the Sn-doped catalysts. Therefore, although the introduction of tin is detrimental to catalytic activity, it is still expected to be of an acceptable level when comparing to the standard industrial catalyst. The effect of tin on the selectivity of the catalysts followed a different trend; increasing amounts of tin led to increasing selectivity towards furfuryl alcohol. In fact, 1.5Sn-Ni/SiO_2 had a selectivity to furfuryl alcohol of around 85 % which is a significant improvement of around 35 % compared to Ni/SiO_2. It should be noted that although the conversions were different for the two catalysts (due to the significant differences in activity), conversion has a minimal impact on selectivity for the Ni/SiO_2 catalyst. As discussed in Chapter 3, the selectivity was maintained throughout a reactor run despite rapid deactivation of the catalyst (due to coking) resulting in progressively lower conversions. The deactivation rate constants (as introduced in Section 3.2.2 in Chapter 3) were not significantly affected by the addition of tin to the nickel-based catalysts. Overall, despite decreases in catalytic activity, the introduction of tin appears to be beneficial due to the significant increase in selectivity.

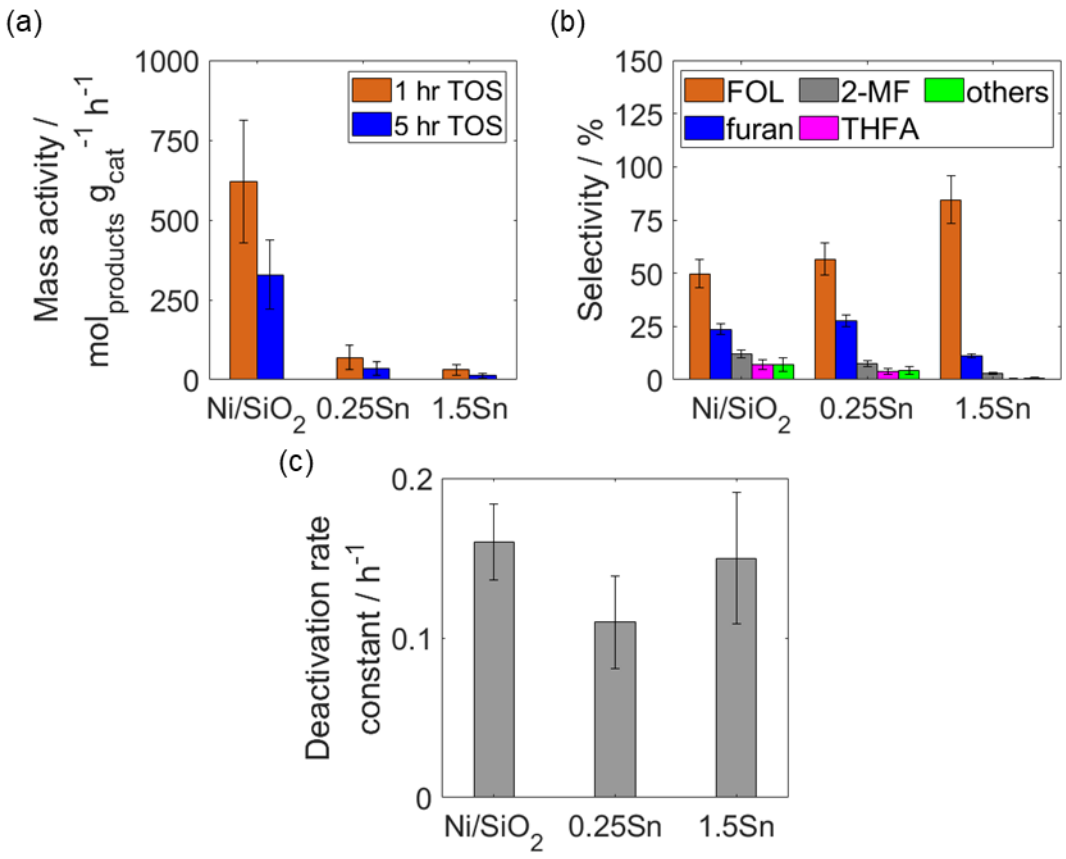

Figure 88: Averaged results for Ni/SiO_2 and Sn-doped Ni/SiO_2 where 0.25Sn and 1.5Sn are 0.25Sn-Ni/SiO_2 and 1.5Sn-Ni/SiO_2 respectively; (a) mass activity at 1 and 5 h TOS; (b) selectivity; (c) deactivation rate constant; errors shown are based on repeat measurements of a typical sample as indicated in the experimental section. Key to product abbreviations: FOL = furfuryl alcohol, 2-MF = 2-methylfuran, furan = furan, THFA = tetrahydrofurfuryl alcohol, other are predominantly butanal, 2-methyl tetrahydrofuran and tetrahydrofuran

5.1.3 Determining the effect of furfural:H_2 ratio and reaction temperature on the catalytic performance of Sn-doped nickel catalysts during furfural hydrogenation

The furfural:H_2 ratio has the potential to impact the selectivity, activity and stability of the catalysts. To study this, furfural hydrogenation was carried out using 1.5Sn-Ni/SiO_2 with a furfural:H_2 ratio of 1:37 compared to the standard conditions of 1:19. Both mass activity and selectivity were not significantly affected by this change and only a minor difference was seen in the deactivation rate constant (see Figure 89). Therefore, changing the furfural:H_2 in this range does not significantly impact the results.

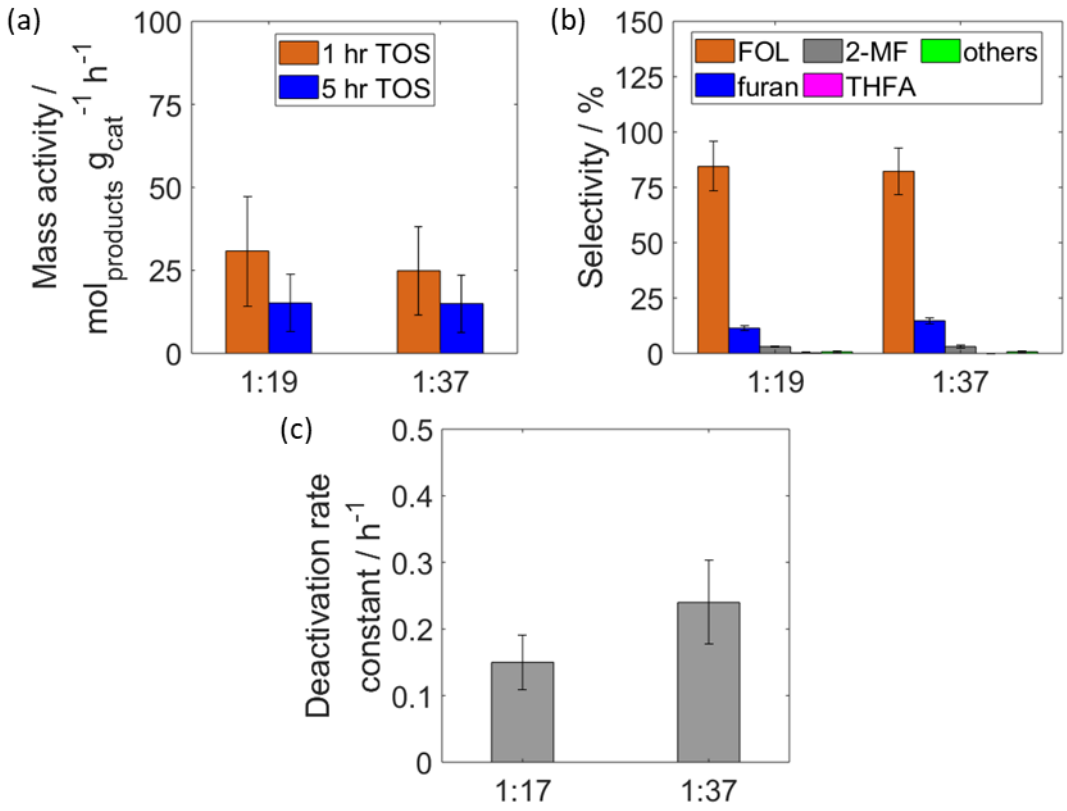

Figure 89: Averaged results comparing the impact of altering furfural:H_2 ratio for 1.5 wt. % Sn-Ni/SiO_2; (a) mass activity at 1 and 5 h TOS; (b) selectivity; (c) deactivation rate constant; errors shown are based on repeat measurements of a typical sample as indicated in the experimental section. Key to product abbreviations: FOL=furfuryl alcohol, 2-MF=2-methyl furan, furan=furan, THFA=tetrahydrofurfuryl alcohol, others are predominantly butanal, 1-butanol, 2-methyl tetrahydrofuran and tetrahydrofuran.

It is also possible for the reaction temperature to impact the selectivity, activity and stability of the catalysts. Furfural hydrogenation was carried out with 1.5Sn-Ni/SiO_2 at a reaction temperature of 165 °C compared to the standard temperature of 180 °C. The results at 165 °C were very similar to those obtained under standard conditions, with only a slight increase in the deactivation rate constant (see Figure 90). The decrease in temperature employed here was only moderate – mainly due to the boiling point of furfural (162 °C) – however, some literature examples have carried out the reaction at significantly different temperatures. Nakagawa *et al.*[7] carried out furfural hydrogenation with Ni/SiO_2 catalysts at lower temperatures such as 130 °C. They reported FOL or THFA as the main product (dependent on conversion), however furan and other side products were not observed in significant quantities, which is markedly different to the results of the Ni/SiO_2 catalyst discussed previously in Chapter 3. However, operating at such low temperatures (~30 °C lower than the boiling point of furfural), may lead to the condensation of reactants and products on the catalyst bed. Though it is unclear what impact this may have, it could be contributing to the differences in selectivity observed between the results of Nakagawa *et al.* and those in this thesis.

However, the impact of temperature on selectivity is also supported by Vargas-Hernández *et al.*[14] They reported that a Ni/SBA-15 catalyst had a selectivity to furan of 98 % when furfural hydrogenation was carried out at 230 °C compared to between 40 % and 70 % (depending on TOS) when the reaction was carried out at 170 °C. Therefore, with Ni/SiO_2-based catalysts, decarbonylation to furan appears to be highly temperature dependent over the range of 130 – 230 °C, going from a minor impurity to the dominant product.

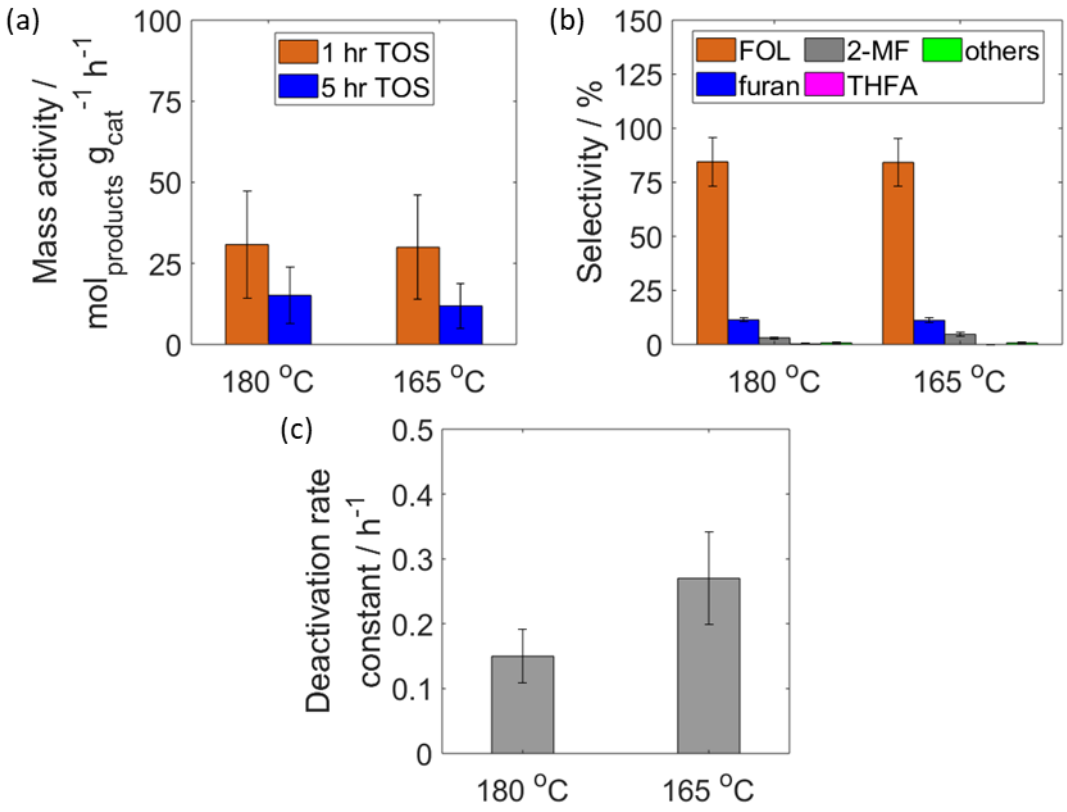

Figure 90: Averaged results comparing the impact of altering temperature for 1.5 wt. % Sn-Ni/SiO_2; (a) mass activity at 1 and 5 h TOS; (b) selectivity; (c) deactivation rate constant; errors shown are based on repeat measurements of a typical sample as indicated in the experimental section. Key to product abbreviations: FOL=furfuryl alcohol, 2-MF=2-methyl furan, furan=furan, THFA=tetrahydrofurfuryl alcohol, others are predominantly butanal, 1-butanol, 2-methyl tetrahydrofuran and tetrahydrofuran.

5.1.3 Investigating the cause of the rapid deactivation observed during furfural hydrogenation

The spent catalysts were analysed using a variety of techniques (as for the pure Ni catalyst in Chapter 3) in order to investigate the potential reasons for the relatively rapid deactivation of the catalysts (complete loss of activity over ~15 – 20 h TOS). Whilst there was no significant change in the pXRD pattern for the nickel reference catalyst apart from some slight narrowing of the reflections likely due to a small amount of sintering, there were some differences observed for the post-reaction 1.5Sn-Ni/SiO_2 catalyst (Figure 91). There does not appear to be any significant

sintering occurring during the reaction, however the relative intensity of the reflection at around 42.3 °, earlier ascribed to one of the cubic variants of Ni_3Sn, has significantly increased compared to the reflection assigned to nickel metal at around 44.5 °. This suggests that during the course of the reaction, tin is migrating throughout or into the nickel metal particles, leading to an increase in the amount of the Ni_3Sn phase present. It is unclear whether the increasing amounts of Ni_3Sn present in the catalyst is a source of the deactivation observed. However, as both the Ni/SiO_2 catalyst and the catalyst doped with 0.25 wt. % Sn both exhibited similar rapid deactivation, it is likely that there is another factor contributing to the rapid deactivation observed. Additionally, the pXRD data indicates that sintering cannot account for the large and rapid loss of activity for the IWI catalysts.

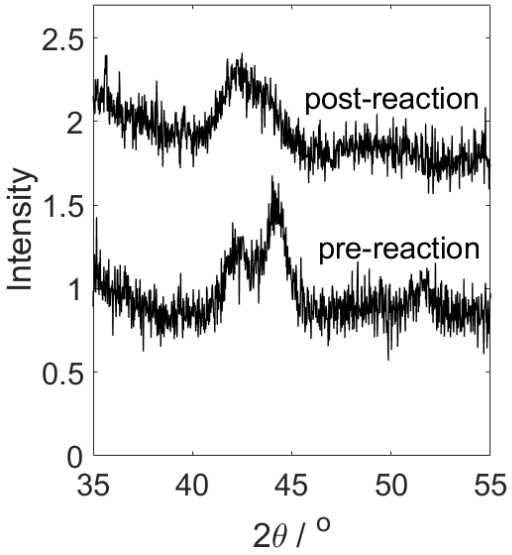

Figure 91: pXRD patterns of 1.5Sn-Ni/SiO_2 pre-reaction (reduction only) and post-reaction (*i.e.* after complete deactivation; ~15 – 20 h TOS). Reduction procedure for pre-reaction sample: the sample was heated to 500 °C at a rate of 15 °C min^{-1} in 30 mL min^{-1} of H_2 and held at 500 °C for 2 h before cooling to room temperature. Furfural hydrogenation was carried out after *in situ* reduction of the catalyst (standard reduction conditions for IWI catalysts) and under standard reaction conditions. The data has been vertically offset for clarity.

Figure 92 shows a TEM image of the spent 1.5Sn-Ni/SiO_2 catalyst, where it can be seen that no significant sintering has occurred (pre-reaction: 9 ± 4 nm; post-reaction: 10 ± 5 nm), in agreement with the pXRD patterns of the spent catalysts. This confirms that sintering is unlikely to be the primary reason for the rapid deactivation observed.

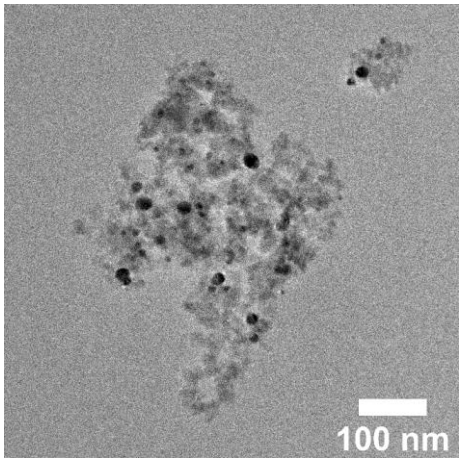

Figure 92: TEM image of spent (*i.e.* after complete deactivation; ~15 - 20 h TOS) 1.5Sn-Ni/SiO_2; furfural hydrogenation was carried out after *in situ* reduction of the catalyst (standard reduction conditions for IWI catalysts) and under standard reaction conditions

As discussed in Chapter 3, the Ni/SiO_2 reference catalyst exhibited rapid deactivation during furfural hydrogenation due to coking, therefore, it may be expected that the Sn-doped catalysts may also deactivate due to coking. To investigate this, the spent 1.5Sn-Ni/SiO_2 catalyst was analysed using DRIFTS and SS NMR.

Figure 93 shows the DRIFT spectra of the spent IWI catalysts. The spectra for the Sn-doped catalysts are very similar to the spectrum for the Ni/SiO_2 catalyst, indicating that the same coke species are likely present on both catalysts. Previous analysis (Chapter 3) of the spent Ni/SiO_2 catalyst identified that the coke species present were related to furfuryl alcohol since the spectrum had several key features that were also present in a sample of silica that was exposed to furfuryl alcohol under standard reaction conditions. This implies that the Sn-doped samples also have coke species related to furfuryl alcohol and that the introduction of tin does not affect this coking mechanism.

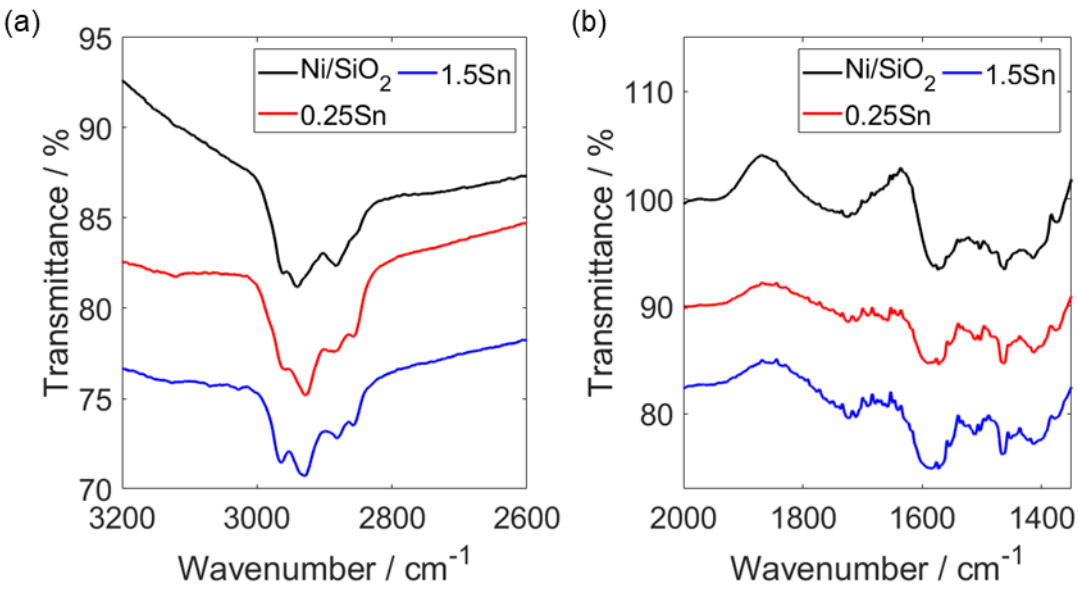

Figure 93: DRIFT spectra of Ni/SiO_2, 0.25Sn-Ni/SiO_2 (0.25Sn) and 1.5Sn-Ni/SiO_2 (1.5Sn) showing (a) 3200 – 2600 cm^{-1} and (b) 2000 – 1350 cm^{-1}. Spectra have been vertically offset for clarity.

Further evidence of the coke species being related to furfuryl alcohol came from solid state cross polarization/magic angle spinning ^{13}C-NMR (CP/MAS ^{13}C-NMR) analysis of spent 1.5Sn-Ni/SiO_2 (Figure 94). The main peaks in the spectrum correspond to furfuryl alcohol (153.0 ppm, 143.1 ppm, 109.4 ppm, 57.7 ppm)[15] and notably, there is no indication that furfural is present on the spent catalyst.[16] There is an additional weak peak at 24.8 ppm, which is in the alkane C-H region. NMR studies of poly(furfuryl alcohol)[17, 18] have shown that the bridging CH_2 groups present in furfuryl alcohol polymers gives a strong peak at around 28 ppm, which is fairly close to the weak peak observed at 24.8 ppm. Additionally, no peak is observed at 57.0 ppm in poly(furfuryl alcohol) since the methylol group is only present at the end of the polymer chain and so not readily detected. In the spectrum for the spent Sn-doped catalyst, the combination of a strong methylol peak and a weak bridging CH_2 peak suggests that rather than furfuryl alcohol polymers, furfuryl alcohol oligomers may be present, as oligomers would have less bridging CH_2 groups and more methylol groups. Alternatively, the signal at 24.8 ppm may correspond to long chain hydrocarbons as these species were previously identified on a sample of the spent IWI Ni/SiO_2 catalyst by Soxhlet extraction/GC-MS analysis, as discussed in Chapter 3. Overall, NMR analysis strongly implicates furfuryl alcohol in the coking process and therefore deactivation of the catalysts.

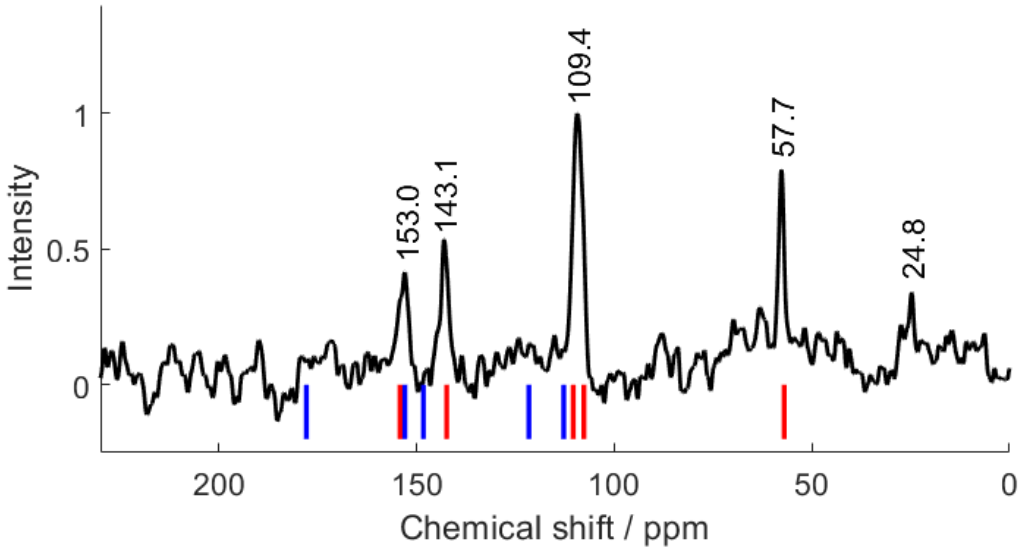

Figure 94: solid state CP/MAS ^{13}C NMR spectrum of spent 1.5Sn-Ni/SiO_2, with the positions of the peaks for furfuryl alcohol (solution-state NMR) shown by the red vertical lines[15] and the positions of the peaks for furfural (solution-state NMR) shown by the blue vertical lines[16]

5.2 Supported colloidal Ni and SnNi nanoparticle catalysts for furfural hydrogenation

The synthesis of small phosphorus-free colloidal nickel and tin-nickel nanoparticles was discussed in detail in Chapter 4. These nanoparticles have a narrow particle size distribution and a relatively uniform distribution of tin. Additionally, the increased uniformity of these nanoparticles allows for clearer interpretation of analysis using more advanced analytical techniques such as near ambient pressure X-ray photoelectron spectroscopy (NAP-XPS) as discussed in Chapter 4, which identified further details on the structure and composition of the surface of the nanoparticles. Therefore, carrying out furfural hydrogenation using these nanoparticles will allow correlations between the structure and composition of the catalyst and catalytic performance to be more reliably established.

5.2.1 Characterisation of the KIT-6 supported colloidal nanoparticle catalysts

In order to test the catalysts during vapour-phase furfural hydrogenation, the nanoparticles had to be supported on silica, in this case mesoporous KIT-6 silica. This support was chosen as it was used effectively in prior work to support nanoparticles by capillary inclusion.[19-21] A targeted nickel loading of 5 wt. % was chosen for ease of comparison to the IWI catalysts, however the sequential addition catalyst was found to have a lower than expected nickel loading of 1.4 wt. % (based on ICP-OES analysis). This was because the amount of nanoparticles loaded onto the support was based on the yield of the other similar nanoparticle reactions, however it was later found that the sequential addition method resulted in a significantly lower yield in the batch used (reason unknown). TEM

images of the supported nanoparticles are shown in Figure 95, which indicate that the nanoparticles have been successfully supported on the KIT-6 silica.

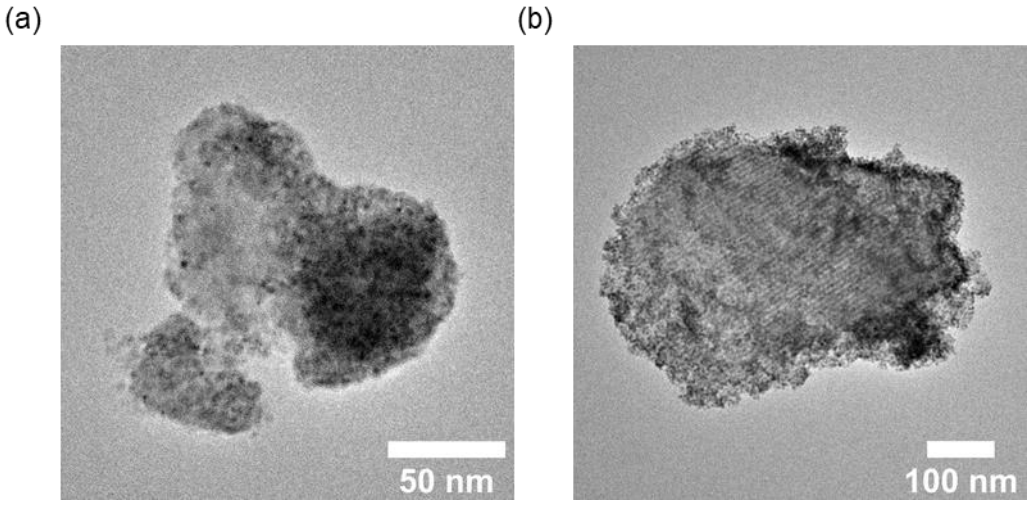

Figure 95: TEM images of the KIT-6 supported nanoparticles; (a) nickel nanoparticles and (b) SnNi sequential addition method nanoparticles

Whilst the nanoparticles were reduced during synthesis, exposure to air during sample storage did result in oxidation of the surface of the nanoparticles, as shown by the HAADF-STEM imaging which revealed they had a core-shell structure. Therefore, a reduction procedure was necessary prior to the catalysts being used for furfural hydrogenation. To investigate the appropriate reduction temperature for these catalysts, TPR analysis was carried out. All of the catalysts consumed hydrogen during the TPR experiment, confirming that the nanoparticles had oxidised to some extent. Although there was some slight variance in the reduction temperature for the nanoparticle catalysts, hydrogen consumption was complete by 300 °C in all cases, and so this temperature was chosen for *in situ* reduction prior to catalysis. It should be noted that the peak for the sequential addition catalyst is smaller than the other colloidal nanoparticle catalysts, however this is due to the fact that the metal loading of the sequential addition catalyst was lower than targeted and so a lower hydrogen consumption would be expected.

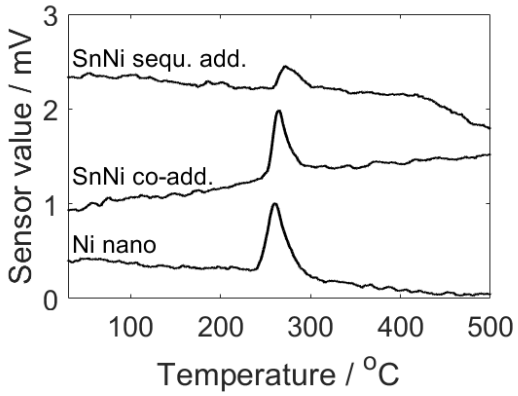

Figure 96: TPR of the supported nanoparticle catalysts, where Ni nano is Ni nano/KIT-6, SnNi co-add. is SnNi co-addition method nanoparticles supported on KIT-6 and SnNi sequ. add. is SnNi sequential addition method nanoparticles supported on KIT-6. The sloping baselines are due to external factors *e.g.* changes in the temperature of the equipment/lab. Spectra are vertically offset for clarity.

Figure 97 shows TEM images of the SnNi sequential addition nanoparticle catalyst after reduction at 300 °C as well as after 30 minutes of furfural hydrogenation (note: the catalyst is still highly active after 30 minutes TOS). In both cases, there is significant sintering, although there are still some areas where smaller nanoparticles can be seen. The presence of capping agents on the surface of colloidal nanoparticles has been shown to modify metal-support interactions,[22, 23] which may offer a possible explanation for the increased sintering.

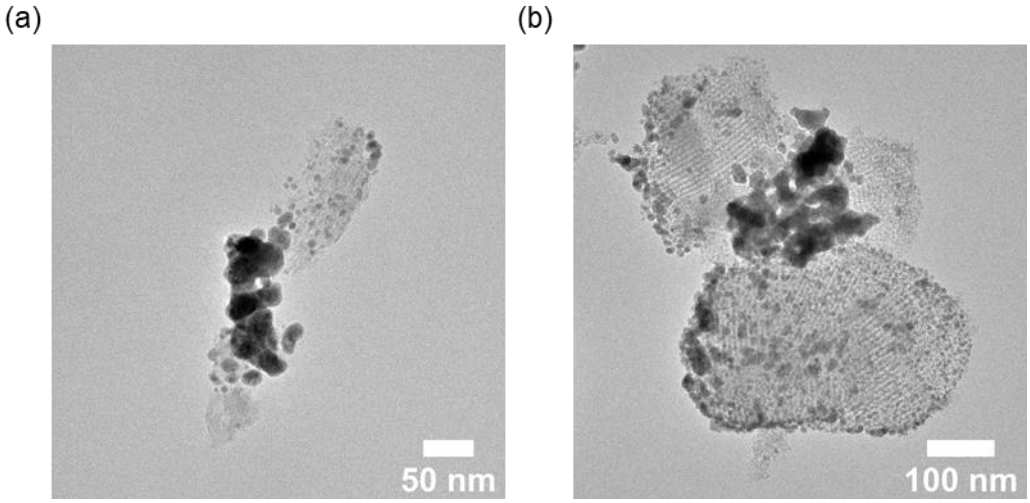

Figure 97: TEM images of the SnNi sequential addition nanoparticle catalyst after (a) reduction at 300 °C and (b) *in situ* reduction at 300 °C followed by 30 minutes of furfural hydrogenation under standard reaction conditions

In order to determine the impact of the sintering on the particle size distribution for the nanoparticle catalysts, the particle size distributions were normalised to the number of particles, the surface area and the volume (Figure 98). The distributions were compared to those of the unsupported nanoparticles as a reference. In the number average graph, there are still a number

of nanoparticles with similar sizes to the unsupported nanoparticles, however there is a notable tail consistent with the significant amount of sintering observed in the TEM images. Since surface area is an important variable for catalysis, the impact on surface area should also be considered. As expected, the sintering had a larger effect on the surface area distribution; the distribution is very broad and most of the contributions to surface area are attributable to larger nanoparticles. Although less important for catalysis, the volume average should still be considered as analytical techniques such as pXRD produce a volume average. The sintering has a very significant effect on the volume distribution, with the large nanoparticles dominating the contributions. Therefore, the results from techniques that produce volume averages like pXRD will favour larger nanoparticles and may not be representative of any smaller nanoparticles present. Overall, the extent of the sintering observed means that significant amounts of the surface area will be coming from larger nanoparticles and therefore the catalysis is likely to be occurring on nanoparticles with a range of different sizes.

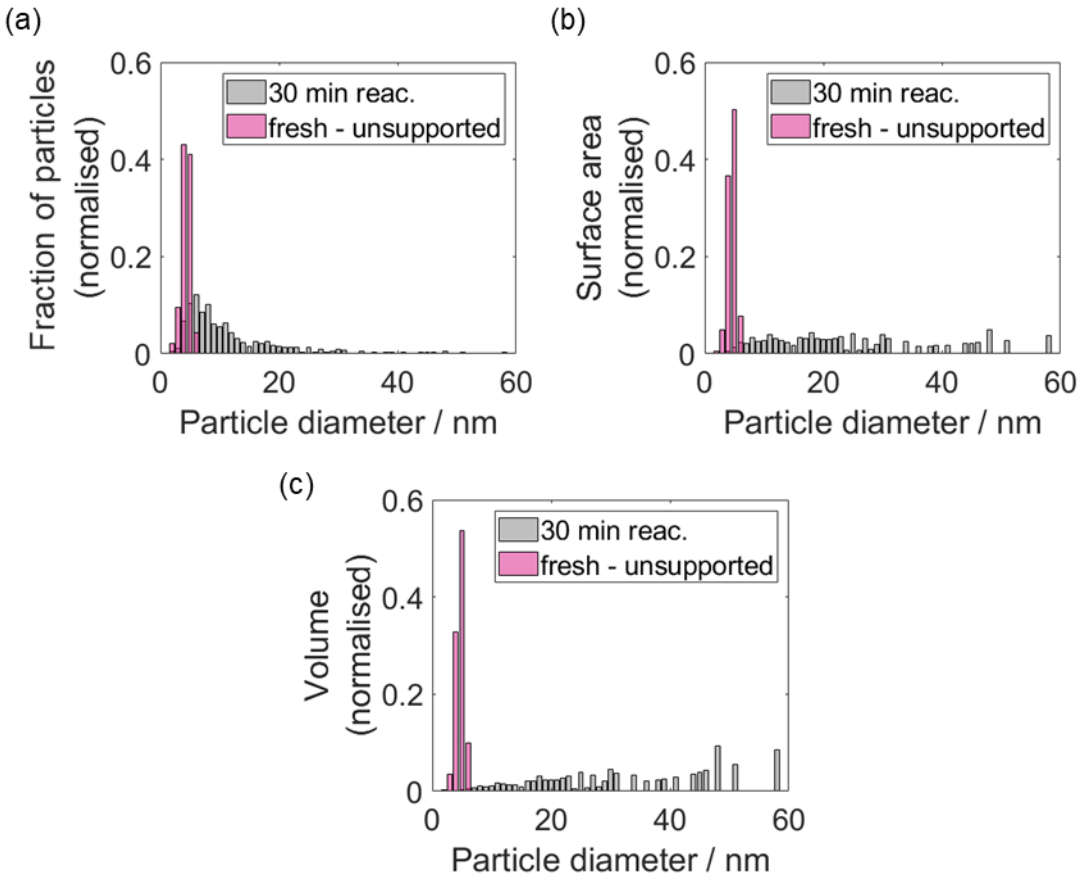

Figure 98: Particle size distributions for SnNi sequential addition nanoparticle catalyst after *in situ* reduction at 300 °C followed by 30 minutes of furfural hydrogenation (30 min reac.) and the unsupported SnNi sequential addition nanoparticles (fresh – unsupported) based on (a) the number of nanoparticles, (b) the surface area and (c) the volume

The extensive sintering of the catalyst during reduction is disappointing, as one of the purposes of preparing colloidal nanoparticles as model catalysts was to produce catalysts with narrow particle size distributions. However, another key reason for preparing colloidal bimetallic nanoparticles was to improve the uniformity of the tin distribution across the nickel particles. Elemental maps of the IWI Sn-doped catalysts revealed that the tin distribution was uneven, with some nickel particles containing almost no tin, and others containing significant quantities. Therefore, the preparation of colloidal bimetallic nanoparticles is still highly beneficial over conventional IWI catalysts. In order to confirm that the Ni:Sn molar ratios still had a narrow distribution in the sintered catalyst (*i.e.* the sample that was reduced *in situ*, followed by 30 minutes of furfural hydrogenation), STEM-EDX analysis was used to produce elemental maps, as well as obtaining point EDX spectra. Elemental mapping (Figure 99b) revealed that both the larger metal particles and smaller metal particles all contained nickel and tin indicating that the sintering does not result in significant segregation of the two metals. Figure 99c shows the distribution of Ni:Sn molar ratios for the sintered catalyst compared to the unsupported, as prepared nanoparticles. There is a significant increase in the average Ni:Sn molar ratio observed by STEM-EDX for the sintered catalyst (5.0 ± 2.3) compared to the as prepared nanoparticles (2.4 ± 0.8). Care must be taken to avoid over-interpretation of the data since there was no verification of the calibration of the EDX detector by external methods (*e.g.* ICP-OES), however this could indicate that the less easily detected smaller metal particles may be enriched with tin. Additionally, the sintered catalyst has a broader distribution of Ni:Sn molar ratios. It should be noted that the areas analysed to obtain the distribution of Ni:Sn molar ratios were generally larger areas with significant sintering, as it was challenging to get enough signal to analyse the smaller particles. Therefore, careful consideration needed to be given to the possibility the significant increase in Ni:Sn molar ratio was due to smaller particles containing more tin, whereas the larger particles contained more nickel. Consequently, it was important to determine if there was a relationship between the size of the metal particle and the amount of nickel that the particle contains relative to tin (Figure 99d). Particles that were larger than around 20 nm generally contained ≥80 % nickel atoms whereas the particles that were smaller than around 20 nm had a broader range of nickel contents. However, overall, there is only a minimal correlation between particle size and metal composition and the key result is that all metal particles contain both nickel and tin. Therefore, despite the sintering and the resulting changes in the composition of the metal particles, the colloidal nanoparticle catalyst is still an improvement over the IWI catalysts since there appears to be no areas of complete segregation.

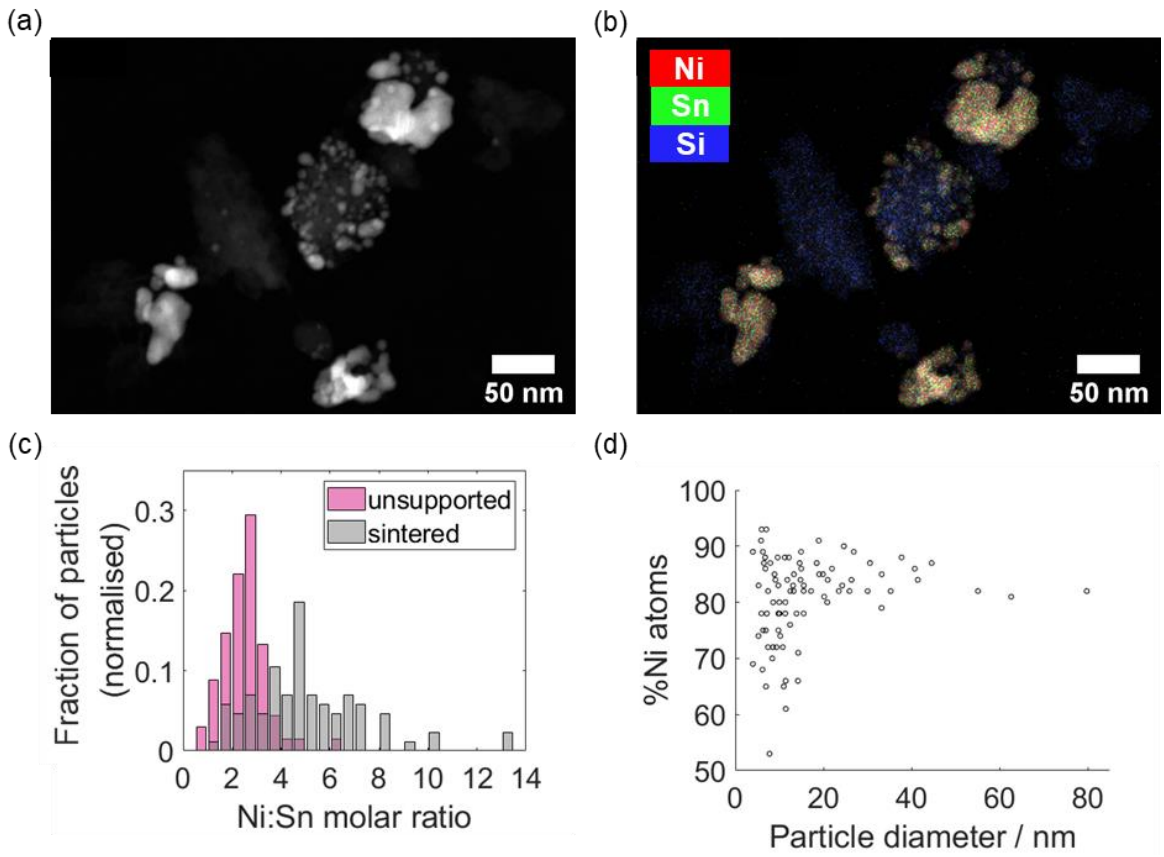

Figure 99: STEM imaging of the KIT-6 supported SnNi sequential addition nanoparticles after *in situ* reduction followed by 30 minutes of furfural hydrogenation; (a) HAADF-STEM image, (b) elemental mapping of nickel, tin and silicon produced using STEM-EDX analysis and (c) comparison of the distributions of Ni:Sn molar ratios for the as prepared unsupported nanoparticles ('unsupported') and the KIT-6 supported nanoparticles after *in situ* reduction followed by 30 minutes of furfural hydrogenation under standard reaction conditions.

It should also be noted that when the spent colloidal nickel nanoparticle catalyst (*i.e.* post-reaction, inactive catalyst) was analysed by TEM, the extent of sintering appeared to be somewhat lessened compared to the SnNi version (Figure 100). In the particle size distributions for the nickel only catalyst, there are significant contributions from smaller nanoparticles to both the number of particles and surface area, in comparison to the SnNi catalyst where the majority of surface area was associated with larger nanoparticles. Therefore, this suggests that tin is playing a role in the sintering process and potentially promoting the sintering of the nanoparticles.

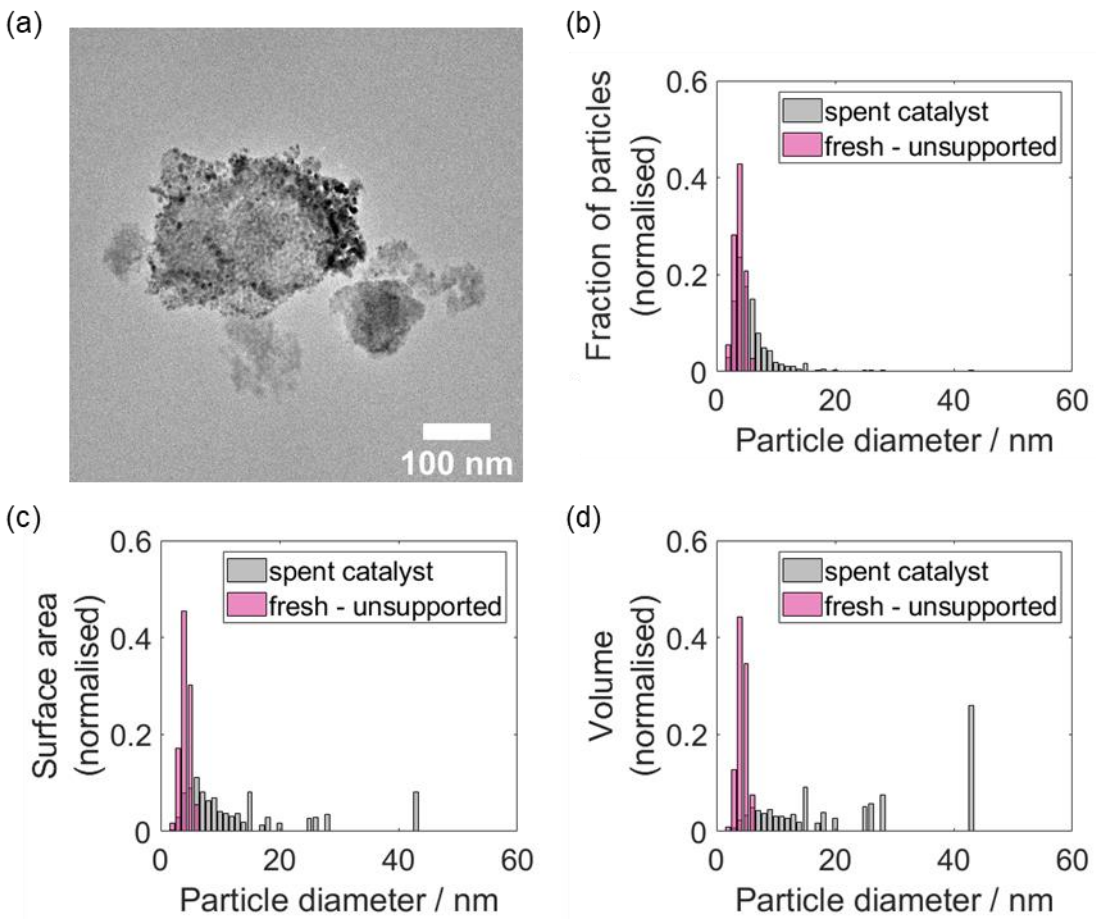

Figure 100: (a) TEM image of spent Ni nano/KIT-6 (post-reaction, inactive catalyst) and the corresponding particle size distributions compared to those of the unsupported nickel nanoparticles ('fresh – unsupported') normalised to the (b) number of particles, (c) surface area and (d) volume

5.2.2 Supported colloidal nanoparticle catalysts for furfural hydrogenation

The supported nickel nanoparticle catalyst was found to have an almost identical selectivity during furfural hydrogenation as the IWI Ni/SiO_2 catalyst (Figure 101), which indicates that the presence of capping agent is not significantly affecting the selectivity. However, in comparison to the IWI Ni/SiO_2 catalyst, the supported nickel nanoparticle catalyst had a mass activity that was an order of magnitude lower (Ni/SiO_2 IWI: 622 ± 192 $mmol_{(prod)}\ g_{(cat)}^{-1}\ h^{-1}$ after 1 h TOS, Ni nano/KIT-6: 66.1 ± 35.4 $mmol_{(prod)}\ g_{(cat)}^{-1}\ h^{-1}$ after 1 h TOS). There could be a number of reasons for this although, since sintering has already been shown to be an issue during the reduction of the colloidal nanoparticle catalysts, this could provide a simple explanation. Alternatively (or in combination), the presence of capping agent on the surface of the nanoparticles may block access to some active sites, resulting in a loss of catalytic activity. The deactivation rate constant was also altered compared to the IWI catalyst, with the nickel nanoparticle catalyst having a deactivation rate constant around 3 times higher (Ni/SiO_2 IWI: 0.16 ± 0.02 h^{-1}, Ni nano/KIT-6: 0.5 ± 0.1 h^{-1}). Whilst

sintering could also be playing a role in the rapid deactivation observed, it was found that for the SnNi nanoparticle catalyst, the reduction step led to significant sintering (this analysis at an intermediate stage was only performed on the bimetallic system), making it likely that at the start of the reaction, the catalyst will already be significantly sintered. Consequently, it is somewhat unlikely that further sintering would result in the rapid deactivation observed. Another potential explanation for the increase in deactivation rate could be the remaining capping agent, which may contribute to coke formation and therefore result in rapid deactivation.

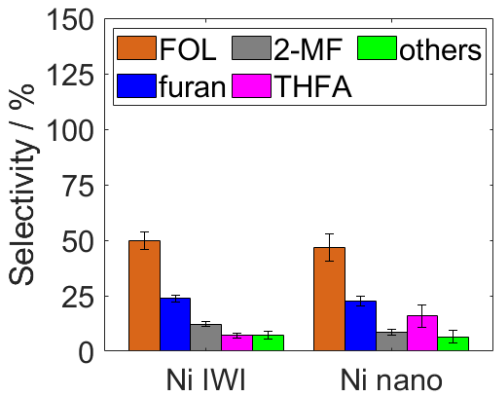

Figure 101: Average selectivity under stable operation of the Ni/SiO2 IWI catalyst ('Ni IWI') and the Ni nano/KIT-6 catalyst ('Ni nano') during furfural hydrogenation under standard reaction conditions. Key to product abbreviations: FOL=furfuryl alcohol, 2-MF=2-methyl furan, furan=furan, THFA=tetrahydrofurfuryl alcohol, others are predominantly butanal, 1-butanol, 2-methyl tetrahydrofuran and tetrahydrofuran.

The supported SnNi (sequential addition) nanoparticles were then evaluated for furfural hydrogenation and compared to the nickel nanoparticle catalyst as well as a Sn-doped IWI catalyst (1.5Sn-Ni/SiO_2), with the results shown in Figure 102. The SnNi nanoparticle catalyst had a >95 % selectivity to furfuryl alcohol, which is significantly higher than even the Sn-doped IWI catalyst that achieved a selectivity of around 85 %. It should be noted that since the SnNi nanoparticles were prepared with a molar Ni/Sn ratio of around 3, that the SnNi nanoparticle catalyst will contain significantly more Sn (roughly double that of the 1.5Sn-Ni/SiO_2 catalyst). Therefore, the improvement in selectivity may be due to the higher amount of Sn in the catalyst. However, STEM-EDX mapping of the IWI catalyst revealed an uneven distribution of tin across the nickel particles, with some nickel particles containing almost no tin. Nickel metal has consistently been seen to produce a much broader range of products, generally achieving a selectivity to furfuryl alcohol of around 50 %. Therefore, if the catalyst contains a mix of Sn-doped nickel and nickel only particles, then the selectivity of the catalyst would be expected to be lower. Since the SnNi nanoparticle catalyst had a more uniform distribution of tin, this may explain the increase in selectivity towards furfuryl alcohol. The mass activity of the SnNi nanoparticle catalyst was around

4 times lower than the nickel nanoparticle catalyst. However, since the nickel content of the catalyst is around 3 times lower due to the low loading of the catalyst, the decrease in activity is likely mostly explained by the lower metal loading. This means that whilst the introduction of tin to the IWI catalysts led to an order of magnitude decrease in activity, the introduction of tin to the nanoparticle catalysts appears to have had a minimal effect. In comparison to the Sn-doped IWI catalyst, the activity is also lower, however again, the nickel content is around 3 times lower in the SnNi nanoparticle catalyst, so the activity is actually likely comparable per metal atom present. The deactivation rate constant for the SnNi nanoparticle catalyst is very similar to the nickel nanoparticle catalyst, but significantly higher than the Sn-doped IWI catalyst. This suggests the introduction of tin to the nanoparticle catalyst is having very little effect on the deactivation rate and that the colloidal nanoparticle catalysts have higher deactivation rates in general. As discussed above, this could potentially be due to sintering, however it is more likely to be related to the presence of capping agent leading to increased coking. Overall, the selectivity of the SnNi nanoparticle catalyst (>95 %) is improved over both the nickel nanoparticle catalyst (~50 %) and the Sn-doped IWI catalyst (~85 %) and is comparable to the copper chromite catalyst (~90 %) discussed in Chapter 3, however nanoparticle catalysts do exhibit more rapid deactivation.

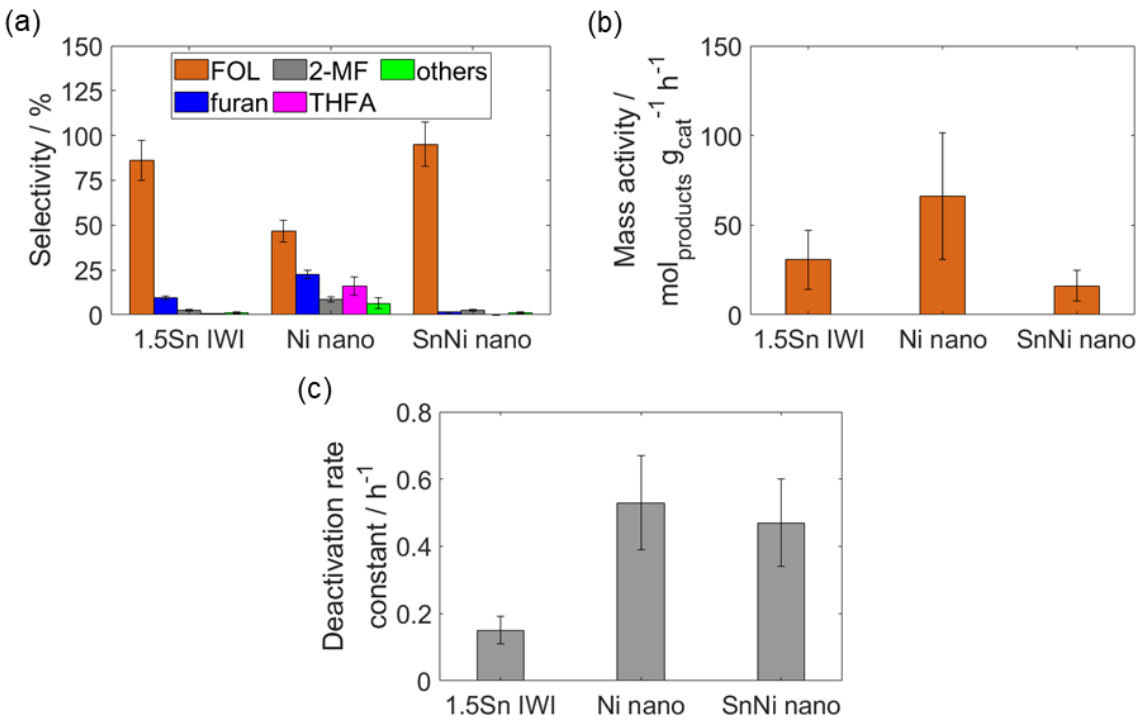

Figure 102: Comparison of 1.5Sn-Ni/SiO_2 IWI catalyst ('1.5Sn IWI') to the KIT-6 supported colloidal nanoparticle catalysts, Ni nano/KIT-6 ('Ni nano') and SnNi nano (sequential addition)/KIT-6 ('SnNi nano') during furfural hydrogenation (a) Average selectivity under stable operation; (b) Mass activity after 1 hr TOS; (c) Deactivation rate constants. Errors shown are based on repeat measurements of a typical sample as indicated in the experimental section. Furfural hydrogenation was carried out under standard reaction conditions. Key to product abbreviations: FOL=furfuryl alcohol, 2-MF=2-methyl furan, furan=furan, THFA=tetrahydrofurfuryl alcohol, others are predominantly butanal, 1-butanol, 2-methyl tetrahydrofuran and tetrahydrofuran.

5.2.3 Characterisation of the spent colloidal nanoparticle catalysts

As discussed above, the nanoparticle catalysts suffer from significant sintering during the reduction step prior to reaction, and so the post-reaction catalyst would be expected to appear sintered. An example image of the spent SnNi sequential addition catalyst is shown in Figure 103, which indeed shows significant sintering.

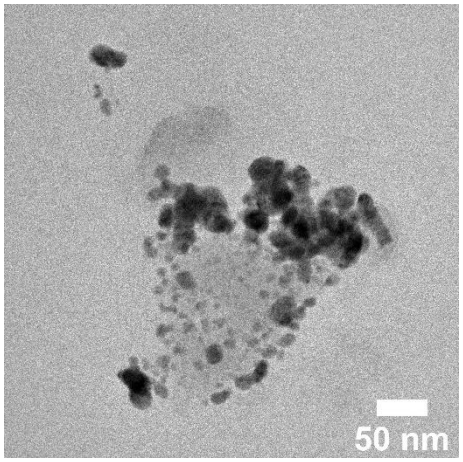

Figure 103: TEM image of the spent KIT-6 supported SnNi (post-reaction, inactive) sequential addition SnNi nanoparticle catalyst

However, as discussed above, the majority of the sintering appears to occur in the reduction step and so the active catalyst is already significantly sintered. Therefore, it was thought that sintering was somewhat unlikely to lead to the rapid deactivation seen in the nanoparticle catalysts. Coking was explored as an alternative since this was identified as the major source of deactivation in the IWI catalysts. The CP/MAS ^{13}C-NMR spectrum of the spent SnNi nanoparticle catalyst is shown in Figure 104. In contrast to the spectrum for the IWI Sn-doped catalyst that contained only furfuryl alcohol peaks, the spectrum here predominantly consists of peaks corresponding to furfural and only has some smaller furfuryl alcohol peaks. This suggests that for the nanoparticle catalyst, furfural species and, to a lesser extent, furfuryl alcohol species are playing a role in catalyst deactivation. However, it is important to note that there is a chance that the catalyst was exposed to furfural at temperatures <180 °C as a result of the shutdown procedure used in this experiment, which could result in the condensation of furfural on the catalyst. This would explain the presence of the furfural peaks in the spectrum, however it would not account for the presence of the furfuryl alcohol peaks since the catalyst was completely deactivated before the reactor was shut down (*i.e.* it would not have been exposed to furfuryl alcohol at temperatures <180 °C). Therefore, whilst it is not possible to determine whether the furfural-based species are due to coking or the condensation of furfural on the catalyst, it is likely that the furfuryl alcohol-based species are related to coking.

Similarly to the spent IWI Sn-doped catalyst, there is also a peak in the alkane region at around 25.2 ppm, however the signal is significantly broader here. As discussed above, this may indicate the formation of oligomers of furfuryl alcohol[17, 18] or, in this case, furfural. The presence of furfuryl alcohol-based species on the spent catalyst indicates that coking is likely contributing to the rapid deactivation seen.

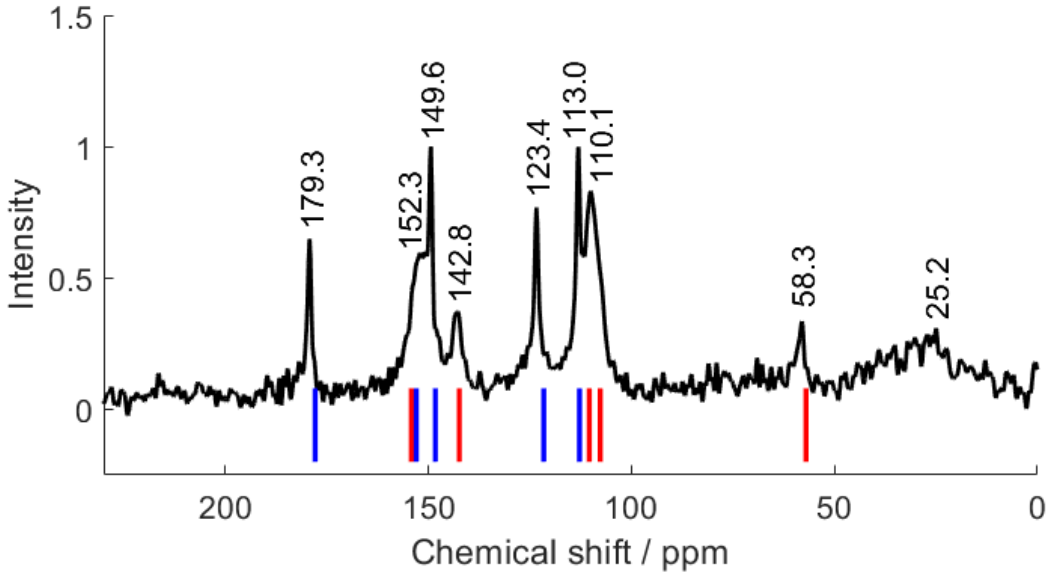

Figure 104: solid state CP/MAS ^{13}C NMR spectrum of the spent SnNi sequential addition nanoparticle catalyst, with the positions of the peaks for furfuryl alcohol (solution-state NMR) shown by the red vertical lines[15] and the positions of the peaks for furfural (solution-state NMR) shown by the blue vertical lines[16]

The role of coking in the deactivation of the SnNi nanoparticle catalyst was also investigated using DRIFTS (Figure 105). Whilst there were only weak peaks in the C-H region for the spent SnNi nanoparticle catalyst, there were strong signals that corresponded to furfural seen in the lower wavenumber region, with the spectrum matching closely to that of the sample of Cab-O-Sil exposed to furfural under reaction conditions (180 °C, 70 mL min^{-1} H_2). This fits well with the SS NMR spectrum, which showed the dominant species on the spent catalyst was related to furfural, however as discussed above, the presence of furfural is likely due to condensation of furfural on the catalyst bed as it was exposed to furfural at temperatures <180 °C. Since the furfural peaks are so strong in the DRIFTS spectrum, it is hard to determine whether there are any other species present, however there are some unaccounted for peaks (~1750 cm^{-1} (broad) and ~1500 cm^{-1}). These peaks roughly fit with some seen in the spectra for furfuryl alcohol and silica exposed to furfuryl alcohol under reaction conditions, suggesting that furfuryl alcohol-based species may also be present. This is consistent with the SS NMR spectrum which also suggested the presence of furfuryl alcohol-based species. Therefore, this provides further evidence that furfuryl alcohol and/or its oligomers are playing a role in the coking and deactivation of the catalyst.

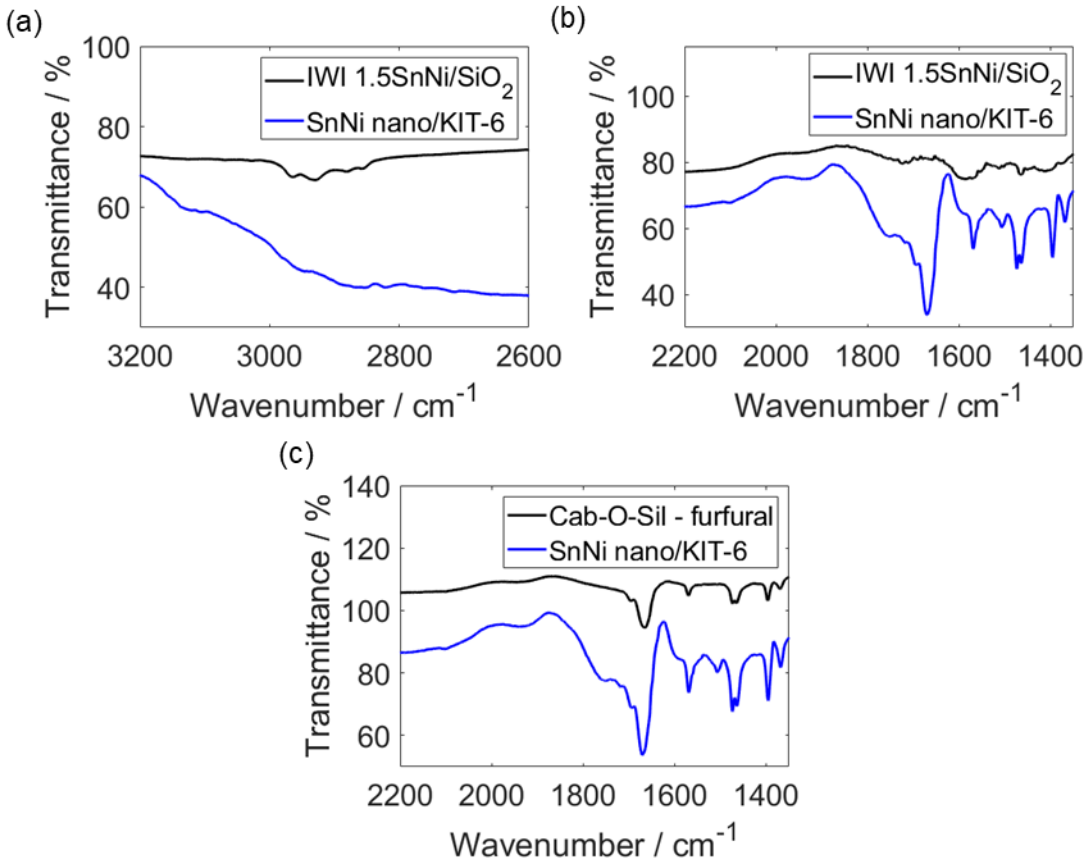

Figure 105: DRIFT spectra of spent IWI 1.5Sn-Ni/SiO_2 and spent SnNi/KIT-6 sequential addition nanoparticle catalyst from (a) 3200 – 2600 cm^{-1} and (b) 2200 – 1350 cm^{-1} and (c) a comparison of the DRIFT spectrum of Cab-O-Sil silica exposed to furfural under reaction conditions ('Cab-O-Sil – furfural'; 180 °C, 70 mL min^{-1} H_2) to the spent SnNi nanoparticle catalyst. Spectra are vertically offset for clarity.

5.3 Conclusions

The introduction of tin to IWI nickel catalysts leads to significant improvements in furfuryl alcohol selectivity, reaching around 85 % when the catalyst contains around 1.5 wt. % Sn. Whilst the deactivation rate was not significantly affected by the introduction of tin, the mass activity decreased by around an order of magnitude when even a moderate amount of tin was included (0.25 wt. %). However, when more tin was included, there was a comparatively minor additional impact on mass activity compared to the lower Sn loading. The colloidal nanoparticle catalysts initially had a significantly narrower particle size distribution and a more even distribution of tin in the nickel nanoparticles, however it was found that the pre-reaction reduction step caused significant sintering. This led to a very broad particle size distribution, however the distribution of tin, although broadened compared to the as prepared nanoparticles, was still an improvement over the IWI Sn-doped catalysts. The sequential addition SnNi nanoparticle catalyst was found to have an excellent furfuryl alcohol selectivity (~95 %), which is higher than the IWI Sn-doped catalysts.

The mass activity of the SnNi nanoparticle catalyst was similar to that of the Sn-doped IWI catalysts, however the deactivation rate constant was significantly higher. Coking was identified as a major source of deactivation, similar to the IWI catalysts, and the main coke species were found likely be related to furfuryl alcohol-based species. Overall, the introduction of tin to nickel-based catalysts led to a significant improvement in furfuryl alcohol selectivity (up to around 95 %), however this does come at the cost of a decrease in mass activity.

5.4 References

1. E. Nikolla, A. Holewinski, J. Schwank and S. Linic, *Journal of the American Chemical Society*, 2006, **128**, 11354-11355.
2. V. S. Marakatti, N. Arora, S. Rai, S. C. Sarma and S. C. Peter, *ACS Sustainable Chemistry & Engineering*, 2018, **6**, 7325-7338.
3. Rodiansono, M. D. Astuti, U. T. Santoso and S. Shimazu, *Procedia Chemistry*, 2015, **16**, 531-539.
4. Rodiansono, S. Khairi, T. Hara, N. Ichikuni and S. Shimazu, *Catalysis Science & Technology*, 2012, **2**, 2139-2145.
5. R. Rodiansono, M. D. Astuti, S. Khairi and S. Shimazu, *Bulletin of Chemical Reaction Engineering & Catalysis*, 2016, **11**, 1-9.
6. V. Vetere, A. B. Merlo, J. F. Ruggera and M. L. Casella, *Journal of the Brazilian Chemical Society*, 2010, **21**, 914-920.
7. Y. Nakagawa, H. Nakazawa, H. Watanabe and K. Tomishige, *ChemCatChem*, 2012, **4**, 1791-1797.
8. R. Rowe, J. D. Grice, G. Poirier, C. J. Stanley and L. s. Horváth, *The Canadian Mineralogist*, 2011, **49**, 651-656.
9. K. Schubert, W. Burkhardt, P. Esslinger, E. Günzel, H. G. Meissner, W. Schütt, J. Wegst and M. Wilkens, *Naturwissenschaften*, 1956, **43**, 248-249.
10. M. Agnelli, H. M. Swaan, C. Marquez-Alvarez, G. A. Martin and C. Mirodatos, *Journal of Catalysis*, 1998, **175**, 117-128.
11. J. Zarfl, D. Ferri, T. J. Schildhauer, J. Wambach and A. Wokaun, *Applied Catalysis A: General*, 2015, **495**, 104-114.
12. K. de Oliveira Rocha, C. M. P. Marques and J. M. C. Bueno, *Chemical Engineering Science*, 2019, **207**, 844-852.
13. R. P. Eischens, S. A. Francis and W. A. Pliskin, *The Journal of Physical Chemistry*, 1956, **60**, 194-201.
14. D. Vargas-Hernández, Rubio-Caballero, J. , Moreno-Tost, R. , Mérida-Robles, J. , Santamaría-González, J. , Jiménez-López, A. , Pérez-Cruz, M. , Hernández-Huesca, R. and Maireles-Torres, P., *Modern Research in Catalysis*, 2016, **5**, 85-94.
15. Z. Jia, F. Zhou, M. Liu, X. Li, A. S. C. Chan and C.-J. Li, *Angewandte Chemie International Edition*, 2013, **52**, 11871-11874.
16. C. Cheng and M. Brookhart, *Angewandte Chemie International Edition*, 2012, **51**, 9422-9424.
17. I. S. Chuang, G. E. Maciel and G. E. Myers, *Macromolecules*, 1984, **17**, 1087-1090.
18. M. Principe, P. Ortiz and R. Martínez, *Polymer International*, 1999, **48**, 637-641.
19. V. Iablokov, S. K. Beaumont, S. Alayoglu, V. V. Pushkarev, C. Specht, J. Gao, A. P. Alivisatos, N. Kruse and G. A. Somorjai, *Nano Letters*, 2012, **12**, 3091-3096.
20. V. V. Pushkarev, K. An, S. Alayoglu, S. K. Beaumont and G. A. Somorjai, *Journal of Catalysis*, 2012, **292**, 64-72.
21. S. Alayoglu, S. K. Beaumont, F. Zheng, V. V. Pushkarev, H. Zheng, V. Iablokov, Z. Liu, J. Guo, N. Kruse and G. A. Somorjai, *Topics in Catalysis*, 2011, **54**, 778.
22. P. Sonström, D. Arndt, X. Wang, V. Zielasek and M. Bäumer, *Angewandte Chemie International Edition*, 2011, **50**, 3888-3891.
23. H. Xia, J. An and W. Zhang, *Nanomaterials*, 2020, **10**.

Chapter 6: The effect of phosphorus on nickel and tin-nickel catalysts for furfural hydrogenation

As discussed in previous chapters, the synthesis of larger colloidal nickel nanoparticles requires the use of phosphine capping agents. This can lead to the incorporation of phosphorus[1-4] since Ni(111) surfaces can catalyse the decomposition of one of the most common capping agents (tri-*n*-octylphosphine, TOP) at temperatures as low as 150 °C[5, 6] whereas the syntheses are typically carried out at temperatures of >200 °C. In fact, XPS analysis revealed that regardless of the bulk structure of the nickel nanoparticles prepared using TOP (*i.e.* amorphous nickel phosphide or crystalline nickel metal), the surface contained nickel phosphide. Nickel phosphide may be expected to behave differently to nickel metal during catalysis as there will be different active sites. In particular, nickel phosphide is slightly Lewis acidic due to a small charge transfer from nickel to phosphorus resulting in $Ni^{\delta+}$ species.[7-9] Therefore, the nanoparticles prepared using TOP may perform differently during furfural hydrogenation compared to the phosphorus-free catalysts discussed in previous chapters. Whilst surface composition is often a key factor in determining catalytic performance, it is unclear whether the bulk composition of the nanoparticles will also play a role. Therefore, the amorphous nickel phosphide and crystalline nickel metal nanoparticle catalysts will be compared. Finally, the addition of tin to nickel-based catalysts has been shown to significantly improve the selectivity towards furfuryl alcohol, and so the impact of tin on phosphorus-containing nickel catalysts will also be studied.

6.1 The effect of phosphine capping agents and phosphorus incorporation on nickel-based catalysts

Two sets of nickel nanoparticles synthesised using TOP as a capping agent were prepared; one with an amorphous morphology and one with a crystalline nickel metal structure. Evaluating these catalysts for furfural hydrogenation will allow a comparison of the impact of phosphorus on catalysis as well as any effects resulting from the differing bulk nanoparticle architecture and structure.

6.1.1 Amorphous nickel phosphide nanoparticles for furfural hydrogenation

Higher P:Ni ratios, among other factors, can lead to significant phosphorus incorporation during the synthesis of nickel nanoparticles, such that the bulk phase of the nanoparticles is amorphous nickel phosphide.[2, 3] This was found to be the case when synthesising nickel nanoparticles using a method outlined by Mézailles *et al.*,[10] which produced amorphous nanoparticles with a size of 11.6 ± 1.3 nm

(Chapter 4). The nanoparticles were supported on KIT-6 silica (Figure 106) so that they could be evaluated for vapour-phase furfural hydrogenation.

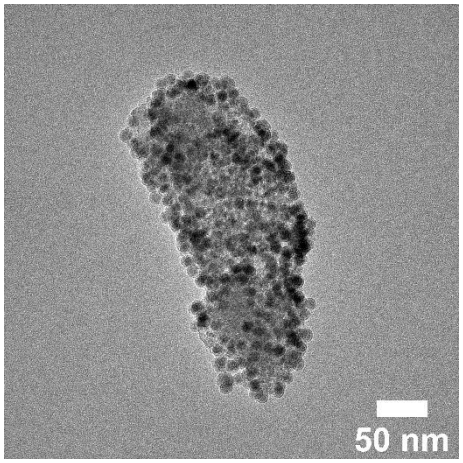

Figure 106: TEM imaging of the amorphous nickel phosphide nanoparticles supported on KIT-6 silica

The amorphous nickel phosphide nanoparticle catalyst was then evaluated for furfural hydrogenation (Figure 107). The selectivity towards furfuryl alcohol was found to be ~67 %, which is roughly 15 % higher than that found for both the IWI Ni/SiO_2 catalyst and smaller nickel nanoparticle catalyst (phosphine-free nanoparticle synthesis). This suggests that the presence of phosphorus is increasing the furfuryl alcohol selectivity.

Maireles-Torres *et al.*[11] investigated silica supported Ni_2P catalysts for vapour-phase furfural hydrogenation. Although they did not carry out the reaction at 180 °C, they did find that at 170 °C only a minimal amount of furfuryl alcohol was produced and at 190 °C, no furfuryl alcohol was produced. The major product in both cases was found to be 2-methylfuran, although the higher temperature also led to increasing amounts of furan formation. Clearly this result is substantially different to the results obtained for the amorphous nickel phosphide nanoparticle catalyst studied here. However it should be noted that the H_2:furfural ratio was around 12, compared to 19 used in this work, and the reactant feed was composed of 5 v/v% furfural in cyclopentanyl methyl ether (CPME). Whilst the relatively small difference in H_2:furfural ratio is fairly unlikely to significantly effect catalysis since there is already a large excess of hydrogen, it is unclear whether the presence of CPME is having any effect on the results. Despite the potential for differing reaction conditions to be affecting the results of catalysis, the difference in selectivity is large and so it is unlikely that the reaction conditions alone can account for the altered selectivity. Other explanations for the difference include differing amounts of phosphorus incorporation in the nickel metal particles or the speciation of the excess phosphorus present. In the case of the catalyst studied by Maireles-Torres *et al.*[11] there was enough phosphorus incorporation that they formed crystalline Ni_2P,

whereas there may be less phosphorus incorporation in the amorphous nickel phosphide nanoparticles studied here. Lower amounts of phosphorus may alter the selectivity of the catalyst, as more of the surface is likely to behave as nickel metal, which is known to have a selectivity to furfuryl alcohol of around 50 %. Alternatively, the selectivity towards 2-methylfuran may be related to the presence of Brønsted acidic P-OH species which are thought to form on the surface of nickel phosphide catalysts. Maireles-Torres *et al.*[11] work actually used relatively large excesses of phosphorus to form the Ni_2P catalysts (P:Ni molar ratios of 1, 2 and 3). XPS analysis of their catalysts suggests that there are significant quantities of oxidised phosphorus species such as PO_4^{3-} and HPO_3H^- present on the surface of the Ni_2P particles. These species would act as Brønsted acid sites, which raises the possibility that the presence of Brønsted acid sites promotes the production of 2-methylfuran. Certainly, there are reports that the introduction of Brønsted acid sites to metal catalysts promotes the hydrodeoxygenation pathway with other similar substrates such as benzyl alcohol.[12] In the case of the nanoparticles synthesised using TOP, the phosphorus that is not incorporated into the nickel nanoparticles is likely still present as a phosphine, and so will not act as a Brønsted acid, hence the minimal selectivity towards 2-methylfuran observed.

The mass activity of the amorphous nickel phosphide nanoparticle catalyst was found to be an order of magnitude lower than that of the IWI Ni/SiO_2 catalyst, however it was similar to that found for the smaller nickel nanoparticle catalyst (phosphine-free synthesis). Whilst the mass activity would be expected to vary significantly with metal particle size (and therefore metal surface area), as discussed in Chapter 5, significant sintering occurred during the reduction step prior to catalysis for the smaller nickel nanoparticle catalyst. This may offer an explanation for the similar mass activities of the catalysts despite the difference in size of the as synthesised nanoparticles. The lower activity compared to the IWI catalyst is likely due to the presence of the capping agent on the surface of the nanoparticles limiting access to the active sites. The deactivation rate constant (as introduced in Section 3.2.2 in Chapter 3) is relatively similar to that found for the IWI Ni/SiO_2 catalyst and is lower than that found for the small nickel nanoparticle catalyst (phosphine-free synthesis). This suggests that the inclusion of phosphorus, either as a nickel phosphide species or as a phosphine capping agent on the surface of the nanoparticles, is helping to reduce coking, as this was identified as a major source of deactivation in the phosphorus-free small nickel nanoparticle catalyst. It should be noted however, that the catalyst does still exhibit fairly rapid deactivation, meaning that any stability provided by the phosphorus is limited and, ultimately, the catalyst still deactivates at a similar rate to the IWI catalyst.

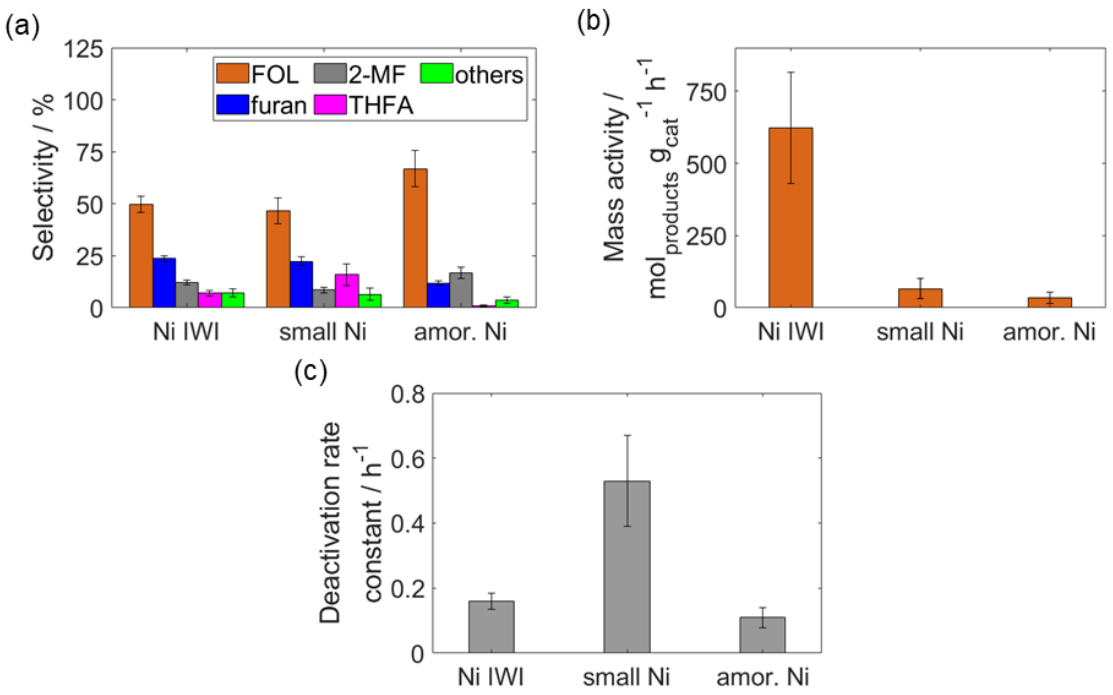

Figure 107: Comparison of the amorphous nickel phosphide nanoparticle catalyst ('amor. Ni') to the IWI Ni/SiO_2 catalyst ('Ni IWI') and the smaller nickel nanoparticle catalyst ('small Ni') during furfural hydrogenation (a) Average selectivity under stable operation; (b) Mass activity after 1 hr TOS; (c) Deactivation rate constants. Errors shown are based on repeat measurements of a typical sample as indicated in the experimental section.

Maireles-Torres *et al.*[11] found that for Ni_2P/SiO_2 catalysts, increasing the reaction temperature favoured the production of 2-methylfuran, reaching a selectivity of around 82 % at 210 °C after 5 h TOS and with the only other significant product found to be furan. Therefore, it was thought that increasing the reaction temperature may also favour the formation of 2-methylfuran for the amorphous nickel phosphide nanoparticle catalyst. The results of furfural hydrogenation at 220 °C are shown in Figure 108. The selectivity towards furfuryl alcohol dropped by around 15 % compared to the selectivity at a reaction temperature of 180 °C, however this still makes furfuryl alcohol the dominant product with a selectivity of around 50 %. The selectivity towards 2-methylfuran did increase as expected, however the increase was very minimal, going from around 17 % at 180 °C to around 20 % at 220 °C. There was more of an increase in the selectivity towards furan, which went from around 16 % at 180 °C to around 23 % at 220 °C, however overall, this increase in selectivity is also fairly minor. The fact that the selectivity to furfuryl alcohol remains high despite the increase in reaction temperature is a somewhat unexpected result. Vargas-Hernández *et al.*[13] reported that for a Ni/SBA-15 silica catalyst, a reaction temperature of 230 °C resulted in a selectivity towards furan of 98 % during vapour-phase furfural hydrogenation. However, again it should be noted that the H_2:furfural ratio was around 12 compared to around 19 in this work and the reactant feed was composed of 5 v/v% furfural in CPME. As discussed above, it is unclear what effect these differing

reaction conditions, especially the presence of CPME, will have on the selectivity of the catalyst. However, such a clear preference for decarbonylation to furan at higher temperatures suggests that nickel catalysts are generally likely to follow this trend. Therefore, if the amorphous nickel phosphide nanoparticle catalyst was behaving like a standard nickel catalyst, higher reaction temperatures would be expected to produce furan as the major product, yet only minimal increases in furan selectivity were observed. Alternatively, if the amorphous nickel phosphide catalyst was behaving like a Ni_2P catalyst, a reaction temperature of 220 °C would be expected to produce 2-methylfuran as the major product, yet again only minimal increases in 2-methylfuran selectivity were observed. This suggests that the amorphous nickel phosphide catalyst is not behaving like nickel metal or Ni_2P catalysts. This could be due to a number of reasons, as discussed above, including a lower amount of phosphorus incorporation compared to Ni_2P or the presence of unincorporated phosphorus as phosphine-based ligands on the surface rather than oxidised phosphorus species which can act as Brønsted acids.

As would be expected by an increase in temperature, there was an increase in the mass activity of the catalyst at 220 °C, however the increase was relatively minor. The deactivation rate constant was also increased, roughly doubling for the reaction carried out at 220 °C. Again, an increase in deactivation rate at higher temperatures is somewhat expected since higher reaction temperatures are likely to promote sintering and coking.

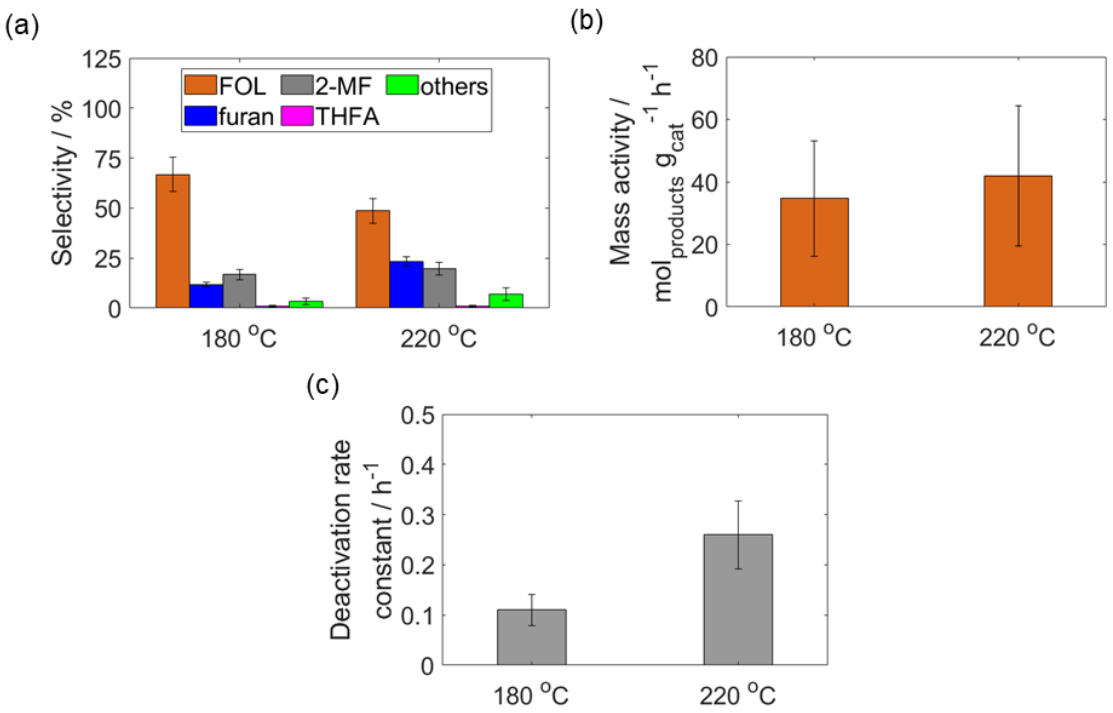

Figure 108: Comparison of the amorphous nickel phosphide nanoparticle catalyst during furfural hydrogenation at the standard reaction temperature of 180 °C and at 220 °C; (a) Average selectivity under stable operation; (b) Mass activity after 5 hrs TOS; (c) Deactivation rate constants. Errors shown are based on repeat measurements of a typical sample as indicated in the experimental section.

Overall, the use of a phosphine capping agent and the resulting incorporation of phosphorus have minor effects on the activity and deactivation rate of the catalyst, however it does result in an increased selectivity to furfuryl alcohol at both 180 °C and 220 °C.

6.1.2 Crystalline nickel nanoparticles, prepared using TOP, for furfural hydrogenation

Based on a method reported by Emmerling *et al.*[14], which used a lower P:Ni ratio, it was found possible to synthesise larger nickel nanoparticles where the bulk structure consisted of crystalline nickel metal whilst still using TOP as the capping agent. The method was found to produce nanoparticles with a size of 15.2 ± 1.3 nm (Chapter 4), which is slightly larger than the amorphous nickel phosphide nanoparticles discussed above. The nanoparticles were supported on KIT-6 silica (Figure 106a and b) so that they could be evaluated for vapour-phase furfural hydrogenation. HRTEM imaging of the unsupported nanoparticles (Figure 106c) showed that the nanoparticles did not have a core-shell structure. However, like with the amorphous nickel phosphide nanoparticles, the procedure used to support the nanoparticles appears to result in the formation of a core-shell structure (Figure 106b). The core-shell structure is likely due to the formation of an oxide layer on the surface of the nanoparticles. The supporting procedure involves drying the catalyst at around

70 °C in static air, which may provide a potential explanation for the formation of the oxide surface layer.

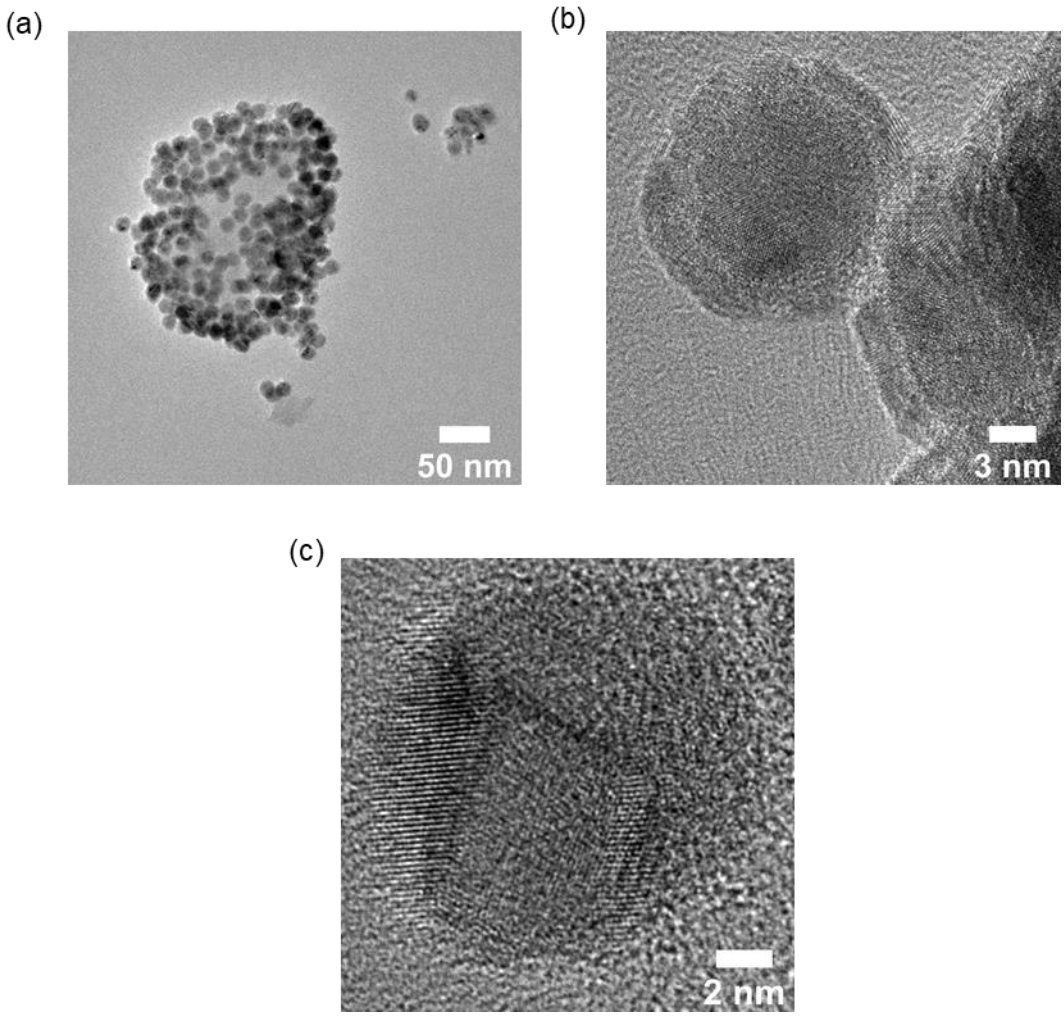

Figure 109: TEM imaging of the crystalline nickel nanoparticles prepared using TOP (a) supported on KIT-6, (b) HRTEM image showing the core-shell structure of the KIT-6 supported nanoparticles and (c) HRTEM image of an unsupported nanoparticle

The catalyst was then evaluated for furfural hydrogenation, with the results shown in Figure 110. Despite the bulk structures of the nanoparticles being very different, the crystalline nickel nanoparticle catalyst has a very similar selectivity to the amorphous nickel phosphide nanoparticle catalyst. The major product was found to be furfuryl alcohol and had a selectivity of around 66 %. The only small difference appears to be slightly higher selectivity for furan compared to 2-methylfuran for the crystalline versus the amorphous nanoparticle catalysts. Nickel phosphide catalysts are known to favour 2-methylfuran production[11], so potentially this suggests the slight increase in 2-methylfuran selectivity in the amorphous nickel phosphide nanoparticle catalyst may be related to increased phosphorus incorporation compared to the crystalline nickel metal catalyst.

However, these changes in selectivity are fairly minor and so the selectivity of the two catalysts are still very comparable, likely since the surface of both catalysts were shown to contain nickel phosphide (Chapter 4).

The mass activity of the crystalline nickel metal nanoparticle catalyst is around 3 – 4 times lower than that of the amorphous version. Whilst the amorphous nickel phosphide nanoparticles are smaller than the crystalline version (11.6 nm vs. 15.2 nm respectively), this only results in a reduction in surface area per mole of nickel of around 1.7 times, which therefore cannot account for the 3 – 4 fold decrease in mass activity, given the same nominal Ni loading of ~5 wt. %. Another potential explanation could be that more of the phosphine capping agent remains on the surface of the nanoparticles since there is significantly less phosphorus incorporation into the bulk of the structure. If this is the case, this may further limit access to active sites on the surface of nanoparticles and therefore, result in a lower mass activity. The deactivation rate of the crystalline nickel nanoparticle catalyst is significantly higher than that of the amorphous version and much more similar to that observed for the small nickel nanoparticle catalyst (phosphine-free synthesis). It is unclear why this is the case, however this may suggest that the formation of a bulk nickel phosphide phase is lowering the deactivation rate. Alternatively, as discussed for the changes in mass activity, if a larger amount of the phosphine capping agent is present on the surface of the catalyst, this may result in increased coking and therefore deactivation. Sintering should also be considered when exploring deactivation, however as discussed below, sintering is very limited or even completely eliminated for nanoparticle catalysts prepared using TOP.

Overall, the bulk phase of the nanoparticles (*i.e.* crystalline nickel metal or amorphous nickel phosphide) appears to have limited effects on the catalytic performance, especially in terms of selectivity. This is likely due to the fact that the surfaces of both sets of nanoparticles contain nickel phosphide (Chapter 4) and so the catalysts are likely to behave in a similar manner during catalysis.

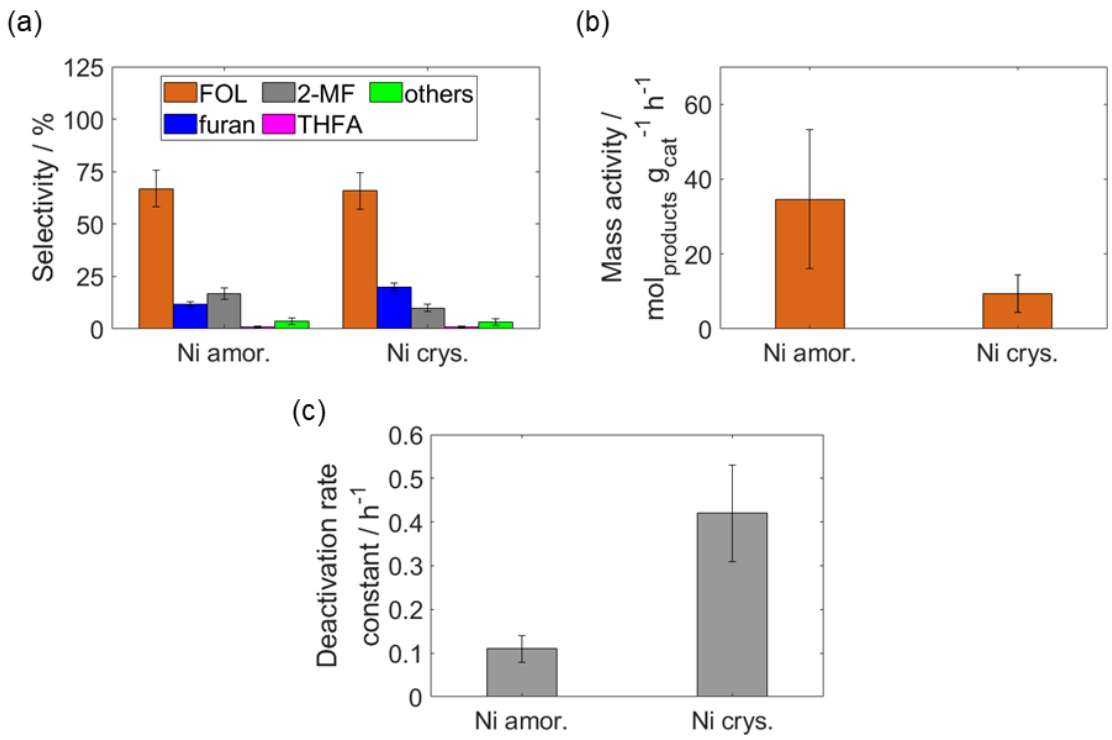

Figure 110: Comparison of the crystalline nickel nanoparticle catalyst, prepared using TOP, ('Ni crys.') to the amorphous nickel phosphide nanoparticle catalyst ('Ni amor.') during furfural; (a) Average selectivity under stable operation; (b) Mass activity after 5 hrs TOS; (c) Deactivation rate constants. Errors shown are based on repeat measurements of a typical sample as indicated in the experimental section.

6.1.3 The effect of phosphorus on sintering in nickel-based nanoparticle catalysts

Significant sintering was found to occur in the small Ni and SnNi nanoparticle catalysts (phosphine-free synthesis). The majority of the sintering was found to occur during the reduction step prior to catalysis and therefore, the active catalyst was actually the sintered version. This led to broader particle size distributions in the working catalyst. Since the IWI catalysts did not exhibit any significant sintering, a possible explanation for the sintering with the small nanoparticle catalysts is a decrease in metal-support interactions due to the layer of capping agent on the surface of the nanoparticles. Therefore, it was important to determine whether sintering was also occurring for the nanoparticle catalysts synthesised using phosphine capping agents.

Figure 111 shows an image of the spent amorphous nickel phosphide nanoparticle catalyst, along with particle size distributions normalised to the number of particles, surface area and volume. The catalyst exhibits some minimal sintering, as seen by the small tails towards higher particle size on the distributions, however compared to the small nickel nanoparticle catalyst (Section 5.2 in Chapter 5), much less sintering is occurring. The surface is key in terms of catalysis and, in this case, the majority of the surface area is still coming from nanoparticles with a similar size to the as

synthesised nanoparticles, confirming the minimal impact that the sintering should have on catalysis. It should be noted that there was a slightly unusual shift of the particle size distribution to lower particle sizes in the spent catalyst compared to both the as prepared unsupported nanoparticles (as shown in Figure 111) but also the fresh supported nanoparticle catalyst (pre-reaction, pre-reduction). In fact, the average metal particle size in the spent catalyst was found to be 10.7 ± 3 nm whereas the as prepared nanoparticles had an average particle size of 11.6 ± 1.3 nm. The cause of the decrease in metal particle size is unclear at this time and further investigation would be required to determine the exact reason. However, a potential explanation could be that some of the phosphorus that is incorporated into the bulk of the as prepared nanoparticles is segregated to the surface during the reduction step or catalysis. This would result in a bulk structure that would be closer to nickel metal, which could lead to smaller nanoparticles. Overall, the slight shift to smaller nanoparticles in the spent catalyst is a minimal change and so will have a relatively minor effect on catalysis. The more important point is that the presence of phosphorus significantly limits the sintering that occurs with nickel-based nanoparticle catalysts compared to nickel nanoparticle catalysts synthesised using only amine capping agents.

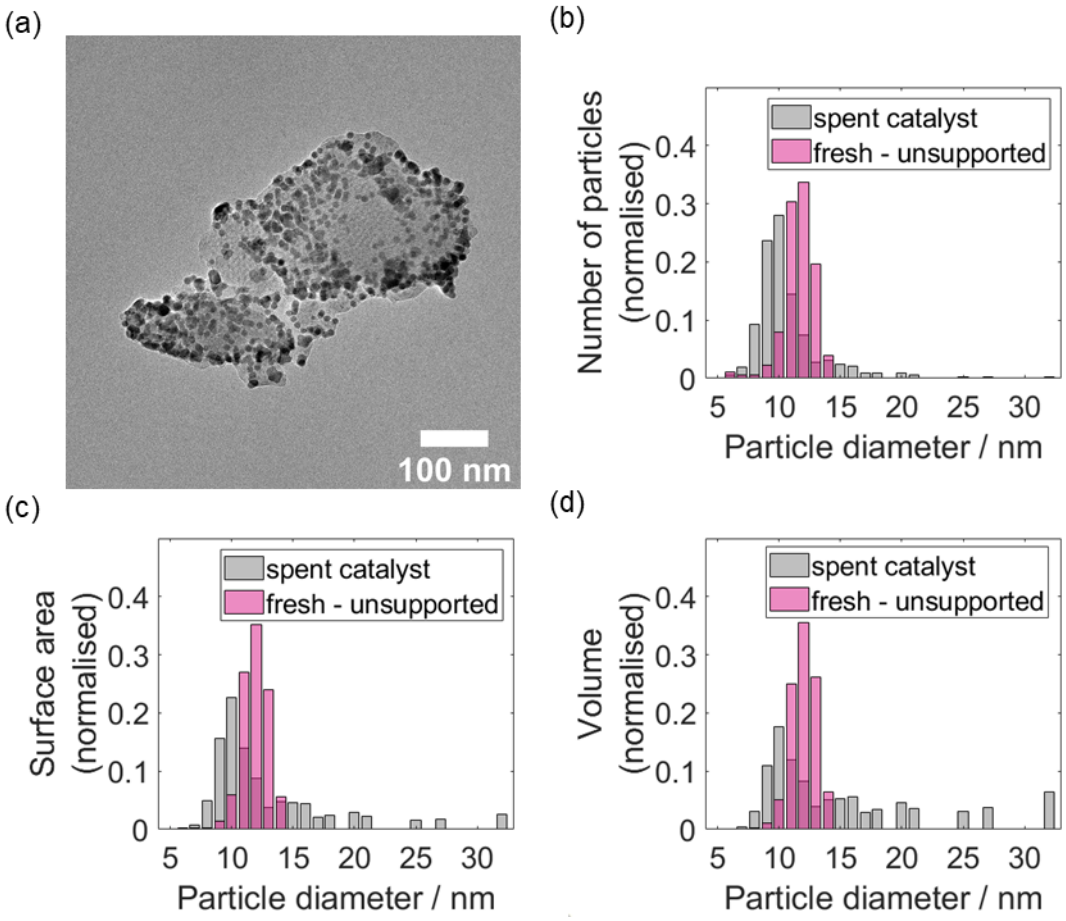

Figure 111: (a) TEM image of spent Ni nano (amor.)/KIT-6 and corresponding particle size distributions normalised to the (b) number of particles, (c) surface area and (d) volume

Figure 112 shows a TEM image of the spent crystalline nickel metal catalyst and the corresponding particle size distributions normalised to the number of particles, surface area and volume. For this catalyst there is even less sintering, to the point where sintering is almost eliminated. This again suggests that the presence of phosphorus is helping to prevent sintering.

However, it should be noted there could also be an alternative explanation since the decrease in sintering also correlates with increasing nanoparticle size. Although there is not specific data for a Ni/SiO_2-based system, Campbell *et al.* determined the chemical potential of various metal atoms in nanoparticles supported on several different oxides.[15-22] They summarised the results by reporting that the chemical potential of metal atoms in a nanoparticle increases rapidly with particle diameters of less than ~6 nm.[23] Chemical potential is a measure of the thermodynamic driving force for sintering, and so this means that particle size plays a significant role in the extent of sintering for metal nanoparticles with a diameter less than ~6 nm. However, for nanoparticles larger than ~6 nm, particle size has a lesser effect on sintering. Therefore, particle size may be contributing to the increase in sintering for the small phosphorus-free nanoparticles (~4 nm) compared to the

larger phosphorus containing nanoparticles (~12 - 15 nm). However, it is unlikely that particle size can explain the increase in sintering between the amorphous nickel phosphide nanoparticles (~12 nm) and the crystalline nickel nanoparticles (~15 nm). Therefore, increasing particle size alone is unlikely to be responsible for the increased sintering resistance. Additionally, the IWI Ni/SiO_2 had a broad distribution of nickel particle sizes, with many particles of a similar size to the small nickel nanoparticles, and yet very little sintering occurred (although this is harder to measure on an already broad distribution) and the smaller particles were still present after catalysis. This suggests that the presence of a capping agent is the major factor contributing to sintering in the smaller nanoparticles, which implies that it is the change to a phosphine capping agent that is lowering or eliminating sintering in the larger nanoparticles. Therefore, the use of a phosphine capping agent may be a facile route to limiting sintering in colloidal nickel-based nanoparticle catalysts.

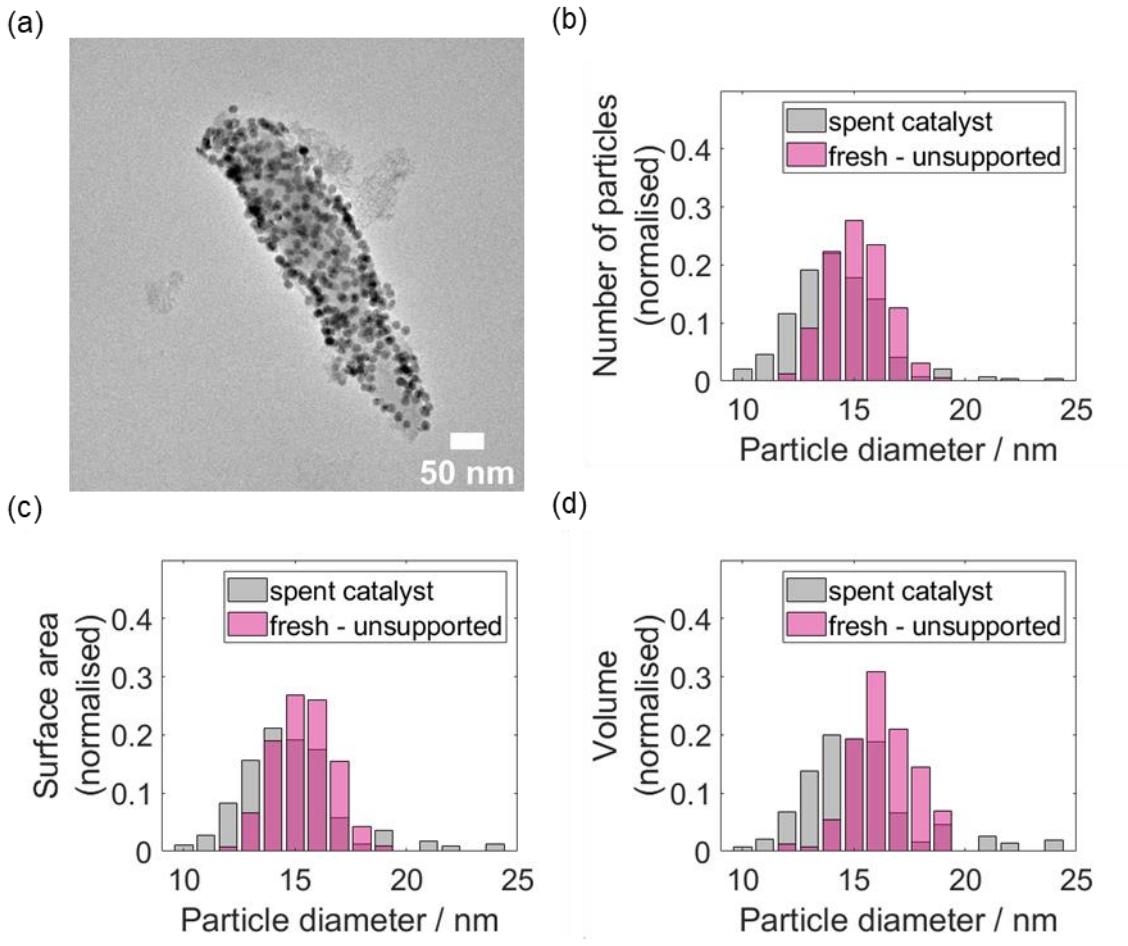

Figure 112: (a) TEM image of spent crystalline Ni nanoparticles supported on KIT-6 and corresponding particle size distributions normalised to the (b) number of particles, (c) surface area and (d) volume

6.1.4 Deactivation of nickel nanoparticle catalysts synthesised using a phosphine capping agent

Since the presence of phosphorus almost eliminates or significantly limits sintering, the rapid deactivation of the catalysts must be mainly attributed another factor. For all of the previous nickel-based catalysts discussed in this thesis, the main cause of the rapid deactivation was found to be coking and so this will also be examined for the catalysts discussed in this chapter.

Solid state cross polarization/magic angle spinning ^{13}C-NMR (CP/MAS ^{13}C-NMR) can be a useful probe of surface carbon species on spent catalysts and so was used to analyse the spent amorphous nickel phosphide nanoparticle catalyst (Figure 113). The strongest peaks (152.0 ppm, 142.6 ppm, 109.3 ppm and 57.7 ppm) correspond to furfuryl alcohol,[24] however there are some additional weaker peaks that correspond to furfural (179.5 ppm and 123.8 ppm, plus possible shoulders on the peaks at 152.0 ppm and 109.3 ppm)[25] and tetrahydrofurfuryl alcohol (THFA; 79.3 ppm, 68.1 ppm, 63.3 ppm and 25.2 ppm).[26] This suggests that the major coke component is related to furfuryl alcohol, similar to many of the other catalysts previously discussed. The presence of peaks corresponding to THFA was slightly unexpected since the catalyst produced very little THFA. One potential explanation may be that the coke species related to furfuryl alcohol, which will be adsorbed on the surface of the catalyst for long periods of time, are further hydrogenated to THFA. In this spectrum, there are also some strong peaks in the alkane region. Whilst some of these may be partially accounted for by the presence of THFA species, the other signals that correspond to THFA are relatively weak, and so THFA alone is unlikely to account for the large peaks in alkane region. It has previously been discussed (Section 5.1.3 in Chapter 5) that the presence of peaks in the alkane region may indicate the formation of furfuryl alcohol oligomers, since their formation results in bridging CH_2 moieties.[27, 28] In the spectra for the spent IWI Sn-doped catalyst and, to a lesser extent, the spent small SnNi nanoparticle catalyst, the presence of a strong methylol peak at around 57 ppm and a weak bridging CH_2 peak at around 25 ppm suggested the presence of relatively short chain oligomers (Chapter 5). In this spectrum, the methylol peak is significantly weaker and the bridging CH_2 peak is significantly stronger, which suggests more extensive oligomerisation than with the previous catalysts. Therefore, the SS NMR data provides evidence that coking is likely to be playing a major role in the deactivation of the catalysts and that furfuryl alcohol and its oligomers appear to be the main species involved.

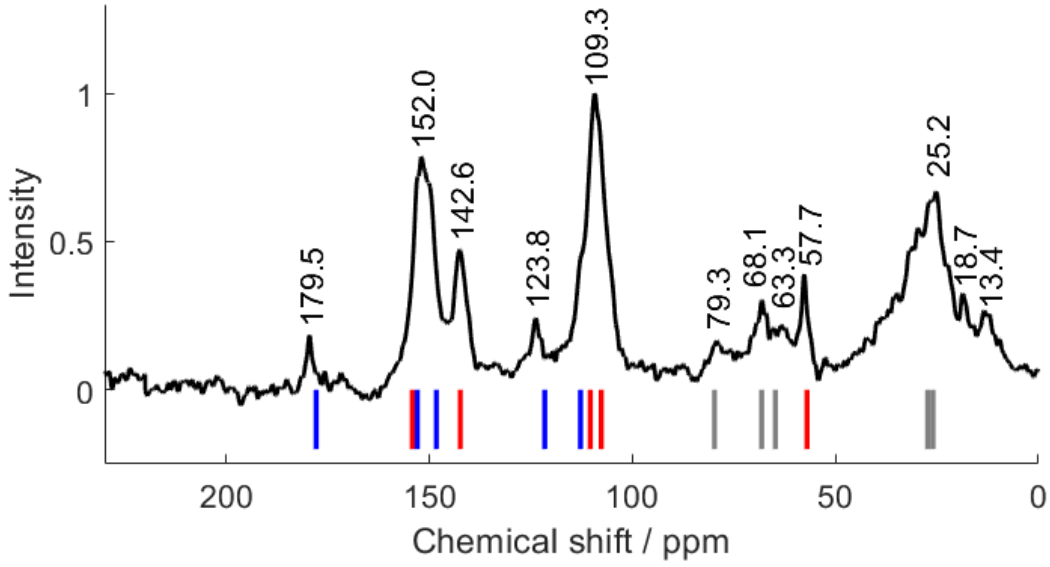

Figure 113: solid state CP/MAS ^{13}C NMR spectrum of the spent amorphous nickel phosphide nanoparticle catalyst, with the positions of the peaks for furfuryl alcohol (solution-state NMR) shown by the red vertical lines[24], the positions of the peaks for furfural (solution-state NMR) shown by the blue vertical lines[25] and the positions of the peaks for tetrahydrofurfuryl alcohol (solution-state NMR) shown by the grey vertical lines[26]

There was some concern that these catalysts were likely to contain some signals relating to the presence of capping agents, rather than coke species. To investigate this, a fresh sample (pre-reaction, pre-reduction) and a reduced sample (pre-reaction but reduced at 300 °C under 30 mL min^{-1} of H_2 for 2 h) were analysed. It should be noted that the sample used was a Sn-doped sample of the amorphous nickel phosphide nanoparticles in order to also account for any effects from the addition of tin. However, a minimal amount of tin was added compared to all other reagents and so it should have a minimal effect. The spectra are shown in Figure 114. Two intense peaks at 59.3 ppm and 15.3 ppm, as well as a weak signal at 29.0 ppm, were observed in both the fresh sample and the reduced sample. Whilst the signal intensities may appear comparable, it should be noted that the acquisition time of spectrum for the reduced sample was significantly longer, and so overall the signal intensity of the reduced sample was around 75 % of that attained for the fresh sample. Therefore, whilst the species appears not to be significantly altered during the reduction procedure, it is partially removed. At this time, the species that corresponds to the spectrum obtained is unclear. The presence of the peak at 59.3 ppm suggests the species contains an alcohol, ether or amine group whilst the signal at 15.3 ppm likely corresponds to alkane CH_3 or CH_2 groups. Both oleylamine and TOP contain many more remote CH_2/CH_3 groups than CH_2-NH_2 or CH_2-PR_2 moieties respectively. Therefore, the fact that the relative intensity of the signal at 59.3 ppm is higher than the alkane signal at 15.3 ppm indicates that neither the presence of oleylamine or TOP could account for the signal at 59.3 ppm. Other reagents included in the

synthesis are 1-octadecene, $Ni(acac)_2$ and tin(II) 2-ethylhexanoate. 1-octadecene does not contain any groups that could account for the signal at 59.3 ppm and the ligands for the nickel and tin reagents would have to react with other reagents to form a molecule with groups that has the potential to account for the signal at 59.3 ppm. In the case of the ligands, it should also be noted that most of the possible products from the ligands reacting with another reagent/species would also produce many other signals that are not present in the spectrum. An important takeaway from this experiment is that the signals present do not correspond directly to the capping agents that may be expected to be present on the catalyst (*i.e.* oleylamine or TOP). Additionally, the signals present on the fresh and reduced catalyst do not appear in the spectrum for the spent catalyst, and so the signals identified on the spent catalyst likely do correspond to coke species.

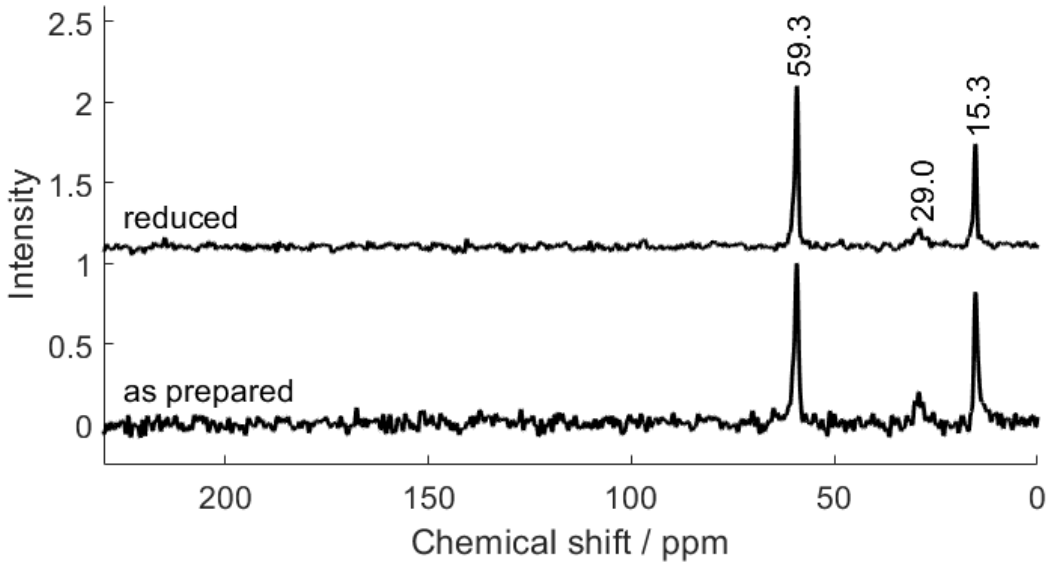

Figure 114: solid state CP/MAS ^{13}C NMR spectrum of an amorphous SnNi nanoparticle catalyst before ('as prepared') and after reduction at 300 °C ('reduced'). The acquisition times for the as prepared sample and reduced sample were 0.67 h and 4 h respectively.

To investigate coking further, a sample of the spent amorphous nickel phosphide nanoparticle catalyst was analysed using DRIFTS (Figure 115). The spectrum has a broad peak at around 1700 cm^{-1}, which fits with a similar peak in the spectrum for silica that was exposed to furfuryl alcohol under standard reaction conditions (180 °C, 70 mL min^{-1} H_2). There is also a peak at around 1505 cm^{-1} which fits well with a peak in the furfuryl alcohol reference spectrum assigned to C=C stretching.[29] This means that furfuryl alcohol species account for the majority of the peaks in the spectrum, which implicates furfuryl alcohol in the coking process. This result is consistent with the NMR data which also suggested that furfuryl alcohol species were involved coking. There are also additional peaks (a small shoulder at ~1670 cm^{-1}, ~1590 cm^{-1}, ~1460 cm^{-1}) which roughly fit with

some of the peaks found when silica was exposed to furfural under reaction conditions, suggesting that small amounts of furfural-based species are also present. Again, this is consistent with the NMR results since they also suggested small amounts of furfural species were present on the spent catalyst. Overall, this suggests that coking is likely to be largely responsible for the deactivation of the catalyst and that coke formation is largely related to furfuryl alcohol and its oligomers.

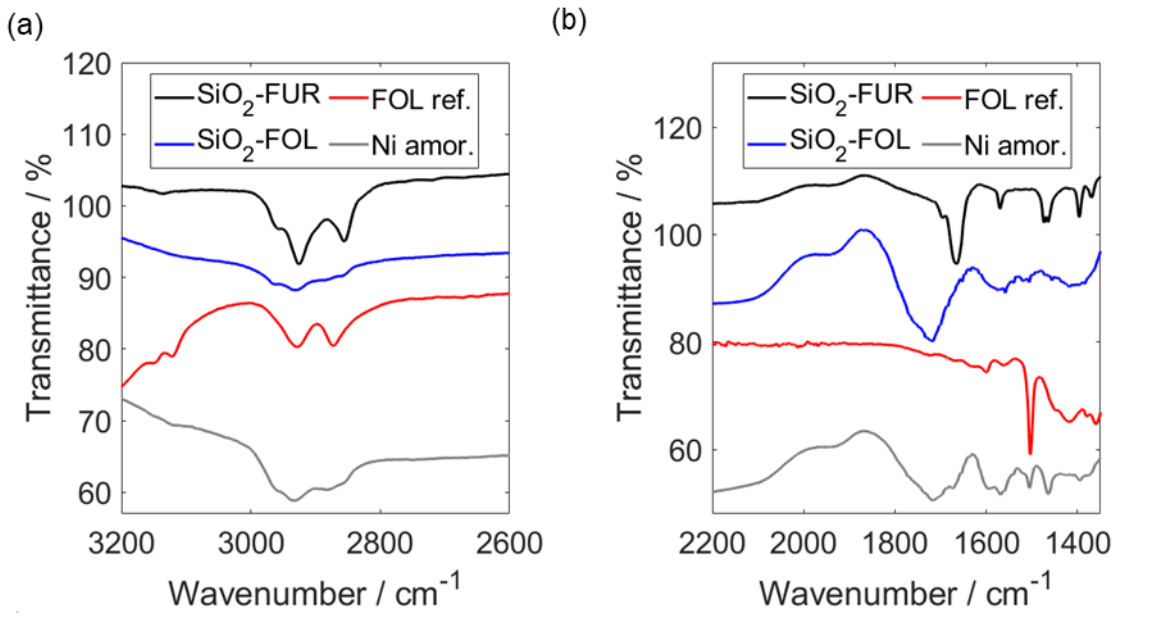

Figure 115: The DRIFT spectrum of the spent amorphous Ni nanoparticle catalyst ('Ni amor.') compared to the spectra of Cab-O-Sil silica exposed to furfural ('SiO_2-FUR') or furfuryl alcohol (SiO_2-FOL) under standard reaction conditions (70 mL min^{-1} H_2, 180 °C) in different key regions of the spectra; (a) 3200 – 2600 cm^{-1} and (b) 2200 – 1350 cm^{-1}

Like with the NMR data, there was some concern that the presence of capping agent on the catalysts may be contributing to the IR spectrum obtained for the spent catalyst. Therefore, a sample of the fresh catalyst was analysed (Figure 116). There was a strong peak at around 1700 cm^{-1}, which couldn't be easily assigned (note: the additional peaks in the ~1900 – 1450 cm^{-1} region are due to atmospheric water not being appropriately cancelled out by the background). After supporting the nanoparticles on the KIT-6 silica, the catalyst is washed several times with a mix of 20 v/v% ethanol in acetone. The catalyst is then dried overnight at ~70 °C in static air, which should remove the majority of the solvent, however the strong peak at around 1700 cm^{-1} in the DRIFT spectrum suggested that this potentially wasn't the case (the frequency is typical of an organic C=O bond). Therefore, a sample of the catalyst was then vacuum dried at 70 °C for ~5 h before a DRIFT spectrum was obtained. In this sample, the peak at around 1700 cm^{-1} had disappeared, confirming that the peak was resulting from the presence of solvent on the catalyst. This likely means that the catalyst used for furfural hydrogenation may also contain traces of the solvents used for washing, however the *in situ* reduction step carried out prior to catalysis should

remove any residual solvent. The spectrum of the vacuum dried catalyst still contained some peaks in the alkane region, likely due to the presence of the long chain capping agents used in the synthesis of the nanoparticles. There was also a broad peak at around 1576 cm^{-1} and two slightly sharper peaks at 1399 cm^{-1} and 1385 cm^{-1}. These peaks are likely associated with the capping agents on the nanoparticles and a very weak peak at around 1399 cm^{-1} can still be seen on the sample of spent catalyst discussed above, however, the contribution of capping agent to the DRIFT spectrum is fairly small and inconsequential. This therefore confirms that the majority of the peaks observed in the DRIFT spectrum of the spent catalyst can be assigned to coke species formed during catalysis.

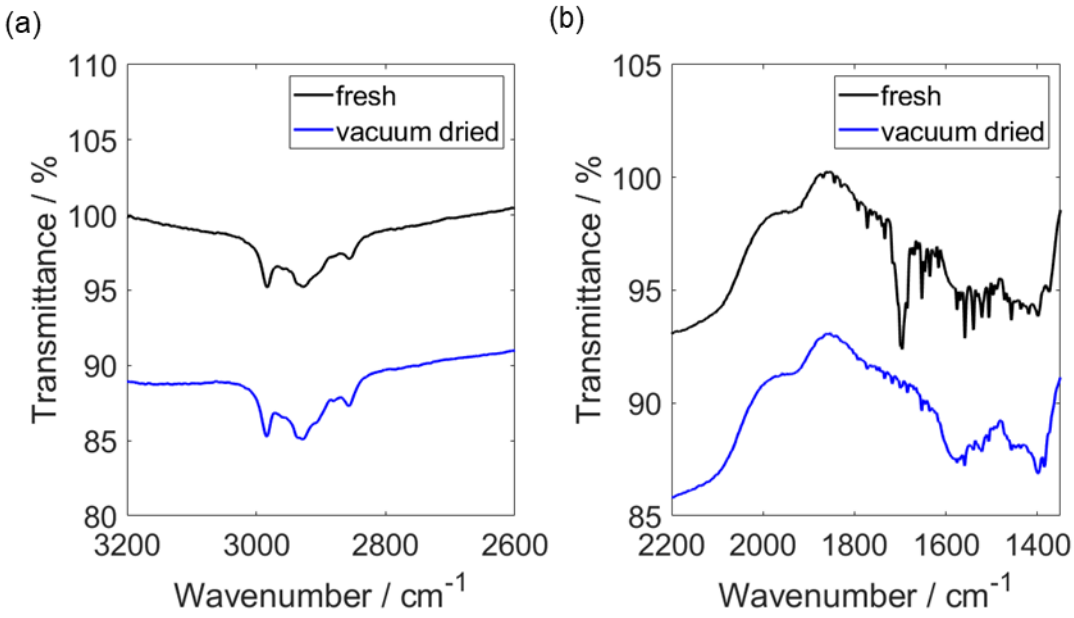

Figure 116: DRIFT spectra of the fresh amorphous Ni nanoparticle catalyst and after vacuum drying at 70 °C for ~5 h for different key regions of the spectra; (a) 3200 – 2600 cm^{-1} and (b) 2200 – 1350 cm^{-1}

6.2 The effect of tin on nickel nanoparticles prepared using a phosphine capping agent

Whilst the presence of phosphorus in nickel-based catalysts led to an increase in furfuryl alcohol selectivity, it was still relatively low at around 67 %. Previously, the introduction of tin to nickel catalysts significantly improved the furfuryl alcohol selectivity, reaching around 95 % for the small colloidal SnNi nanoparticle catalyst. Therefore, in order to further improve the selectivity of the phosphorus containing nickel nanoparticle catalysts, nanoparticles with varying tin contents were synthesised and their evaluation for furfural hydrogenation is discussed below.

6.2.1 The effect of tin on amorphous nickel phosphide nanoparticle catalysts for furfural hydrogenation

Initially, the nanoparticles with a nominal Ni:Sn molar ratio of 3:1 were supported on KIT-6 and evaluated for furfural hydrogenation, since the small SnNi nanoparticle catalyst tested previously was prepared with this 3:1 Ni:Sn molar ratio and was found to be highly selective to furfuryl alcohol. However, when the larger SnNi amorphous nanoparticles were tested, they were almost completely inactive. Whilst increasing the mass of catalyst may have meant some activity could be observed, significant conversions similar to other catalysts would only be achieved with at least an order of magnitude increase in activity. The mass of catalyst required for this increase in activity would not be feasible in the current reactor setup. The lack of activity for this catalyst may be explained by the fact that the surface area per mole of nickel will be around 12 times lower for the larger nanoparticles (~13.6 nm) than the smaller nanoparticles (~4 nm). The chosen synthetic method for both sizes of nanoparticle is likely to result in most of the tin being located on the surface of the nanoparticles, as confirmed by elemental maps produced using STEM-EDX analysis (Chapter 4). Whilst reducing the nanoparticles appears to result in some migration of the tin to the bulk of the nanoparticles, it is likely that significant amounts will remain on the surface. Assuming this is the case, then the lower overall surface area for the larger nanoparticles would result in a higher concentration of tin on the surface compared to the smaller nanoparticles. It was seen that the introduction of tin to nickel catalysts resulted in lower activities, and therefore, a higher concentration of tin on the surface of the larger nanoparticles is a likely explanation for their inactivity. Subsequently, it was decided to prepare some nanoparticles using an analogous method but with substantially lower amounts of tin in order to obtain active catalysts.

Nanoparticles with nominal Ni:Sn molar ratios of 20:1 and 50:1 (Note: ICP revealed the nanoparticles prepared with a nominal Ni:Sn molar ratio of 50:1 actually had a ratio of ~30:1) were therefore prepared and supported on KIT-6 silica so that they could be evaluated for their performance during furfural hydrogenation. An image of the KIT-6 supported SnNi nanoparticles (nominal Ni:Sn molar ratio of 20) is shown in Figure 117, indicating an even distribution of the nanoparticles on the support.

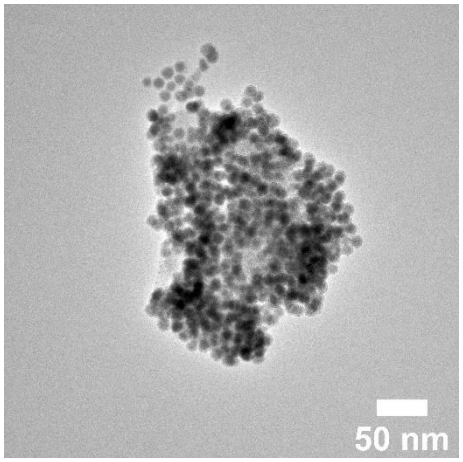

Figure 117: TEM image of fresh KIT-6 supported amorphous SnNi (nominal Ni:Sn molar ratio of 20)

The amorphous SnNi nanoparticle catalysts were then evaluated for furfural hydrogenation (Figure 118). Increasing the tin content of the amorphous nickel nanoparticles led to increasing furfuryl alcohol selectivity, reaching around 93 % for nanoparticles with a Ni:Sn molar ratio of around 20. This selectivity is only slightly lower than that achieved by the smaller SnNi nanoparticles (Ni:Sn molar ratio of around 3) that had a selectivity of ~95 %. This confirms the need for significantly lower tin levels to achieve the same excellent selectivity in the larger amorphous nanoparticles, likely due the lower surface area per mole of nickel as discussed above. Additionally, this also means that the presence of phosphorus is not significantly changing the behaviour of the catalyst when tin is introduced, since the addition of tin is still leading to significant improvements in selectivity.

The mass activity of the amorphous SnNi nanoparticle catalysts was found to be around half that of the nickel only equivalent, therefore the introduction of tin is leading to a decrease in the activity of the catalyst. This is consistent with the results of the IWI catalysts, where the introduction of tin also led to decreased mass activity, however the decrease observed for the amorphous nanoparticles here is to a much lesser extent than seen for the IWI catalysts. The deactivation rate constants do not follow a consistent trend in terms of increasing tin levels, however both of the Sn-doped catalysts have higher deactivation rate constants, suggesting that the presence of tin is resulting in slightly more rapid deactivation. Deactivation of the catalysts will be discussed in further detail in Sections 6.2.3 and 6.2.4, however the increased deactivation rate may be related to the introduction of tin resulting in a slight increase in sintering.

Overall, the introduction of tin to the amorphous nickel phosphide nanoparticles has produced very similar results to that observed when tin is introduced to other nickel-based catalysts, meaning that the selectivity of this catalyst can also be successfully tuned towards furfuryl alcohol. Additionally,

this suggests the presence of phosphorus is having a limited impact on the change to the catalyst caused when tin is introduced.

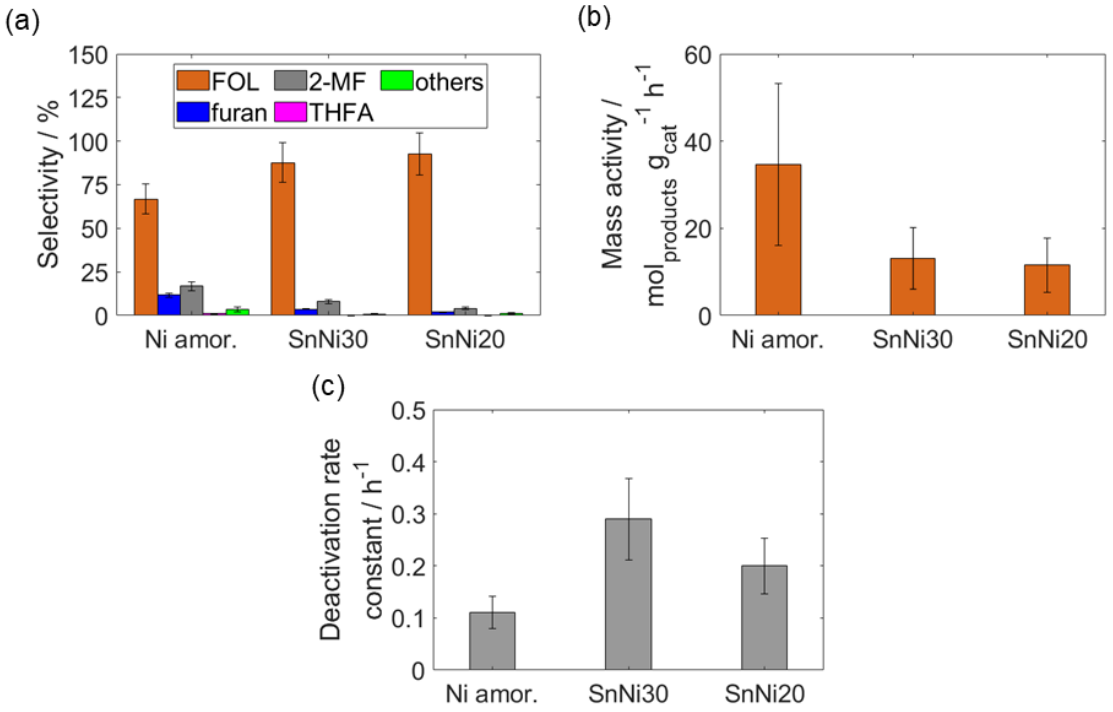

Figure 118: Comparison of the amorphous SnNi nanoparticle catalysts with Ni:Sni molar ratios of around 30 and 20 ('SnNi30' and 'SnNi20' respectively) to the amorphous nickel phosphide nanoparticle catalyst ('Ni amor.') during furfural hydrogenation (a) Average selectivity under stable operation; (b) Mass activity after 1 hr TOS; (c) Deactivation rate constants. Errors shown are based on repeat measurements of a typical sample as indicated in the experimental section.

6.2.2 The effect of tin on crystalline nickel nanoparticle catalysts (prepared using TOP) for furfural hydrogenation

Since the furfuryl alcohol selectivity of the crystalline nickel nanoparticles (prepared using TOP) was around 66 %, SnNi versions of these nanoparticles were also prepared in an attempt to improve the selectivity. Since significantly lower levels of tin were required to achieve suitable activity in the amorphous nanoparticles, which have a roughly similar size to the crystalline nanoparticles, they were also prepared with nominal Ni:Sn molar ratios of 50 and 20. An example TEM image of the KIT-6 supported nanoparticles (nominal Ni:Sn molar ratio of 20) is shown in Figure 119, which indicates the nanoparticles have been successfully supported and have a relatively even distribution.

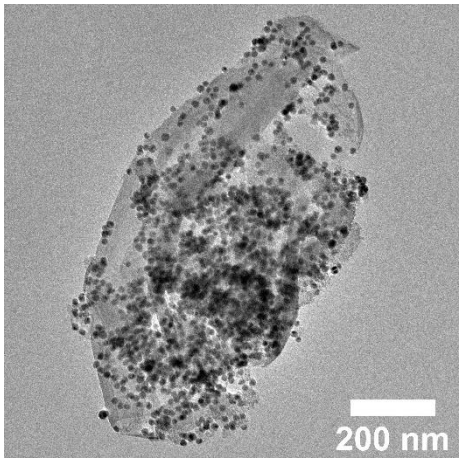

Figure 119: TEM image of fresh KIT-6 supported crystalline SnNi (nominal Ni:Sn molar ratio of 20)

Again, the increasing tin content leads to increasing furfuryl alcohol selectivity, with the nanoparticles with a nominal Ni:Sn molar ratio of 20 achieving a furfuryl alcohol selectivity of 88 %. This is slightly lower than the amorphous catalyst with a similar Ni:Sn molar ratio, however only by a small amount. The addition of tin still clearly results in significant improvements to selectivity. Unlike previous catalysts, the introduction of tin to these nanoparticles appears to initially improve mass activity, with further addition of tin resulting in slightly lower mass activity, although still higher than the nickel only catalyst. At this time there is no clear reasoning for this result, since in most other samples the introduction of tin resulted in lower mass activity, however one hypothesis might be the presence of tin is resulting in less phosphorus (either as metal phosphide or as capping agent) on the surface of the catalyst. This may initially improve activity, however with further addition of tin, the benefits are outweighed by the increasing presence of tin and so the activity starts to decrease again. The deactivation rate constants for this catalyst remain relatively constant, with no clear trend associated with tin content. This suggests the introduction of tin is not having any major effects on the deactivation of the catalyst. As discussed in detail in Section 6.2.3 below, this is may be because the crystalline nanoparticles exhibit almost no sintering regardless of whether tin is present or not, meaning deactivation is likely a result of coking which, as seen with other catalysts, is not largely impacted by the presence of tin.

Overall, the introduction of tin to the crystalline nickel nanoparticles has again led to significant improvements in the selectivity towards furfuryl alcohol, however not quite to the same extent as seen with the amorphous SnNi nanoparticle catalyst or the smaller phosphorus-free SnNi nanoparticle catalyst. However, since the overall trend is very similar, this again suggests that the presence of phosphorus is not having a significant impact on the behaviour of the catalyst when tin is introduced.

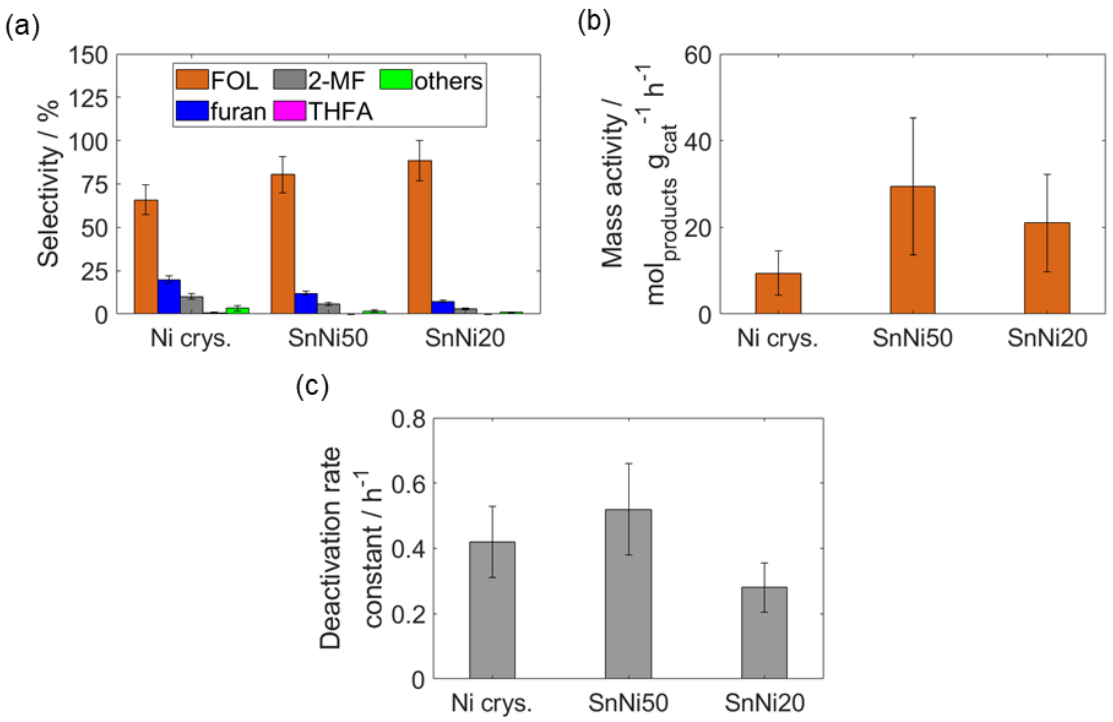

Figure 120: Comparison of the crystalline SnNi nanoparticle catalysts with nominal Ni:Sni molar ratios of 50 and 20 ('SnNi50' and 'SnNi20' respectively) to the crystalline nickel nanoparticle catalyst ('Ni crys.') during furfural hydrogenation (a) Average selectivity under stable operation; (b) Mass activity after 1 hr TOS; (c) Deactivation rate constants. Errors shown are based on repeat measurements of a typical sample as indicated in the experimental section.

6.2.3 The effect of tin on sintering in nickel nanoparticles prepared using a phosphine capping agent

The presence of phosphorus on nickel nanoparticles appears to significantly improve their resistance to sintering, with the crystalline nickel version of the nanoparticles exhibiting almost no sintering. However, it was previously found that the introduction of tin to the small phosphorus-free nickel nanoparticles appeared to promote sintering. Therefore, it was important to determine if that was also the case with the phosphorus-containing nickel nanoparticles.

Figure 121 shows a TEM image of the spent amorphous SnNi nanoparticle catalyst (nominal Ni:Sn molar ratio of 20) and the corresponding particle size distributions normalised to the number of particles, surface area and volume. Whilst to a significantly lesser extent than observed for the small phosphorus-free SnNi nanoparticles, some sintering has definitely occurred. Additionally, when compared to the nickel-only version of this catalyst, there appears to be more sintering as the tail towards higher particle size is more significant. This suggests that similar to the smaller phosphorus-free nanoparticles, the addition of tin is promoting sintering, which could explain the slight increase in deactivation rate for the Sn-doped catalysts in comparison to the nickel-only equivalent. However, especially when considering the particle size distribution by surface area, the

extent of the sintering would not be expected to have a significant impact on selectivity, since there is still a large fraction of the surface area coming from particles of a similar size to the as prepared nanoparticles. Additionally, whilst sintering may be contributing to the deactivation of the catalysts, it is unlikely to account for the rapid and complete loss of activity observed, suggesting that there is another source of deactivation such as coking (which may of course also be affected by the presence of tin).

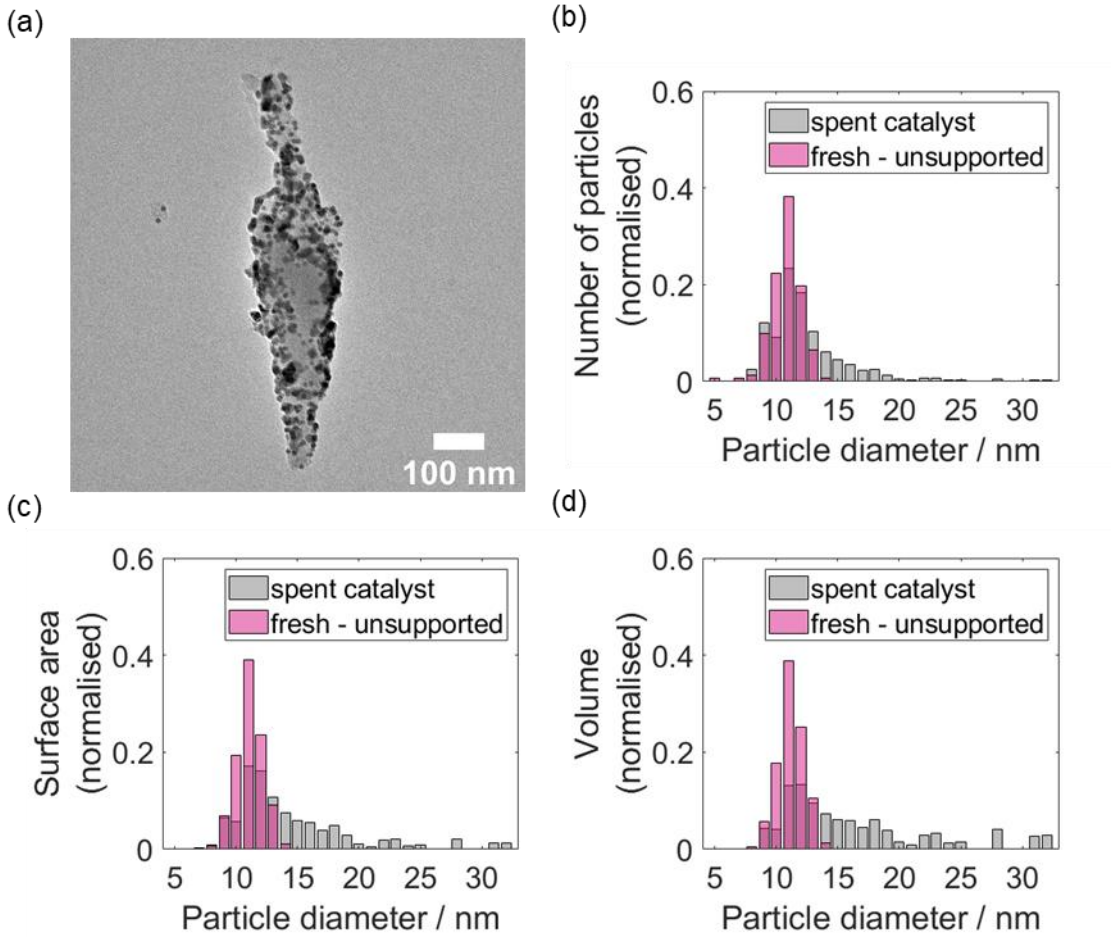

Figure 121: (a) TEM image of spent amorphous SnNi nanoparticles (nominal Ni:Sn molar ratio of 20) supported on KIT-6 and corresponding particle size distributions normalised to the (b) number of particles, (c) surface area and (d) volume

It was also important to consider whether tin would have a promotional effect on sintering in the crystalline version of the catalyst. Figure 122 shows a TEM image of the spent SnNi crystalline nanoparticle catalyst (nominal Ni:Sn ratio of 20) and the corresponding particle size distributions based on the number of particles, surface area and volume. The particle size distributions are almost identical to the as prepared nanoparticles, indicating almost no sintering has occurred. Therefore, the introduction of tin does not appear to have had any effect on sintering for the crystalline nanoparticles. Additionally, this means that sintering is not the cause of the rapid

deactivation of the catalyst, which indicates there is another source of the deactivation such as coking.

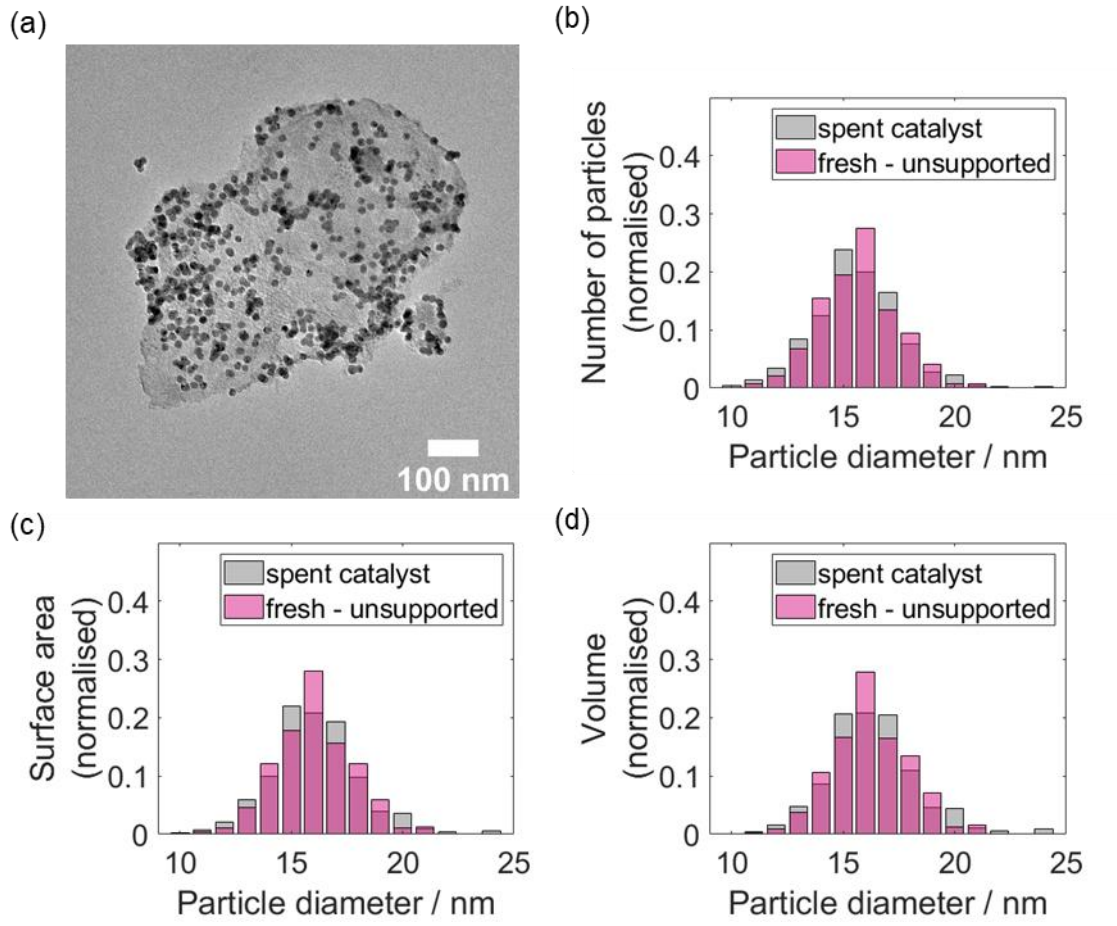

Figure 122: (a) TEM image of spent crystalline SnNi nanoparticles (nominal Ni:Sn molar ratio of 20) supported on KIT-6 and corresponding particle size distributions normalised to the (b) number of particles, (c) surface area and (d) volume

Therefore, the introduction of tin to phosphorus-containing nickel nanoparticle catalysts does appear to promote sintering in the case of the amorphous nanoparticles but has little effect on the crystalline version. Overall, the beneficial effects of phosphorus mean that despite tin possibly promoting sintering, significantly less sintering is observed in both the amorphous and crystalline nanoparticles compared to the smaller phosphorus-free nanoparticles (Section 5.2 in Chapter 5).

6.2.4 Deactivation of tin-doped nickel nanoparticles prepared using a phosphine capping agent

As discussed above (Section 6.2.3), the rapid deactivation of the catalysts cannot be explained by sintering alone. In fact, in the case of the crystalline SnNi nanoparticles, almost no sintering was observed, meaning that sintering cannot be contributing to deactivation. Therefore, the rapid deactivation observed must be caused by a different mechanism, likely coking. In order to

determine whether this is indeed the case, as well as to gain further understanding of the coking process, the spent catalysts were analysed using SS NMR and DRIFTS.

Figure 123 shows the CP/MAS ^{13}C NMR spectrum of spent amorphous SnNi nanoparticle catalyst (nominal Ni:Sn ratio of 20). The main signals fit well with furfuryl alcohol (152.2 ppm, 142.9 ppm, 109.5 ppm and 58.0 ppm),[24] however there are also some additional signals in the alkane region of the spectrum. In contrast to the nickel-only version of this catalyst, there are no additional peaks that correspond to furfural or THFA, suggesting that the introduction of tin limited the coke to furfuryl alcohol-based species. Additionally, in this spectrum, the methylol peak at 58.0 ppm is relatively strong compared to the other furfuryl alcohol peaks whereas the peaks in the alkane region are relatively weak. This suggests less extensive oligomerisation compared to the nickel-only equivalent which had a fairly weak methylol peak and stronger alkane peaks. Therefore, this potentially means that the introduction of tin is also limiting the extent of furfuryl alcohol oligomerisation. If this hypothesis is correct, it might be expected that the introduction of tin, by preventing extensive oligomerisation and therefore coking, would help to prevent deactivation. However, in this catalyst, the introduction of tin did appear to lead to small increases in the deactivation rate (although there was no clear pattern with regard to tin content). As discussed above, the introduction of tin does appear to promote sintering, and so perhaps despite the decrease in coking, the increase in sintering means that overall, the catalyst deactivates at a slightly increased rate.

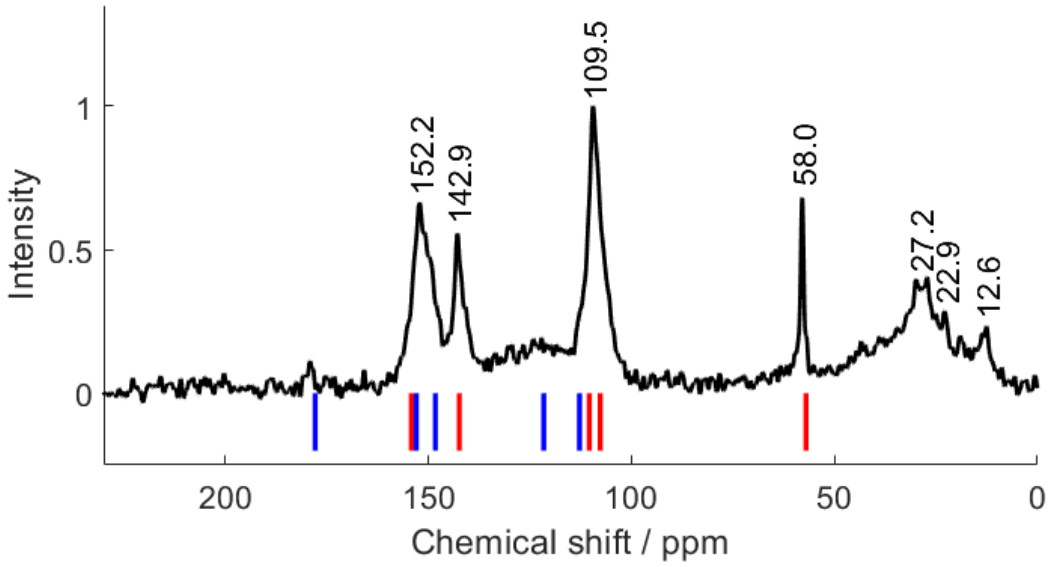

Figure 123: solid state CP/MAS ^{13}C NMR spectrum of the spent amorphous SnNi (nominal Ni:Sn molar ratio of 20) nanoparticle catalyst, with the positions of the peaks for furfuryl alcohol (solution-state NMR) shown by the red vertical lines[24] and the positions of the peaks for furfural (solution-state NMR) shown by the blue vertical lines[25]

DRIFTS was also used to analyse the coke species present on the spent SnNi amorphous catalysts (Figure 124). The spectra for the Sn-doped catalysts are fairly similar to the nickel-only equivalent, however there are some key differences. The peak at around 1700 cm^{-1} that corresponds to a similar peak seen in a sample of silica exposed to furfuryl alcohol under reaction conditions is notably less distinct in the Sn-doped catalysts. However, they do still have a relatively intense peak at around 1505 cm^{-1} which is observed in a furfuryl alcohol reference spectrum. This suggests that the furfuryl alcohol species present on the Sn-doped catalysts are more similar to furfuryl alcohol, which fits reasonably with the NMR data that suggested a lower extent of furfuryl alcohol oligomerisation in the Sn-doped catalysts. However, contrary to the NMR data, the DRIFTS analysis suggests the presence of furfural species in addition to furfuryl alcohol, since there are a number of peaks which correspond to those observed in a sample of silica that was exposed to furfural under reaction conditions. This implicates both furfuryl alcohol and furfural in the coking process, however the NMR data suggests that it is mainly furfuryl alcohol. The reason for this discrepancy is not clear, however it should be noted that DRIFTS is a more surface sensitive technique, whereas NMR looks at the bulk, so DRIFTS may be more sensitive if small amounts of a species are present on the surface of the catalyst.

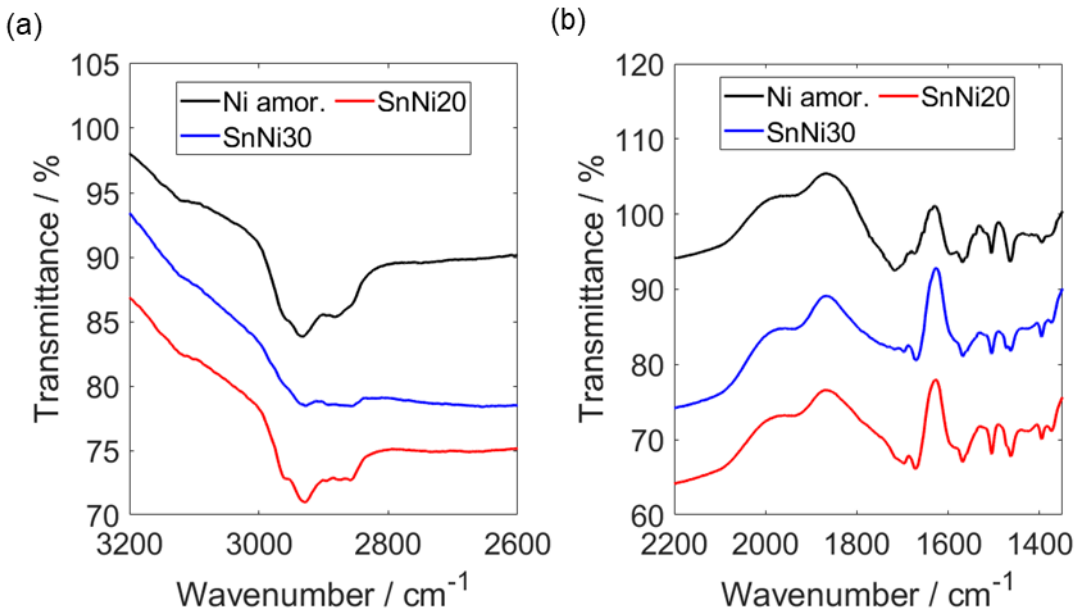

Figure 124: The DRIFT spectrum of the spent amorphous SnNi nanoparticle catalysts (Ni:Sn molar ratios of 30 and 20, corresponding to 'SnNi30' and 'SnNi20' respectively) compared to the spectra of spent amorphous nickel phosphide nanoparticle catalyst ('Ni amor.') in different key regions of the spectra; (a) 3200 – 2600 cm^{-1} and (b) 2200 – 1350 cm^{-1}

Overall, coking appears to be contributing significantly to catalyst deactivation, with the main coke species being furfuryl alcohol and, to some extent, furfuryl alcohol oligomers. The presence of tin seems to limit the extent of furfuryl alcohol oligomerisation occurring when compared to the

nickel-only equivalent. However, as tin also promotes sintering in the amorphous nanoparticle catalysts, the potential improvement tin provides in terms of coking is counteracted by the increase in sintering and so the catalysts still deactivate rapidly.

6.3 Conclusions

The use of a phosphine capping agent and subsequent presence of phosphorus in colloidal nickel nanoparticles resulted in a furfuryl alcohol selectivity of around 67 %, which is an increase of around 15 % compared to phosphorus-free nickel catalysts. The mass activity and deactivation rate constants were not significantly affected when compared to the phosphorus-free colloidal nickel nanoparticle catalyst. However, the mass activities of all colloidal nanoparticle catalysts were significantly lower than the catalyst prepared *via* IWI, likely due to the presence of capping agents limiting access to active sites. The morphology and structure of the nanoparticles (*i.e.* amorphous nickel phosphide *vs.* crystalline nickel metal) was found to have minimal impact on catalytic performance. The use of a phosphine capping agent significantly limited or even eliminated sintering during reduction and/or catalysis. This is in contrast to nanoparticles prepared using only an amine capping agent, which actually promoted sintering when compared to the IWI nickel catalysts and resulted in a severe sintering during the *in situ* reduction step prior to catalysis. Whilst particle size may be playing a role in sintering, the choice of capping agent appears to be the major factor in determining the extent of sintering. The use of a phosphine capping agent instead of, or in addition to, an amine capping agent may be a facile way to prevent sintering in colloidal nickel nanoparticles. Since sintering was significantly limited in the nickel catalysts prepared using a phosphine capping agent, the likely cause of the rapid deactivation was determined to be coking. The main coke species was found to be furfuryl alcohol and its oligomers.

The introduction of tin to nickel nanoparticles prepared using a phosphine capping agent increased the furfuryl alcohol selectivity to around 93 %, which is comparable to the smaller phosphine-free SnNi nanoparticle catalyst. The mass activity and deactivation rates were only minimally affected by the presence of tin. In the case of the amorphous nanoparticles, the presence of tin appears to have a slight promotional effect on sintering, however the introduction on tin to the crystalline nanoparticles still exhibited almost no sintering like with the nickel-only equivalent. The rapid deactivation of the catalysts was again mostly attributed to coking due to furfuryl alcohol and its oligomers.

Overall, the use of phosphine capping agents appears to be mostly beneficial, increasing the furfuryl alcohol selectivity and preventing sintering. Additionally, like with previous nickel-based catalysts, the introduction of tin can be used to further tune the selectivity towards furfuryl alcohol.

6.4 References

1. X. Lu, M. A. Baker, D. H. Anjum, W. Papawassiliou, A. J. Pell, M. Fardis, G. Papavassiliou, S. J. Hinder, S. A. A. Gaber, D. A. A. Gaber, Y. Al Wahedi and K. Polychronopoulou, *ACS Applied Nano Materials*, 2021, DOI: 10.1021/acsanm.1c00044.
2. J. Wang, A. C. Johnston-Peck and J. B. Tracy, *Chemistry of Materials*, 2009, **21**, 4462-4467.
3. L. M. Moreau, D.-H. Ha, H. Zhang, R. Hovden, D. A. Muller and R. D. Robinson, *Chemistry of Materials*, 2013, **25**, 2394-2403.
4. E. Muthuswamy, G. H. L. Savithra and S. L. Brock, *ACS Nano*, 2011, **5**, 2402-2411.
5. S. Carenco, Z. Liu and M. Salmeron, *ChemCatChem*, 2017, **9**, 2318-2323.
6. R. García-Muelas, Q. Li and N. López, *The Journal of Physical Chemistry B*, 2018, **122**, 672-678.
7. Y. Wang, X. Feng, S. Yang, L. Xiao and W. Wu, *Journal of Nanoparticle Research*, 2020, **22**, 67.
8. K. Li, R. Wang and J. Chen, *Energy & Fuels*, 2011, **25**, 854-863.
9. Y.-K. Lee and S. T. Oyama, *Journal of Catalysis*, 2006, **239**, 376-389.
10. S. Carenco, C. Boissière, L. Nicole, C. Sanchez, P. Le Floch and N. Mézailles, *Chem. Mater.*, 2010, **22**, 1340-1349.
11. C. P. Jiménez-Gómez, J. A. Cecilia, R. Moreno-Tost and P. Maireles-Torres, *ChemCatChem*, 2017, **9**, 2881-2889.
12. M. J. Rasmussen and J. W. Medlin, *Catalysis Science & Technology*, 2020, **10**, 414-423.
13. D. Vargas-Hernández, Rubio-Caballero, J. , Moreno-Tost, R. , Mérida-Robles, J. , Santamaría-González, J. , Jiménez-López, A. , Pérez-Cruz, M. , Hernández-Huesca, R. and Maireles-Torres, P., *Modern Research in Catalysis*, 2016, **5**, 85-94.
14. M. Heilmann, H. Kulla, C. Prinz, R. Bienert, U. Reinholz, A. Guilherme Buzanich and F. Emmerling, *Nanomaterials*, 2020, **10**, 713.
15. C. T. Campbell, S. C. Parker and D. E. Starr, *Science*, 2002, **298**, 811-814.
16. C. T. Campbell, J. C. Sharp, Y. X. Yao, E. M. Karp and T. L. Silbaugh, *Faraday Discussions*, 2011, **152**, 227-239.
17. C. T. Campbell and D. E. Starr, *Journal of the American Chemical Society*, 2002, **124**, 9212-9218.
18. J. A. Farmer and C. T. Campbell, *Science*, 2010, **329**, 933-936.
19. J. H. Larsen, J. T. Ranney, D. E. Starr, J. E. Musgrove and C. T. Campbell, *Physical Review B*, 2001, **63**, 195410.
20. Z. Mao, P. G. Lustemberg, J. R. Rumptz, M. V. Ganduglia-Pirovano and C. T. Campbell, *ACS Catalysis*, 2020, **10**, 5101-5114.
21. Z. Mao, W. Zhao, Z. A. Al-Mualem and C. T. Campbell, *The Journal of Physical Chemistry C*, 2020, **124**, 14685-14695.
22. D. E. Starr, D. J. Bald, J. E. Musgrove, J. T. Ranney and C. T. Campbell, *The Journal of Chemical Physics*, 2001, **114**, 3752-3764.
23. C. T. Campbell and J. R. V. Sellers, *Faraday Discussions*, 2013, **162**, 9-30.
24. Z. Jia, F. Zhou, M. Liu, X. Li, A. S. C. Chan and C.-J. Li, *Angewandte Chemie International Edition*, 2013, **52**, 11871-11874.
25. C. Cheng and M. Brookhart, *Angewandte Chemie International Edition*, 2012, **51**, 9422-9424.
26. D. K. Ahn, Y. W. Kang and S. K. Woo, *The Journal of Organic Chemistry*, 2019, **84**, 3612-3623.
27. I. S. Chuang, G. E. Maciel and G. E. Myers, *Macromolecules*, 1984, **17**, 1087-1090.
28. M. Principe, P. Ortiz and R. Martínez, *Polymer International*, 1999, **48**, 637-641.
29. C. Araujo-Andrade, A. Gómez-Zavaglia, I. D. Reva and R. Fausto, *J. Phys. Chem. A*, 2012, **116**, 2352-2365.

Chapter 7: The effect of phosphorus on the oxidation of nickel and tin-nickel colloidal nanoparticles

Up to this point, the general focus of this thesis has been on nickel-based catalysts for furfural hydrogenation. However, the nanoparticles synthesised as part of this work can also act as model catalysts for other applications including as electrocatalysts for anion exchange membrane fuel cells[1] or solid oxide fuel cells[2, 3] or for other heterogeneous catalytic processes such as the methanation of CO_2.[4, 5] In these applications, oxidation stability is an important consideration; for instance, nickel catalysts used for the methanation of CO_2 are susceptible to oxidation if a highly reducing atmosphere is not maintained, which leads to deactivation of the catalyst.[4, 5] Therefore, the stability of nickel-based nanoparticles (in particular those containing phosphorous) in oxidising environments was assessed using near ambient pressure X-ray photoelectron spectroscopy (NAP-XPS).

7.1: NAP-XPS of nickel-based nanoparticles to investigate the stability of the nanoparticles in oxidising environments

In Chapter 4, a series of nickel-based nanoparticles were synthesised, including a set of small (~4 nm) phosphorus-free SnNi nanoparticles, larger (~12 nm) amorphous nickel phosphide nanoparticles, a Sn-doped variant of the amorphous nickel phosphide nanoparticles and larger (~15 nm) crystalline nickel nanoparticles (prepared using a phosphine capping agent). Evaluating the stability of these nanoparticles variants in oxidising environments then allows the impact of various factors on the extent of oxidation to be assessed, including the presence of tin and/or phosphorus and differences in the bulk structures of the nanoparticles. It must be noted that the synthesis of large phosphorous free nanoparticles was not found to be possible, but the results are still strongly indicative of an important role of size and/or (perhaps more likely) phosphorous.

7.1.1: Oxidation of phosphorus-free small SnNi nanoparticles

The NAP-XP spectra for the small phosphorus-free SnNi nanoparticles under different conditions are shown in Figure 125. The Ni 2p spectra were recorded at both 1100 eV and 1490 eV (kinetic energies (KE's) of 250 eV and 640 eV respectively) in order to probe different depths into the nanoparticles (Figure 125a and b). The sample was initially reduced *in situ* at 300 °C in 1 mbar of H_2 and then spectra were recorded sequentially under varying the conditions. The first spectra were recorded at 180 °C in 1 mbar of H_2 and at both lower and higher kinetic energies, there is one main

peak at 852.6 eV, which fits well with the $2p_{3/2}$ peak for metallic nickel.[6] This means the *in situ* reduction step has successfully reduced the nickel surface.

When the gas was changed to 1 mbar of O_2, still at a temperature of 180 °C, there was a distinct change in the spectra obtained at both lower and higher kinetic energies, with the main peak now centred at 855.7 eV. There is some debate about the assignment of this peak; it is often attributed to Ni^{3+} species,[7, 8] possibly as part of a structure such as Ni_2O_3, however it has also been proposed to correspond to lattice distortions that form due to vacancies in nickel oxide[9] or nickel hydroxide species.[10] Ultimately, the appearance of this peak signifies the oxidation of nickel upon the introduction of oxygen at 180 °C. Although the main peak corresponds to oxidised nickel, there is still a small shoulder present in both the lower and higher kinetic energy spectra at around 852.7 eV, which indicates that very small amounts of metallic nickel remain.

In order to study the reversibility of the oxidation, the gas was then changed back to 1 mbar of H_2, still at a temperature of 180 °C. This resulted in minimal changes to the spectra at both lower and higher kinetic energies, indicating that the sample remained oxidised, despite being placed into a reducing environment. This is not completely unexpected, since TPR analysis of these nanoparticles, after supporting them on KIT-6 silica, showed no significant hydrogen consumption below temperatures of around 300 °C. Therefore, the sample was then heated to 300 °C in 1 mbar of H_2 to confirm that the nickel would reduce. There was one main peak in the spectra at both lower and higher kinetic energies at 852.6 eV, which is consistent with the $2p_{3/2}$ peak for metallic nickel. Therefore, whilst 180 °C was not sufficient to reduce the nickel, heating to 300 °C has resulted in full reduction/complete reversal of the oxidation process.

The Sn 3d spectra (Figure 125c and d) were recorded with appropriate photon energies (700 eV and 1100 eV) to match the kinetic energies (~200 eV and ~600 eV) of the nickel spectra. At 180 °C in 1 mbar of H_2, both the lower and higher kinetic energy spectra have two main peaks at 484.7 eV and 493.2 eV which correspond to the $3d_{3/2}$ and $3d_{1/2}$ peaks of metallic tin.[6] However, there are some significant shoulders at around 486.5 eV and 494.9 eV especially in the lower kinetic energy, more surface sensitive spectrum, which correspond to the $3d_{3/2}$ and $3d_{1/2}$ peaks for SnO_2.[6] Therefore, despite reduction at 300 °C, the tin was not fully reduced.

When the gas was changed to 1 mbar of O_2, still at 180 °C, the only peaks present corresponded to SnO_2, indicating the tin had been fully oxidised. This is expected since tin appears to favour oxidation (reduction at 300 °C did not fully reduce the tin) and, as described in Chapter 4, cooling from 300 °C to 180 °C in 1 mbar of H_2 resulted in an increase in the extent of oxidation. Switching the gas back to 1 mbar of H_2 made no significant difference to the extent of reduction, therefore,

similar to nickel, 180 °C is not sufficient to reduce the tin. A temperature of 300 °C was required to achieve partial reduction, similar to that of sample before the oxidation procedure.

Overall, exposure of the sample to oxygen at 180 °C results in almost complete oxidation of both the nickel and tin, which is only reversible after heating the sample to 300 °C in 1 mbar of H_2.

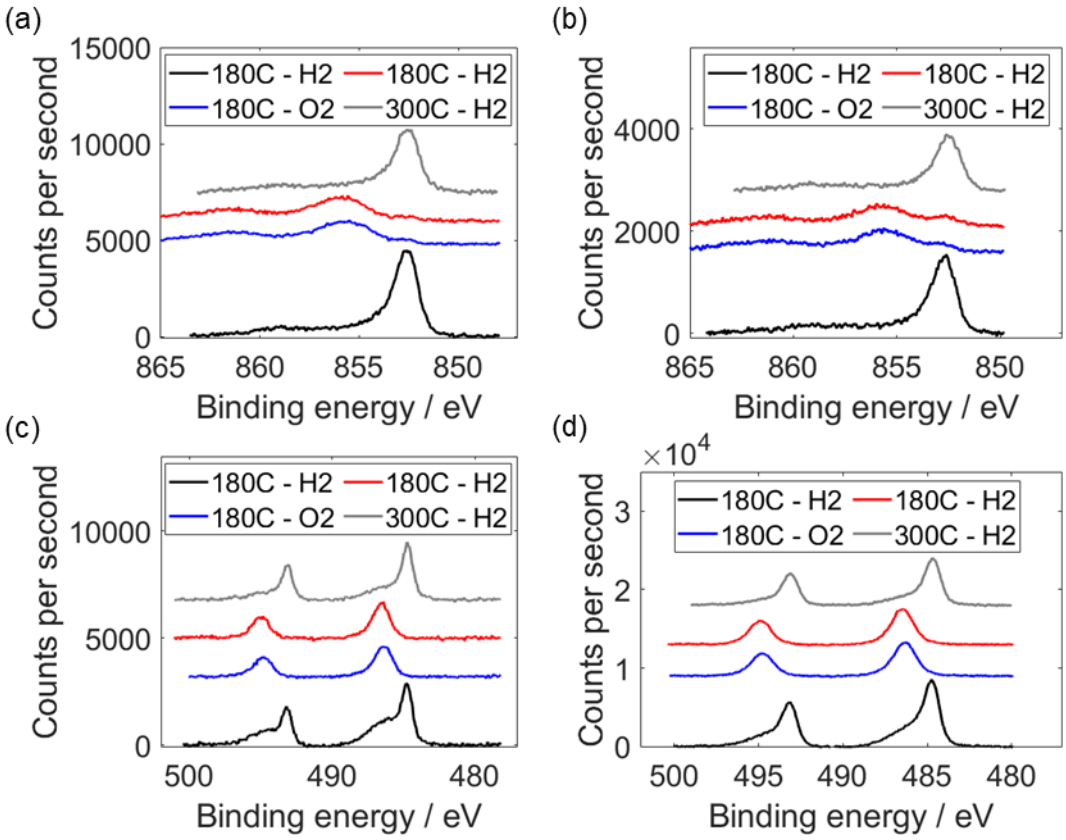

Figure 125: NAP-XP spectra of the SnNi sequential addition nanoparticles deposited on a silicon wafer after *in situ* reduction in 1 mbar of H_2 at 300 °C. A series of spectra were recorded sequentially under different conditions: 180 °C under 1 mbar of H_2 (black - '180C – H2'), followed by 1 mbar of O_2 at 180 °C (blue - '180C – O2'), 1 mbar of H_2 at 180 °C (red - '180C – H2') and finally 1 mbar of H_2 at 300 °C (grey - '300C – H2'). (a) Ni 2p spectra recorded with a photon energy (E_{ph}) of 1100 eV (kinetic energy (KE) of 250 eV), (b) Ni 2p spectra recorded with a E_{ph} of 1490 eV (KE of 640 eV), (c) Sn 3d spectra recorded with a E_{ph} of 700 eV (KE of 220 eV) and (d) Sn 3d spectra recorded with a E_{ph} of 1100 eV (KE of 620 eV). Spectra are vertically offset for clarity.

7.1.2: Oxidation of amorphous nickel phosphide nanoparticles

As discussed in Chapter 4, it was not possible to synthesise larger (10 – 15 nm) colloidal nickel nanoparticles without the use of a phosphine capping agent. The result of using a phosphine capping agent was incorporation of phosphorus into the surface and/or bulk of the nanoparticles, depending on the chosen synthetic method (Chapter 4). When investigating the oxidation of the larger amorphous SnNi nanoparticles that were prepared using a phosphine capping agent, it was

first important to establish the effect of phosphorus on oxidation in a simpler system *i.e.* the nickel only nanoparticles prepared using the same synthetic method.

The amorphous nickel phosphide nanoparticles were examined using NAP-XPS (Figure 126). The sample was first reduced *in situ* at 300 °C in 1 mbar of H_2, before being cooled down to 180 °C, still in 1 mbar of H_2. The Ni 2p spectra were recorded with different photon energies (1100 eV and 1650 eV) in order to probe different depths into the nanoparticles (Figure 126a and b respectively). At 180 °C in 1 mbar of H_2, the Ni 2p spectra, both at lower and higher kinetic energies, contain one main peak at 852.6 eV. This could be consistent with the $2p_{3/2}$ peak for metallic nickel[6] or $Ni^{\delta+}$ as part of nickel phosphide since the small charge transfer from nickel to phosphorus does not typically lead to identifiable shifts in the peak position when compared to metallic nickel.[11-13] However, particularly in the lower kinetic energy, more surface sensitive spectrum, there is a weaker second peak at 856.8 eV. As discussed above, there is some debate about the assignment of this peak, however it is generally thought to be related to oxidised nickel or nickel hydroxide species.[7-10] Additionally, increasing amounts of phosphorus in nickel oxide materials has been shown to lead to an increase in this peak compared to the standard Ni^{2+} peak for NiO.[14] Ultimately, the presence of this peak in the most surface sensitive spectrum indicates that a small amount of the top surface of the sample was not completely reduced.

The gas was then switched to 1 mbar of O_2, with the temperature still at 180 °C. In both the lower and higher kinetic energy spectra this led to a significant increase in the oxidised nickel peak relative to the metallic nickel/$Ni^{\delta+}$ peak, however the increase was substantially higher in the lower kinetic energy spectrum. Additionally, the metallic nickel/$Ni^{\delta+}$ peak is still also present in both the lower and higher kinetic energy spectra indicating that full oxidation has not occurred. The amount of oxidised species, relative to reduced species, is significantly less in the higher kinetic energy spectrum, which indicates that oxidation is mostly limited to the top surface of the nanoparticles. This is in contrast to the small phosphorus-free SnNi nanoparticles where almost complete oxidation occurred, which may suggest that the presence of phosphorus, either as capping agent or nickel phosphide, may be offering some protection against oxidation. In fact, there are some reports that metal phosphides, including nickel phosphide, are more resistant to oxidation than their metal-only counterparts.[15, 16] However, it is important to also consider size effects since the phosphorus-free nanoparticles are significantly smaller than the amorphous nickel phosphide nanoparticles (4 nm vs. 12 nm respectively) and the size of nickel nanoparticles is known to have significant effect on both the rate and extent of oxidation.[3] Additionally, it is unclear what impact the presence of tin may be having, especially since tin itself appears to favour oxidation (*e.g.* not fully reduced at 300 °C in 1 mbar H_2 and an increase in the oxide peak upon cooling to 180 °C in a

reducing atmosphere). Therefore, whilst the presence of phosphorus may be having an impact on oxidation resistance, other factors cannot be ruled out.

The P 2p spectra were also recorded at different photon energies (550 eV and 1100 eV) to probe different depths into the nanoparticles (Figure 126c and d). At 180 °C in 1 mbar of H_2, there are two peaks present in both the lower and higher kinetic energy spectra; one at 133.5 eV and a second at 129.7 eV. There is only small difference between the $2p_{3/2}$ and $2p_{1/2}$ peaks for phosphorus (~0.84 eV)[6] and so there is often significant overlap. The peak at 133.5 eV can then be assigned as the $2p_{3/2}$ and $2p_{1/2}$ peaks for the phosphine capping agent interacting with the surface and the peak at 129.7 eV can be assigned as the $2p_{3/2}$ and $2p_{1/2}$ peaks for nickel phosphide.[17]

Upon changing the gas to 1 mbar of O_2 at a temperature of 180 °C, a new peak appears as a shoulder on the higher binding energy side of the peak corresponding to the phosphine capping agent and is particularly strong in the lower kinetic energy spectrum. Additionally, the amount of phosphide present relative to the capping agent peak is lowered in the oxidising atmosphere. This suggests that some phosphide species, particularly on the top surface of the nanoparticles, are being oxidised to phosphates since this would explain both the decrease in the amount of phosphide and the introduction of the new higher binding energy peak.

Overall, the amorphous nickel phosphide nanoparticles are significantly more resistant to oxidation than the small phosphorus-free SnNi nanoparticles. A number of factors could explain this, including the larger particle size, the absence of tin or the presence of nickel phosphide.

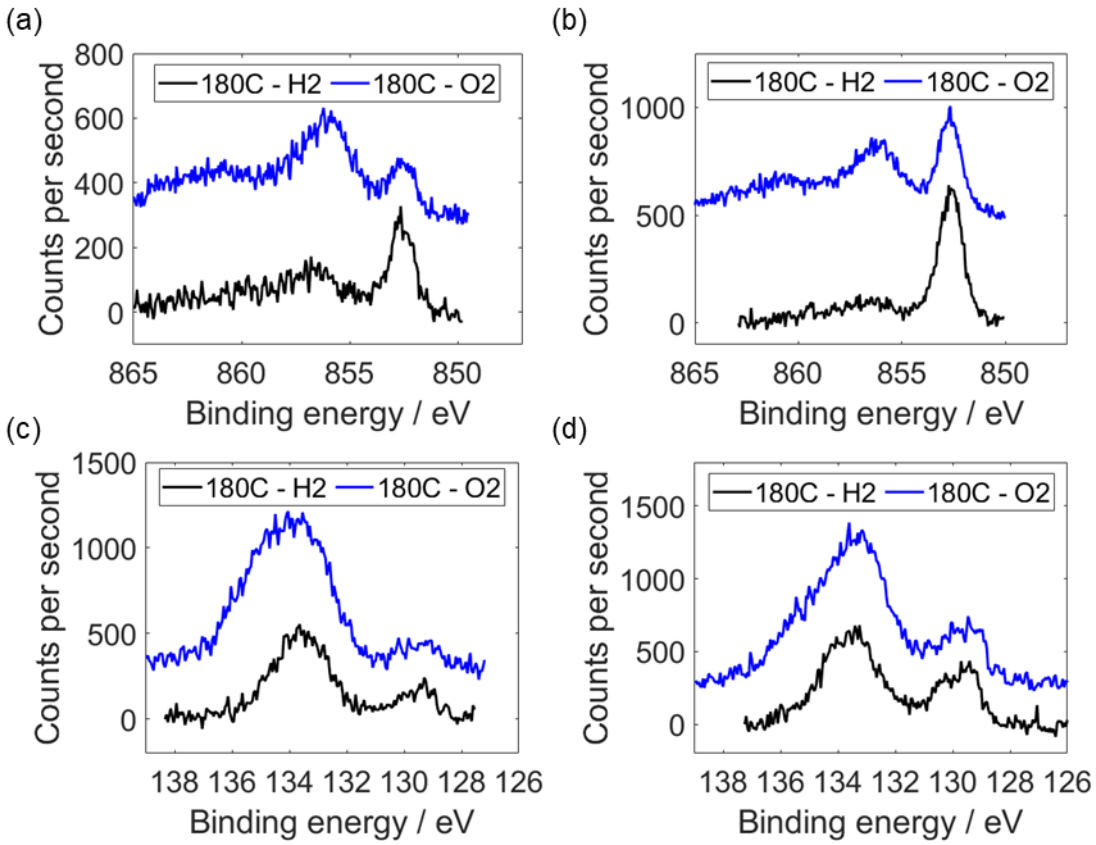

Figure 126: NAP-XP spectra of the amorphous nickel phosphide nanoparticles deposited on a silicon wafer after *in situ* reduction in 1 mbar of H_2 at 300 °C. The spectra were recorded sequentially under different conditions: 180 °C under 1 mbar of H_2 (black - '180C – H2'), followed by 1 mbar of O_2 at 180 °C (blue - '180C – O2'). (a) Ni 2p spectra recorded with a photon energy (E_{ph}) of 1100 eV (kinetic energy (KE) of 250 eV), (b) Ni 2p spectra recorded with a E_{ph} of 1490 eV (KE of 640 eV), (c) P 2p spectra recorded with a E_{ph} of 550 eV (KE of 420 eV) and (d) P 2p spectra recorded with a E_{ph} of 1100 eV (KE of 970 eV). Spectra are vertically offset for clarity.

7.1.3: Oxidation of amorphous SnNi nanoparticles

The effect of tin on the oxidation resistance of the amorphous nickel phosphide nanoparticles was then examined using NAP-XPS (Figure 127). As with the previous samples, the nanoparticles were reduced *in situ* at 300 °C in 1 mbar of H_2 before being cooled to 180 °C, still in 1 mbar of H_2, and then exposed sequentially to a variety of conditions. The Ni 2p spectra were recorded at different photon energies (1100 eV and 1650 eV) in order to probe different depths into the nanoparticles (Figure 127a and b). At 180 °C in 1 mbar of H_2, both the lower and higher kinetic energy spectra contain one main peak at around 852.8 eV, which is consistent with the $2p_{3/2}$ peak for metallic nickel[6] or, as discussed previously, $Ni^{\delta+}$ as part of nickel phosphide.[11-13] When the gas was switched to 1 mbar of O_2 at 180 °C, a small peak at around 856.3 eV appears in the spectra at both lower and higher kinetic energies, but to larger extent in the lower kinetic energy spectrum. This indicates that the oxidation has been mostly limited to the top surface of the nanoparticles and that the bulk has

remained as nickel metal/nickel phosphide, similar to the results seen for the tin-free nanoparticles. However, in comparison to the tin-free equivalent, the extent of oxidation is more limited, particularly in the higher kinetic energy spectrum. This suggests that the introduction of tin has, to some extent, helped to protect the nickel from oxidation.

Changing the gas back to 1 mbar of H_2 has little impact on the higher kinetic energy spectrum, likely since minimal oxidation was observed whilst in an oxidising environment anyway. However, in the lower kinetic energy spectrum, there is a significant increase in the metallic nickel/nickel phosphide peak relative to the oxidised nickel peak. This indicates that the presence of H_2 at the relatively low temperature of 180 °C is enough to reduce at least some of the oxidised species on the surface of the nanoparticles. In comparison, the small phosphorus-free SnNi nanoparticles showed no significant reduction of oxidised nickel until the sample was heated to 300 °C in the presence of hydrogen. This raises the possibility that not only might phosphorus be contributing to the increased oxidation resistance of these nanoparticles, but also promoting reduction when the oxidised species are then placed into a reducing environment. However, again it is important to consider other possibilities, such as size differences or the fact that the phosphorus-free nanoparticles were almost completely oxidised, whereas only the top surface of the phosphorus-containing nanoparticles were oxidised. Heating the nanoparticles to 300 °C in 1 mbar of H_2 resulted in further reduction of nickel and the spectra at both lower and higher kinetic energies were very similar to the spectra obtained for the sample prior to oxidation, indicating the oxidation was fully reversed.

The Sn 3d spectra are shown in Figure 127c and d and were recorded with photon energies of 700 eV and 1300 eV in order to obtain data with similar KE's to those used for nickel. The spectra recorded for the sample at 180 °C in 1 mbar of H_2 contain two sets of peaks. As discussed in Chapter 4, the main peaks at 487.2 eV and 495.6 eV could be assigned as the $3d_{5/2}$ and $3d_{3/2}$ peaks of SnO_2[6] or the Sn^{2+}/Sn^{4+} species found in tin phosphides such as trigonal Sn_3P_4.[18] Given the nanoparticle synthesis method employed, which is known to result in phosphorus incorporation, and the fact that the species showed limited reducibility, it was thought that these peaks likely corresponded to tin phosphide. The second set of peaks at 484.7 eV and 493.1 eV, which appear as small shoulders, correspond to the $3d_{5/2}$ and $3d_{3/2}$ peaks for metallic tin.[6]

Changing the gas to 1 mbar of O_2 results in the disappearance of the metallic tin peaks in both the lower and higher kinetic energy spectra, however there is no significant change to the peak likely corresponding to tin phosphide. This likely indicates that the metallic tin species have been oxidised and now the main set of tin peaks correspond to a mix of tin phosphide and oxidised tin species.

Since the peaks for oxidised tin and tin phosphide species would be expected to have very similar peak positions, it is not possible to conclusively determine whether the tin phosphide has been oxidised.

When the gas was switched back to 1 mbar of H_2 at 180 °C, the small shoulders corresponding to metallic tin re-appeared in both the lower and higher kinetic energy spectra. This indicates that, like with the nickel in this sample, a reducing environment at the relatively low temperature of 180 °C is enough to reduce the oxidised tin. This is again contrary to that seen for the small phosphorus-free SnNi nanoparticles, where heating to 300 °C in hydrogen was required for any reduction of the oxidised tin to occur. As discussed in relation to nickel, this does imply that the presence of phosphorus may be promoting the reduction of oxidised species, resulting in significantly lower reduction temperatures. However, particle size differences and the extent of oxidation that occurs could also be contributing and so should also be considered. Heating the sample to 300 °C in 1 mbar of H_2 did not result in any significant changes in the spectra both at lower and higher kinetic energies.

The P 2p spectra were recorded with two different photon energies (550 eV and 1100 eV) in order to probe different depths into the nanoparticles (Figure 127e and f). At 180 °C in 1 mbar of H_2, the spectra at both lower and higher kinetic energy contain two main peaks at 133.6 eV and 129.4 eV. Similar to the nickel-only variant of these nanoparticles, these peaks are consistent with the phosphine capping agent interacting with the surface of the nanoparticles and the formation of phosphides, in this case either nickel phosphide, tin phosphide or a combination of both.[17]

Changing the gas to 1 mbar of O_2, whilst maintaining a temperature of 180 °C, did not result in significant changes to the spectrum recorded at higher kinetic energy, however in the lower kinetic energy spectrum, there was a significant decrease in the phosphide peak, relative to the phosphine capping agent peak. This suggests that some of the phosphide species on the top surface of the nanoparticles are being oxidised to some extent. Unlike with the nickel-only version of these nanoparticles, there is not any significant quantity of a species that appears at a slightly higher energy to the phosphine capping agent peak. It is unclear why this is the case, however it is likely to do with the introduction of tin, since this is the key difference between the samples.

When the gas was changed back to 1 mbar of H_2 at 180 °C, there was again no significant difference in the higher kinetic energy spectrum, however in the lower kinetic energy spectrum, there was an increase in the phosphide peak relative to the phosphine capping agent, with the ratio now appearing similar to that seen for the sample prior to oxidation. This is consistent with the fact that most of the oxidation of the metals in this sample was reversible in a reducing environment at

180 °C. Heating the sample to 300 °C in 1 mbar of H_2 led to no significant changes to either lower or higher kinetic energy spectra.

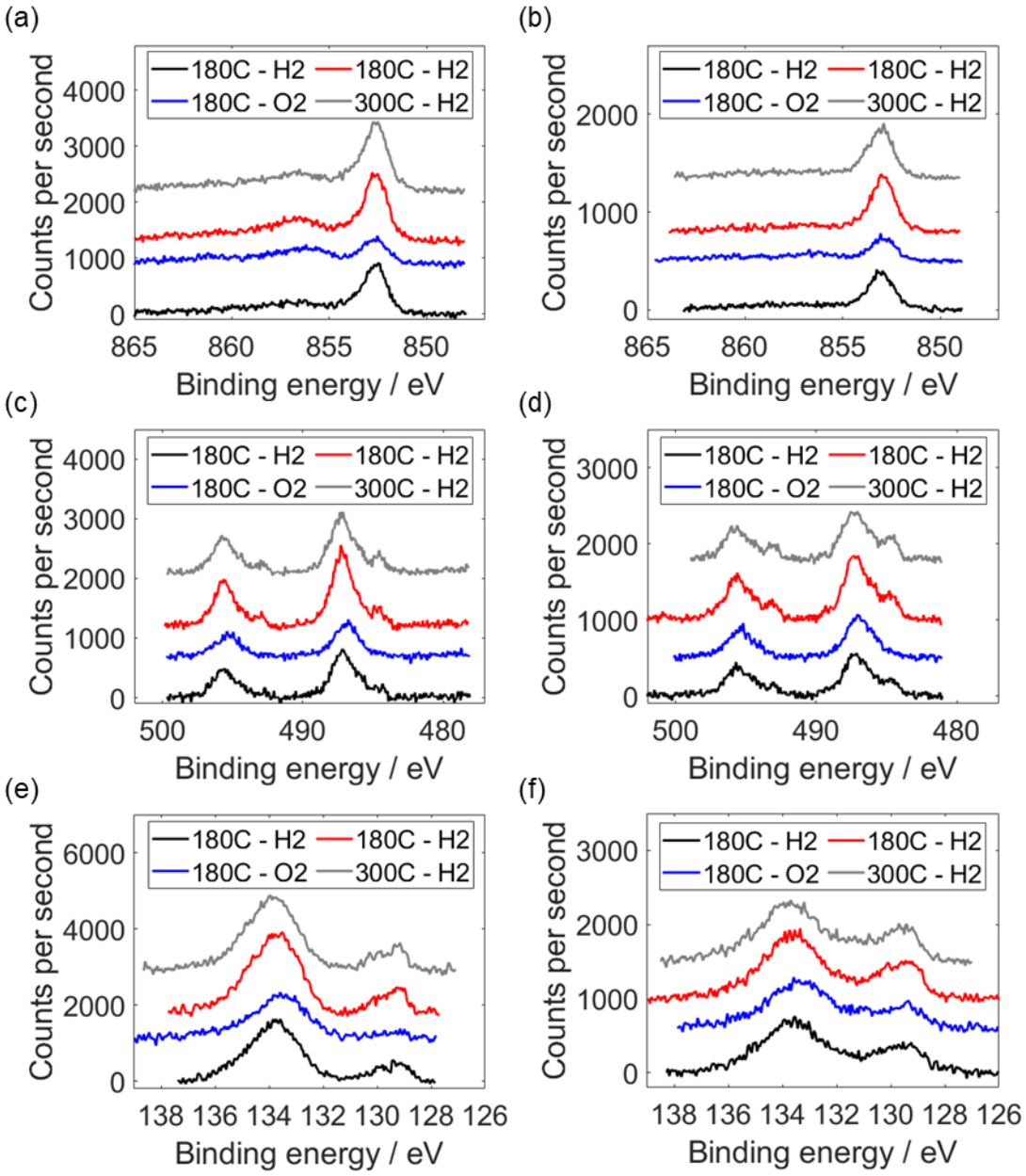

Figure 127: NAP-XP spectra of the amorphous SnNi nanoparticles (nominal Ni:Sn molar ratio of 20) deposited on a silicon wafer after *in situ* reduction in 1 mbar of H_2 at 300 °C. A series of spectra were recorded sequentially under different conditions: 180 °C under 1 mbar of H_2 (black - '180C – H2'), followed by 1 mbar of O_2 at 180 °C (blue - '180C – O2'), 1 mbar of H_2 at 180 °C (red - '180C – H2') and finally 1 mbar of H_2 at 300 °C (grey - '300C – H2'). (a) Ni 2p spectra recorded with a photon energy (E_{ph}) of 1100 eV (kinetic energy (KE) of 250 eV), (b) Ni 2p spectra recorded with a E_{ph} of 1650 eV (KE of 800 eV), (c) Sn 3d spectra recorded with a E_{ph} of 700 eV (KE of 220 eV), (d) Sn 3d spectra recorded with a E_{ph} of 1300 eV (KE of 820 eV), (e) P 2p spectra recorded with a E_{ph} of 550 eV (KE of 420 eV) and (f) P 2p spectra recorded with a E_{ph} of 1100 eV (KE of 970 eV). Spectra are vertically offset for clarity.

A comparison of the Ni 2p spectra in 1 mbar of O_2 at 180 °C, recorded at both lower and higher kinetic energies, is shown in Figure 128, in order to highlight and summarise the key differences in the oxidation of nickel for the different samples discussed thus far. The small phosphorus-free SnNi nanoparticles were almost completely oxidised, with only a small shoulder corresponding to nickel metal seen in both the lower and higher kinetic energy spectra. The larger amorphous nickel phosphide nanoparticles exhibit a noticeable decrease in the extent of oxidation, particularly in the higher kinetic energy spectrum. Additionally, the higher ratio of metal to oxide in the higher kinetic energy spectrum compared to the lower kinetic energy spectrum suggests the oxidation is limited to the surface of the nanoparticles. There are a few likely explanations for this result; the smaller size of the SnNi nanoparticles makes them more susceptible to oxidation, the presence of tin is promoting oxidation or the presence of phosphorus, particularly as nickel phosphide, is increasing the oxidation resistance.

Finally, the introduction of tin to the amorphous nickel phosphide nanoparticles further improves the oxidation resistance of nickel, with a proportion of the top surface remaining as reduced species and very little oxidation observed deeper in the nanoparticles. It has been shown for a variety of metals, although not specifically tin, that the metal phosphide version is more stable to oxidising environments than the metal-only equivalent.[15, 16] Additionally, computational studies have predicted that tin phosphide monolayers would be stable in air up to temperatures of over 900 °C.[19] Although not conclusive, it appears likely that the majority of the tin present in these nanoparticles is there as tin phosphide. Assuming this is the case, a possible explanation for the increase in stability upon addition of tin is that tin phosphide species on or near the surface of the nanoparticles provide additional protection for nickel against oxidation.

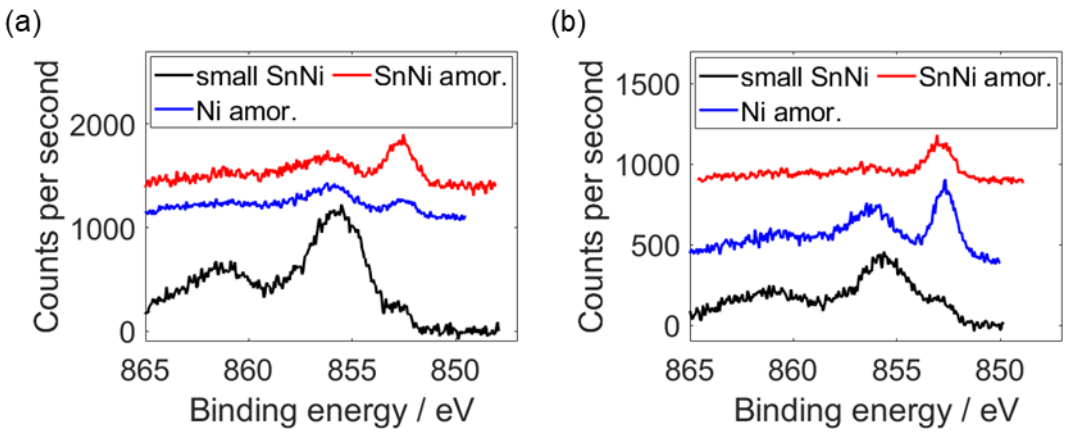

Figure 128: A comparison of the Ni 2p NAP-XP spectra for the small phosphorus-free SnNi nanoparticles ('small SnNi'), the amorphous nickel phosphide nanoparticles ('Ni amor.') and the amorphous SnNi after *in situ* reduction in 1 mbar of H_2 at 300 °C and then exposure to 1 mbar of O_2 at 180 °C. More and less surface sensitive spectra were recorded by varying the E_{ph}; (a) more surface sensitive - E_{ph} of 1100 eV (kinetic energy (KE) of 250 eV) and (b) less surface sensitive - E_{ph} of 1490 eV for the small phosphorus-free SnNi nanoparticles (KE of 640 eV) and 1650 eV for the other samples (KE of 800 eV). Spectra are vertically offset for clarity.

7.1.4: Oxidation of crystalline nickel nanoparticles prepared using a phosphine capping agent

Whilst the surface of the crystalline nickel nanoparticles (prepared using TOP) and the amorphous nickel phosphide nanoparticles were both found to contain nickel phosphide, the bulk structures of these nanoparticles were found to be very different. Therefore, in order to investigate whether this would have any effect on oxidation resistance, the crystalline nickel nanoparticles were also examined with NAP-XPS under reducing and oxidising conditions (Figure 129).

The Ni 2p spectra were recorded with photon energies of 1100 eV and 1650 eV in order to probe different depths into the nanoparticles (Figure 129a and b). At 180 °C in 1 mbar of H_2, both the lower and higher kinetic energy spectra contain one main peak at 852.7 eV, which corresponds to the $2p_{3/2}$ peak for metallic nickel[6] or, as discussed above, $Ni^{\delta+}$ as part of nickel phosphide.[11-13] Particularly in the lower kinetic energy spectrum, there is also a weak peak at 856.6 eV that corresponds to oxidised nickel species,[7-10] indicating the top surface of the nanoparticles was not fully reduced. When the gas was switched to 1 mbar of O_2 at 180 °C, the peak corresponding to oxidised species relative to the peak for metallic nickel/$Ni^{\delta+}$ becomes significantly stronger in both the lower and higher kinetic energy spectra, although this is to a much larger extent in the lower kinetic energy spectrum. This indicates that the majority of the oxidation is limited to the top surface of the nanoparticles and that the bulk likely remains reduced. In comparison to the amorphous nickel phosphide nanoparticles, there does appear to be a slightly higher ratio of

metallic nickel/$Ni^{\delta+}$ compared to oxidised species in the lower kinetic energy spectrum, suggesting that there is a slight increase in oxidation resistance, however this difference is relatively small.

When the gases were changed back to 1 mbar of H_2, there is actually a slight decrease in the amount of metallic nickel/$Ni^{\delta+}$ species relative to the oxidised species in the lower kinetic energy spectrum, though the higher kinetic energy spectrum remains mostly unchanged. One possible explanation is that the rate of oxidation of the nanoparticles is slow, and so since the sample remained in an oxidising atmosphere for a period of time after the lower kinetic energy nickel spectrum was recorded in order to obtain other spectra, further oxidation may have occurred. The ratio of metallic nickel/$Ni^{\delta+}$ species to oxidised species in the lower kinetic energy spectrum is now much more similar to that obtained for the amorphous nickel phosphide nanoparticles. Therefore, this suggests that the differing bulk structures is having a limited effect on the oxidation of the nanoparticles. Additionally, unlike with the amorphous SnNi nanoparticles, 1 mbar of H_2 at 180 °C is not enough to reverse or even partially reverse the oxidation that has occurred.

The P 2p spectra were also taken with different photon energies (550 eV and 1100 eV) in order to probe different depths into the nanoparticles (Figure 129c and d). Like with the amorphous nickel phosphide nanoparticles, the spectra contain two main peaks at 133.6 eV and 129.7 eV that correspond to the phosphine capping agent interacting with the surface of the nanoparticles and nickel phosphide respectively.[17] Changing the gases from 1 mbar of H_2 to 1 mbar of O_2 and then back again at 180 °C had a minimal effect on the higher kinetic energy spectra, apart from a slight decrease in the amount of phosphide present relative to capping agent. Oxidised phosphorus species would be expected to appear at similar binding energies to the peak for phosphine capping agent interacting with the surface. Therefore, this decrease of the phosphide peak may be explained by oxidation. The decrease in the phosphide peak relative to the phosphine capping agent was more noticeable in the lower kinetic energy spectrum, again suggesting that some phosphorus species are oxidised and also, that there is more oxidation on the top surface of the nanoparticles. An oxidising environment resulted in a new peak in the phosphorus spectra of the amorphous nickel phosphide nanoparticles, likely corresponding to oxidised phosphorus species. There are no significant observable quantities of this phosphorus species here, however it does appear that in both sets of nanoparticles, the phosphorus is oxidised to some degree.

Overall, there appears to be little difference in the oxidation susceptibility of the amorphous nickel phosphide nanoparticles and the crystalline nickel nanoparticles (prepared with a phosphine-capping agent). This indicates that the bulk structure of the nanoparticles has little effect on the extent of oxidation that occurs. The surfaces of both sets of nanoparticles contain nickel

phosphide and so it is likely that this provides an explanation for the very similar extent of oxidation seen.

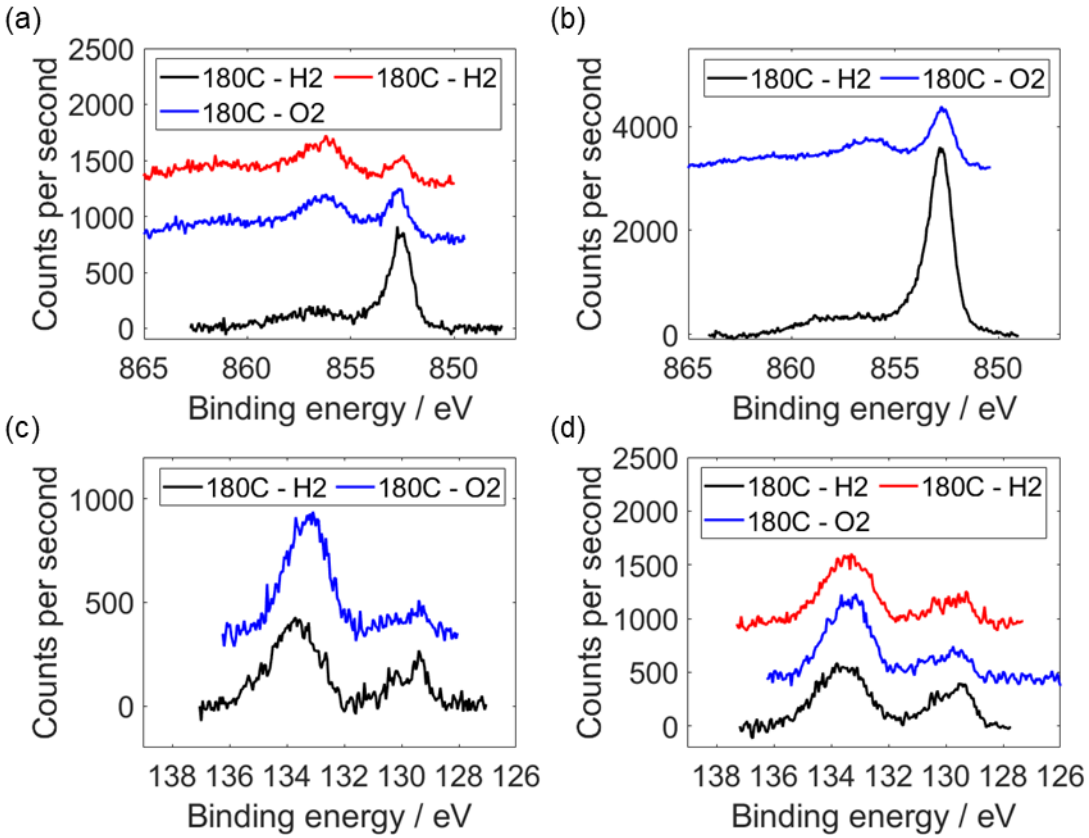

Figure 129: NAP-XP spectra of the crystalline nickel nanoparticles (prepared using TOP) deposited on a silicon wafer after *in situ* reduction in 1 mbar of H_2 at 300 °C. The spectra were recorded sequentially under different conditions: 180 °C under 1 mbar of H_2 (black - '180C – H2'), followed by 1 mbar of O_2 at 180 °C (blue - '180C – O2') and in some cases, after changing back to 1 mbar of H_2 at 180 °C. (a) Ni 2p spectra recorded with a photon energy (E_{ph}) of 1100 eV (kinetic energy (KE) of 250 eV), (b) Ni 2p spectra recorded with a E_{ph} of 1490 eV (KE of 640 eV), (c) P 2p spectra recorded with a E_{ph} of 550 eV (KE of 420 eV) and (d) P 2p spectra recorded with a E_{ph} of 1100 eV (KE of 970 eV). Spectra are vertically offset for clarity.

7.2 Conclusions

The small phosphorus-free SnNi nanoparticles suffered almost complete oxidation at 180 °C in oxidising conditions. Additionally, the sample had to be heated to 300 °C in reducing conditions to reverse the oxidation that occurred. In comparison, the larger amorphous nickel phosphide nanoparticles suffered significantly less oxidation and the oxidation that did occur was mostly limited to the surface, with the bulk relatively unaffected. The key differences between the nanoparticles were the size and the presence of phosphorus, both of which are known to have an impact on stability in oxidising environments. The introduction of tin to the amorphous nickel phosphide nanoparticles, likely in the form of tin phosphide on the surface, led to an increase in

the stability of the nanoparticles in an oxidising environment. This suggests the presence of tin phosphide on the surface of nickel-based nanoparticles may provide additional protection for the nickel against oxidation. Additionally, a significant portion of the oxidation that did occur was reversible at the low temperature of 180 °C in a reducing environment, suggesting that either the tin or phosphorus is also promoting the reduction of oxidised species. Finally, the bulk structure of the nanoparticles (amorphous nickel phosphide *vs.* crystalline nickel metal) had little impact on their oxidation stability. This suggests that the presence of nickel phosphide on the surface of both sets of nanoparticles was the major factor in determining oxidation stability. Overall, this provides possible avenues for exploration to increase the oxidation stability of nickel-based catalysts.

7.3 References

1. E. S. Davydova, F. D. Speck, M. T. Y. Paul, D. R. Dekel and S. Cherevko, *ACS Catalysis*, 2019, **9**, 6837-6845.
2. C. Song, *Catalysis Today*, 2002, **77**, 17-49.
3. V. Vonk, N. Khorshidi and A. Stierle, *The Journal of Physical Chemistry C*, 2017, **121**, 2798-2806.
4. B. Mutz, H. W. P. Carvalho, S. Mangold, W. Kleist and J.-D. Grunwaldt, *Journal of Catalysis*, 2015, **327**, 48-53.
5. B. Mutz, A. M. Gänzler, M. Nachtegaal, O. Müller, R. Frahm, W. Kleist and J.-D. Grunwaldt, *Catalysts*, 2017, **7**.
6. J. F. Moulder and J. Chastain, *Handbook of X-ray Photoelectron Spectroscopy: A Reference Book of Standard Spectra for Identification and Interpretation of XPS Data*, Physical Electronics Division, Perkin-Elmer Corporation, 1992.
7. C. N. R. Rao, V. Vijayakrishnan, G. U. Kulkarni and M. K. Rajumon, *Applied Surface Science*, 1995, **84**, 285-289.
8. A. F. Carley, S. D. Jackson, M. W. Roberts and J. O'Shea, *Surface Science*, 2000, **454-456**, 141-146.
9. D. Alders, F. C. Voogt, T. Hibma and G. A. Sawatzky, *Physical Review B*, 1996, **54**, 7716-7719.
10. J. C. Vedrine, G. Hollinger and D. Tran Minh, *The Journal of Physical Chemistry*, 1978, **82**, 1515-1520.
11. Y. Pan, Y. Liu, J. Zhao, K. Yang, J. Liang, D. Liu, W. Hu, D. Liu, Y. Liu and C. Liu, *J. Mater. Chem. A*, 2015, **3**, 1656-1665.
12. G. Yun, Q. Guan and W. Li, *RSC Advances*, 2017, **7**, 8677-8687.
13. S. Fujita, K. Imagawa, S. Yamaguchi, J. Yamasaki, S. Yamazoe, T. Mizugaki and T. Mitsudome, *Scientific Reports*, 2021, **11**, 10673.
14. Ş.-B. Ivan, I. Popescu, I. Fechete, F. Garin, V. I. Pârvulescu and I.-C. Marcu, *Catalysis Science & Technology*, 2016, **6**, 6953-6964.
15. A. Düttmann, P. Bottke, T. Plaggenborg, C. Gutsche, J. Parisi, M. Knipper and J. Kolny-Olesiak, *Nanoscale Advances*, 2019, **1**, 2663-2673.
16. S. Motojima, T. Wakamatsu and K. Sugiyama, *Journal of the Less Common Metals*, 1981, **82**, 379-383.
17. S. Carenco, Z. Liu and M. Salmeron, *ChemCatChem*, 2017, **9**, 2318-2323.
18. V. Tallapally, R. J. A. Esteves, L. Nahar and I. U. Arachchige, *Chemistry of Materials*, 2016, **28**, 5406-5414.
19. J. Wu, J.-H. Li and Y.-X. Yu, *ChemPhysChem*, 2020, **21**, 2539-2549.

Chapter 8: Overall conclusions and future work

8.1 Overall conclusions

In summary, nickel-based catalysts have been thoroughly investigated for vapour-phase furfural hydrogenation, with the performance of key catalysts displayed in Table 10. The main conclusions from this work are as follows:

i) IWI nickel catalysts were found to be an order of magnitude more active than a commercially available copper chromite catalyst, however it had a low furfuryl alcohol selectivity of ~50 % compared to ~90 % for copper chromite. The IWI nickel catalysts exhibited rapid deactivation, with evidence from various analytical techniques suggesting the source of the deactivation was due to the formation of oligomeric/polymeric forms of furfuryl alcohol or furfural. The high activity of the nickel-based catalyst meant that there was some potential for modifying the catalyst to improve the poor furfuryl alcohol selectivity.

ii) A series of colloidal nickel and tin-nickel nanoparticle were successfully synthesised. Smaller (~4 nm) nanoparticles were able to be synthesised with an amine capping agent (phosphorus-free), however larger nanoparticles (~10 -15 nm) required the use of a phosphine capping agent. NAP-XPS revealed that the use of a phosphine capping agent led to the incorporation of phosphorus into the surface of the nanoparticles, regardless of whether the bulk structure indicated phosphorus incorporation. NAP-XPS studies of both the smaller tin-nickel and larger amorphous tin-nickel nanoparticles indicated that the top surface of the nanoparticles consisted of a tin-nickel phase with a Ni:Sn molar ratio of around 3:1 (depending on the sample/conditions), followed by a Sn-rich layer and then likely a nickel-based core. These uniform and well-characterised nanoparticle catalysts can be employed for furfural hydrogenation in order to elucidate structure-activity relationships.

iii) The introduction of tin to nickel-based IWI catalysts resulted in a significant improvement in the furfuryl alcohol selectivity (~85 % for a catalyst with 1.5 wt. % Sn, compared to ~50 % for the nickel-only equivalent), but an order of magnitude decrease in activity compared to the nickel-only catalyst. However, the lower activity was still comparable to that achieved by the commercially available copper chromite catalyst. Rapid deactivation was due to coking, which was found to be related to furfuryl alcohol-based species (likely oligomers). Further improvements to the furfuryl alcohol selectivity were achieved with the small tin-nickel colloidal nanoparticle catalyst

(~96 %), which is comparable to the selectivity of the copper chromite catalyst (~90 %). Despite significant sintering occurring during the reduction step prior to catalysis, the catalyst was also found to have a comparable activity to the copper chromite catalyst. Rapid deactivation was again found to be due to coking, likely related to furfuryl alcohol-based species. Ultimately, the introduction of tin to nickel-based catalysts results in a significant improvement in furfuryl alcohol selectivity, such that the catalyst is comparable to copper chromite.

iv) The presence of phosphorus in nickel nanoparticle catalysts resulted in an increase in the selectivity towards furfuryl alcohol (~67 %) compared to the IWI nickel catalyst (~50 %) and the small phosphorus-free nickel nanoparticle catalyst (~50 %). The bulk structure of the nickel nanoparticle catalysts (*i.e.* crystalline nickel metal versus amorphous nickel phosphide) did not affect the selectivity of the catalysts. The introduction of tin to the larger phosphine capped nanoparticles resulted in a further increase in furfuryl alcohol selectivity, reaching around 92 % for the amorphous tin-nickel nanoparticle catalyst. Whilst significant sintering was found to occur in the small phosphorus-free nanoparticle catalysts, there was minimal to no sintering observed for the larger phosphine capped nanoparticle catalysts, suggesting the presence of phosphorus may help to prevent sintering. The rapid deactivation in these catalysts was found to be caused by coking, likely due to furfuryl alcohol-based species (or other products and/or the reactant in the case of the nickel-only catalyst). Overall, the presence of phosphorus was seen to be largely beneficial, since high furfuryl alcohol selectivities were still able to be achieved with the introduction of tin (~92 %) and sintering was significantly limited or, in some cases, eliminated, resulting in more uniform catalysts.

v) The small phosphorus-free tin-nickel nanoparticles were found to suffer complete oxidation when placed in an oxidising environment at 180 °C. The larger amorphous nickel nanoparticles, prepared with a phosphine capping agent, exhibited significantly less oxidation and the oxidation was mostly limited to the top surface of the nanoparticles, with the bulk remaining reduced. It is likely that the size difference and the presence of phosphorus are playing a role in the difference in stability in an oxidising environment. The addition of tin to the larger amorphous nickel nanoparticles led to a significant decrease in the extent of nickel oxidation that occurred. This suggests that the presence of tin, likely as tin phosphide, may provide additional protection for the nickel against oxidation. The bulk structure of the phosphine capped

nickel nanoparticles (*i.e.* amorphous versus crystalline) had little impact on their oxidation stability, implying that the presence of phosphorus on the surface of the nanoparticles is key for determining their stability against oxidation.

Table 10: Summary of the performance of key catalysts for vapour-phase furfural hydrogenation under standard conditions

Catalyst	**Nominal Sn:Ni molar ratio**	**Selectivity to FOL / %**	**Mass activity after 1 h TOS/ $mmol_{prod}\ g_{cat}^{-1}\ h^{-1}$**	**Deactivation rate constant / h^{-1}**
IWI Ni/SiO_2	-	50 ± 4	622 ± 192	0.16 ± 0.02
IWI 1.5 wt. % $Sn\text{-}Ni/SiO_2$	1:7	85 ± 11	30 ± 17	0.15 ± 0.04
Copper chromite	-	90 ± 12	26 ± 14	0.06 ± 0.02
Small Ni nanoparticle catalyst	-	47 ± 6	66 ± 35	0.5 ± 0.1
Small SnNi nanoparticle catalyst	1:3	95 ± 12	16 ± 9	0.5 ± 0.1
Amorphous Ni-P nanoparticle catalyst	-	67 ± 9	35 ± 19	0.11 ± 0.03
Amorphous Sn-doped Ni-P catalyst	1:20	93 ± 12	12 ± 6	0.20 ± 0.05
Polycrystalline Ni nanoparticle catalyst (phosphine capped)	-	66 ± 9	10 ± 5	0.4 ± 0.1
Polycrystalline SnNi nanoparticle catalyst (phosphine capped)	1:20	88 ± 12	21 ± 11	0.28 ± 0.08

8.2 Future work

Some suggestions for possible areas of further research, based on the key findings of this thesis, are provided below.

The addition of tin to nickel catalysts led to remarkable increases in furfuryl alcohol selectivity, however the rapid deactivation exhibited in these catalysts remained an issue (although it should be noted that the current industrial catalyst, copper chromite, also exhibited comparably rapid deactivation). The main cause of the rapid deactivation was found to be coking, which was fairly consistently found to be associated with furfuryl alcohol-based species. Therefore, a topic for further research could be methods of preventing the rapid deactivation by limiting the coking that occurs. Both furfural and furfuryl alcohol polymerisation typically occurs *via* an acid-catalysed reaction,[1-5] and so one possible way of limiting coking may be to use supports that do not contain acid sites. This thesis briefly explored the use of less acidic supports such as titania and ceria, which was found to have no significant effect on the rate of deactivation observed. However, titania and ceria would still be expected to contain weakly acidic Lewis acid sites.[6-8] Although a lot of reports discuss using Brønsted acid sites for furfuryl alcohol polymerisation,[1-4] Lewis acid sites have also been shown to catalyse the reaction.[9] Therefore, investigating the use of non-acidic or basic supports could be of interest.

The synthesis of larger colloidal nickel nanoparticles without the use of a phosphine capping agent was briefly investigated in this thesis, however the method employed was unfortunately unsuccessful as it resulted in a bimodal particle size distribution (Chapter 4). Therefore, larger nickel nanoparticles were synthesised using a phosphine capping agent, though this was found to lead to phosphorus incorporation (Chapter 4). In the case of furfural hydrogenation, phosphorus incorporation was found to be somewhat beneficial as it led to a small increase in furfuryl alcohol selectivity and limited sintering (Chapter 6), however, this may not be the case for all reactions. Additionally, the incorporation of phosphorus leads to a more complicated system, which may make elucidating structure-activity relationships more challenging. Finally, the inability to currently synthesise larger nickel nanoparticles without the use of a phosphine capping agent means that it is not possible to make a direct comparison of any particle size effects on catalysis. Therefore, synthesising uniform, monodisperse larger nickel nanoparticles without a phosphine capping agent would have several benefits. Possible approaches could include a variant on the seeded growth mechanism attempted in this thesis, using a more unstable nickel pre-cursor or a Ni(0) pre-cursor as the source of the additional nickel that is added to the seeds.

Whilst the incorporation of phosphorus in colloidal nickel nanoparticles can be problematic (as discussed above), in the case of furfural hydrogenation, it led to a small increase in furfuryl alcohol selectivity. Additionally, the phosphine capped nanoparticles exhibited minimal to no sintering during reduction at 300 °C or during catalysis, in contrast to the small phosphorus-free nanoparticles that suffered significant sintering. Therefore, the presence of phosphorus in nickel nanoparticles does have some benefits. NAP-XPS was used to investigate the surface of the nanoparticles, revealing the presence of nickel phosphide species, however additional investigations of the structure of these catalysts could provide further insights into the reasons behind the decrease in sintering and increase in selectivity. Characterisation of the nanoparticles using *in situ* XAS could elucidate information about the bulk structure of the nanoparticles under working conditions and CO-DRIFTS could provide information about the positioning of phosphorus on the surface of the nanoparticles.

Further insights into structure-activity relationships for the tin-nickel catalysts may be gained by carrying out additional advanced characterisation, such as *in situ* X-ray absorption spectroscopy (XAS), *in situ* DRIFTS or NAP-XPS in the presence of both furfural and hydrogen (only hydrogen was available for the current work due to health and safety concerns regarding the use of furfural with the COVID-19 restrictions that were in place at the time). NAP-XPS with both hydrogen and furfural would allow the surface of the working catalyst to be identified, however this technique has limitations in that the pressure of gases would have to be significantly lower than in the standard reaction (*i.e.* <25 mbar *vs.* ~1000 mbar). Therefore, a technique such as *in situ* XAS could also be employed, as this would allow the catalyst to be studied under standard reaction conditions and provide information regarding the bulk structure of the working catalysts. CO-DRIFTS experiments may provide information on the positioning of tin on the surface of the nickel nanoparticles particles and *in situ* DRIFTS (*i.e.* carrying out furfural hydrogenation in the *in situ* DRIFTS cell) may provide information regarding the species involved in furfural hydrogenation and if/how this changes in the presence of tin. In combination, these advanced characterisation techniques would allow for a detailed understanding of the structure of the catalyst under reaction conditions (or close to reaction conditions) and so enable further conclusions to be drawn about the role of tin in nickel-based catalysts.

With the addition of tin to nickel catalysts affording such significant improvements in selectivity for vapour-phase furfural hydrogenation, it raises the possibility that this could be applicable to other similar hydrogenation reactions. For instance, tin-nickel catalysts may prove highly selective for the hydrogenation of α,β-unsaturated compounds (*e.g.* cinnamaldehyde), which is important since the ability to selectively hydrogenate C=O in the presence of other unsaturated bonds is necessary to

produce various industrially relevant allylic alcohols.[10] Therefore, future work could involve the application of this highly selective catalyst to a variety of other important hydrogenation reactions.

Overall, further understanding of the role of tin in drastically improving the selectivity of nickel-based catalysts, as well as of the coking process that results in rapid deactivation, is key for the rational design of an active, selective and stable catalyst for vapour-phase furfural hydrogenation and/or other similar hydrogenation reactions.

8.3 References

1. A. O. Iroegbu and S. P. Hlangothi, *Chemistry Africa*, 2018, **1**, 187-197.
2. T. Kim, R. S. Assary, C. L. Marshall, D. J. Gosztola, L. A. Curtiss and P. C. Stair, *ChemCatChem*, 2011, **3**, 1451-1458.
3. L. He, D. Li, D. Dong, J. Yao, Y. Huang and H. Wang, *Journal of Applied Polymer Science*, 2012, **124**, 3383-3391.
4. T. Kim, R. S. Assary, H. Kim, C. L. Marshall, D. J. Gosztola, L. A. Curtiss and P. C. Stair, *Catalysis Today*, 2013, **205**, 60-66.
5. K. J. Zeitsch, *The chemistry and technology of furfural and its many by-products*, Elselvier Science, Amersterdam, The Netherlands, 1 edn., 2000.
6. K. Nakajima, R. Noma, M. Kitano and M. Hara, *The Journal of Physical Chemistry C*, 2013, **117**, 16028-16033.
7. K. Bhattacharyya, A. Danon, B. K.Vijayan, K. A. Gray, P. C. Stair and E. Weitz, *The Journal of Physical Chemistry C*, 2013, **117**, 12661-12678.
8. N. C. Nelson, Z. Wang, P. Naik, J. S. Manzano, M. Pruski and I. I. Slowing, *J. Mater. Chem. A*, 2017, **5**, 4455-4466.
9. R. Zavaglia, N. Guigo, N. Sbirrazzuoli, A. Mija and L. Vincent, *The Journal of Physical Chemistry B*, 2012, **116**, 8259-8268.
10. X. Lan and T. Wang, *ACS Catalysis*, 2020, **10**, 2764-2790.

Appendix 1 – Calculation of the fraction of planar and corner/edge surface atoms in nanoparticles

The following set of equations and values were used to calculate the total number of atoms, the total fraction of surface atoms, the fraction of planar surface atoms and the fraction of edge/corner surface atoms in fcc cuboctahedron shaped particles of nickel between around 1 and 7 nm in size.[1-3]

For fcc crystals:

$$d_{sph} = 1.105 d_{at} {N_T}^{1/3}$$

where d_{sph} = diameter of the particle ('particle size'), d_{at} = the atomic diameter (for nickel this is 0.248 nm) and N_T = the total number of atoms in the particle, assuming it is a perfect crystal

Equation 13

For a cuboctahedron:

$$N_T = \frac{1}{3}[10m^3 - 15m^2 + 11m - 3]$$

where m = the number of atoms lying on an equivalent edge including corner atoms (see Figure 130)

Equation 14

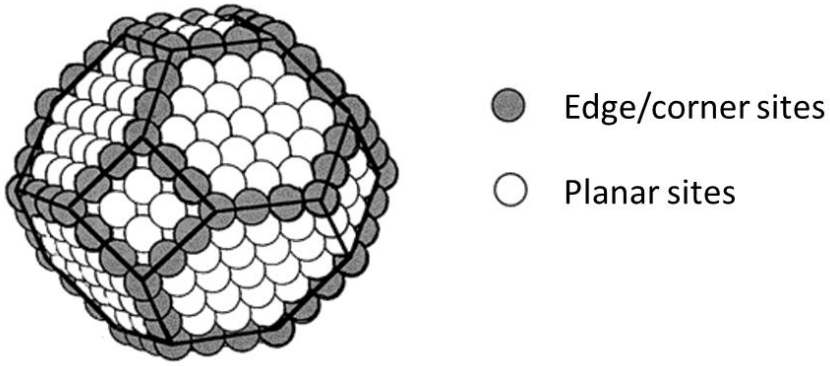

Figure 130: Diagram of an m = 4, cubooctahedron particle, reproduced from Blackmond *et al.*[3]

$$N_{DS} = 24(m-2) + 12$$

where N_{DS} = the number of corner and edge sites

Equation 15

$$N_{TS} = 6(m-2)^2 + 4(m-3)(m-2)$$

where N_{TS} = the number of planar sites

Equation 16

The fraction of total surface sites, corner/edge sites and planar sites, relative to the total number of atoms in the particle, is then given by the following equations:

$$D_{TDS} = \frac{N_{TS} + N_{DS}}{N_T}$$

where D_{TDS} = the fraction of total surface sites relative to the total number of atoms in the particle

Equation 17

$$D_{DS} = \frac{N_{DS}}{N_T}$$

where D_{DS} = the fraction of edge/corner sites relative to the total number of atoms in the particle

Equation 18

$$D_{TS} = \frac{N_{TS}}{N_T}$$

where D_{TS} = the fraction of edge/corner sites relative to the total number of atoms in the particle

Equation 19

References

1. R. Van Hardeveld and F. Hartog, *Surface Science*, 1969, **15**, 189-230.
2. B. Veisz, Z. Király, L. Tóth and B. Pécz, *Chemistry of Materials*, 2002, **14**, 2882-2888.
3. J. Le Bars, U. Specht, J. S. Bradley and D. G. Blackmond, *Langmuir*, 1999, **15**, 7621-7625.

Appendix 2 – Calibration of the TCD detector used for TPR experiments

The calibration of the TCD detector used in the TPR set-up was done by using known masses of CuO diluted in SiC, since CuO consumes one mole of hydrogen during reduction (Figure 131). Silicon carbide was used since very small masses of copper oxide were required to obtain peaks with areas similar to the supported metal catalysts. The silicon carbide was analysed in the TPR set-up prior to its use as the diluent to confirm that it was inert under the experimental conditions. The resulting calibration graph is shown in Figure 132 and gave an equation relating peak area to molar hydrogen consumption.

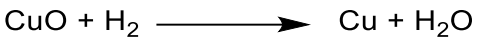

Figure 131: Reduction process of copper oxide

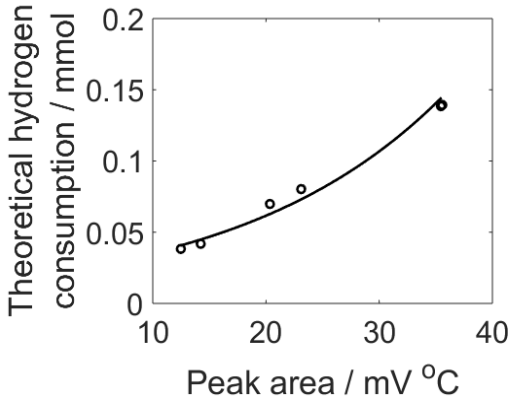

Figure 132: Calibration graph for the TCD in TPR set-up obtained *via* reduction of varying masses of CuO diluted in SiC

It should be noted that, initially, TCD calibration was attempted by simply changing the concentration of hydrogen in a flow nitrogen. However, the changes in hydrogen concentration achievable with the mass flow controllers connected to the TPR set-up greatly exceeded the changes in hydrogen concentration observed in a typical experiment. Additionally, the residence time of the gases on the detector was not taken into account using this method. As a result, this method of calibration was not suitable.

Appendix 3 – Calculation of the thickness of a Sn shell in a SnNi nanoparticle

The thickness of a Sn shell in the amorphous SnNi nanoparticles with a Ni:Sn ratio of 20:1 and a diameter of around 11 nm was calculated as follows.

First, the volume of a nanoparticle was calculated, assuming a spherical particle:

$$V_{nano} = \frac{4}{3}\pi\left(\frac{d_{nano}}{2}\right)^3 = \frac{4}{3}\pi\left(\frac{11\ \text{nm}}{2}\right)^3 = 697\ \text{nm}^3$$

where V_{nano} is the volume of the nanoparticle and d_{nano} is the diameter of the nanoparticle

Equation 20

The volume of a unit cell for metallic nickel[1] and tin[2] are 0.0439 nm^3 and 0.108 nm^3 respectively. Each unit cell for both nickel and tin contain four atoms, therefore the volume per nickel atom is 0.0110 nm^3 and the volume per tin atom is 0.0270 nm^3.

Given a Ni:Sn molar ratio of 20:1, the total number of atoms (both nickel and tin in the correct ratio) and the number of nickel atoms were calculated:

$$Total\ No.atoms = \frac{21V_{nano}}{(20V_{Ni} + V_{Sn})} = \frac{21 * 697\ \text{nm}^3}{(20 * 0.0110 + 0.0270)\ \text{nm}^3} = 59366$$

where V_{Ni} is the volume per nickel atom and V_{Sn} is the volume per tin atom

Equation 21

$$No.of\ Ni\ atoms = \frac{Total\ No.atoms}{21} * 20 = \frac{59366}{21} * 20 = 56539$$

Equation 22

Assuming the nanoparticle consists of a Ni core and Sn shell and that the nanoparticle is a sphere, the radius of the Ni core was calculated:

$$r_{Ni\ core} = \left(\frac{No.of\ Ni\ atoms * V_{Ni} * 3}{4\pi}\right)^{\frac{1}{3}} = \left(\frac{56539 * 0.0110\ \text{nm}^3 * 3}{4\pi}\right)^{\frac{1}{3}} = 5.3\ \text{nm}$$

where $r_{Ni\ core}$ is the radius of the nickel core

Equation 23

This allowed the thickness of the Sn shell to be calculated:

$$r_{Sn\ shell} = \left(\frac{d_{nano}}{2}\right) - r_{Ni\ core} = \left(\frac{11\ \text{nm}}{2}\right) - 5.3\ \text{nm} = 0.2\ \text{nm}$$

where $r_{Sn\ shell}$ is the radius of the tin shell

Equation 24

References

1. J. Rouquette, J. Haines, G. Fraysse, A. Al-Zein, V. Bornand, M. Pintard, P. Papet, S. Hull and F. A. Gorelli, *Inorganic Chemistry*, 2008, **47**, 9898-9904.
2. M. Wołcyrz, R. Kubiak and S. Maciejewski, *physica status solidi (b)*, 1981, **107**, 245-253.

Appendix 4: Development of a DRIFTS cell for CO-DRIFTS experiments

Diffuse reflectance infra-red Fourier transform spectroscopy (DRIFTS) is a technique that is often used for studying surface species since it has been shown to be more sensitive to surface species than transmission infra-red spectroscopy techniques.[1] It is therefore useful in the context of heterogeneous catalysis where the reactions are carried out on the surface of catalysts. The ability to carry out CO-DRIFTS and other *in situ* experiments can provide information on the surface structure of metal catalysts and chemical intermediates present on the catalyst during catalysis respectively. However, these experiments require the use of a DRIFTS cell rather than a simple sample cup. The design of a suitable DRIFTS cell for these *in situ* measurements is discussed below.

Although there are commercially available cells for carrying out *in situ* DRIFTS experiments, there are often issues that lead to inaccurate and unreliable results, such as gas by-passing the sample bed, inaccurate temperature readings and issues with backgrounding.[2-4]

Meunier *et al.*[3] investigated the performance of a commercially available high temperature/high pressure Spectra-Tech cell for *in situ* DRIFTS experiments. Figure 133 shows a schematic of the as received cell and highlights a key issue; there is a small gap between the bottom of the ceramic crucible and the metal base. This allows gas to leave the cell without passing through the sample bed. Since there is a porous frit which supports the sample bed and creates a significant back-pressure, the small gap then becomes the favoured gas outlet. Although the authors report that the manufacturers have produced updated versions which aim to seal this gap with a ceramic overlay, this area is subjected to large temperature changes and so an acceptable seal cannot be achieved. Therefore, without in-house modification, the large majority of gas will not pass through the sample as desired. Modification of this cell by applying Teflon tape to the bottom of the ceramic crucible was reported greatly improve this issue and give satisfactory results.[3]

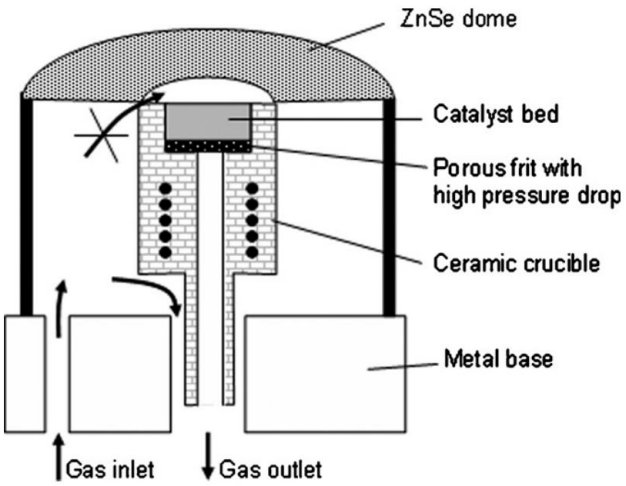

Figure 133: Schematic representation of a Spectra-Tech high temperature/high pressure cell for *in situ* DRIFTS measurements, reproduced from Meunier *et al.*[3]

The accuracy of temperature readings has also been found to be problematic in commercial DRIFTS cells.[2] Two DRIFTS cells were investigated; a Harrick cell and Spectra-Tech cell. As seen in Figure 134, at temperatures less than 100 °C, both of the cells' thermocouples provide reasonably accurate readings. However, at higher temperatures, particularly with the Harrick cell, there are quite substantial deviations. For instance, whilst the thermocouple in the Harrick cell reads a temperature of ~465 °C, the optical pyrometer records a bed temperature ~100 °C cooler. Although the temperature readings for the Spectra-Tech cell are more accurate, there is still a discrepancy at higher temperatures (cell thermocouple: ~490 °C, optical pyrometer: ~455 °C). This issue likely results from the thermocouples in the cells, particularly with the Harrick cell, not being placed close to the sample bed (see Figure 135). Therefore, thermocouple position within the cell is important to obtain accurate temperature measurements and, ideally, should be placed in position that sits within the catalyst bed.

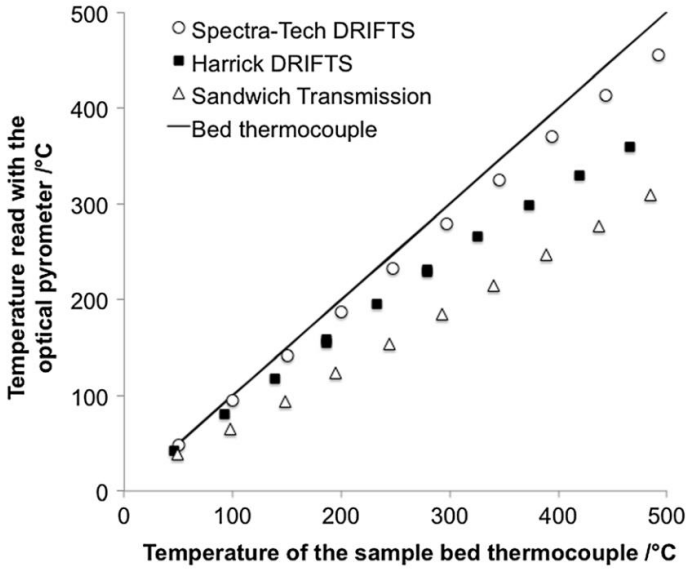

Figure 134: A comparison of the temperature readings of the cell thermocouple and an optical pyrometer for different commercially available DRIFTS cells (Harrick and Spectra-Tech) and a quartz U-tube reactor (Bed thermocouple), reproduced from Meunier *et al.*[2]

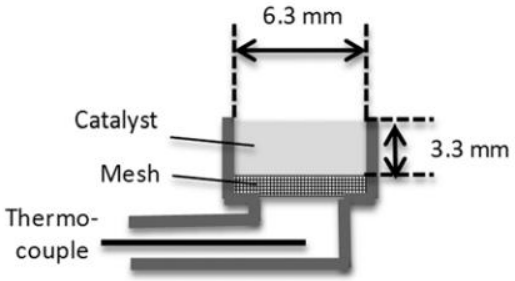

Figure 135: Schematic of the Harrick DRIFTS cell highlighting the thermocouple position, reproduced from Meunier *et al.*[2]

Another key problem with these commercial cells is that it is only possible to carry out measurements on one material at a time. This means that a background spectrum has to be taken separately to the sample and, especially during *in situ* experiments where the sample may heated/under gas flows, this may introduce some problems.[5] Due to the often lengthy pre-treatment procedures required for *in situ* measurements, background spectra frequently have to be taken a day before the sample spectra. The atmosphere in the DRIFTS instrument chamber (external to the DRIFTS cell, but including the beam path), can change significantly from day to day, in terms of both CO_2 and H_2O concentrations. This can make backgrounding sample spectra using background spectra that were taken the previous day challenging.

Additionally, during catalysis, certain adsorbed species may have short lifetimes on the catalyst, and so in the time it takes to purge the cell with inert gas, the species may desorb and/or change

structure. Therefore, the ability to take a background spectrum that will account for the presence of the gas phase species under reaction conditions is necessary to study these reactive species. This would not be possible if background spectra had to be taken at a separate time to the sample spectra.[5] Another issue, where higher boiling point species may condense on the windows in constantly changing amounts, would also prevent suitable backgrounding if the background spectra had to be taken separately to the sample spectra.[5]

Therefore, a cell that includes two bed sections, one for the sample and one for a reference material, and mechanism that allows for moving between the sample and reference without opening the DRIFTS cell or the instrument chamber is required. There is an example of a custom-made cell with this feature in the literature,[5] however there are potential pitfalls of the design, such as thermocouple position and the gas flow (since the outlet position means gas will only pass through the one bed at a time). The design is also fairly complex, using gear mechanisms to move from sample to reference. Consequently, the development/optimisation of a cell that accounts for the issues discussed above is required to carry out accurate and reliable *in situ* DRIFTS experiments. A cell for carrying out *in situ* DRIFTS experiments (including CO-DRIFTS), with a suitable mechanism for obtaining a background, was therefore developed as described below.

Appendix 4.1: Development and optimisation of the DRIFTS cell

The initial DRIFTS cell design and the current cell design are shown in Figure 136a and b respectively. The main areas of development were improving signal and separating the bed into two sections – one for the sample and the other for a reference material that can be used as a background. In the initial design, the depth of the section where the window will be screwed in, is about twice that of the current cell. Since DRIFTS uses the diffuse reflections, these high sides were a significant source of signal loss, and so reducing the depth of this section resulted in improved signal. Sample height also plays a key role in the signal obtained. In the original cell, the shape of the mirrors/width of the cell prevented the cell reaching the sample height that resulted in the best signal. Therefore, the cell was further modified by 'smoothing' the edges of the cell. These changes combined meant that a satisfactory signal, in comparison to a standard sample cup, was obtained.

Next, a suitable method of splitting the bed into two parts whilst still allowing an even gas flow through the bed was developed. The design involved inserting two thin pieces of metal, with numerous small holes to ensure even gas flow, into the centre of the bed. To prevent any of the sample transferring into the background section (or *vice versa*) whilst the gases are flowed through the bed, a small amount of quartz wool can be placed between the two pieces of perforated metal.

Quartz wool can also be inserted where the gases enter and exit the bed to prevent the sample/background material moving into these areas.

At this stage, the decision was made to proceed with producing the cell out of stainless steel and adding the necessary fittings (see Figure 136c).

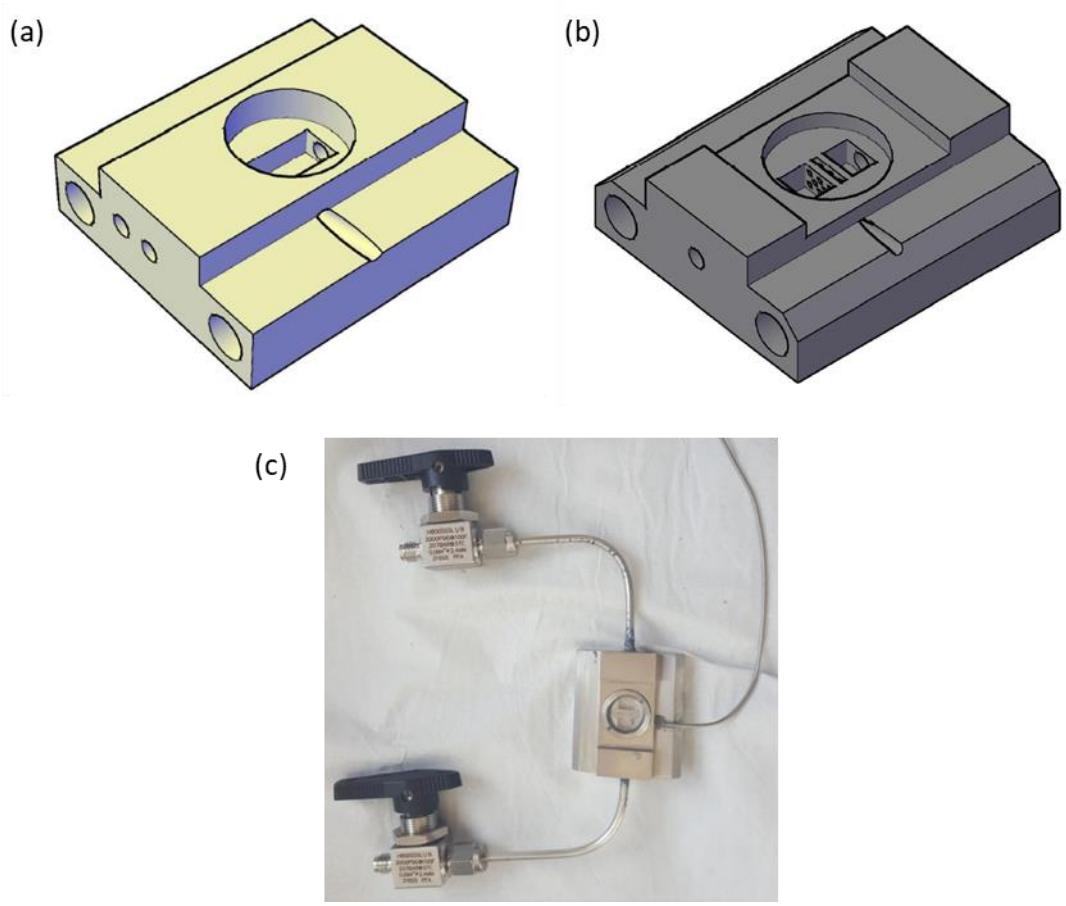

Figure 136: (a) the initial DRIFTS cell design, (b) the current DRIFTS cell design and (c) the produced DRIFTS cell including the necessary fittings

Appendix 4.2: Comparison of DRIFTS cell and sample cup

Once the DRIFTS cell had been made out of stainless steel, it was possible to compare the cell, including the window and small ring which is used to attach the window (see Figure 137), to a standard sample cup. For this comparison, a sample of SBA-15 was used, and as seen in Figure 138, whilst there is a decrease in the signal of around 30 % between the sample cup and the cell when the ring is partially unscrewed (as will likely be the case when the O-ring and window are present), a good signal was still obtained. Therefore, the DRIFTS cell is suitable for further testing.

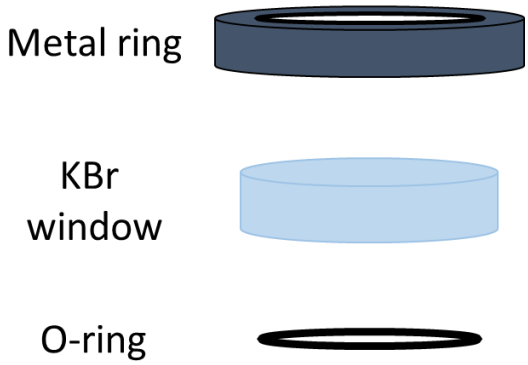

Figure 137: Schematic representation of the window sealing mechanism

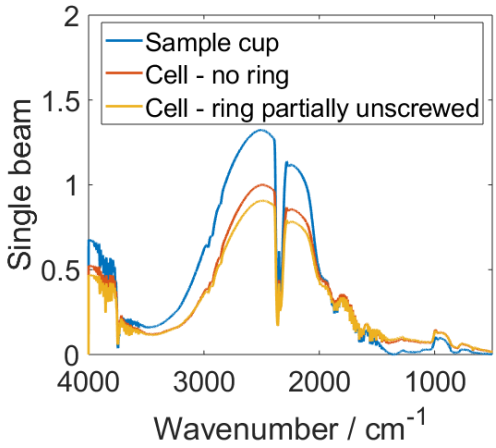

Figure 138: DRIFT spectra (no background – single beam) comparing the signal obtained using a sample cup to that of the DRIFTS cell without the ring (for attaching the window) and with the ring partially unscrewed (1 turn out)

Appendix 4.3: Testing of the mechanism for obtaining background measurements

A key benefit of this cell design is the ability to take background measurements continually throughout experiments, with the background material under the same conditions as the sample. The mechanism for obtaining a background relies on a sliding component, which moves a set distance, corresponding to the distance between the sample and the background material (see Figure 139). Metal wires are attached to the sliding section, which allows the cell to be moved back and forth (between sample and background), without opening the DRIFTS instrument.

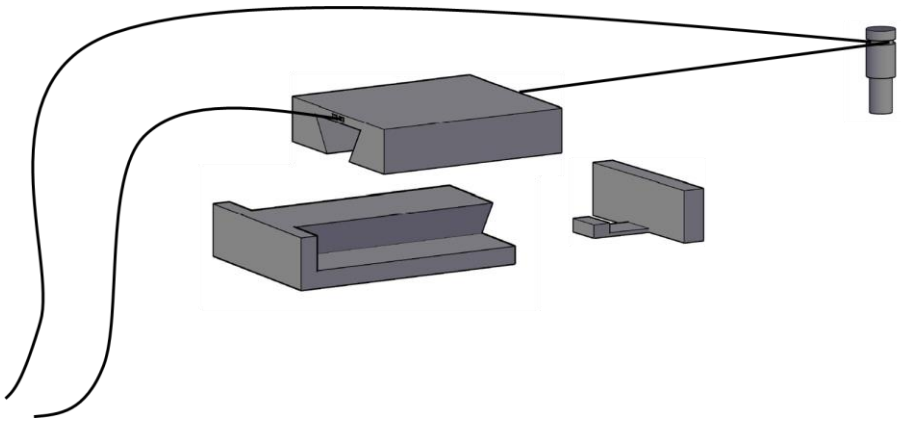

Figure 139: Schematic of sliding mechanism for use with the DRIFTS cell

It is important to test this mechanism to ensure it is operating appropriately. Silane-grafted SBA-15 was chosen as the sample, with unmodified SBA-15 then acting as the background material. As a comparison, a sample cup was used to obtain spectra for the silane-grafted and unmodified SBA-15 separately. The silane chosen was 3-(trimethyoxysilyl)propyl methacrylate, which contains one carbonyl group per molecule, with the silane-grafted SBA-15 then found to contain around 0.16 wt. % carbonyl based on CHN analysis. Two sharp peaks are expected at 1643 cm^{-1} and 1728 cm^{-1} based on the reference spectrum of the silane compound.[6] The results are shown in Figure 140. Although the peaks are more distinct when the sample cup is used, the peaks are also present when the DRIFTS cell with the sliding mechanism for backgrounding is used. As noted previously, there was around a 30 % reduction in signal when the DRIFTS cell was used compared to the sample cup. Therefore, this likely explains the less distinct peaks observed when using the DRIFTS cell with the sliding mechanism to obtain a background. Overall, although there is some loss of signal, the cell and sliding mechanism are performing well enough to detect the low amount of carbonyl (0.16 wt. %) present in the silane-grafted SBA-15.

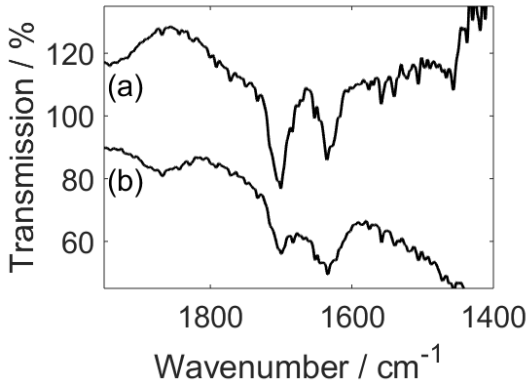

Figure 140: DRIFT spectra for silane-grafted SBA-15; (a) using sample cup; (b) using DRIFTS cell with sliding mechanism for backgrounding

Appendix 4.4: Optimising the gas flow setup

Initial attempts to flow gases through the cell led to the beds of sample and reference material being disturbed. The main issue was that a slight build-up of pressure occurred whilst attaching the gas line, which is flowing with gas at a low flow rate to ensure it remains vented, and opening the valves to the cell. This slight pressure build-up was released when the valves to the cell were opened, which resulted in the beds being disturbed. Therefore, a setup similar to that shown in Figure 141 was used. Whilst attaching the gas line to the cell, the ball valve to the oil bubbler was open, allowing the gas to be vented through the oil bubbler and so avoiding any significant pressure build up. Once the cell was attached to the gas line and the ball valves either side of the cell were open, the ball valve for the oil bubbler was closed to avoid any gas by-passing the bed. Since this setup results in no significant pressure build up, gas can successfully be flowed through the beds with no disturbances.

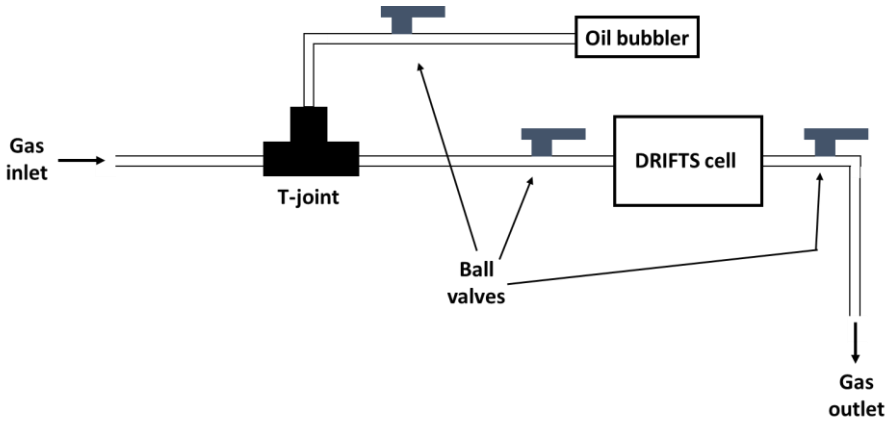

Figure 141: Schematic of the method of CO exposure

Appendix 4.5: CO-DRIFTS with a standard nickel reference catalyst

In order to confirm that the cell was able to operate correctly, a CO-DRIFTS experiment was carried out on a sample of post-reduction IWI Ni/KIT-6 catalyst. The sample was reduced under the standard conditions for the IWI nickel catalysts (Chapter 3), and then transferred to a glovebox air sensitively to prevent oxidation of the catalyst. The cell was loaded with the reduced catalyst and KIT-6 (to act as the background material) and then sealed. The catalyst was exposed to pure CO using the gas flow set up described above and the cell was then vented with Ar and sealed. The spectrum (Figure 142) contained three main peaks; one centred at 1994 cm^{-1}, the second centred at 1874 cm^{-1} and the third centred at around 1626 cm^{-1}. These peaks are consistent with the literature for similar nickel catalysts and correspond to CO binding to the metal linearly, CO binding to the metal in a bridging manner and an adsorbed carbonate species that forms when CO interacts

with the support or NiO.[7, 8] The good match between spectra obtained in the literature and the spectrum obtained here indicates that the cell is operating appropriately. However, it should be noted that there were some issues with obtaining a suitable background. This was mainly due to the dark colour of reduced nickel catalysts since DRIFTS relies on reflectance and dark coloured materials will absorb the radiation and significantly lower the signal obtained. Therefore, applying a background from a material that is white in colour (KIT-6) did not produce reliable data. In this case, the Ni/KIT-6 catalyst, prior to CO exposure, was used as the background, since this was not an *in situ* experiment (*i.e.* no flowing gas during data acquisition) and so this background procedure was appropriate. However, if an *in situ* experiment was attempted, it would be important to also take into account any changes in the spectrum for the reference material when compared to the pre-exposure spectrum. This correction should allow for appropriate backgrounds to be applied under *in situ* conditions.

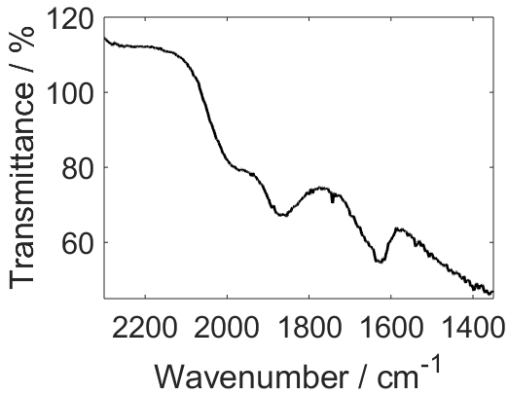

Figure 142: DRIFT spectrum of a sample of reduced IWI Ni/KIT-6 catalyst after exposure to CO

References

1. M. B. Mitchell, in *Structure-Property Relations in Polymers*, American Chemical Society, 1993, vol. 236, ch. 13, pp. 351-375.
2. H. Li, M. Rivallan, F. Thibault-Starzyk, A. Travert and F. C. Meunier, *Physical Chemistry Chemical Physics*, 2013, **15**, 7321-7327.
3. F. C. Meunier, A. Goguet, S. Shekhtman, D. Rooney and H. Daly, *Applied Catalysis A: General*, 2008, **340**, 196-202.
4. F. C. Meunier, *Reaction Chemistry & Engineering*, 2016, **1**, 134-141.
5. A. Drochner, M. Fehlings, K. Krauß and H. Vogel, *Chemical Engineering & Technology*, 2000, **23**, 319-322.
6. W. E. Wallace and NIST Mass Spectrometry Data Center, in *NIST Chemistry WebBook, NIST Standard Reference Database Number 69*, eds. P. J. Linstrom and W. G. Mallard, National Institute of Standards and Technology, Gaithersburg MD, DOI: https://doi.org/10.18434/T4D303, ch. Infrared Spectra.
7. J. Zarfl, D. Ferri, T. J. Schildhauer, J. Wambach and A. Wokaun, *Applied Catalysis A: General*, 2015, **495**, 104-114.

8. M. Agnelli, H. M. Swaan, C. Marquez-Alvarez, G. A. Martin and C. Mirodatos, *Journal of Catalysis*, 1998, **175**, 117-128.